Convection, Radiation, and Climate: Fundamental Mechanisms and Impacts of a Changing Atmosphere

By

Jacob T. Seeley

A dissertation submitted in partial satisfaction of the

requirements for the degree of

Doctor of Philosophy

in

Earth and Planetary Sciences

in the

Graduate Division

of the

University of California, Berkeley

Committee in charge:

Professor David M. Romps, Chair
Professor John C. H. Chiang
Professor Willam D. Collins
Professor Inez Fung

Fall 2018

Convection, Radiation, and Climate: Fundamental Mechanisms and Impacts of a Changing Atmosphere

Abstract

Convection, Radiation, and Climate: Fundamental Mechanisms and Impacts of a Changing Atmosphere

by

Jacob T. Seeley

Doctor of Philosophy in Earth and Planetary Sciences

University of California, Berkeley

Professor David M. Romps, Chair

A hierarchy of models is used to connect fundamental mechanisms to impacts in a changing atmosphere. On the subject of forcings, an intermediate-complexity model for the radiative forcing of carbon dioxide is developed. This model is used to provide simple explanations for well-known properties of carbon dioxide (CO_2) forcing such as its magnitude, dependence on atmospheric conditions, and logarithmic scaling. In the realm of impacts, climate models are used to investigate the impact of global warming on the kind of severe thunderstorms that produce hail and damaging winds. The results suggest that severe thunderstorms will become more damaging in the future, and that increases in Convective Available Potential Energy (CAPE) are the culprit. This motivates the subsequent use of cloud-resolving simulations to develop of a theory of CAPE and its dependence on temperature, which highlights the importance of the atmospheric saturation deficit. Another result of that theory for CAPE is an explanation for why cloud buoyancy and updraft strength are largest in the upper troposphere, a property that has traditionally been attributed to the release of the latent heat of fusion above the melting line. It is shown that this ice-based explanation is a fallacy: cloud buoyancy and updraft strength are the same in a world with or without ice. Finally, on the topic of feedbacks, the relationship between high clouds and the tropopause is investigated in cloud-resolving simulations. The results support the existence of a Fixed Tropopause Temperature (FiTT) rather than a Fixed Anvil Temperature (FAT), which implies a decoupling of anvil clouds from the tropopause. This decoupling motivates further investigation into the formation mechanisms of anvil clouds; it is found that anvil clouds do not result from enhanced detrainment below the tropopause, as is the traditional view, but from the slow evaporation of cloudy air in the cold upper troposphere.

For Joseph and Robert.

Contents

Acknowledgments

Choosing a PhD advisor on the basis of a few interactions is always a bit of a gamble, but my gamble paid off in a big way. David Romps has been a brilliant collaborator, mentor, and role model, and the time I spent in his presence was incredibly formative. I can only hope that some small amount of information, insight, wisdom — or at the very least, entertainment — flowed upstream.

Another benefit of working with David is that he has surrounded himself with an incredible group of scientists. To the Romps group, past and present: Bowen, Wolfgang, Nadir, Rusen, Jake E., Da, Yi-Chuan, Suqin, Bolei, Nathaniel — I learned so much from you, and I cherished our time together. I look forward to visiting each other in remote parts of the world in years to come.

McCone Hall has been a wonderful home for the past six years, and that is mainly due to the people who inhabit it. I came to Berkeley off-cycle, in January, which turned out to be a boon, because I became an honorary member of two separate incoming classes of graduate students. This enlarged cohort turned out to be full of funny, kind, and highly intelligent future friends, whose camaraderie over the years was invaluable. I owe a particular debt to the Firetrail Running Club for reliably getting me out of the office and thereby keeping me sane. To my officemates Ben, Jake E., and Nathaniel: moldy carpet and all, Room 449 was one of my favorite places to hang out. Finally, I am deeply grateful to many members of the EPS staff: Margie, Nadine, Rachel, Siti, and Veronica — thank you for saving me from being swallowed by bureaucracy, over and over.

To the other members of my committee: John Chiang, Inez Fung, Bill Collins — thank you for your interest in my work, the great classes you taught, and for your letters of support.

I also must acknowledge my second home, 1934 Stuart St., and the people who shared it with me: Jacob, Nathan, Danielle, Akriti, Emma, Mike — it was a great privilege to spend my graduate school years in communal housing with such fine folks.

All graduate careers have low points, and I may not have made it through mine without the support of my mother, Jan, my brother, Paul, and my grandmother, Char. I am also thankful to my therapist, Joanne, for helping me to manage my fear of public speaking.

Finally, I am thankful for Rosa for always reminding me that the world is big.

Chapter 1

Introduction

I came to graduate school to study global warming, but quickly learned that there are many ways to do so. One can study the drivers of the problem, which are called *forcings* because they are what is forcing the Earth system to change. Or, instead of studying the cause of the warming, one can study its effects. Roughly speaking, these effects can be divided into two categories. On one hand, there are *impacts*: the consequences of warming for things that people care about, such as human health, the infrastructure of our societies, the biodiversity of the planet, and so on. On the other hand, there are *feedbacks*: ways in which the Earth system responds to warming that feed back on, or modify, the original cause of the warming itself. The reason to study feedbacks is to determine just how hot the planet will get due to our influence.

This dissertation weaves together the contributions I have made to these three areas of climate science during graduate school. On the subject of forcings, Chapter 2 develops an intermediate-complexity model for the radiative forcing of carbon dioxide, and uses that model to provide simple explanations for well-known properties of carbon dioxide (CO_2) forcing such as its magnitude, dependence on atmospheric conditions, and logarithmic scaling.

In the realm of impacts, Chapter 3 uses climate models to investigate the impact of global warming on the kind of severe thunderstorms that produce hail and damaging winds. The results suggest that severe thunderstorms will become more damaging in the future, and that increases in Convective Available Potential Energy (CAPE) are the culprit. This points to the need for a theory of CAPE and its dependence on temperature, which is developed in Chapter 4. One of the results of that theory for CAPE is an explanation for why cloud buoyancy and updraft strength are largest in the upper troposphere, a property that has traditionally been attributed to the release of the latent heat of fusion above the melting line. Chapter 5 shows that this ice-based explanation is a fallacy: cloud buoyancy and updraft strength are the same in a world with or without ice. Taken together, Chapters 4 and 5 provide theoretical support for the severe-weather impacts derived from global climate models in Chapter 3.

Finally, on the topic of feedbacks, Chapters 6 and 7 focus on the relationship between high clouds and the tropopause. The principal result of Chapter 6 is a *decoupling* of anvil clouds and the tropopause; our results support the existence of a Fixed Tropopause Temperature (FiTT) rather than a Fixed Anvil Temperature (FAT), which has implications for the sign of the high-cloud feedback. Chapter 7 provides an explanation for this decoupling: tropical anvil clouds do not result from enhanced detrainment below the tropopause, but from the slow evaporation of cloudy air in the cold upper troposphere. This is a significant revision of the conventional understanding of anvil clouds, with consequences for how high-cloud fraction will change in a warming atmosphere.

Although I have chosen to organize this dissertation in terms of forcings, impacts, and feedbacks, it can also be assorted by the subfield of physics involved — radiation, convection, or both — as well as by the type of research tools employed. Chapter 2, about CO_2, involves radiation physics alone, and uses tools at either end of the spectrum of complexity: from analytical models to full line-by-line radiative transfer calculations. Chapter 3, about severe weather, is about intense convection, and uses the output of full-complexity global climate models in conjunction with a simple proxy for severe thunderstorms. The final four chapters use high-resolution, but idealized, simulations of convection, the results of which are often further analyzed with pencil-and-paper ("bulk-plume") models of convecting atmospheres. Chapters 4 and 5, about CAPE, cloud buoyancy, and ice, are about tropical convection, with a particular emphasis on how thermodynamics couples to dynamics. Finally, chapters 6 and 7 concern the interplay between radiation and convection. Taken all together, this dissertation uses a hierarchy of models to connect fundamental mechanisms to impacts in a changing atmosphere.

Chapter 2

Insights from a simple model for CO_2 radiative forcing

Although CO_2 radiative forcing can be computed very precisely with comprehensive radiative transfer models, there is still value in simpler models that can explain well-known properties of CO_2 forcing such as its magnitude, dependence on atmospheric conditions, and logarithmic scaling. Here, we use approximations to the equations of radiative transfer and CO_2 spectroscopy to rederive the analytical model for CO_2 forcing originally proposed by Wilson and Gea-Banacloche (2012). We extend this simple model to account for non-isothermal stratospheres and overlap with water-vapor absorption bands, and use line-by-line calculations of outgoing longwave radiation to verify that the simple model reproduces the dependence of CO_2 forcing on atmospheric structure and composition. We also use the simple model to show that the logarithmic scaling of CO_2 forcing derives from the exponential decay of CO_2 absorptivity in the 15-μm band. This spectroscopic explanation stands in opposition to an alternative explanation based on line-by-line radiative forcing that was recently proposed by Huang and Shahabadi (2014). We show that this alternative line-by-line explanation is not relevant to the logarithmic scaling of the spectrally-integrated forcing.

2.1 Introduction

How sensitive is Earth's temperature to changes in atmospheric carbon dioxide (CO_2)? To answer this question, we must first know the imbalance in Earth's energy budget, or "radiative forcing", caused by a CO_2 perturbation. It is conventional to discuss CO_2 radiative forcing in terms of a standardized perturbation, typically taken to be an instantaneous doubling of the CO_2 concentration. Since anthropogenic activities are projected to lead to a doubling of the preindustrial CO_2 concentration during the 21st century, one CO_2 doubling provides a convenient yardstick for contemporary climate change. Here we will refer to the top-of-atmosphere (TOA), instantaneous radiative forcing from a doubling of CO_2 as F_{2x} (W/m^2).

Compared to other fundamental quantities in climate science — such as Earth's feedback parameter, or equilibrium climate sensitivity — $F_{2\mathrm{x}}$ is, in principle, straightforward to calculate. Since $F_{2\mathrm{x}}$ measures the imbalance in the energy budget after a $\mathrm{CO_2}$ doubling but before temperature and other state variables have had time to evolve, $F_{2\mathrm{x}}$ depends only on the equations of radiative transfer, the spectroscopic properties of $\mathrm{CO_2}$, and the initial state of the atmosphere, all of which are known or measurable to a high level of precision. Indeed, for a given atmospheric state, there is a ground-truth standard for $F_{2\mathrm{x}}$: a line-by-line (LBL) radiative transfer calculation run with a contemporary spectroscopic database. The spectroscopic foundation for such calculations is so robust that uncertainties in the absorption properties of $\mathrm{CO_2}$ are estimated to yield only a 1% uncertainty in $\mathrm{CO_2}$ forcing (Mlynczak et al. 2016).

Example LBL calculations of $\mathrm{CO_2}$ forcing are shown in Figure 2.1. We use the Reference Forward Model (RFM; Dudhia 2017) with the HITRAN2016 spectroscopic database (Gordon et al. 2017) to compute the outgoing longwave radiation from representative tropical (Maritime continent), midlatitude (Southern Ocean), and high-latitude (Arctic) atmospheric columns, with $\mathrm{CO_2}$ concentrations varied about the preindustrial value of 280 ppm by several factors of two in either direction. For simplicity, water vapor ($\mathrm{H_2O}$) is the only other radiatively active gas in these calculations, and we assume clear-sky conditions. For each $\mathrm{CO_2}$ concentration q and atmospheric column S, we calculate $F_{2\mathrm{x}}(q, S)$ as

$$F_{2\mathrm{x}}(q, S) = \mathrm{OLR}(q, S) - \mathrm{OLR}(2q, S), \tag{2.1}$$

where OLR ($\mathrm{W/m^2}$) is the upwelling longwave radiation at TOA, and the sign convention is such that a decrease in OLR from a $\mathrm{CO_2}$ doubling is a positive radiative forcing. Further details of the LBL calculations are given in Appendix A.

Several interesting and well-known properties of $\mathrm{CO_2}$ forcing are immediately apparent from Figure 2.1. First, we note that a typical value for $F_{2\mathrm{x}}$ is about 3 $\mathrm{W/m^2}$. Since Earth's gross incoming/outgoing radiative fluxes in equilibrium are about 240 $\mathrm{W/m^2}$, a $\mathrm{CO_2}$ doubling causes about a 1-2% perturbation to these steady-state energy flows. This crucial number sets the scale of the contemporary climate-change problem, and is well-known from decades of detailed radiative transfer calculations. But, must our understanding of $F_{2\mathrm{x}}$ derive only from complicated numerical models, or can we estimate $F_{2\mathrm{x}}$ in a back-of-the-envelope fashion?

It is also apparent from Figure 2.1 that $F_{2\mathrm{x}}$ depends on the atmospheric state: $\mathrm{CO_2}$ forcing is systematically higher for the tropical column than for the high-latitude column, with the midlatitude column falling in between. This, too, is a well-known property of $\mathrm{CO_2}$ forcing, reflected in the fact that a spatially-uniform $\mathrm{CO_2}$ perturbation produces a substantial pole-to-equator gradient in TOA radiative forcing (Huang et al. 2016). This has important implications for the polar amplification of global warming (Merlis and Henry 2018). But, of the many differences between tropical and higher-latitude atmospheres, what aspects in particular produce the observed geographical variation in $\mathrm{CO_2}$ forcing?

Figure 2.1d also shows the results of a second computation of $F_{2\mathrm{x}}$, identical to the first except that the $\mathrm{H_2O}$ concentrations were zeroed out in the radiative transfer calculations. This reveals that the presence of $\mathrm{H_2O}$ damps the radiative forcing from $\mathrm{CO_2}$ for the tropical

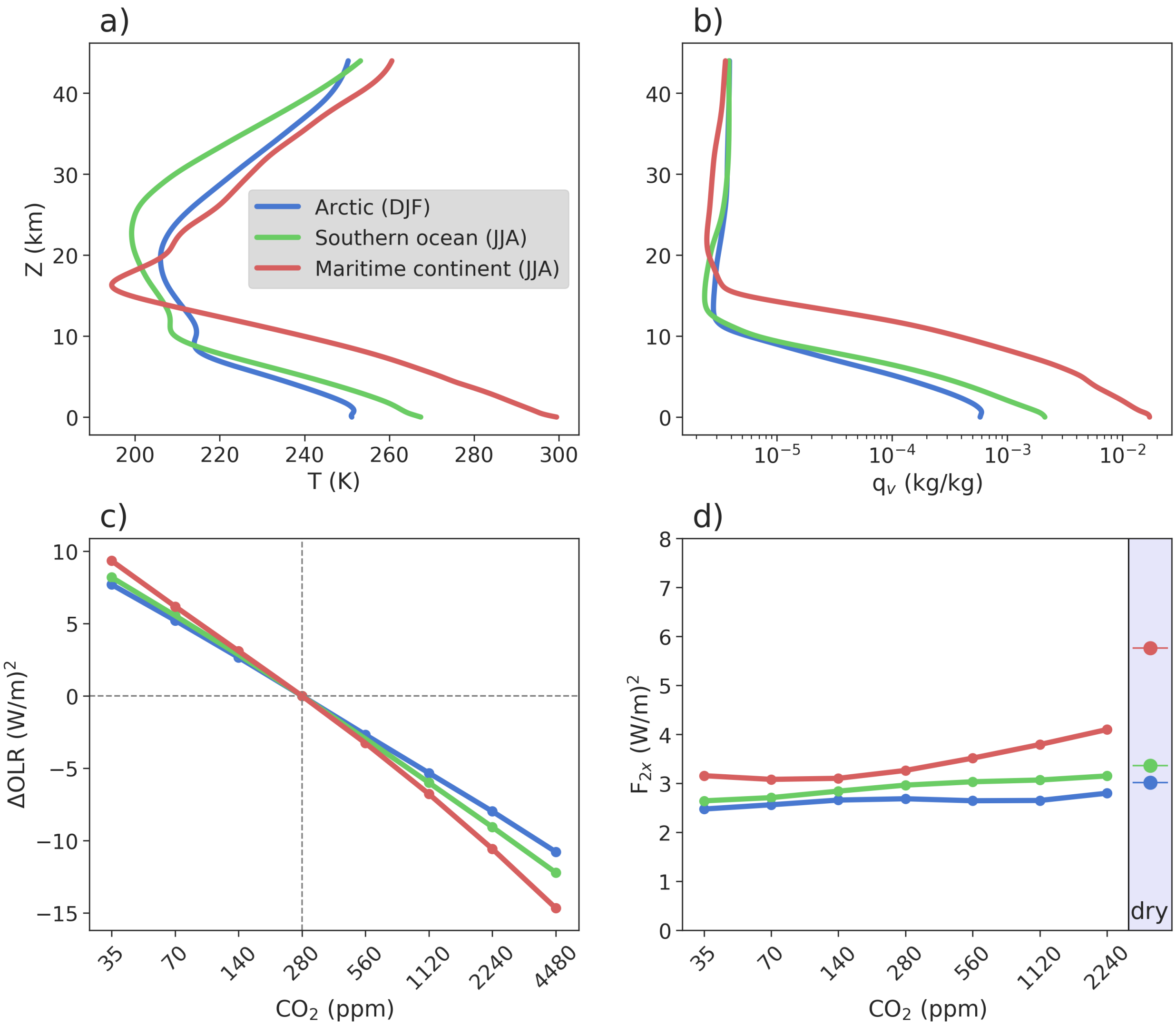

Figure 2.1: Profiles of (a) temperature and (b) specific humidity averaged over representative tropical (Maritime continent; 10S–10N, 100E–150E), midlatitude (Southern Ocean; 60S–65S), and high-latitude (Arctic; 80N–90N) regions from the ERA5 reanalysis. All averages are taken from the year 2017, with the months December, January, and February (DJF) used for the Arctic region and the months June, July, and August (JJA) used for the other two regions. To avoid complications due to topography, only ocean gridpoints are included in the averages. (c) Changes in outgoing longwave radiation (relative to an atmosphere with 280 ppm CO$_2$) computed by the line-by-line radiative transfer model RFM (Dudhia 2017), as a function of CO$_2$ concentration. (d) Instantaneous TOA radiative forcing from a doubling of CO$_2$ (F_{2x}). In (d), the mean CO$_2$ forcings without inclusion of water vapor are indicated for each sounding in the shaded blue box to the right (labeled “dry”).

column by about 40%, whereas the impact of H$_2$O is much reduced for the higher-latitude columns. It is natural to expect the impact of water vapor to be reduced in relatively colder (and therefore drier) soundings, and surely overlap between the absorption bands of H_2O and CO_2 is to blame for the damping effect. But, what explains the magnitude of the H_2O damping effect in moist atmospheres?

Finally, Figure 2.1 also shows that, for a given atmospheric column, $F_{2x}(q, S)$ is fairly independent of q: the radiative forcing of a CO_2 doubling is nearly the same whether the initial CO_2 concentration is small or large, varying by less than $\simeq 30\%$ as CO_2 is varied by a factor of 64. In other words, the radiative forcing from CO_2 scales approximately logarithmically with CO_2 concentration. For brevity, we will refer to this property as the "log-scaling" of CO_2 forcing. Indeed, this well-known log-scaling behavior is the motivation for the conventional focus on CO_2 forcing *per doubling*, rather than per increment of (absolute) CO_2 concentration. But, what physics explains the log-scaling of CO_2 forcing?

These LBL calculations have recapitulated several well-known properties of CO_2 forcing, while also raising a number of fundamental questions, namely:

1. Why is a typical value of F_{2x} about 3 $\mathrm{W/m^2}$?
2. What aspects of atmospheric structure and composition influence F_{2x}?
3. What physics explains the log-scaling of F_{2x}?

The purpose of this chapter is to answer these questions with an analytical model for F_{2x} that is accurate enough to be quantitatively useful, yet simple enough to be explicit about its dependence on CO_2 spectroscopy and atmospheric composition/structure. The simplest version of the model we develop is identical to that proposed by Wilson and Gea-Banacloche (2012), but we rederive it here using novel heuristics. We also extend this model to apply to somewhat more realistic atmospheres. Even when applied to realistic atmospheres, of course, the analytical model is not meant to replace comprehensive LBL calculations, or to stand in for empirical functions for F_{2x} that have been tuned to accurately reproduce LBL calculations over very large ranges of CO_2 (Etminan et al. 2016, e.g.,). The goal is to aid our understanding of CO_2 forcing with a simple model that makes the relevant physics transparent.

We will address all three of the questions listed above, but the third will be a particular focus. The reason for this is that there are currently two distinct explanations for the log-scaling of CO_2 forcing to be found in the literature. The first explanation is based on the band-integrated absorption properties of the CO_2 molecule — specifically, the fact that CO_2 absorption coefficients generally fall off exponentially away from the center of the most strongly-absorbing (15-μm) absorption band (Pierrehumbert 2010). The second explanation, on the other hand, hinges on the fact that the optical depth profile of a well-mixed greenhouse gas *at any given wavenumber* is exponential in height when pressure is exponential in height (Huang and Shahabadi 2014). This basic fact causes the line-by-line radiative forcing to exhibit log-scaling in typical tropospheric conditions, regardless of the CO_2 band structure within which these lines are embedded. What is the connection between these two seemingly

ingredient	**simplification**
radiative transfer	“unit optical depth” approximation
CO_2 spectroscopy	piecewise-exponential fit to 15-μm absorption band
atmospheric structure	constant tropospheric lapse rate, isothermal stratosphere

Table 2.1: (left column) The physical ingredients on which CO_2 radiative forcing depends, and (right column) the simplified versions of these ingredients used to derive the analytical model for $F_{2\text{x}}$.

independent explanations? Does the spectrally-integrated forcing actually inherit its log-scaling from the line-by-line behavior, rather than the CO_2 band structure, or are both mechanisms involved? Since log-scaling is such a fundamental property of CO_2 forcing that it underlies the very vocabulary we use to discuss contemporary climate change (i.e., the “per-doubling” emphasis), it is imperative that we reconcile these divergent explanations.

2.2 Heuristic derivations of CO_2 forcing

To make the problem of CO_2 forcing analytically tractable, we must approximate each of the three “ingredients” on which $F_{2\text{x}}$ depends: the equations of radiative transfer, the spectroscopic properties of CO_2, and the initial state of the atmosphere. The approximations we make for each of these three ingredients are described below and listed in table 2.1.

To simplify the equations of radiative transfer, we make the “unit optical depth” approximation. This commonly-invoked approximation says that radiative emission to space from a given CO_2 line can be regarded as occurring entirely at the level where $\tau_k = 1$, where τ_k is the optical depth at wavenumber k (Pierrehumbert 2010). The unit optical depth approximation is accurate to within $\simeq 10\%$ for standard conditions in terrestrial atmospheres (Appendix B). For CO_2 forcing, this means that we can approximate the outgoing longwave radiation at wavenumber k, OLR_k ($\text{W/m}^2/\text{cm}^{-1}$), as

$$\text{OLR}_k \simeq B(k, T_\text{e}), \tag{2.2}$$

where $B(k, T)$ ($\text{W/m}^2/\text{cm}^{-1}$) is the Planck function evaluated at wavenumber k and temperature T, and T_e is the *emission temperature*, which obeys $T_\text{e} = T(\tau_k = 1)$. Note that T_e is wavenumber-dependent, although we have suppressed this k-dependence in the notation to avoid clutter. This definition of T_e only applies when a $\tau_k = 1$ level occurs somewhere in the atmosphere; otherwise, we assume that wavenumber to be essentially transparent to longwave radiation, and take T_e to be the surface temperature.

Next, to motivate our simplification of CO_2 spectroscopy, Figure 2.2 shows the HITRAN2016 mass absorption coefficient $\kappa(k)$ (m^2/kg) of CO_2 at a reference pressure of $p_0 = 10^4$ Pa, sampled at a spectral resolution of 1 cm^{-1} and focusing on the most strongly-absorbing (15-μm, or 667.5 cm^{-1}) band. We also show the absorption spectrum coarse-grained in bins of width 10 cm^{-1}. Apparent from Figure 2.2 is the fact that CO_2 absorption coefficients in this band decay approximately exponentially away from band-center, such that $\kappa(k)$ plotted on a logarithmic scale appears piecewise-linear. Motivated by this observation and following Wilson and Gea-Banacloche (2012), we will adopt the simplified CO_2 spectroscopy given by

$$\kappa(k) = \kappa_0 \exp\left(\frac{-|k-k_0|}{l_k}\right), \tag{2.3}$$

where k_0 is the most strongly-absorbing wavenumber at band-center, κ_0 is the absorption coefficient at k_0, and the scale parameter l_k sets the rate at which κ declines (exponentially) away from band-center. We obtain best-fit values for the parameters in equation 2.3 by a least-squares minimization of the difference between actual and parameterized $\log \kappa$. Figure 2.2 shows that the parameterized spectroscopy with these best-fit values ($\kappa_0 = 40$ m^2/kg, $k_0 = 671$ cm^{-1}, $l_k = 11.25$ cm^{-1}) does a very good job of capturing the overall shape of CO_2 absorption coefficients in this band. Although CO_2 does have some opacity in other bands at which terrestrial longwave emission is non-negligible, the 15-μm band accounts for the bulk of the CO_2 greenhouse effect for contemporary CO_2 concentrations, and we will show that it is straightforward to quantify the error caused by neglecting other bands.

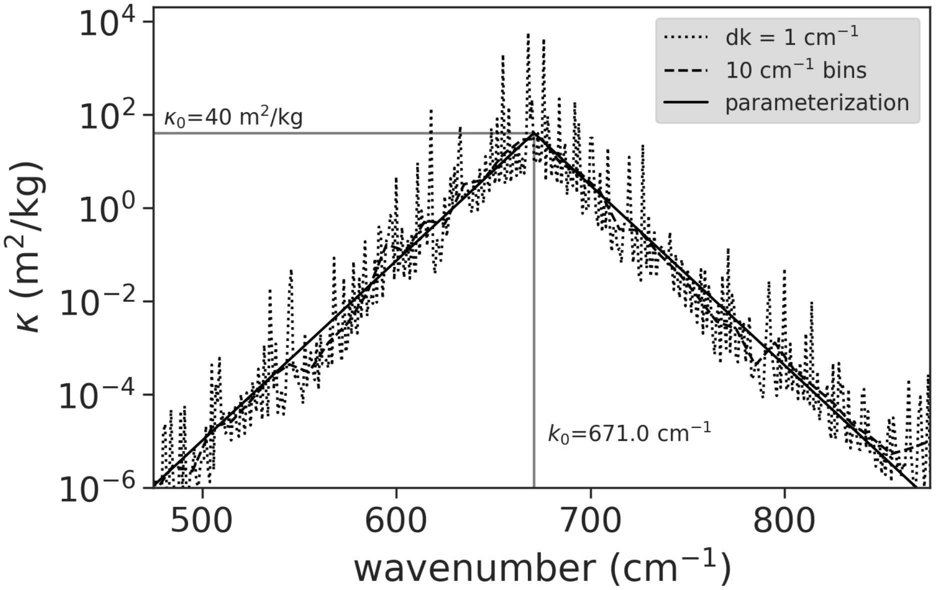

Figure 2.2: Mass absorption coefficient κ (m^2/kg) of CO_2 in the 15-μm (667.5 cm^{-1}) band at a reference pressure of $p_0 = 10^4$ Pa and a reference temperature of 250 K. Data are plotted at three levels of granularity: 1) (dotted) sampled at 1 cm^{-1} resolution from the HITRAN2016 database; 2) (dashed) coarse-grained (geometric mean) HITRAN data in bins of width 10 cm^{-1}; 3) (solid) parameterized as $\kappa(k) = \kappa_0 \exp(-|k-k_0|/l_k)$, with $\kappa_0 = 40$ m^2/kg, $k_0 = 671$ cm^{-1}, $l_k = 11.25$ cm^{-1}, where these parameter values were obtained from least-squares minimization between the parameterized $\log \kappa$ and the coarse-grained data.

Finally, to understand how the background atmospheric state affects F_{2x}, we will proceed hierarchically. To develop intuition for the problem, we will first consider idealized atmospheric soundings characterized by a surface temperature T_s, a constant tropospheric lapse rate Γ, and an isothermal stratosphere at the tropopause temperature T_t. For now, we will also assume the atmospheres are dry, such that an atmosphere's longwave opacity stems entirely from CO_2. Once we understand CO_2 forcing in this simple case, we will see how the story is modified by complicating factors such as non-isothermal stratospheres (section 2.4) and inclusion of water vapor (section 2.5). We do not consider the effects of clouds in this chapter.

With these approximations in place, we can now develop an analytical expression for F_{2x}. For an atmosphere with well-mixed CO_2 mass fraction q (kg/kg), the optical depth at wavenumber k is

$$\tau_k(p) = \int_0^p \kappa(k) q \left(\frac{p'}{p_0}\right) \frac{dp'}{g} = \frac{\kappa(k)q}{2gp_0} p^2, \tag{2.4}$$

where the p/p_0 factor accounts for pressure-broadening with respect to the reference pressure $p_0 = 10^4$ Pa (Pierrehumbert 2010). Using the unit optical depth approximation (equation 2.2) and our simplified spectroscopy (equation 2.3), we can find the pressure level from which OLR_k emanates by setting $\tau_k = 1$ and solving for the emission pressure p_e:

$$p_e(k,q) = \sqrt{\frac{2gp_0}{\kappa_0 q}} \exp\left(\frac{|k-k_0|}{2l_k}\right). \tag{2.5}$$

Equation 2.5 can also be inverted to find the wavenumbers $k_e^\pm$ emitting at a given p and q:

$$k_e^\pm(p,q) = k_0 \pm l_k \ln\left(\frac{p^2\kappa_0 q}{2gp_0}\right). \tag{2.6}$$

Equations 2.5 and 2.6 pave the way for our first heuristic derivation of an analytical expression for CO_2 forcing. This derivation is based on Figure 2.3a, where we plot p_e for $q_0 = 280$ ppm × 44/32 = .000385 kg/kg and for $8q_0$ (we consider the effect of 3 doublings of CO_2 simply to make the perturbations easier to visualize). The key insight provided by Figure 2.3a is that each point on the black segment of the q_0 emission-pressure curve has a corresponding point on the black segment of the $8q_0$ curve at the same height, and thus both points have the same temperature. Neglecting the wavenumber-dependence of the Planck function across these small spectral intervals, the black portions of the two curves have the same total emission to space, and therefore make identical contributions to the OLR before and after the CO_2 increase. This means the black curves can be neglected in calculating the CO_2 forcing. In Figure 2.3a, then, there are two contributions to the radiative forcing: one is the addition of new stratospheric emission from the $8q_0$ curve (dashed green), and the other is the loss of surface emission at wavenumbers which were previously optically thin and emitting from the surface (solid red). For a given surface temperature T_s and stratospheric temperature T_t, these contributions can be quantified once we know the spectral width Δk

over which these contributions are made (Figure 2.3a). Using equation 2.6, we find for a change in CO$_2$ from q_0 to q,

$$\Delta k = l_k \ln(q/q_0). \tag{2.7}$$

For $q/q_0 = 2$ and with $l_k = 11.25\ \mathrm{cm}^{-1}$, $\Delta k \simeq 8\ \mathrm{cm}^{-1}$, which gives a sense for the small spectral intervals involved. Therefore, using the unit optical depth approximation and considering a CO$_2$ doubling, we obtain

$$F_{2\mathrm{x}} = 2 l_k \ln(2) \left[B(k_0, T_\mathrm{s}) - B(k_0, T_\mathrm{t}) \right], \tag{2.8}$$

where the factor of 2 reflects the symmetric contributions to the forcing from either side of the CO$_2$ band, and we have evaluated the Planck function at band-center (k_0) in keeping with our neglect of wavenumber-dependence over these small spectral intervals. For general CO$_2$ perturbations from q_0 to q, the radiative forcing is (Wilson and Gea-Banacloche 2012)

$$F = 2 l_k \ln(q/q_0) \left[B(k_0, T_\mathrm{s}) - B(k_0, T_\mathrm{t}) \right], \tag{2.9}$$

which exhibits the well-known logarithmic dependence on q.

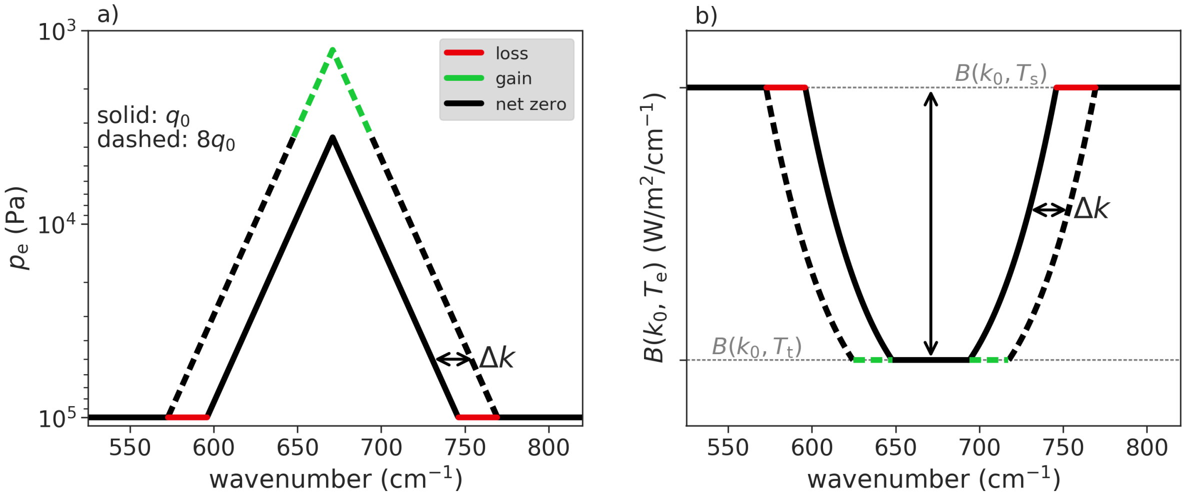

Figure 2.3: Diagrams corresponding to the two heuristic derivations of equation 2.8 for CO$_2$ forcing. (a) CO$_2$ emission pressures p_e (given by equation 2.5) for CO$_2$ concentrations of (solid) 280 ppm and (dashed) 8×280 ppm. (b) The widening "ditch" in OLR. See section 2.2 for further explanation.

A second (complementary, but equivalent) heuristic derivation of equation 2.8 is based on Figure 2.3b. There we show that the greenhouse effect of CO$_2$ — that is, the reduction of OLR due to the presence of CO$_2$ in the atmosphere — can be visualized as a "ditch" dug out of the surface temperature's Planck emission curve (Pierrehumbert 2010). The radiative forcing of a CO$_2$ doubling, then, is just the increase in the area of this ditch resulting from the doubling. For CO$_2$ concentrations such that the most strongly absorbing line emits from the stratosphere (as is the case for all CO_2 concentrations in the geological record), increasing CO_2 reduces OLR by widening, but not deepening, this ditch, because the most strongly absorbing wavenumbers are already emitting from the coldest available temperature, T_t (assuming an isothermal stratosphere). Therefore, the depth of the ditch is fixed at $B(k_0, T_s) - B(k_0, T_t)$, and the change in ditch area is just this constant depth times the change in width. From equation 2.6, the change in width is $2l_k \ln(2)$. Multiplying the ditch depth times the change in ditch width per doubling, we recover equation 2.8 for F_{2x}.

Because equation 2.8 is explicit about its dependence on CO_2 spectroscopy and atmospheric structure, it makes clear predictions about what does and does not affect the radiative forcing from CO_2. In particular, equation 2.8 says that F_{2x} depends on the parameter l_k, which controls the rate of exponential decay of the CO_2 absorption band: the larger l_k is, the more wavenumbers per CO_2 doubling effectively transition from surface emission to stratospheric emission (or, equivalently, the more rapidly the ditch in OLR widens per CO_2 doubling). Strikingly, equation 2.8 also says that the only other quantities on which F_{2x} depends — at least in this idealized case — are the surface and stratospheric temperatures. These two temperatures determine the drop in OLR_k when a wavenumber transitions from surface to stratospheric emission. It is noteworthy that F_{2x} as given by equation 2.8 does not depend on the tropospheric lapse rate (or, indeed, any details about tropospheric temperatures or vertical structure between the surface and tropopause).

These are intriguing analytical results, but before we put too much stock in them, we must check whether equation 2.8 is quantitatively accurate. In Figure 2.4, we test equation 2.8 by comparing its predictions to line-by-line RFM calculations. We use idealized atmospheres with $T_s \in \{260, 280, 300, 320\}$ K, $T_t \in \{180, 200, 220, 240\}$ K, and tropospheric lapse rates $\Gamma \in \{3, 6, 9\}$ K/km. For each unique combination of T_s, T_t, and Γ values, we use RFM to compute the OLR at CO_2 concentrations of 140, 280, and 560 ppm, and fit a line to these three OLR values to obtain a single value of F_{2x} for that sounding. We then compare that experimentally-determined F_{2x} to the prediction of equation 2.8.

Comparing the top and bottom rows of Figure 2.4, it is clear that equation 2.8 does indeed quantitatively predict the dependence of F_{2x} on T_s, T_t, and Γ. Focusing on the first row (the RFM results), the first column shows that, for fixed T_t, increasing T_s increases F_{2x}. Meanwhile, the second column shows that the dependence of F_{2x} on T_t is of smaller magnitude and opposite sign. The reduced sensitivity of F_{2x} to T_t results from the positive curvature of $B(k_0, T)$ in T, so that a fixed ΔT causes a smaller ΔB at colder temperatures. Finally, the last column shows that the lapse rate Γ has essentially no influence on F_{2x}. All of these results from RFM are quantitatively reproduced by the analytical model given by equation 2.8 (bottom row of Figure 2.4).

Given the simplicity of equation 2.8, its significant skill in emulating much more complicated LBL calculations is quite remarkable. But, so far we have only tested the analytical model on highly idealized atmospheric soundings. What happens if we allow for more realistic non-isothermal stratospheres, or include the effects of water vapor? We will return to these questions in sections 2.4–2.5. First, however, we will investigate the connection between the analytical model for F_{2x} and the debate over the origin of the log-scaling of F_{2x}.

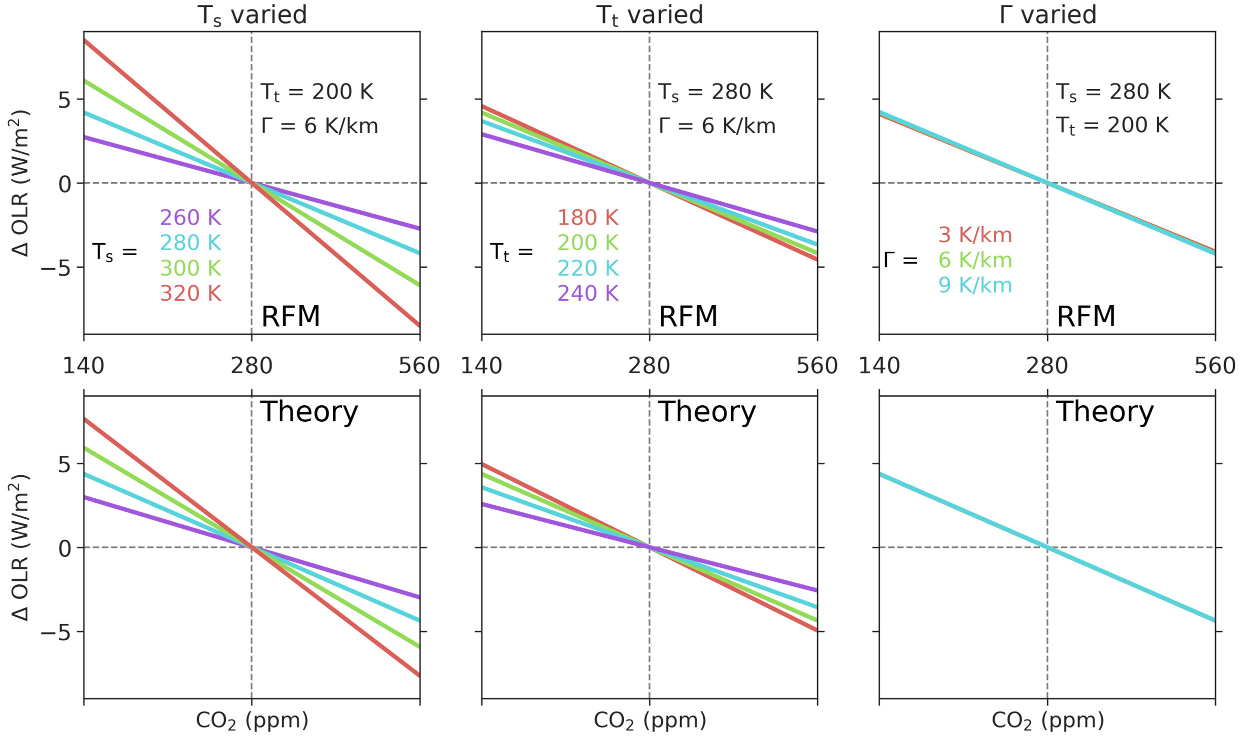

Figure 2.4: (top row) From RFM, the dependence of F_{2x} on (left) T_s, (center) T_t, and (right) Γ. In each plot, the quantity displayed is the change in OLR for a CO$_2$ doubling and halving (relative to the value at 280 ppm CO$_2$), such that the F_{2x} values are the negatives of line slopes. Full CO$_2$ spectroscopy from HITRAN2016 is used for the RFM calculations. (bottom) As for the top row, but with results from the simple model for CO$_2$ forcing (equation 2.8).

2.3 Connection to line-by-line logarithmic scaling

Equation 2.9 is an expression for spectrally-integrated CO$_2$ forcing F, and exhibits the well-known logarithmic dependence on q. The origin of the log-scaling of equation 2.9 is clear: it derives from the 15-μm CO$_2$ absorption-band structure, which is an approximately piecewise-exponential function of wavenumber (equation 2.3). This spectroscopic explanation for the log-scaling of F can be found in textbook treatments of the subject (e.g., Pierrehumbert 2010), although equation 2.9 itself only dates to Wilson and Gea-Banacloche (2012).

However, an ostensibly distinct explanation for log-scaling was recently derived in Huang and Shahabadi (2014) (hereafter HS14). HS14 derived a logarithmic scaling for the *line-by-line* (LBL) radiative forcing (F_k), and proposed that F actually inherits its log-scaling from the log-scaling of F_k. Since we did not invoke LBL log-scaling in our heuristic derivations of equation 2.9 — and since the LBL log-scaling derived by HS14 would hold regardless of the overall CO$_2$ band structure in which the lines are embedded — the connection between these two explanations is unclear. Here we will first review the argument of HS14 for the log-scaling of F_k, and then explicitly integrate the spectrally-resolved forcing in order to reconcile these two perspectives.

To begin, note that the condition for log-scaling of LBL radiative forcing can be written as

$$\frac{d\mathrm{OLR}_k}{d\ln q} = \text{constant}, \tag{2.10}$$

where the constant is independent of q (but not necessarily k). Let us first determine if this condition holds for $\mathrm{CO_2}$ in a typical terrestrial atmosphere. Using the unit optical depth approximation, we can rewrite the left-hand-side of equation 2.10 as

$$\frac{d\mathrm{OLR}_k}{d\ln q} = \left.\frac{\partial B}{\partial T}\right|_{T_\mathrm{e}} \frac{\partial T_\mathrm{e}(k,q)}{\partial \ln q}. \tag{2.11}$$

If we now assume, as in section 2.2, a constant tropospheric lapse rate Γ up to an isothermal stratosphere with constant temperature T_t, as well as a constant pressure scale height H so that $p = p_\mathrm{s}\exp(-z/H)$ (this assumes an isothermal troposphere rather than a constant lapse rate, a slight inconsistency), then we have the following expression for pressure as a function of temperature in the troposphere:

$$p(T) = p_\mathrm{s}\exp\left(-\frac{T_\mathrm{s}-T}{\Gamma H}\right). \tag{2.12}$$

We may plug this into equation 2.5 and solve for tropospheric emission temperatures, T_e:

$$T_\mathrm{e}(k,q) = T_\mathrm{s} - \frac{\Gamma H}{2}\left[\ln\left(\frac{q\kappa_0 p_\mathrm{s}^2}{2gp_0}\right) - \frac{|k-k_0|}{l_k}\right]. \tag{2.13}$$

Taking a derivative with respect to $\ln q$, we find

$$\frac{\partial T_\mathrm{e}}{\partial \ln q} = -\frac{\Gamma H}{2}, \tag{2.14}$$

which is a constant independent of k and q. Therefore, we have

$$\frac{d\mathrm{OLR}_k}{d\ln q} = -\left.\frac{\partial B}{\partial T}\right|_{T_\mathrm{e}} \frac{\Gamma H}{2}. \tag{2.15}$$

Neglecting any variations in $\partial B/\partial T$ (i.e., approximating the Planck function as linear over tropospheric temperatures), this expression is then also independent of q. Therefore, OLR_k scales as $\ln q$, as argued by HS14. The physical content of equation 2.15 is just that the emission height of each line moves upward by a fixed distance of $H\ln(2)/2$ each doubling, which results in a fixed decrease in OLR_k for a linear temperature profile and source function B.

How does this LBL log-scaling relate to the log-scaling of the spectrally-integrated forcing, F? The condition for log-scaling of F can be written as

$$\frac{d\mathrm{OLR}}{d\ln q} = \int_0^\infty \frac{d\mathrm{OLR}_k}{d\ln q}\, dk = \text{constant}. \tag{2.16}$$

If every wavenumber obeyed equation 2.15, then LBL log-scaling would trivially explain the log-scaling of F because equation 2.16 would reduce to the integral of constant coefficients over a fixed wavenumber interval. However, equation 2.15 does not apply at every wavenumber: it only applies to *tropospheric* emission (i.e., wavenumbers that have $\tau_k = 1$ in the troposphere). For very optically-thin wavenumbers well outside the core of the 15-μm $\mathrm{CO_2}$ band, $d\mathrm{OLR}_k/d\ln q \simeq 0$ because the emission temperature is the surface temperature, independent of q. Likewise, for the most optically-thick wavenumbers, emission heights are well into the stratosphere and $T_\mathrm{e}(k,q) = T_\mathrm{t}$, independent of q (assuming again an approximately isothermal stratosphere). Therefore, only those wavenumbers of intermediate optical thickness that emit from within the troposphere can contribute to the spectrally-integrated forcing. Let us denote the wavenumbers bracketing these spectral intervals as

$$k_\mathrm{t}^\pm(q) = k_\mathrm{e}^\pm(p_\mathrm{t}, q), \tag{2.17}$$

$$k_\mathrm{s}^\pm(q) = k_\mathrm{e}^\pm(p_\mathrm{s}, q), \tag{2.18}$$

so that $k_\mathrm{t}^\pm$ are the wavenumbers that have $\tau_k = 1$ at the tropopause pressure p_t, and likewise for the surface pressure p_s. For generic $\mathrm{CO_2}$ spectroscopy that is symmetric about a central wavenumber, the condition for log-scaling of F then reduces to

$$\int_{k_\mathrm{t}^+}^{k_\mathrm{s}^+} \frac{d\mathrm{OLR}_k}{d\ln q}\, dk = \text{constant}, \tag{2.19}$$

where we have used symmetry to integrate only over the right-half of the band. In the following subsections, we will use equation 2.19 to reason about the necessary and sufficient conditions for log-scaling of F to hold.

2.3.1 Is LBL log-scaling sufficient?

First, let us determine whether the LBL log-scaling of HS14 is sufficient to ensure log-scaling of F. If we assume that equation 2.15 holds, then the integrand on the left-hand-side of equation 2.19 is a constant, and can be taken outside the integral. But, the integral itself will be a constant only if $k_\mathrm{s}^+ - k_\mathrm{t}^+ = \Delta k_\mathrm{trop}$ is independent of q. Therefore, the LBL log-scaling of HS14 is not sufficient to ensure log-scaling of F: $\mathrm{CO_2}$ must also have spectroscopy such that the width of the spectral intervals emitting from within the troposphere are independent of q. It is easy to verify that the piecewise-exponential spectroscopy of equation 2.3 satisfies this condition; by equation 2.6, $\Delta k_\mathrm{trop} = 2 l_k \ln\left(p_\mathrm{s}/p_\mathrm{t}\right)$, which is indeed independent of q.

However, we can imagine an alternate world with a different CO_2 spectroscopy that does not satisfy this condition. For example, suppose the 15-μm band were shaped like a Lorentzian distribution, such that

$$\kappa_L(k) = \kappa_0 \left[\left(\frac{k - k_0}{w} \right)^2 + 1 \right]^{-1}, \tag{2.20}$$

for scale parameter w (Figure 2.5, top). Then Δk_{trop} would depend on q:

$$\Delta k_{\mathrm{trop,L}} = w \left[\left(\frac{\kappa_0 q p_{\mathrm{s}}^2}{2 g p_0} - 1 \right)^{\frac{1}{2}} - \left(\frac{\kappa_0 q p_{\mathrm{t}}^2}{2 g p_0} - 1 \right)^{\frac{1}{2}} \right], \tag{2.21}$$

which would cause $F_{2\mathrm{x}}$ to depend on q as well.

We confirm this prediction in Figure 2.5, where we compare line-by-line calculations of OLR and $F_{2\mathrm{x}}$ for two different worlds: one with the (approximately realistic) CO_2 spectroscopy given by equation 2.3, and one with the Lorentzian spectroscopy of equation 2.20. The realistic CO_2 spectroscopy reproduces the log-scaling of F, such that $F_{2\mathrm{x}}$ is independent of q (and predicted very precisely by equation 2.8). On the other hand, the Lorentzian spectroscopy causes $F_{2\mathrm{x}}$ to vary by roughly 700% over the range of CO_2 we consider. As can be seen in the top panel of Figure 2.5, the increase of $F_{2\mathrm{x}}$ in the world with Lorentzian spectroscopy results from the large increase in Δk_{trop} with q. Since HS14's argument for LBL log-scaling of tropospheric emission lines would apply to both worlds, this example reinforces the mathematical conclusion of equation 2.19: LBL log-scaling is not sufficient to ensure log-scaling of F.

2.3.2 Is LBL log-scaling necessary?

Next, let us determine whether LBL log-scaling is necessary for log-scaling of F. We saw from equation 2.14 that the LBL log-scaling derives from the fact that tropospheric emission temperatures drop by an approximately fixed amount per doubling. This result was contingent on two pieces of physics: 1) that tropospheric emission *heights* move upward by a fixed distance per doubling, and 2) that the lapse rate in the troposphere is approximately constant, so that a fixed Δz_{e} corresponds to a fixed ΔT_{e}. Therefore, we can break the LBL log-scaling by changing the temperature profile in the troposphere. In particular, let T in the troposphere have the form

$$T(z) = T_{\mathrm{s}} - \Gamma z - \Delta T \sin(2\pi z / z_{\mathrm{t}}). \tag{2.22}$$

An example of such a temperature profile with $\Delta T = 150$ K is shown in the top panel of Figure 2.6, along with a standard constant-Γ troposphere for comparison. Also shown for each temperature profile are the emission temperatures for a sample wavenumber (740 cm^{-1}) whose emission level moves upwards through the troposphere for CO_2 concentrations in the range 128 – 2048 ppm. Figure 2.6 shows that for a constant-Γ troposphere, ΔT_{e} is

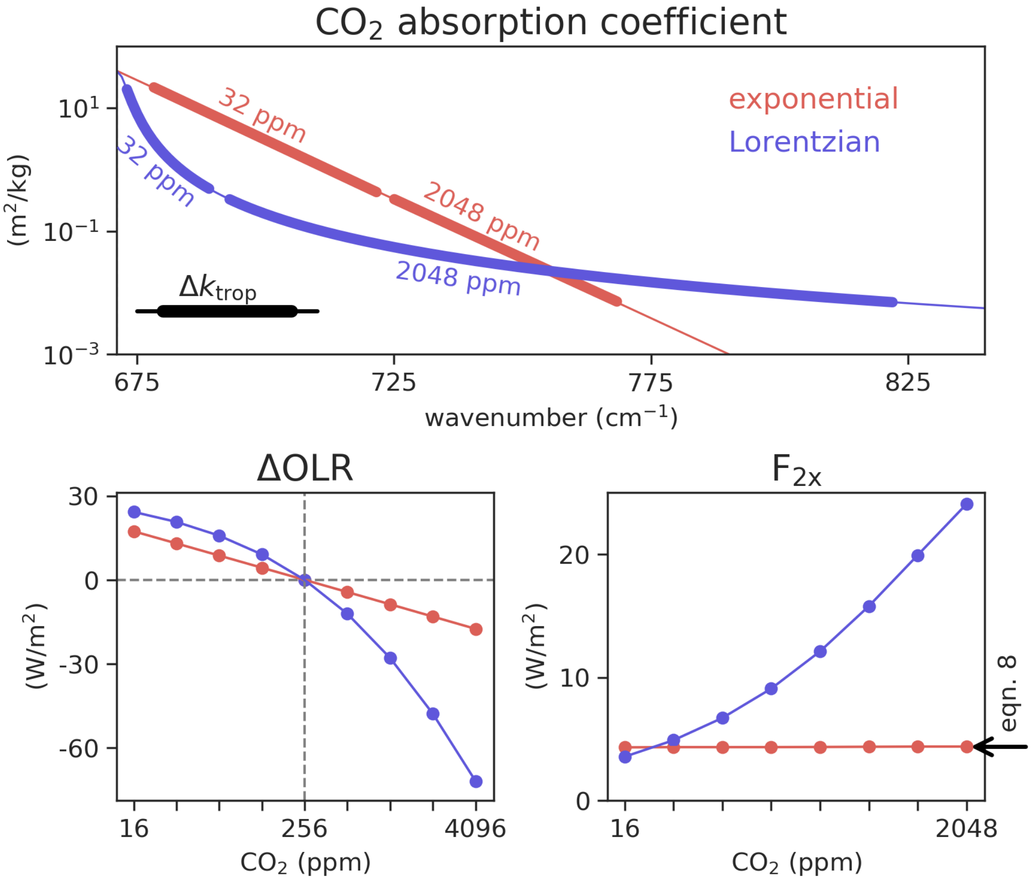

Figure 2.5: (top) CO_2 mass absorption coefficients, parameterized according to equation 2.3 (red) and equation 2.20 (blue). For simplicity, we show only the right half of the CO_2 band ($k > k_0$). Thick lines indicate the spectral intervals that have $\tau_k = 1$ within the troposphere for CO_2 concentrations of 32 and 2048 ppm (for an atmosphere with $T_s = 280$ K, $T_t = 200$ K). (bottom-left) Change in OLR relative to OLR at 256 ppm CO_2. (bottom-right) F_{2x} as a function of CO_2. The prediction of equation 2.8 for the piecewise-exponential spectroscopy (eqn. 2.3) is marked by the black arrow at right.

essentially independent of q, as argued by HS14. However, for the sinusoidal temperature profile of equation 2.22, the magnitude and even the sign of ΔT_e vary as a function of q.

The bottom-left panel of Figure 2.6 shows the corresponding LBL radiative forcings, $F_{k,2x}$. For the constant-Γ troposphere, $F_{k,2x}$ is relatively independent of q, although not entirely so (mostly due to the nonlinearity of the Planck function). However, for the sinusoidal troposphere, $F_{k,2x}$ takes on values between roughly ± 0.075 W/m^2/cm^{-1}. Therefore, imposing the sinusoidal tropospheric temperature profile has broken the LBL log-scaling of HS14.

Nevertheless, the bottom-right panel of Figure 2.6 shows that the spectrally-integrated forcing F_{2x} remains independent of q even when LBL log-scaling is broken. In fact, F_{2x} has the same magnitude for the sinusoidal and constant-Γ tropospheres. We will discuss the origin of this perhaps surprising result in section 2.3.3. For now, we can conclude from this example that LBL log-scaling is not necessary for the log-scaling of F.

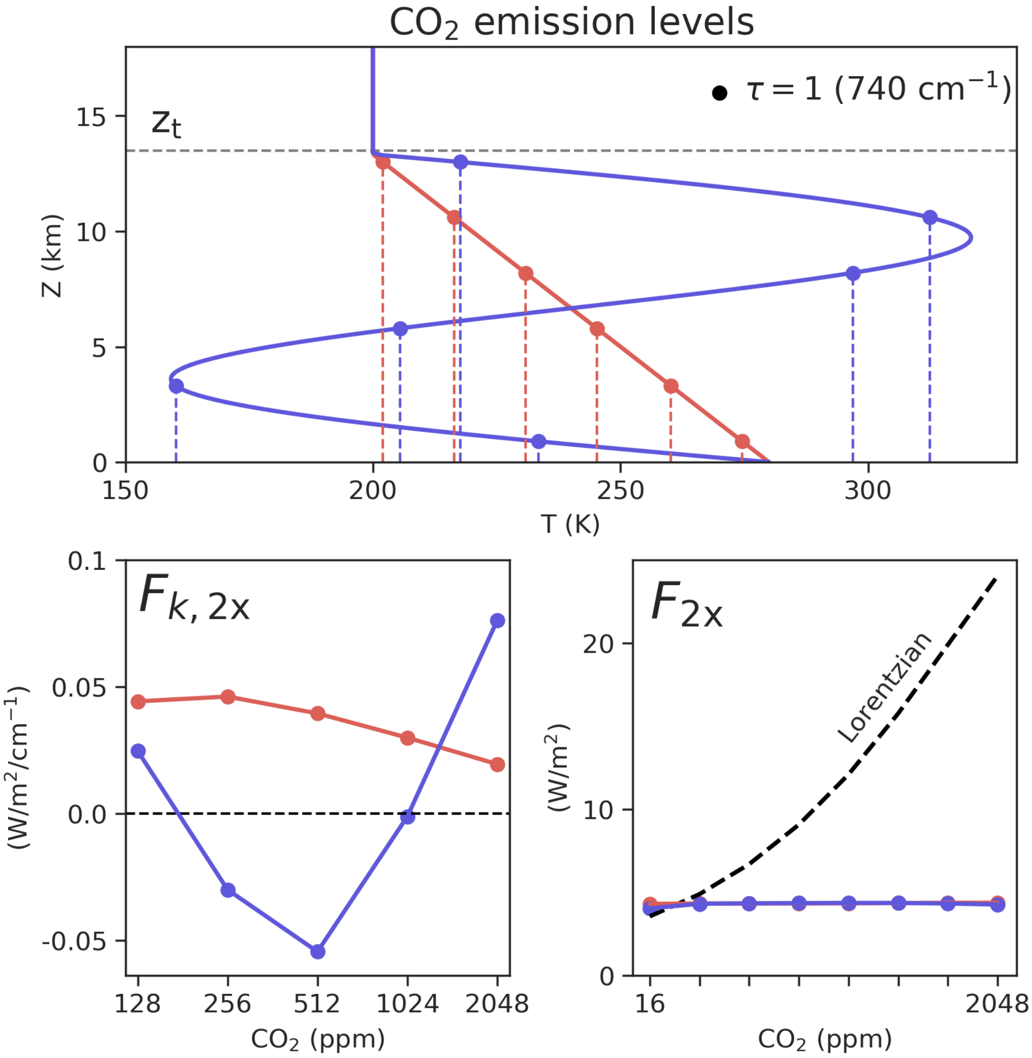

Figure 2.6: (top) Tropospheric temperature structure for a standard constant-Γ profile (red) and for the sinusoidal profile of equation 2.22 (blue). On each profile, the $\tau_k = 1$ levels for $k = 740$ cm^{-1} are marked with circles for CO_2 concentrations of 128 – 4096 ppm (low altitudes to high altitudes, increasing in multiples of 2). (bottom-left) The radiative forcing at 740 cm^{-1} for the two temperature profiles as computed by RFM. (bottom-right) The spectrally-integrated radiative forcing for the two temperature profiles as computed by RFM. Here the piecewise-exponential spectroscopy of equation 2.3 is used. The F_{2x} curve from the Lorentzian-spectroscopy world of Figure 2.5 is shown for comparison.

In the following subsections, we consider the necessity and sufficiency of the traditional *spectroscopic* explanation for the log-scaling of F.

2.3.3 Is exponential spectroscopy sufficient?

In Figure 2.6, we saw one example where exponential spectroscopy resulted in log-scaling of F even when LBL log-scaling was broken. Here we show that this result is general: exponential spectroscopy alone is sufficient to ensure log-scaling of F, regardless of whether LBL log-scaling holds. This is somewhat redundant with the heuristic derivations given in section 2.2 (which did not invoke LBL log-scaling), but illuminating nevertheless.

To prove that exponential spectroscopy is sufficient, we must invoke a subtle but crucial aspect of equation 2.4, namely that κ and q only appear multiplied by each other. This is true regardless of the form of $\kappa(k)$ or of the atmosphere's vertical profiles, and is a fundamental consequence of radiation physics: optical depth is simply an integrated cross-sectional area, which depends equally on the concentration of molecules (q) and the cross-section per molecule (proportional to κ). As a consequence, several quantities of interest (such as τ_k, p_e, T_e, etc.) also depend on κq only, not on κ and q separately. Therefore, if we define $\alpha = \kappa q$, then for any function $f(\alpha)$, we have

$$\frac{\partial f}{\partial \ln q} = \frac{\partial f}{\partial \alpha}\frac{\partial \alpha}{\partial \ln q} = \frac{\partial f}{\partial \alpha}\frac{\partial \alpha}{\partial \ln \kappa} = \frac{\partial f}{\partial \ln \kappa}, \tag{2.23}$$

which is just the mathematical form of the statement that scaling κ is equivalent to scaling q. We will see that this connection is essential to the logarithmic dependence of CO_2 forcing.

Let us assume the exponential spectroscopy of equation 2.3, and consider the function $\beta(\alpha) = B(k_0, T_\mathrm{e}(\kappa(k), q))$, which is just the Planck function restricted to the solid line in Figure 2.3a (ignoring the small direct dependence of the Planck function on k within the CO_2 band). Then, using the unit optical depth approximation and invoking symmetry, we can write

$$\begin{aligned}
\frac{d\mathrm{OLR}_k}{d\ln q} &= 2\int_{k_\mathrm{t}^+}^{k_\mathrm{s}^+} \frac{\partial \beta}{\partial \ln q}\, dk \\
&= 2\int_{k_\mathrm{t}^+}^{k_\mathrm{s}^+} \frac{\partial \beta}{\partial \ln \kappa}\, dk \\
&= 2\int_{k_\mathrm{t}^+}^{k_\mathrm{s}^+} \frac{\partial \beta}{\partial k}\left(\frac{\partial \ln \kappa}{\partial k}\right)^{-1} dk \\
&= -2 l_k \int_{k_\mathrm{t}^+}^{k_\mathrm{s}^+} \frac{\partial \beta}{\partial k}\, dk \\
&= -2 l_k \left[B(k_0, T_\mathrm{s}) - B(k_0, T_\mathrm{t})\right],
\end{aligned} \tag{2.24}$$

which is equivalent to equation 2.8 upon considering a finite difference in q and noting that $F_{2\mathrm{x}}$ has the opposite sign convention as OLR. The principles used in this derivation of equation 2.24 are minimal and hard to escape: going from line 1 to line 2 is fundamental to radiation physics (equation 2.23); line 2 to line 3 is just the chain rule; line 3 to line 4 is the result of exponential spectroscopy; and line 4 to line 5 is just the fundamental theorem of calculus. Since we have not invoked LBL log-scaling anywhere in this derivation, this proves that exponential spectroscopy alone is sufficient to ensure log-scaling of F.

2.3.4 Is exponential spectroscopy necessary?

Let us assume that the LBL log-scaling of HS14 (equation 2.15) holds. Then we can rewrite the condition for log-scaling of F as

$$k_{\mathrm{s}}^{+} - k_{\mathrm{t}}^{+} = \Delta k_{\mathrm{trop}} = \text{constant}. \tag{2.25}$$

Here we will show that Δk_{trop} is independent of q if and only if CO_2 spectroscopy is exponential in k. We already saw in section 2.3.1 that the exponential spectroscopy of equation 2.3 satisfies equation 2.25, so we know that exponential spectroscopy implies the constancy of Δk_{trop} and therefore the log-scaling of F. If we can also prove the converse (i.e., *assume* the constancy of Δk_{trop}, and show that this implies exponential spectroscopy), then we can conclude that exponential spectroscopy is necessary and sufficient to ensure log-scaling of F (given LBL log-scaling).

To prove this, we first note that the absorption coefficient of lines with $\tau_k = 1$ at a given pressure p and CO_2 concentration q is, by equation 2.4,

$$\kappa_{\mathrm{e}}(p, q) = \frac{2 g p_0}{q p^2}. \tag{2.26}$$

Let us denote the κ values that emit from the tropopause and the surface as κ_{t} and κ_{s}, respectively. Then, by equation 2.26,

$$\ln \kappa_{\mathrm{t}} - \ln \kappa_{\mathrm{s}} = 2 \ln(p_{\mathrm{s}}/p_{\mathrm{t}}), \tag{2.27}$$

which is independent of q. This conclusion — which holds for any functional form of $\kappa(k)$ — means that the range of $\ln(\kappa)$ that would emit from within the troposphere for given p_{s} and p_{t} does not vary with CO_2 concentration (this can also be seen graphically in the top panel of Figure 2.5). Therefore, we can write

$$\begin{aligned}
0 &= \frac{d}{d \ln q} \left(\ln \kappa_{\mathrm{t}} - \ln \kappa_{\mathrm{s}} \right) \\
&= \frac{d}{d \ln q} \int_{k_{\mathrm{s}}^{+}}^{k_{\mathrm{t}}^{+}} \frac{d \ln \kappa}{dk}\, dk \\
&= \frac{d k_{\mathrm{t}}^{+}}{d \ln q} \frac{d \ln \kappa}{dk}\bigg|_{k_{\mathrm{t}}^{+}} - \frac{d k_{\mathrm{s}}^{+}}{d \ln q} \frac{d \ln \kappa}{dk}\bigg|_{k_{\mathrm{s}}^{+}}.
\end{aligned} \tag{2.28}$$

But by our assumption that Δk_{trop} is independent of q, we must have $(dk_{\mathrm{t}}^{+}/d\ln q) = (dk_{\mathrm{s}}^{+}/d\ln q)$. Therefore, from equation 2.28,

$$\left.\frac{d\ln\kappa}{dk}\right|_{k_{\mathrm{t}}^{+}} = \left.\frac{d\ln\kappa}{dk}\right|_{k_{\mathrm{s}}^{+}}. \tag{2.29}$$

For this condition to hold for all q, we must have

$$\frac{d\ln\kappa}{dk} = \text{constant}, \tag{2.30}$$

which is exponential spectroscopy: $\kappa \sim \exp(ck)$ for some constant c. This concludes the proof: given LBL log-scaling, exponential spectroscopy is the only way to ensure the log-scaling of F.

The results of this section can be summarized as follows. The LBL log-scaling of HS14 is neither necessary nor sufficient for the log-scaling of F, and therefore is not relevant to this fundamental property CO_2 forcing. The correct explanation for log-scaling of F is that CO_2 spectroscopy is exponential in wavenumber. This property of CO_2 is sufficient by itself to ensure the log-scaling of F, and even when LBL log-scaling holds, exponential spectroscopy is still necessary to ensure the log-scaling of F.

2.4 Non-isothermal stratospheres

Let us now relax the isothermal-stratosphere assumption, and see how we must modify the story so far. On this topic, a simplifying observation is that the division between the stratosphere and the troposphere is completely artificial if we are calculating instantaneous, TOA radiative forcing. It is only when we allow the system to adjust to the radiative forcing that the division between these two layers of the atmosphere becomes relevant.

With this in mind, we can build intuition by first imagining a stratosphere that is *locally* isothermal in the vicinity of $p_{\mathrm{e}}(k_0, q)$ (the emission level of the most strongly-absorbing line), such that $T_{\mathrm{e}}(k_0, q_0) \simeq T_{\mathrm{e}}(k_0, q)$. It is obvious that this situation is functionally identical to the isothermal-stratosphere cases we have considered so far. Therefore, in this case the only modification we must make to equation 2.9 is to replace the tropopause temperature T_{t} with $T_{\mathrm{e}0} \equiv T_{\mathrm{e}}(k_0, q_0)$. This is just a recapitulation the basic insight of Figure 2.3a, where we showed that the net effect of increasing CO_2 is a loss of surface emission to space and a gain of stratospheric emission to space. For the locally-isothermal stratosphere, the new stratospheric emission is given by $\Delta\mathrm{OLR}_{\mathrm{strat}} = 2l_k \ln(q/q_0) B(k_0, T_{\mathrm{e}0})$.

If the stratosphere is not locally isothermal in the vicinity of $p_{\mathrm{e}}(k_0, q)$, but instead has a local lapse rate of Γ_{st}, then we can make a correction to the amount of new stratospheric emission. Note that for a change in CO_2 from q_0 to q, we have

$$\Delta T_{\mathrm{e}0} = -\Gamma_{\mathrm{st}} R T_{\mathrm{e}0} \ln(q/q_0)/(2g), \tag{2.31}$$

where we have replaced the (local) pressure scale-height H with RT_{e0}/g. Therefore, the full expression for the new stratospheric emission after $\mathrm{CO_2}$ changes is

$$\Delta\mathrm{OLR_{st}} = 2l_k \ln(q/q_0) \left[\overbrace{B(k_0, T_{\mathrm{e0}})}^{\text{locally-isothermal}} - \underbrace{\ln(q/q_0) \left(\frac{\Gamma_{\mathrm{st}} R T_{\mathrm{e0}}}{4g} \right) \frac{\partial B(k_0, T)}{\partial T} \bigg|_{T_{\mathrm{e0}}}}_{\text{correction}} \right] \tag{2.32}$$

It turns out that for a $\mathrm{CO_2}$ doubling and for a wide range of Γ_{st} and T_{e0} values, this correction term is approximately an order of magnitude smaller than the locally-isothermal term. Since we are building a simple model, we will drop this term from now on, which means our generalization of equation 2.8 becomes simply

$$F_{2\mathrm{x}} = 2l_k \ln(2) \left[B(k_0, T_{\mathrm{s}}) - B(k_0, T_{\mathrm{e0}}) \right]. \tag{2.33}$$

Note that for a piecewise-linear temperature profile with a tropospheric lapse rate Γ and a stratospheric lapse rate Γ_{st}, equation 2.33 remains fully analytic because we have the following expression for T_{e0}:

$$T_{\mathrm{e0}} = T_{\mathrm{t}} \left(\frac{T_{\mathrm{s}}}{T_{\mathrm{t}}} \right)^{\Gamma_{\mathrm{st}}/\Gamma} \left(\frac{2gp_0}{q\kappa_0 p_{\mathrm{s}}^2} \right)^{R\Gamma_{\mathrm{st}}/(2g)}. \tag{2.34}$$

What are the implications of this generalized equation for $F_{2\mathrm{x}}$? First of all, since T_{e0} depends on q, we should expect a non-isothermal stratosphere to introduce deviations from log-scaling of F. The larger the magnitude of Γ_{st}, the more rapidly T_{e0} varies with q, and the larger these deviations should be. We confirm this prediction in Figure 2.7, and find that the generalized expression for $F_{2\mathrm{x}}$ (equation 2.33) reproduces the RFM results quite well. The dashed lines in the bottom-right panel of Figure 2.7 show the predicted $F_{2\mathrm{x}}$ with the non-locally-isothermal correction term of equation 2.32 included.

Equation 2.33 also suggests an interesting possibility: if $T_{\mathrm{e0}} \gtrsim T_{\mathrm{s}}$, then we should expect $F_{2\mathrm{x}} \lesssim 0$. This prediction is also confirmed in Figure 2.7: $F_{2\mathrm{x}}$ changes sign for the atmospheres with strong stratospheric inversions at high $\mathrm{CO_2}$ concentrations. While it is quite interesting to note that there are situations in which increasing $\mathrm{CO_2}$ produces a TOA radiative forcing that is negative or close to zero, it would be incorrect to conclude that the ultimate result of such forcings would be global cooling or no temperature change. This is because fast ($\sim$ 1-month) adjustments in the stratosphere modify the radiative forcing that is ultimately felt by the troposphere on the timescale of surface temperature adjustment (Hansen et al. 2005; Sherwood et al. 2015). In other words, warming the stratosphere in order to decrease the instantaneous TOA radiative forcing of $\mathrm{CO_2}$ is not a proven geoengineering strategy for global warming mitigation. However, further investigation of this intriguing result is warranted.

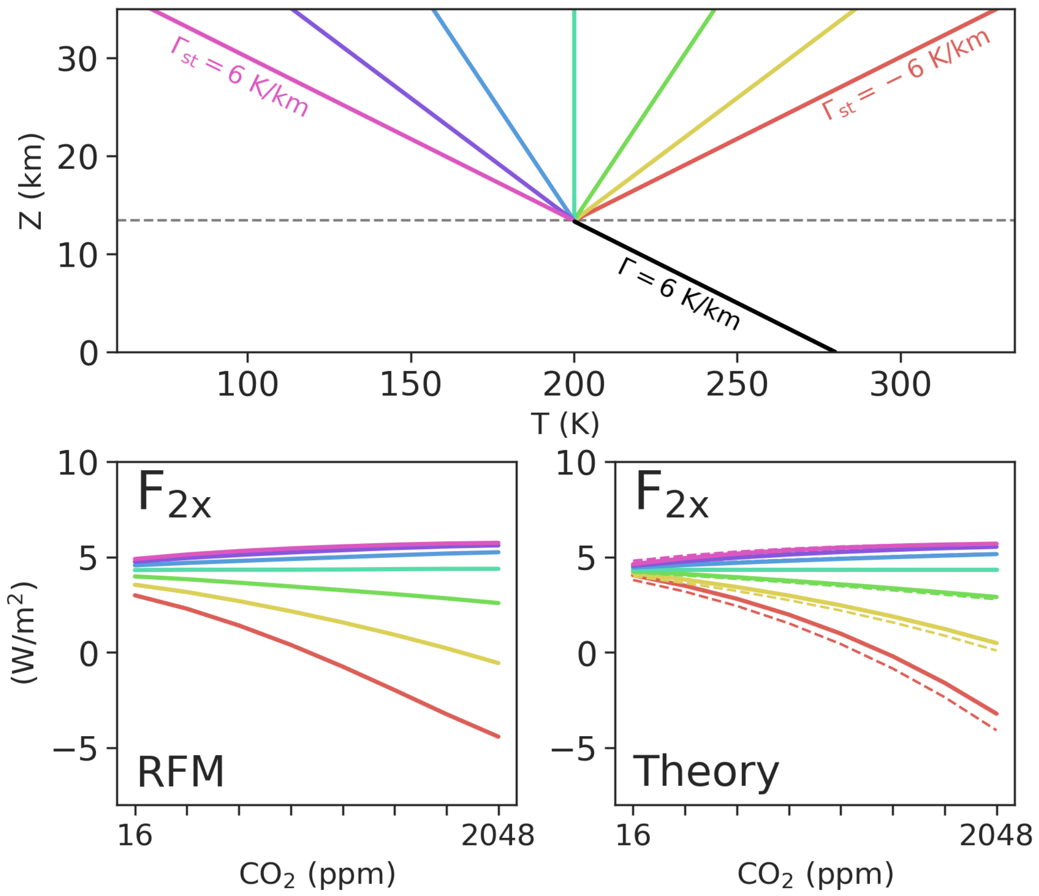

Figure 2.7: (top) Idealized piecewise-linear temperature profiles with $T_s = 280$ K, $T_t = 200$ K, tropospheric lapse rate $\Gamma = 6$ K/km, and stratospheric lapse rates Γ_{st} ranging from -6 K/km to 6 K/km, in increments of 2 K/km. (bottom-left) From RFM, the radiative forcing from CO_2 doubling as a function of CO_2, for each of the 7 different stratospheric lapse rates shown in the top panel. (bottom-right) F_{2x} as predicted by equation 2.33, with T_{e0} calculated from equation 2.34. The dashed lines show the prediction for F_{2x} with the non-locally-isothermal correction term of equation 2.32 included.

2.5 Effect of water-vapor overlap

So far, we have focused on atmospheres in which CO_2 is the only greenhouse gas. But, to make the connection to Earthlike atmospheres, it is crucial to incorporate the effects of water vapor. These effects can be significant: Figure 2.1 shows that the inclusion of water vapor reduces F_{2x} by roughly 40% for a tropical column.

To understand how H_2O damps F_{2x}, we must turn to the spectrally-resolved OLR. In Figure 2.8a-b, we show the spectrally-resolved effect of a CO_2 quadrupling for an idealized tropical atmosphere ($T_s = 300$ K, $T_t = 200$ K, $\Gamma = 6$ K/km), both with and without H_2O.

This reveals the essential reason that inclusion of H_2O reduces F_{2x}: when water vapor is present in appreciable quantities, OLR_k at the edges of the CO_2 band does not come from surface Planck emission, as it does for a dry atmosphere. Instead, OLR_k at band-edge comes from H_2O emission from within the troposphere (primarily from the level where the optical depth of H_2O at these wavenumbers equals 1, according to the unit optical depth approximation). Since the troposphere is colder than the surface, replacing tropospheric H_2O emission to space with stratospheric CO_2 emission to space (which is the net effect of increasing CO_2 in the presence of H_2O) decreases outgoing flux less than replacing surface emission to space with stratospheric CO_2 emission to space (which is the net effect of increasing CO_2 without H_2O).

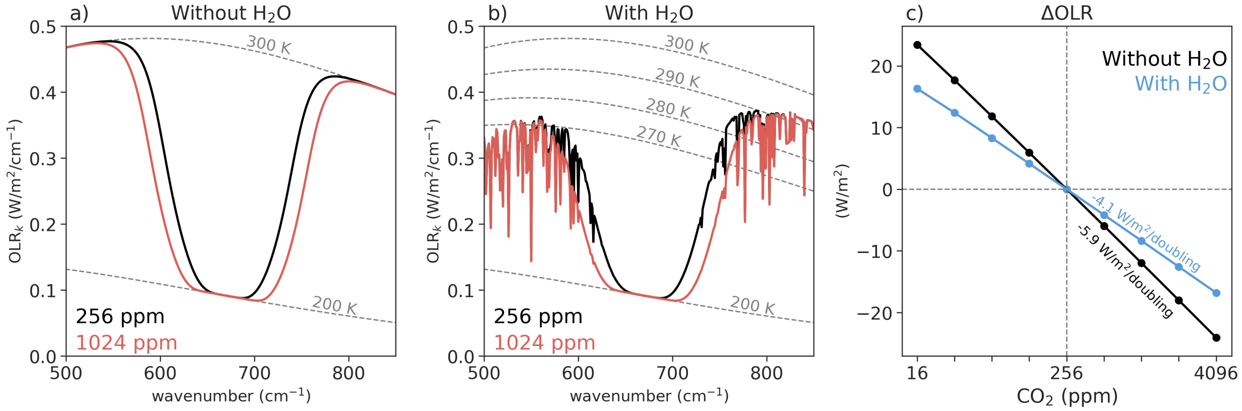

Figure 2.8: (a) Spectrally-resolved OLR with (black) 256 ppm and (red) 1024 ppm CO_2, as computed by RFM for a dry atmosphere with $T_s = 300$ K, $T_t = 200$ K, $\Gamma = 6$ K/km, and $\Gamma_{st} = 0$ K/km. For these calculations, CO_2 spectroscopy was approximated as piecewise-exponential in wavenumber (equation 2.3); H_2O opacities were obtained from HITRAN2016. (b) As in (a), but for an atmosphere with constant tropospheric relative humidty of 70%. (c) Change in OLR (relative to an atmosphere with 256 ppm CO_2) as a function of CO_2, with and without water vapor included in the radiative transfer calculations.

Therefore, understanding the magnitude of H_2O damping is equivalent to asking: By how much does H_2O decrease OLR_k at the edges of the CO_2 band? For the idealized tropical column we consider here, H_2O reduces the average OLR_k at band-edge from about 0.45 $W/m^2/cm^{-1}$ to about 0.35 $W/m^2/cm^{-1}$. Since the bottom of the "ditch" in OLR for our atmosphere with $T_t = 200$ K is at about 0.1 $W/m^2/cm^{-1}$, H_2O reduces the depth of the ditch by about $(0.45 - 0.35)/0.35 = 30\%$, which explains why F_{2x} is smaller for the moist column than for the dry column by about 30% (Figure 2.8c).

Can we make a further modification to equation 2.33 for F_{2x} to account for this water vapor damping? Unfortunately, we do not yet have an analytical expression for H_2O optical depth (analogous to equation 2.4 for CO_2) that applies equally to the line-dominated and continuum-dominated parts of the H_2O absorption spectrum. For now, we must simply diagnose the OLR_k at band-edge in atmospheres with H_2O. If we denote this diagnosed quantity by $\mathrm{OLR}^{\mathrm{H_2O}}_{\mathrm{edge}}$, our modified expression for $F_{2\mathrm{x}}$ becomes:

$$F_{2\mathrm{x}} = 2 l_k \ln(2) \left[\mathrm{OLR}^{\mathrm{H_2O}}_{\mathrm{edge}} - B(k_0, T_{\mathrm{e0}}) \right] . \tag{2.35}$$

2.6 Discussion

Let us now return to the observational soundings shown in Figure 2.1, and apply what we have learned. To use equation 2.35 on real soundings, we need to diagnose T_{e0} and $\mathrm{OLR}^{\mathrm{H_2O}}_{\mathrm{edge}}$. Although T_{e0} is not analytic for real soundings, we can calculate $p_{\mathrm{e0}} \equiv p_{\mathrm{e}}(k_0, q)$ using equation 2.5, and then simply find the temperature on the sounding that corresponds to p_{e0}. The results of this procedure are shown in Figure 2.9a. We find that T_{e0} is between roughly 200 K and 240 K for our soundings.

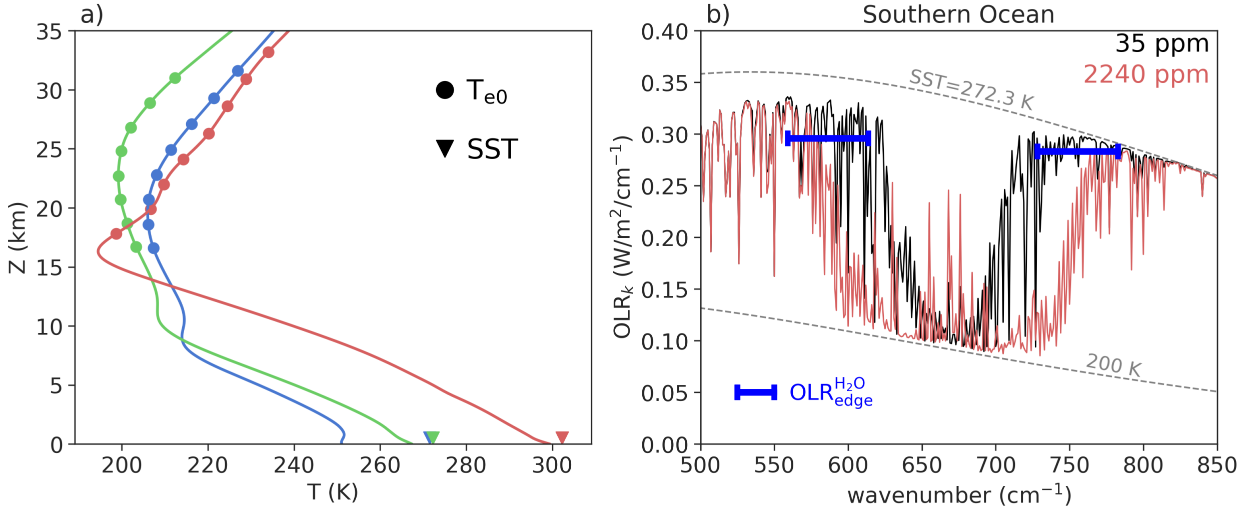

Figure 2.9: (a) The ERA5 temperature profiles from Figure 2.1, with the band-center emission temperatures T_{e0} marked with circles. On each profile, the lowest-altitude circle corresponds to the lowest CO_2 concentration, with higher CO_2 corresponding to higher altitudes of emission. (b) Spectrally-resolved OLR for the Southern Ocean profile at (black) 35 ppm and (red) 2240 ppm CO_2. For each side of the band, $\mathrm{OLR}^{\mathrm{H_2O}}_{\mathrm{edge}}$ is calculated by averaging the OLR_k at 35 ppm CO_2 within the demarcated blue wavenumber intervals, the bounds of which are obtained via equation 2.18 for $k_{\mathrm{s}}^{\pm}$. The y-axis position of the blue intervals corresponds to the value of $\mathrm{OLR}^{\mathrm{H_2O}}_{\mathrm{edge}}$ obtained by this procedure.

To diagnose $\mathrm{OLR}^{\mathrm{H_2O}}_{\mathrm{edge}}$, we must perform a radiative transfer calculation at a low CO_2 concentration. This allows us to determine the typical value of OLR_k that will be replaced with stratospheric emission when CO_2 is increased and its absorption band widens. Figure 2.9b shows an example of spectrally-resolved OLR for the Southern Ocean sounding at 35 ppm CO_2. We first calculate the spectral intervals corresponding to the "band-edge" by using equation 2.18 to find the wavenumbers emitting from the surface at the lowest and highest CO_2 concentrations we consider, and then we average OLR_k over these wavenumber intervals (Figure 2.9b). For the Southern Ocean sounding, this yields $\mathrm{OLR}^{\mathrm{H_2O}}_{\mathrm{edge}} \simeq 0.3\ \mathrm{W/m^2/cm^{-1}}$.

The predictions of equation 2.35 for the ERA5 soundings are compared to the RFM results in Figure 2.10. We separate the RFM results into the contributions from the 15-μm absorption band (500–850 $\mathrm{cm^{-1}}$) and from the rest of the spectrum. Although the match is not exact, equation 2.35 does a reasonable job of estimating the magnitude of F_{2x} in the 15-μm band, and the small changes in F_{2x} with increasing CO_2 in this band can be understood in terms of changes in T_{e0} (which is all that varies as a function of CO_2 in Figure 2.10b). The most obvious failure of equation 2.35 is that it only accounts for the 15-μm absorption band. At low CO_2, this is not such a bad approximation, but it is clear from Figure 2.10a that at CO_2 concentrations much above a doubling of the preindustrial value of 280 ppm, other bands make contributions to F_{2x} that almost rival the forcing from the 15-μm band. Evidently, the increase in forcing in these other bands counteracts (or even overpowers) the general decline of F_{2x} within the 15-μm band itself. While it would be possible, in principle, to incorporate other bands in the framework we have developed here, it is not obvious that doing so would improve our understanding of the physics.

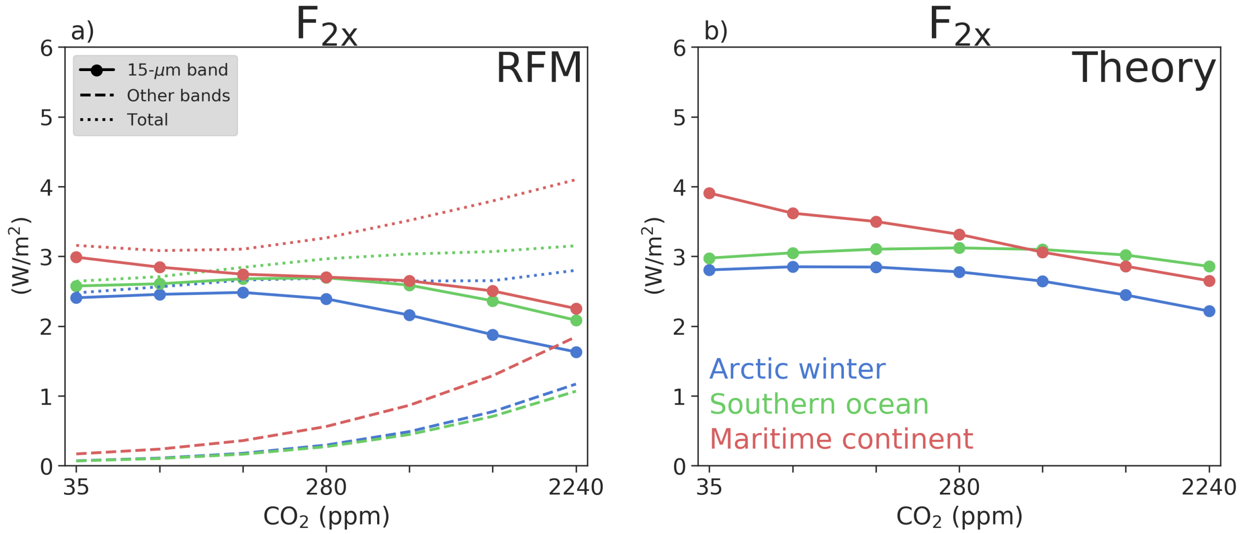

Figure 2.10: (a) F_{2x} calculated from RFM calculations for the ERA5 soundings of Figure 2.1. The total forcing (dotted lines) is split into contributions from the 15-μm band (solid; 500–850 $\mathrm{cm^{-1}}$) and other bands (dashed). (b) As in (a), but as predicted by equation 2.35. The procedures for diagnosing T_{e0} and $\mathrm{OLR}^{\mathrm{H_2O}}_{\mathrm{edge}}$ are described in the main text and Figure 2.9.

2.7 Conclusions

The conceptual model for CO_2 forcing presented in this chapter can be summarized as follows. Under typical conditions, the net effect of increasing CO_2 is to cause a small interval of wavenumbers to transition from emitting radiation to space from a relatively "hot" place to emitting to space from a relatively "cold" place. The magnitude of the resulting radiative forcing depends on the size of the wavenumber packet and the temperature difference between the hot place and the cold place. The size of the wavenumber packet that transitions is determined by CO_2 spectroscopy — specifically, the rate of (exponential) decay of CO_2 absorption coefficients. In the simplest type of atmosphere we consider, which is dry and has an isothermal stratosphere, the hot place is the surface and the cold place is the stratosphere — both of which have temperatures that are independent of q. This simple case most closely exhibits log-scaling of F. If we consider a non-isothermal stratosphere, the cold place becomes the emission level of the most strongly-absorbing line, whose temperature $T_{\mathrm{e}0}$ varies as a function of q. This explicit dependence of the cold temperature on CO_2 introduces a deviation from logarithmic scaling. If we add water vapor to the picture, the hot temperature becomes the emission temperature of water vapor at the edges of the CO_2 band. If the edges of the CO_2 band are not located in water-vapor windows, these H_2O emission temperatures will be colder than the surface temperature, and therefore water vapor reduces the temperature difference between the hot place and the cold place and decreases the magnitude of $F_{2\mathrm{x}}$.

These basic principles allow us to understand why a typical value for $F_{2\mathrm{x}}$ on Earth is about 3 $\mathrm{W/m^2}$. For spectroscopic exponential-decay parameter $l_k = 11.25$, the width of the wavenumber packet that transitions from surface emission to stratospheric emission is about $2 l_k \ln(2) \simeq 16\ \mathrm{cm}^{-1}$ per doubling. A typical spectral power at which new stratospheric emission is added is about $0.1\ \mathrm{W/m^2/cm^{-1}}$ (corresponding to an emission temperature $T_{\mathrm{e}0}$ of about 200 K), whereas the typical spectral power at which tropospheric emission is lost is around $0.3\ \mathrm{W/m^2/cm^{-1}}$ (corresponding to an H_2O emission temperature of around 260 – 270 K). Mutliplying the difference between these spectral powers ($0.2\ \mathrm{W/m^2/cm^{-1}}$) by 16 cm^{-1}, we obtain $F_{2\mathrm{x}} \simeq 3\ \mathrm{W/m^2}$.

The other central result of this chapter was to clearly demonstrate the origin of the logarithmic scaling of CO_2 forcing. The traditional explanation for log-scaling is based on the exponential decay of CO_2 absorption coefficients in the 15-μm absorption band (Pierrehumbert 2010), whereas the more recent explanation of HS14 argues that CO_2 forcing actually inherits its log-scaling from the log-scaling of line-by-line radiative forcing. By explicitly integrated the spectrally-resolved radiative forcing, we showed that LBL log-scaling is neither necessary nor sufficient to ensure the log-scaling of spectrally-integrated forcing. In contrast, exponential spectroscopy is sufficient on its own to ensure the log-scaling of F, and even when LBL log-scaling holds, exponential spectroscopy is the only way to ensure log-scaling. The conclusion is that the traditional spectroscopic explanation for log-scaling is correct. This is the physics that is formalized, at varying levels of complexity, in equations 2.8, 2.33, and 2.35 for CO_2 forcing.

Appendix A: Line-by-line radiative transfer calculations

In this chapter, we use the Reference Forward Model (RFM; Dudhia 2017) to compute longwave radiative transfer through plane-parallel atmospheres in a nadir-viewing geometry. We use the two-stream approximation with a diffusivity factor of 1.66 to account for hemispheric integration; as a result, all values of optical depth in this chapter should be considered to be prescaled by this diffusivity factor (Pierrehumbert 2010). We performed all line-by-line calculations at a spectral resolution of 1 cm^{-1} over the wavenumber range 0–3000 cm^{-1}, which sensitivity tests showed was sufficient to achieve convergence. RFM calculations used a vertical grid with a uniform 100-m spacing, and underlying sea surfaces were assumed to have an emissivity of 1.

For the RFM calculations using realistic spectroscopy, the mass absorption coefficients were obtained from the HITRAN2016 database (Gordon et al. 2017). For calculations with H_2O, RFM uses the MTCKD continuum (Mlawer et al. 2012). For RFM calculations using parameterized CO_2 spectroscopy (e.g., equations 2.3 or 2.20), we ran RFM with synthetic lookup tables for κ that include standard linear pressure-broadening. Temperature scaling of line strength was not included in the calculations with synthetic spectroscopy. We did not model shortwave radiative transfer.

Appendix B: The unit optical depth approximation

The "unit optical depth" approximation states that the outgoing longwave radiation at a given wavenumber can be well-approximated by blackbody emission from the level of the atmosphere at which the optical depth equals 1. The purpose of this section is to justify this approximation and give a sense for its quantitative accuracy.

The outgoing longwave radiation at wavenumber k can be written as

$$\text{OLR}_k = B(k, T_\text{s})e^{-\tau_\text{s}} + \int_0^{\tau_\text{s}} B(k, T(\tau))e^{-\tau}\text{d}\tau, \tag{2.36}$$

where $B(k, T)$ is the Planck function evaluated at wavenumber k and temperature T, τ is the optical depth (for wavenumber k), and τ_s is the total optical depth of the atmospheric column at wavenumber k. Let us suppose that $B(k, T)$ can be parameterized as

$$B(k, T) \simeq B(k, T_\text{e}) \left(\frac{T}{T_\text{e}}\right)^n, \tag{2.37}$$

where T_e is a reference temperature and n is an exponent that must be determined. An example of such a parameterization for a wavenumber near the center of the 15-μ CO_2 band, with $T_\text{e} = 250$ K and $n = 3.5$, is shown in Figure 2.11.

To proceed, we must relate T and τ. For pressure-broadened, well-mixed CO_2, the optical depth as a function of pressure is given by equation 2.4. Meanwhile, in a hydrostatic atmosphere with a fixed lapse rate, pressure and temperature are related by

$$p(T) = p_\text{s}(T/T_\text{s})^{g/(R\Gamma)}. \tag{2.38}$$

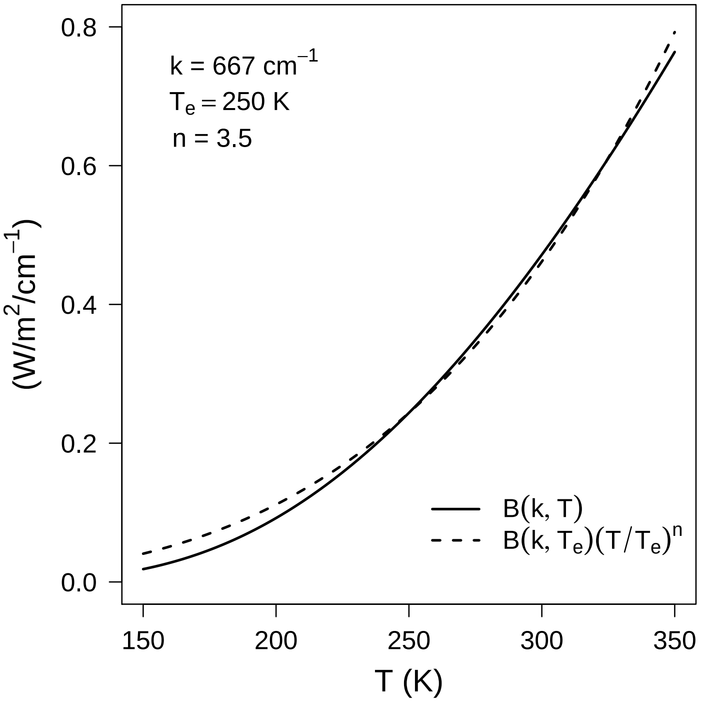

Figure 2.11: An example of the power-law parameterization of $B(k,T)$ given by equation 2.37. Here, we take $k = 667$ cm^{-1}, $T_\mathrm{e} = 250$ K, and $n = 3.5$.

Combining equations 2.4 and 2.38, we find

$$T(\tau) = T_s(\tau/\tau_\mathrm{s})^{\frac{R\Gamma}{2g}}, \tag{2.39}$$

where T_s is the surface temperature, R is the gas constant, Γ is the temperature lapse rate, and g is the gravitational constant. Note that there is nothing special about the T_s and τ_s appearing in equation 2.39, so we can replace them with a pair of T and τ at any reference level we choose. Let us define the *emission temperature* as $T_\mathrm{e} \equiv T(\tau = 1)$, and choose T_e and $\tau = 1$ as our reference point. Then, plugging the resulting expression for $T(\tau)$ into equation 2.37, we find

$$B(k,\tau) \simeq B(k,T_\mathrm{e})\tau^{\frac{nR\Gamma_\mathrm{t}}{2g}}. \tag{2.40}$$

Plugging this expression for B_k into equation 2.36 and evaluating the integral, we find

$$\mathrm{OLR}_k \simeq B(k,T_\mathrm{s})e^{-\tau_\mathrm{s}} + B(k,T_\mathrm{e})\gamma_-\left(\frac{nR\Gamma}{2g}+1,\tau_\mathrm{s}\right), \tag{2.41}$$

where γ_- is the lower incomplete gamma function, which is defined as $\gamma_-(a,x) \equiv \int_0^x t^{a-1}e^{-t}\mathrm{d}t$. Finally, let us assume that $\tau_\mathrm{s} \gg 1$ so that we are well clear of the lower boundary. Then we have

$$\mathrm{OLR}_k \simeq B(k, T_\mathrm{e})\gamma\left(\frac{nR\Gamma}{2g} + 1\right), \tag{2.42}$$

where γ is the gamma function, which is defined as $\gamma(a) \equiv \int_0^\infty t^{a-1}e^{-t}\mathrm{d}t$. The "unit optical depth" approximation, then, amounts to the assumption that $\gamma\left(\frac{nR\Gamma}{2g} + 1\right)$ is of order unity, so that OLR_k can be well-approximated by $B_k(T_\mathrm{e})$, the Planck emission from the temperature at which $\tau = 1$.

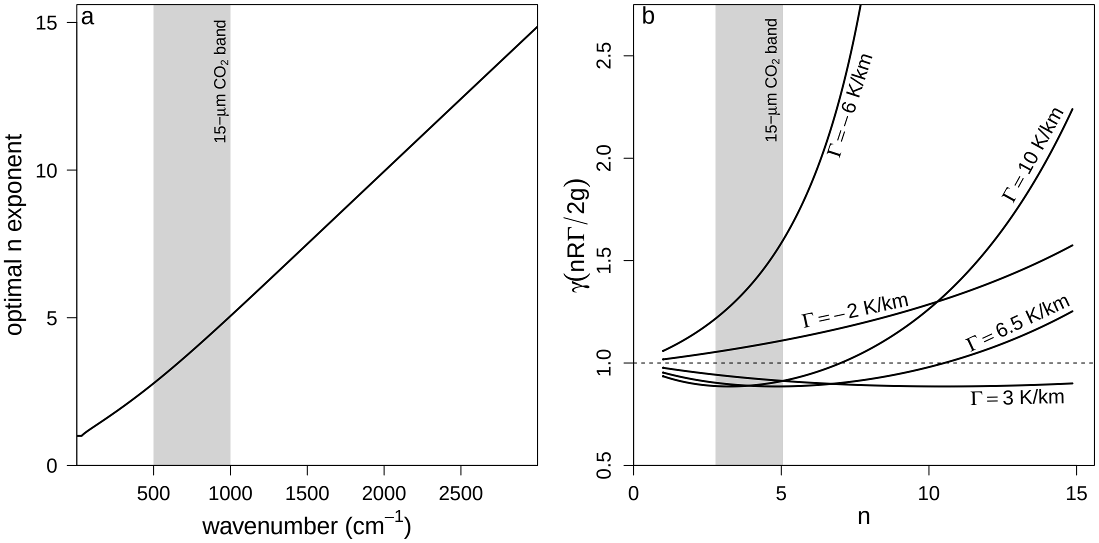

Figure 2.12: (a) As a function of wavenumber, the optimal-n exponent found by minimizing the cost function (equation 2.43). (b) As a function of n, the value of $\gamma\left(\frac{nR\Gamma}{2g} + 1\right)$ for a range of lapse rates that could plausibly be found in Earth's troposphere or stratosphere. We take $R = 287.04$ J/kg/K and $g = 9.81$ m/s^2. The wavenumber- and n-ranges corresponding to the 15-μm CO$_2$ band are shaded in gray in each panel.

How well should we expect the unit optical depth approximation to work for terrestrial atmospheres? The answer depends on the value of the gamma function for the relevant parameter range. For characteristic temperatures between 150 K and 350 K, the Planck function is negligible at wavenumbers greater than about 3000 cm^{-1}, so we will restrict our interest to this part of the spectrum. In Figure 2.12a, we show the optimal-n exponent for the parameterization of the Planck function given by equation 2.37, for temperatures between 150 K and 350 K and wavenumbers between 0 and 3000 cm^{-1}. The optimal n at each wavenumber k is found by minimizing the cost function

$$C_k(n) = \int_{150}^{350} \left[B(k, T_\mathrm{e})\left(\frac{T}{T_\mathrm{e}}\right)^n - B(k, T)\right]^2 \mathrm{d}T, \tag{2.43}$$

where we take $T_{\mathrm{e}} = 250$ K. The optimal n increases with wavenumber, from about 1 to around 15 at 3000 cm^{-1}. Within the principal 15-μm CO$_2$ band (between roughly 500 and 1000 cm^{-1}), n is in the range of 3–5. Similar ranges of n are found for different values of T_{e}.

Figure 2.12b shows the value of $\gamma\left(\frac{nR\Gamma}{2g}+1\right)$ for n values in the range of 1–15, $R = 287.04$ J/kg/K (i.e., Earth's dry air gas constant), $g = 9.81$ m/s^2, and for several different lapse rates. In the 15-μm CO$_2$ band, $\gamma\left(\frac{nR\Gamma}{2g}+1\right)$ is in the range 0.9–1.1 for lapse rates that are currently found in Earth's troposphere or stratosphere. Therefore, we can conclude that the unit optical depth approximation should be accurate to within about 10% for most purposes in this chapter. Important exceptions to this conclusion include: wavenumbers where $\tau_s \gtrsim 1$, for which neglect of the boundary term will bias the unit optical depth approximation low; wavenumbers that have $\tau = 1$ in a part of the atmosphere where the lapse rate is changing rapidly with height; and parts of the atmosphere with large negative lapse rates, in which the unit optical depth approximation can underestimate OLR$_k$ by $\gtrsim 25\%$ in the core of the CO$_2$ band. This fact partly explains the overestimation of $F_{2\mathrm{x}}$ for large negative stratospheric lapse rates in the "Theory" panel of Figure 2.7.

Chapter 3

The effect of global warming on severe thunderstorms in the United States

How will warming temperatures influence thunderstorm severity? This question can be explored by using climate models to diagnose changes in large-scale convective instability (CAPE) and wind shear, conditions that are known to be conducive to the formation of severe thunderstorms. Here, we first evaluate an ensemble of CMIP5 climate models on their ability to reproduce a radiosonde climatology of such storm-favorable conditions in the current climate's spring and summer seasons, focusing on the contiguous United States (CONUS). Of the eleven climate models evaluated, a high-performing subset of four (GFDL-CM3, GFDL-ESM2M, MRI-CGCM3, and NorESM1-M) is identified. Second, we calculate 21st-century changes in the frequency of severe-thunderstorm-favorable environments in these high-performing models as they are forced by the RCP4.5 and RCP8.5 emissions pathways. For the RCP8.5 scenario, the models predict consistent CONUS-mean fractional springtime increases in the range of 50–180% by the end of the 21st century, while for the summer, three of the four models predict increases in the range of 40–120% and one model predicts a small decrease. This disagreement between the models is traced to divergent projections for future CAPE and boundary-layer humidity in the Great Plains. We also explore the sensitivity of our results to the relative weight given to wind shear in determining how "favorable" a large-scale environment is for the development of severe thunderstorms, and find that this weighting is not the dominant source of uncertainty in projections of future thunderstorm severity.

---

[1] This chapter is a slightly edited version of Seeley and Romps (2014).

3.1 Introduction

In the United States, a thunderstorm is classified as "severe" if it produces wind speeds above a damaging threshold, hail exceeding a certain diameter, or a tornado (National Weather Service 2014). These storms down trees, loft roofs, flood roads, ignite fires with their lightning, and damage cars and crops with large hailstones. They are a significant cause of property damage, and are often deadly—in 2011 alone, over 500 people were killed by tornadoes in the United States (NOAA Storm Prediction Center 2012a). In spite of the catastrophic damage caused by severe thunderstorms in the current climate, their response to enhanced greenhouse forcing remains a poorly understood regional climate-change impact (IPCC 2012; Kunkel et al. 2013).

There are several reasons for this ongoing uncertainty. Most importantly, inconsistent reporting practices have obscured any storm trends that may have accompanied 20th-century anthropogenic global warming (Brooks and Doswell 2001; Doswell et al. 2005; Verbout et al. 2006; Brooks and Dotzek 2008; Diffenbaugh et al. 2008). As a consequence, research has instead focused on identifying the large-scale "ingredients" of severe convective storms and evaluating how these ingredients will respond to increasing atmospheric greenhouse-gas concentrations.

It has been recognized for quite some time that convective available potential energy (CAPE) and deep-layer wind shear—as well as other measures of wind shear, such as helicity—have skill in predicting the severity of thunderstorms in the case that such storms develop at all (Brooks et al. 1994; Rasmussen and Blanchard 1998; Rasmussen 2003). CAPE is a common measure of convective instability and sets an upper bound on the speed of updrafts, while ambient wind shear prolongs and intensifies storms by physically displacing deep-convective updrafts from rain shafts and promoting storm-scale rotation. It is not surprising, therefore, that operational weather forecasters use combinations of CAPE and wind shear (along with other information) to issue "watches" for severe thunderstorms, where a watch indicates that meteorological conditions are favorable for the development of severe weather within a few hours (Johns and Doswell 1992). In particular, Brooks et al. (2003) showed that a weighted product of CAPE and 0-6 km wind shear in reanalysis is well-correlated with the intensity of nearby observed storms.

The challenge is to determine how CAPE and wind shear—and specifically, their regional and sub-daily covariation—will change with warming temperatures. Increases in CAPE with global warming have been documented in both climate models [e.g., Sobel and Camargo (2011a)] and cloud-system resolving models (Romps 2011), and these increases were recently given theoretical support by Singh and O'Gorman (2013). On the other hand, a first-order prediction for future wind shear calls for a reduced thermal wind gradient, and hence mean shear, as a result of polar amplification of warming [e.g., Trapp et al. (2007a)]. These qualitative predictions for how global warming should affect CAPE and wind shear have opposing implications for the severity of future thunderstorms.

In light of this opposition, several recent climate model studies have attempted to quantitatively settle the competition between increasing CAPE and decreasing shear. Trapp et al.

(2007a) (hereafter, T07) performed the first multimodel comparison of future severe thunderstorms in the United States and found significant divergence between a regional climate model and three general circulation models (e.g., their Figure 3). Trapp et al. (2009) used NCAR's CCSM3 to predict increases in CAPE that outpaced decreases in wind shear, resulting in an increase in environments favorable for severe thunderstorms; however, results from a single GCM should not be given too much weight, considering the disagreement between models shown in T07. Most recently, Diffenbaugh et al. (2013) (hereafter, D13) expanded on the results of T07 with an enlarged ensemble of ten GCMs from the CMIP5 archive (Taylor et al. 2012). D13 found robust increases in the frequency of severe-thunderstorm environments in the spring and fall across most of the United States, again as a result of increases in CAPE that were large enough to overcome decreases in wind shear. However, the ensemble of models used in D13 diverged significantly in their predictions for the summer months of June, July, and August, which constitute half of the peak severe-thunderstorm season in the current climate (Kelly et al. 1985). The lingering uncertainty regarding these important months merits additional study.

Furthermore, in the context of these studies, it is clear that the relative weight given to CAPE and shear in defining storm-favorable conditions is of central importance; depending on this weighting, the same fractional changes in CAPE and shear derived from a climate model's global warming response could lead to quite different conclusions about changes in the frequency of severe thunderstorms. In fact, multiple studies have argued that the value of ambient wind shear is more strongly tied to a given thunderstorm's severity than the background CAPE (Brooks et al. 2003; Allen et al. 2011; Brooks 2013). However, previous climate model studies of the effect of global warming on severe thunderstorms in the United States have used a threshold for the unweighted product of CAPE and shear to define when a GCM gridpoint is storm-favorable. This discrepancy between observational severe-thunderstorm proxies and the proxies that have been used in previous modeling studies is an unnecessary source of uncertainty in our current understanding of the future of thunderstorms.

This chapter puts this line of research on more solid ground in two major ways. First, since the ensemble of climate models in D13 was not selected based on demonstrated skill at replicating the contemporary climatology of severe-thunderstorm conditions, it is plausible that some of the divergence in their ensemble's predictions for the future, especially in the summer, can be traced to differences between the models in their base state of simulated severe-thunderstorm conditions. To test this hypothesis, in Section 3.2, we derive an observational climatology of United States severe-thunderstorm environments from a decade of radiosonde observations and evaluate an ensemble of eleven CMIP5 climate models on their ability to capture the spatial pattern of these observations throughout the principal severe-thunderstorm season of March–August. Second, in Section 3.3, we focus on the changes in severe-thunderstorm conditions predicted by the high-performing subset of models identified in Section 3.2 as they respond to the range of greenhouse forcing spanned by the RCP4.5 and RCP8.5 emissions scenarios (van Vuuren et al. 2011). We explore the sensitivity of our results to the relative weight given to CAPE and shear in the definition of a severe-thunderstorm environment by repeating our analysis of future changes for a plausible range of shear weightings. Some conclusions and directions for future work are presented in Section 3.4.

3.2 Evaluating the GCMs

The predictions of a global climate model (GCM) about the future of severe thunderstorms are more trustworthy if the model demonstrates skill at simulating where and how frequently these storms occur in the current climate. Unfortunately, since the typical size of thunderstorms ($\simeq$25 km in diameter) remains below the threshold of resolution for current climate models, evaluating models requires identifying severe-thunderstorm-favorable environments (hereafter, "STEnvs") when the large-scale conditions of CAPE and wind shear are simultaneously abundant at the scale of a GCM grid cell. A loose analogy can be drawn between STEnvs and the severe-thunderstorm watches issued for the United States by the National Weather Service's Storm Prediction Center, although the latter typically cover an area larger than a GCM grid cell and are issued by meteorologists with access to more detailed characterizations of the atmosphere (Johns and Doswell 1992). Clearly the application of such individual expertise is infeasible for the systematic analysis of large quantities of GCM data. Nevertheless, the framework of severe-thunderstorm watches is instructive in the context of GCMs that do not resolve thunderstorms because a "watch" indicates only that atmospheric conditions are primed for the development of a storm, not that one has yet been observed. (This is in contrast to "warnings", which are issued once a storm has been confirmed.) Identifying storm-favorable environments based on the ambient levels of CAPE and wind shear in the weather of a climate model results in a picture of where and when the simulated atmosphere could have supported severe thunderstorms.

In order to benchmark GCMs against observations of severe-thunderstorm conditions, we have derived maps of CAPE and 0-6 km wind shear at 1°-resolution over the continental United States (CONUS) at 00 GMT — mid to late afternoon local time, the peak hours of severe thunderstorm formation (Kelly et al. 1985) — from a decade of radiosonde data as well as CMIP5 output for each of eleven GCMs. The radiosonde observations are provided by the Stratosphere-troposphere Processes and Their Role in Climate [SPARC, World Climate Research Programme (2014)] high-vertical-resolution radiosonde data (HVRRD); each 00 GMT sounding is filtered to detect instrument malfunction and interpolated to a uniform 100-meter vertical resolution. The eleven CMIP5 GCMs we evaluate, listed in Table 3.1, have a range of spatial resolutions and are drawn from modeling agencies from around the world (Taylor et al. 2012). CAPE was calculated assuming the adiabatic, undiluted ascent of a near-surface parcel of air; parcel densities were computed using a root solver and an exact expression for equivalent potential temperature derived by Romps and Kuang (2010a), which includes the effects of latent heat of fusion and the different heat capacities of the water phases. Wind shear was calculated as the magnitude of the vector difference between the near-surface winds and the winds at a pressure level with a mean altitude of 6 km above the ground. For more details about the radiosonde network, the ensemble of GCMs, and the

Table 3.1: The global climate models included in this chapter. Resolution is indicated in terms of (longitudinal points)×(latitudinal points)×(levels in the vertical).

GCM	**Institute**	**Resolution**
BCC-CSM1.1	Beijing Climate Center	128×64×26
BCC-CSM1.1(m)	Beijing Climate Center	320×160×26
CanESM2	Canadian Center for Climate Modelling and Analysis	128×64×35
CCSM4	National Center for Atmospheric Research	288×192×26
CNRM-CM5	Centre National de Recherches Meteorologiques	256×128×31
FGOALS-g2	Institute of Atmospheric Physics, Tsinghua University	128×60×26
GFDL-CM3	Geophysical Fluid Dynamics Laboratory	144×90×48
GFDL-ESM2M	Geophysical Fluid Dynamics Laboratory	144×90×24
MIROC5	Japan Agency for Marine-Earth Science and Technology	256×128×40
MRI-CGCM3	Meteorological Research Institute	320×160×48
NorESM1-M	Norwegian Climate Centre	144×96×26

calculation of CAPE and wind shear, see the Appendix.

Throughout this chapter, we identify 1° cells in the continental United States as STEnvs whenever the weighted product of CAPE and shear in that cell at 00 GMT exceeds a threshold. The criterion for STEnvs can be generally expressed as

$$[\text{CAPE}] \cdot [\text{shear}]^{\gamma} \geq \beta, \tag{3.1}$$

where CAPE is expressed in $\text{J}\cdot\text{kg}^{-1}$, shear in $\text{m}\cdot\text{s}^{-1}$, γ is the relative weight given to shear, and β is a threshold value with units of $(\text{m}\cdot\text{s}^{-1})^{2+\gamma}$. There are numerous precedents for using such a discriminator line in CAPE–shear phase space to identify large-scale environments that are conducive to the formation of severe thunderstorms. Brooks et al. (2003) found that equation 3.1 with $\gamma = 1.6$ and $\beta = 46800$ $(\text{m}\cdot\text{s}^{-1})^{3.6}$ was most effective at detecting reanalysis "pseudo-soundings" associated with significant severe thunderstorms in the United States, while Allen et al. (2011) found $\gamma = 1.67$ and $\beta = 115000$ $(\text{m}\cdot\text{s}^{-1})^{3.67}$ could do the same for short-term forecasts from a Numerical Weather Prediction model for Australia. Both of these studies used databases of observed thunderstorms and arrived at $\gamma > 1$, reflecting that the value of environmental shear is apparently of greater importance than the local CAPE in determining the severity of a given thunderstorm. Building on these insights, Allen et al. (2014a,b) used a discriminator line with $\gamma = 1.67$ in a detailed study of current and future severe-thunderstorm environments in Australia. On the other hand, climate-model studies of severe-thunderstorm environments in the United States have almost exclusively used $\gamma = 1$ and $\beta = 10000$ $(\text{m}\cdot\text{s}^{-1})^{3}$ (Marsh et al. 2007; Trapp et al. 2007a, 2009; Diffenbaugh et al.

2013), with one study using $\beta = 20000$ $(\mathrm{m \cdot s^{-1}})^3$ (Gensini et al. 2013). One purpose of this chapter is to quantify the extent to which previous work may have reported inflated increases in United States severe-thunderstorm environments as a result of underweighting the effect of future decreases in shear.

However, for the purpose of evaluating climate models on their simulation of current-climate severe-thunderstorm conditions, we take $\gamma = 1$ and $\beta = 36300$ $(\mathrm{m \cdot s^{-1}})^3$. The choice of $\gamma = 1$ in this section was made for simplicity and in order to have the most contact with previous multi-model studies of United States severe thunderstorms; in any case, the value of γ is much more important when considering trends in STEnvs than it is when seeking a general picture of GCM performance in the current climate, and γ will be allowed to vary substantially in Section 3.3 when we analyze trends in STEnvs. The chosen value of β selects the upper 3% of [CAPE]·[shear] in the radiosonde data, and was found to result in a mean annual number of STEnvs that compares well with what was found in reanalysis by D13 and others, building confidence that we are considering a similarly extreme population of CAPE and shear combinations despite potential differences in the calculation of CAPE.

NOAA climatologies of past severe-thunderstorm watches indicate that the region of peak storm activity in today's climate is the central United States, beginning east of the Rocky Mountains, extending from the middle of Texas north to the Dakotas, and tailing off toward the East Coast (NOAA Storm Prediction Center 2012b). This region of significant severe-thunderstorm activity in the central US is readily apparent in historical reports of large hail and severe convective winds (left panel of Figure 3.1), and is the most salient feature of the current climate's pattern of severe-thunderstorm activity. Overall, Figure 3.1 shows that the climatology of STEnvs derived from radiosondes is well-correlated with the region of observed severe-thunderstorm damage in the central US.

An exception is the region of south Texas, where a large number of STEnvs occur but there have been few reports of severe-thunderstorm damage. This feature has been noted previously in United States reanalysis by Gensini and Ashley (2011) and others, and highlights an important point about what information can be gleaned from STEnvs. STEnvs do not account for factors that are known to be closely tied to storm initiation — from small-scale outflow boundaries to large-scale inversions — and are therefore agnostic about whether thunderstorms actually occurred. It is well-known that southern Texas is frequently capped by an elevated mixed layer that is advected eastward from the high desert terrain of the Mexican plateau (Carlson and Ludlam 1966). In the absence of mechanisms to erode the inversion, this "lid" has such a strong inhibiting effect on thunderstorm formation in south Texas that, even though CAPE and shear are abundant, severe thunderstorms are rare.

Clearly, this uncertainty regarding storm initiation limits our ability to translate trends in STEnvs into projections for future severe thunderstorms. Changes in the processes that inhibit and promote storm initiation, which cannot at present be resolved by GCMs, may have an attenuating or amplifying effect on the way STEnv trends will influence future thunderstorms. van Klooster and Roebber (2009) derived an index of convective initiation potential from the large-scale variables resolved by climate models and found no change in this initiation potential over the 21st century, but that study only considered a single GCM. Another

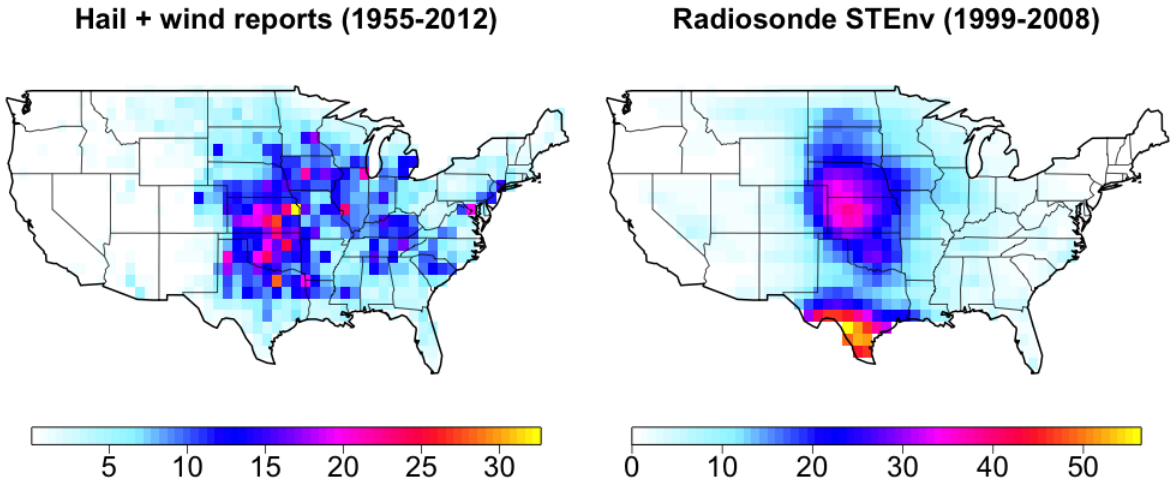

Figure 3.1: Left: Mean annual reports (per square degree) of hail greater than 1 inch in diameter or winds in excess of 50 knots, from 1955–2012 (NOAA Storm Prediction Center 2012b). Reports are binned in 1cells based on the longitude and latitude coordinates recorded for the report by the Storm Prediction Center. Right: Mean annual STEnvs (days per year with CAPE·shear $\geq$ 36300 $(\mathrm{m{\cdot}s^{-1}})^3$ at 00 GMT) derived from the SPARC radiosonde network for the years 1999–2008.

promising avenue for studying convective initiation is dynamically downscaling GCM output with a high-resolution regional climate model that can explicitly resolve convective storms, although such results are still model-dependent and generating long integrations with this technique is computationally intensive (Trapp et al. 2007b, 2011; Robinson et al. 2013). A self-contained multi-model analysis of future changes in convective-initiation may become a tractable problem only once GCM resolutions have substantially improved. Therefore, for the moment the best one can do is assume that the fraction of STEnvs that develop severe storms will be the same in the future as in the present, but there is not much to justify this assumption besides necessity.

With these limitations in mind, it is encouraging that the observational climatology of STEnvs does highlight the region of maximum severe-thunderstorm damage in the central US. It is also worth noting the similarity between the radiosonde observations in the right panel of Figure 3.1 and the distribution of severe-thunderstorm environments found previously in reanalysis by, for example, Brooks et al. (2003) and D13. Given the widely recognized deficiencies in the ability of reanalysis fields to represent sharp vertical gradients of thermodynamic quantities (Gensini et al. 2013), it was not a foregone conclusion that severe-thunderstorm conditions estimated from high-vertical-resolution radiosonde data would not appear substantially different from those derived from reanalysis. The similarity of the radiosonde climatology of STEnvs presented here with reanalysis data confirms that

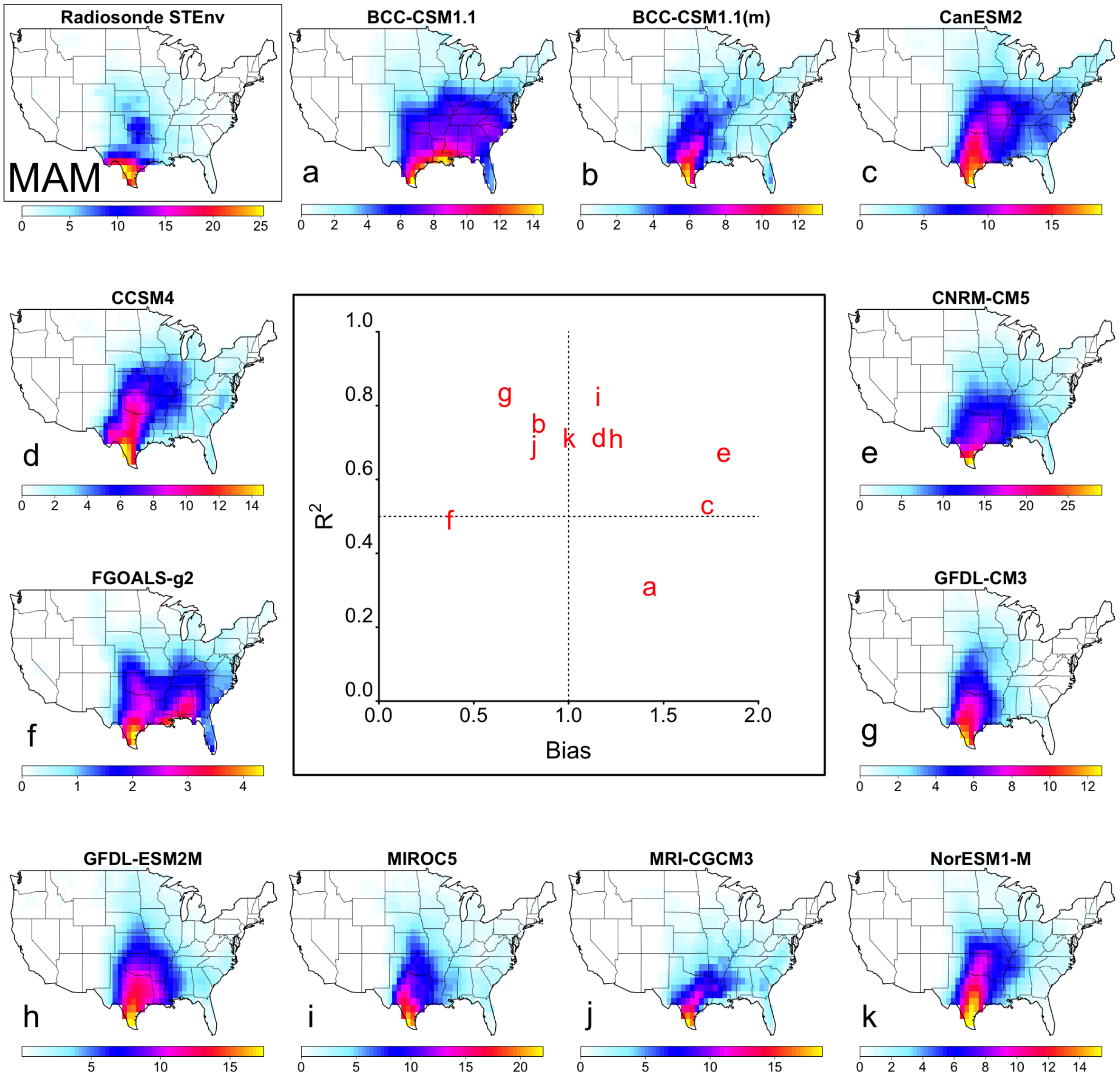

Figure 3.2: Mean STEnvs per spring (March, April, May) for the years 1999–2008 in SPARC radiosonde observations (upper left) and for the years 1996–2005 in eleven CMIP5 global climate models (edge panels). The center panel is a summary of the ability of the 11 GCMs in our ensemble to simulate the radiosonde observations. The ordinate of the center panel is the spatial coefficient of determination (R^2) and is a measure of how well a GCM's geographical distribution of STEnvs matches the distribution in the radiosonde data. The abscissa ("Bias") is the ratio of a GCM's CONUS-mean STEnvs (land grid points only) to that of the radiosonde climatology, and thus is a measure of how well a GCM predicts the observed number of STEnvs per season per year.

reanalysis is a suitable tool for the study of large-scale environments associated with severe thunderstorms.

But how well can CMIP5 GCMs reproduce the observed pattern of storm activity? 93% of STEnvs in the radiosonde data occur between the months of March and August, and it has been previously noted by Kelly et al. (1985) that more than 80% of thunderstorms producing damaging winds and large hail occur during these months. Therefore, we focus our analysis on the spring (MAM) and summer (JJA) seasons. The edge panels in Figures 3.2 and 3.3 show the climatologies of STEnvs derived from the radiosonde data and eleven CMIP5 climate models for the current-climate's spring and summer seasons, respectively. The differences in model skill are most apparent during summer, when there is significant spread in how well the climate models capture the radiosonde observations' concentration of STEnvs in the central US. A majority of the GCMs depicted in Figure 3.3 predict that much of the East Coast of the United States should be at least as frequently favorable for the development of summertime severe thunderstorms as the Great Plains, in stark contrast to the radiosonde observations, and some models actually have local STEnv minima in the Great Plains (e.g., BCC-CSM1.1(m) and CanESM2). These differences between the models are not nearly as apparent for the spring months shown in Figure 3.2, when most models qualitatively capture the concentration of STEnvs creeping up from Texas into the southern Great Plains. A likely explanation for the better performance of the models in the spring is the predominance of synoptic forcing, which is on a scale better resolved by GCMs, as compared to the mesoscale-system-dominated summer (Fritsch et al. 1986).

The GCM ensemble's performance is summarized in the center panels of Figures 3.2 and 3.3, where we show pattern correlations between the climatologies of STEnvs for the radiosonde data and the GCMs. We also quantify the overall seasonal bias in the number of STEnvs that occur in the GCMs. The pattern correlations confirm that many of the GCMs in our ensemble have very little predictive power in the summer. In this chapter, we stipulate that a GCM must have a pattern correlation of 0.5 for both MAM and JJA current-climate STEnvs (R^2 in the center panels of Figures 3.2 and 3.3) in order to be considered skillful at simulating severe-thunderstorm conditions. According to this criterion, the four high-performing models are GFDL-CM3, GFDL-ESM2M, MRI-CGCM3, and NorESM1-M. The principal difference between high-performing and low-performing GCMs is the zonal distribution of STEnvs in the summer: the high-performing group has its summertime peak of STEnvs in the central United States, collocated with the defining feature of the radiosonde observations. On the other hand, the low-performing GCMs display a much broader swath of STEnvs and/or significant peaks in activity on the East Coast in the summer. When we consider the effect of global warming on STEnvs in Section 3.3, we will focus our attention on this subset of high-performing models to see if they display a more consistent summertime response than was found for the larger ensemble of D13. However, given the inherent subjectivity in evaluating climate models to determine which are "high-performing" (Tebaldi and Knutti 2007), we will also present a summary of results for all eleven GCMs in our ensemble.

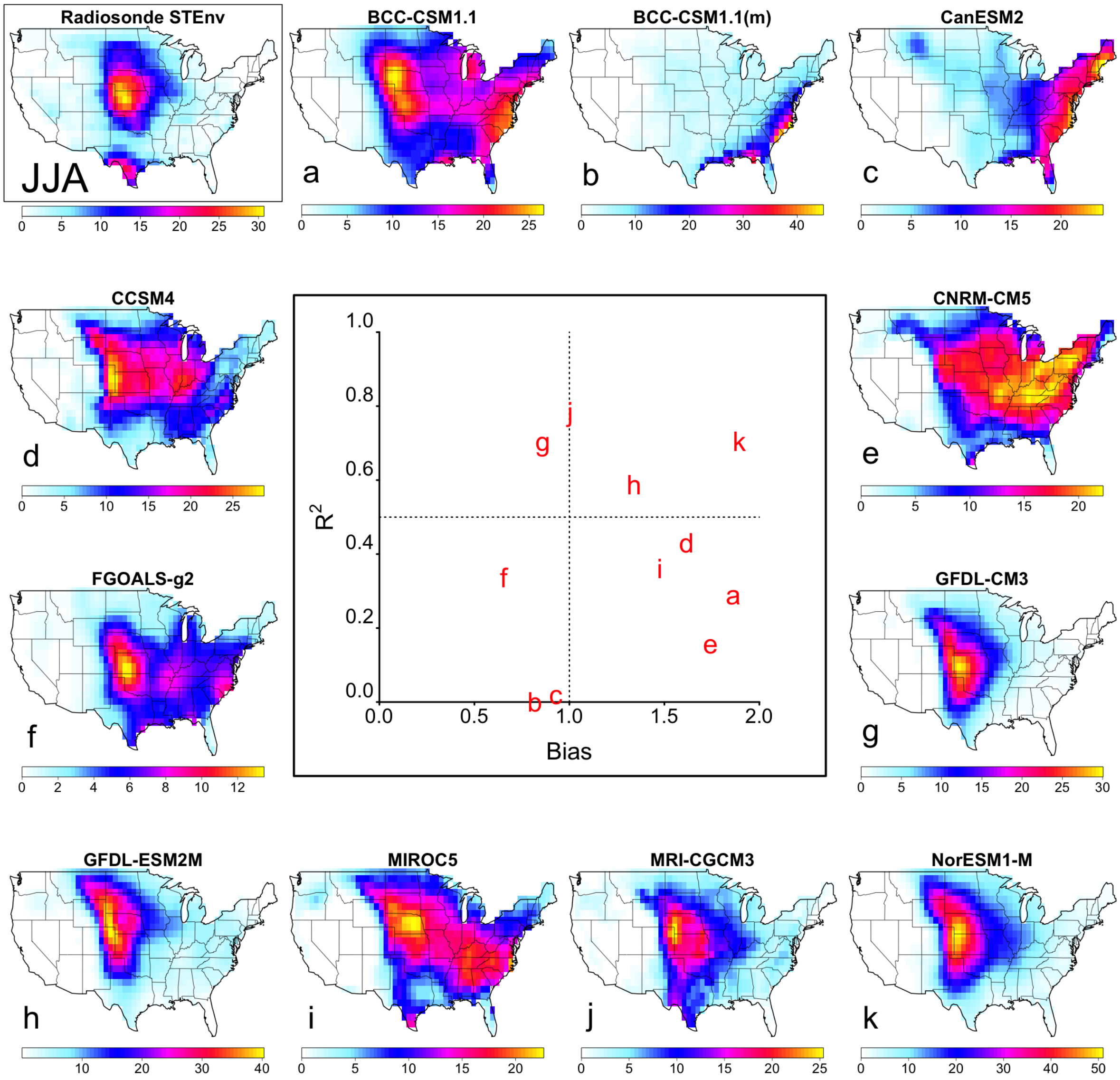

Figure 3.3: As in Figure 3.2, but for the summer months of June, July, August (JJA).

3.3 Severe thunderstorms in a warm future United States

The high-performing models identified in Section 3.2 are used here to predict changes in thunderstorm severity approximately 75 years in the future. We use CMIP5 data from the decade 2079–2088 of the RCP4.5 and RCP8.5 experiments to represent the future climate under medium and high levels of greenhouse forcing, respectively (van Vuuren et al. 2011), and identify STEnvs in the simulated weather of the GCMs for this decade using the same method presented in Section 3.1. Under the assumption that the same fraction of STEnvs will be actualized into storms in the future as at present, changes in STEnvs tell us about how GCMs predict the frequency of severe thunderstorms will change. In section 3.3.1, we again use $\gamma = 1$ and $\beta = 36300$ $(\mathrm{m{\cdot}s^{-1}})^3$ as a $[\mathrm{CAPE}]{\cdot}[\mathrm{shear}]^\gamma$ threshold, allowing us to diagnose how often in each GCM's simulated future the sub-daily product of CAPE and shear at local mid to late afternoon would cause the environment to be classified as a STEnv. The sensitivity of changes in STEnvs to the relative weight given to shear is explored in section 3.3.2.

3.3.1 $\gamma = 1$ (CAPE and shear equally weighted)

The changes in annual mean spring and summer STEnvs due to global warming are shown for the high-performing GCMs in Figures 3.4 and 3.5, respectively. In order to probe the models' response to a range of radiative forcing, we show results for both the RCP4.5 and RCP8.5 greenhouse emissions scenarios, which respectively represent medium-mitigation and high-carbon business-as-usual pathways (van Vuuren et al. 2011). Figure 3.4 shows that in the spring, the ensemble of high-performing models predict a consistent response of increased STEnvs extending from Texas into the southern and central Great Plains. This region of increase coincides with the current climate's spatial pattern of STEnvs — evident in both the radiosonde and GCM data shown in Figure 3.2 — suggesting a "stormy gets stormier" response for springtime severe thunderstorms. These results agree with those of Diffenbaugh et al. (2013), who found consistent increases in severe-thunderstorm environments during the spring for a 10-member ensemble of CMIP5 models. The trends for this season are robust to the range of greenhouse forcing spanned by the RCP4.5 and RCP8.5 scenarios, with the magnitude of predicted CONUS-mean increases ranging from 30 to 150% for the RCP4.5 scenario, and from 50 to 180% for the RCP8.5 scenario. The fact that the increases for the RCP4.5 scenario are smaller than the RCP8.5 increases by 20–50% suggests that the climate policies adopted in the coming decades will affect the severity of the spring thunderstorm season in the United States.

The summertime response of the high-performing ensemble of models is considerably more diverse (Figure 3.5). For the RCP8.5 scenario, three of the four high-performing models predict increases in the range of 40–120%, while one model (NorESM1-M) predicts an approximately 10% decrease. In all cases, these changes are concentrated in the central and northern Great Plains, around the climatological maximum of STEnvs for the current-climate radiosonde data and four high-performing GCMs shown in Figure 3.3. In contrast

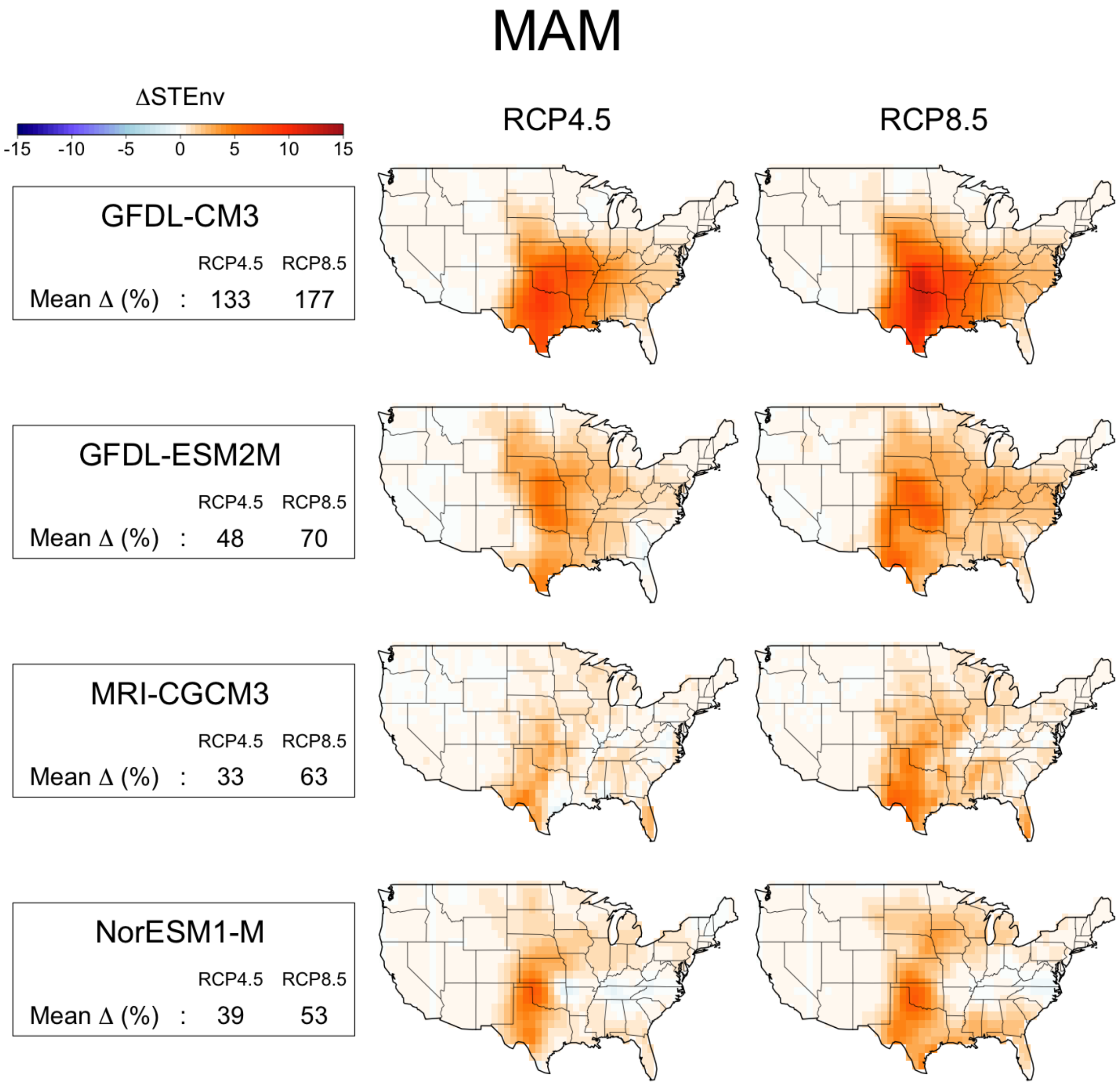

Figure 3.4: Changes due to global warming in annual mean STEnvs during the spring months of March, April, and May in the high-performing GFDL-CM3, GFDL-ESM2M, MRI-CGCM3, and NorESM1-M models. Results for both the RCP4.5 and RCP8.5 greenhouse gas forcing scenarios are presented. Changes are calculated as the mean of the period 1996–2005 of the CMIP5 historical experiment subtracted from the mean of the period 2079–2088 of the RCP experiment. A summary of the fractional CONUS-mean changes is given for each of the four models in the boxes at left.

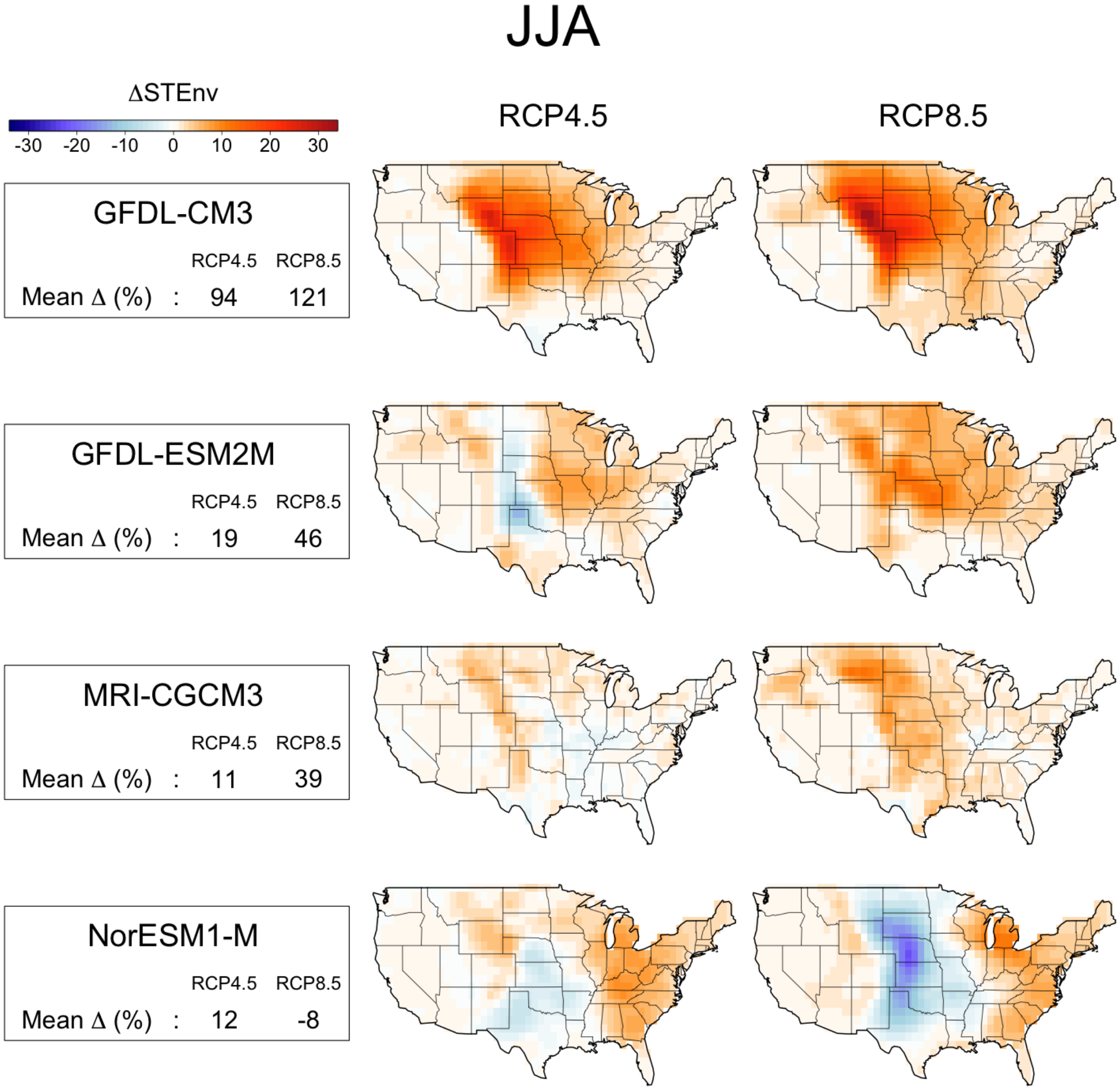

Figure 3.5: As in Figure 3.4, but for the summer months of June, July, August (JJA).

to the spring season, during the summer the RCP4.5 response is qualitatively different from the RCP8.5 response for two of the models, changing sign locally in the central Great Plains for GFDL-ESM2M and in the CONUS-mean for NorESM1-M.

One motivation for this chapter was the hypothesis that a restricted ensemble of CMIP5 climate models, selected for their demonstrated skill at matching a radiosonde climatology of STEnvs, might display a more consistent response to greenhouse forcing than the larger ensemble used by D13, particularly in the summer. The results shown in Figure 3.5 partially discredit this hypothesis, because the four highest-performing models identified in Section 3.2 do not agree on even the sign of CONUS-mean changes in the frequency of summer STEnvs under the strong radiative forcing of the RCP8.5 scenario, and there is no clear distinction between the response of the "high-performing" and "low-performing models" in CONUS-mean percent increases in STEnvs (Figure 3.6).

However, there is a clear outlier among the "high-performing" models: NorESM1-M predicts decreases in summer STEnvs throughout the Great Plains—unlike GFDL-CM3, GFDL-ESM2M, and MRI-CGCM3, which together show a consistent increase in this region when forced by RCP8.5-level emissions. Variations in simulated future shear are not the source of the difference between NorESM1-M and the other three models, as all four of these models predict decreasing CONUS-wide wind shear in the range of -5 to -14% for this season under RCP8.5 forcing. However, NorESM1-M is a significant outlier in this small ensemble of high-performing models for its predicted changes in CAPE and boundary-layer humidity (Figure 3.7). While the GFDL models and MRI-CGCM3 predict increases in CAPE on the order of 1 kJ$\cdot$kg^{-1} throughout the Great Plains, NorESM1-M predicts that mean summertime CAPE will decrease by roughly 500 J$\cdot$kg^{-1} in this region. The increases in CAPE in the first three models appear to be driven by increases in boundary-layer specific humidity (q_v) that roughly follow Clausius-Clapeyron scaling, while NorESM1-M's decreases in CAPE are driven by a widespread aridification of the Great Plains. A time series of NorESM1-M's boundary-layer humidity throughout the 21st century (not shown) indicates that our chosen time period is not simply anomalously dry for this model—the drying trend emerges around the year 2050 and persists thereafter. Such a drying-out in the 21st century, while being opposite the observed 20th century trend (Dai 2006), is not impossible.

In any case, the results of Figures 3.5 and 3.7 show that simulated future changes in thunderstorm severity are closely tied to changes in boundary-layer humidity, as has been argued previously (Trapp et al. 2007a, 2009; Diffenbaugh et al. 2013). This suggests that focusing model development on the processes responsible for low-level humidification — such as the influence of soil moisture and advection from the Gulf of Mexico into the Great Plains — is an important step toward further constraining the severe thunderstorms–global warming connection.

3.3.2 Sensitivity to γ

In the analysis presented thus far, STEnvs were identified for radiosonde and GCM data when equation 3.1 with $\gamma = 1$ and $\beta = 36300$ (m$\cdot$s^{-1})^3 was satisfied. These choices of parameters

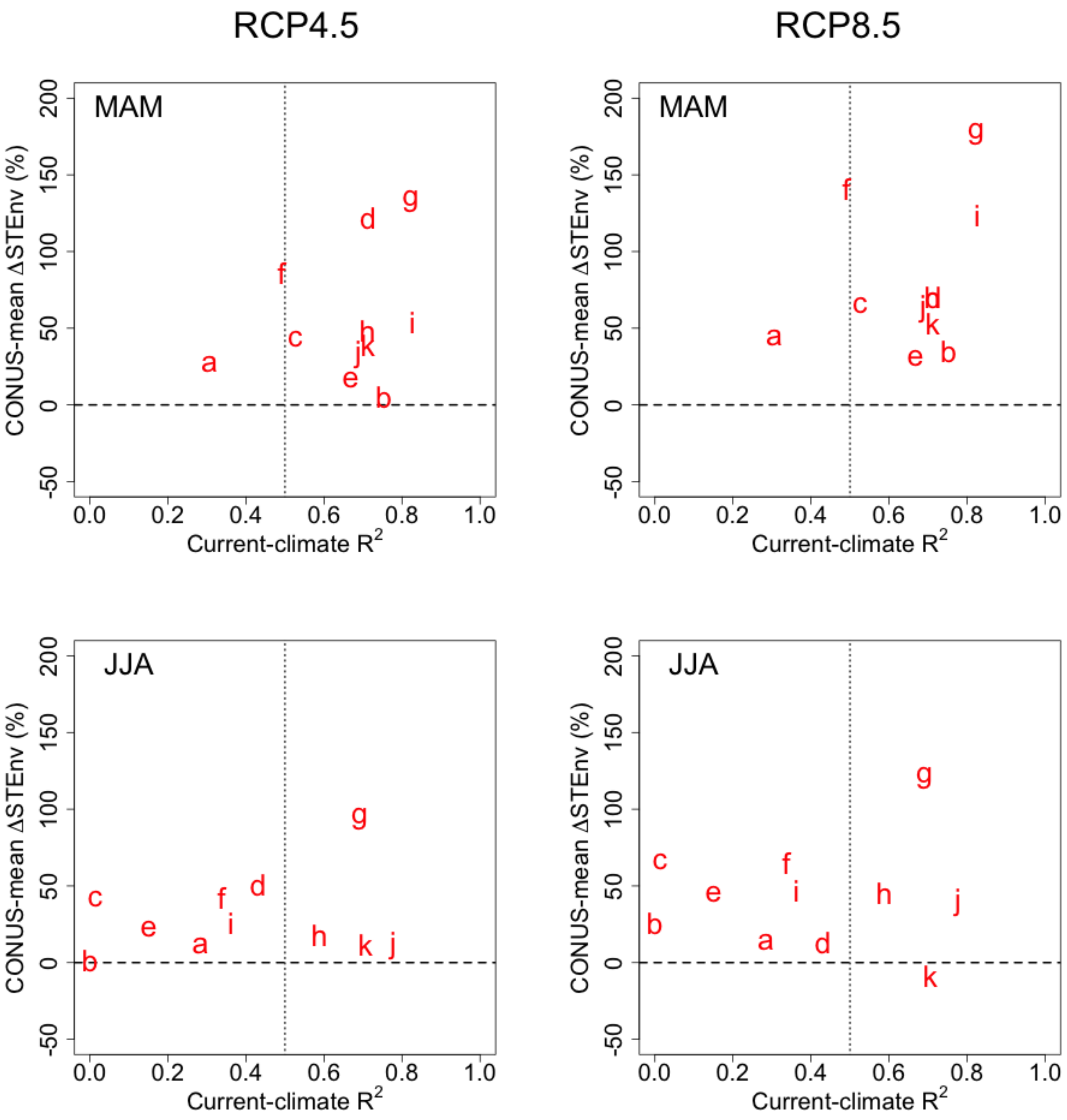

Figure 3.6: Changes in spring (MAM) and summer (JJA) CONUS-mean STEnvs in the eleven GCMs listed in Table 3.1, as a function of their R^2 "score" on their ability to match the spatial pattern of observed current-climate STEnvs. The letters correspond to the same models as in Figures 3.2 and 3.3; the "high-performing" models are those that have an R^2 above 0.5 for both spring and summer.

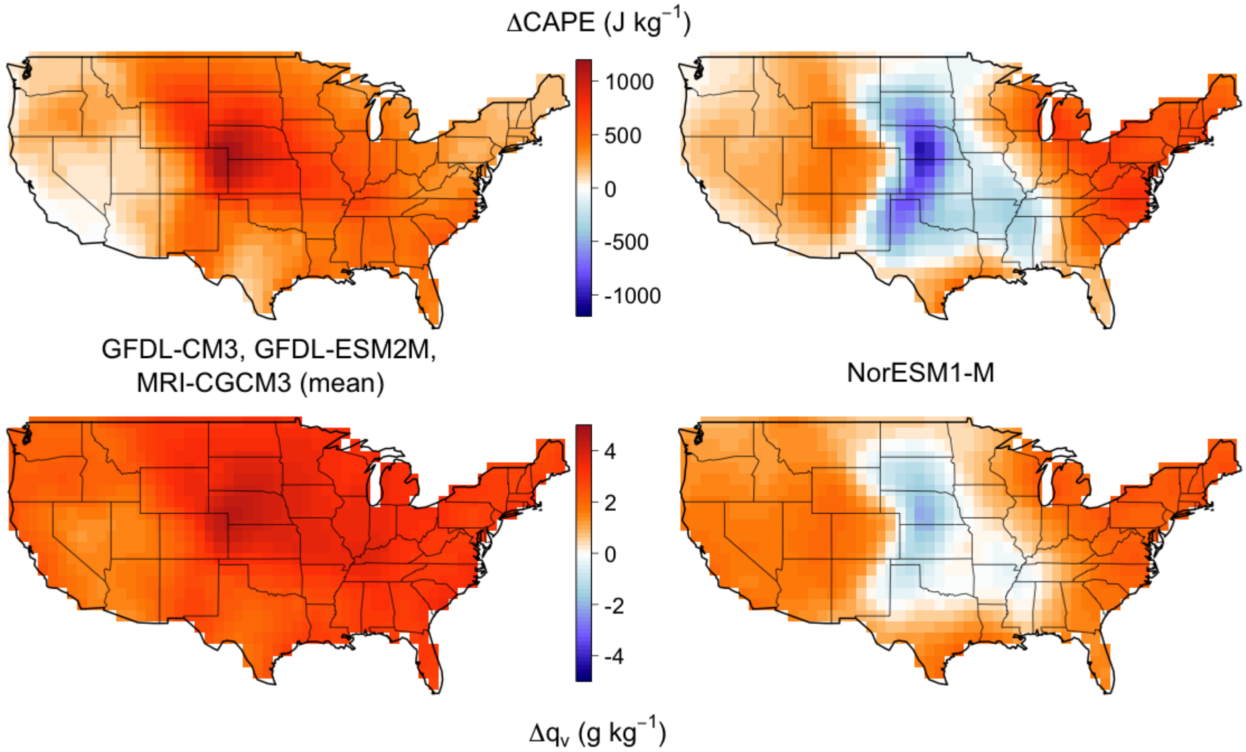

Figure 3.7: Changes in summertime (JJA) CAPE (first row) and boundary-layer humidity (q_v, second row) in the high-performing GFDL-CM3, GFDL-ESM2M, and MRI-CGCM3 models (mean of these three models, left column), and the NorESM1-M model (right column). Changes are calculated as the mean of the period 1996–2005 of the CMIP5 historical experiment subtracted from the mean of the period 2079–2088 of the RCP8.5 experiment.

Table 3.2: The value for the threshold β in equation 3.1, for each value of γ used to test the sensitivity of modeled changes in STEnvs. β is varied to always select the top 3% of [CAPE]$\cdot$[shear]$^\gamma$ in the decade 1999-2008 of radiosonde data.

γ **(shear weight)**	β **(threshold)** $[(\mathrm{m}\cdot\ \mathrm{s}^{-1})^{2+\gamma}]$
1.0	36300
1.1	48630
1.2	65270
1.3	87740
1.4	118230
1.5	159540
1.6	215590
1.7	291640
1.8	395270
1.9	536300
2.0	729000

give equal weight to the value of CAPE and the value of shear, and select the upper 3% of the product of CAPE·shear at 00 GMT in the decade of radiosonde data spanning 1999-2008. However, multiple studies have argued that the value of ambient wind shear has more influence on a given thunderstorm's severity than the local CAPE environment, and therefore suggested that equation 3.1 with a value of γ closer to 1.6 or 1.7 is better at identifying environments favorable for severe thunderstorms (Brooks et al. 2003; Allen et al. 2011; Brooks 2013). In this section, we test the sensitivity of the results presented in Section 3.33.3.1 to the choice of γ by repeating our analysis of CONUS-mean fractional changes in STEnvs while allowing γ to range from 1 to 2.

As γ is varied, the threshold β is varied as well to keep constant the number of STEnvs occurring for the radiosonde data. (That is, β is adjusted to select the upper 3% of [CAPE]$\cdot$[shear]$^\gamma$ in the decade of observations, regardless of γ. This reflects the fact that the number of severe thunderstorms that actually occur does not depend on the details of an empirical threshold.) Varying β and γ in this way does not qualitatively affect the observational climatology of STEnvs (the annual climatologies are correlated with one another with an R^2 in the range of 0.99–0.85 over the range of γ), nor does it significantly affect the separation of models into the high-performing and low-performing groups presented in Section 3.2. Table 3.2 gives the threshold β used for each value of γ in this analysis.

The sensitivity to γ of the changes in CONUS-mean STEnvs predicted by the high-performing models is shown in Figure 3.8. Given that the effect of climate change on severe thunderstorms has long been cast as a competition between increasing CAPE and decreasing

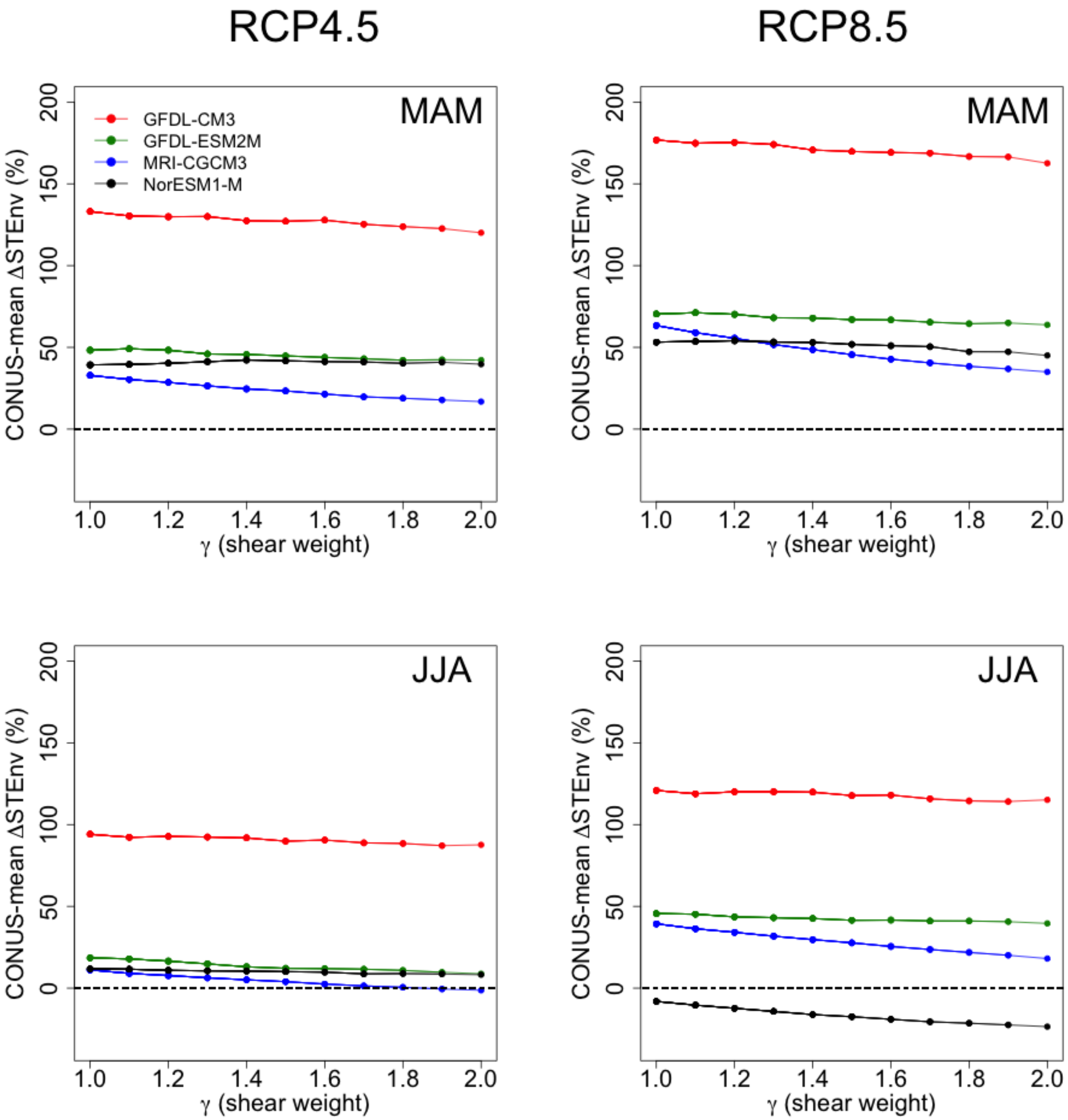

Figure 3.8: The dependence of global-warming-induced CONUS-mean percent changes in STEnvs on the value of γ in equation 3.1, which defines the relative weight given to shear with respect to CAPE in determining whether a large-scale environment is considered favorable for severe thunderstorms. Results for the RCP4.5 and RCP8.5 emissions pathways and both MAM and JJA seasons are shown. The slope of the line for each model gives an estimate of the sensitivity of that model's CONUS-mean percent changes in STEnvs to a unit increase in γ from 1 to 2.

shear, one expects increasing γ to generally suppress increases in STEnvs. The sensitivity varies across models, seasons, and RCP forcing pathways, but the negative slope of the lines in Figure 3.8 confirms this prediction. The MRI-CGCM3 model is the most sensitive to changes in γ for all seasons and forcing pathways, with its summertime increases in RCP8.5 STEnvs reduced from roughly 60% to 30%. Similarly, the small decreases predicted by NorESM1-M in the summer when forced by RCP8.5 emissions become more negative when γ is increased from 1 to 2.

Overall, the relatively gentle slopes of the sensitivity lines in Figure 3.8, even up to values of γ that exceed what has been suggested before by Brooks (2013) and others, imply that the qualitative results of GCM experiments when using $\gamma = 1$ will not differ substantially from those for $\gamma = 1.6-1.7$. Given the many other sources of unpredictability inherent to modeling future large-scale convective environments, Figure 3.8 suggests that the relative weight given to shear and CAPE in the definition of a severe-thunderstorm-favorable environment is not the dominant source of uncertainty in this line of research. This builds confidence in the picture of future severe-thunderstorm increases given by our Figures 3.4 and 3.5 and puts previous work by D13 and others who used $\gamma = 1$ to predict increases in United States severe-thunderstorm environments on more solid ground.

3.4 Conclusions

This chapter was motivated by two significant holes in our current understanding of the influence of global warming on severe thunderstorms in the United States. First, the analysis of Diffenbaugh et al. (2013) did not find statistically robust changes for summertime severe-thunderstorm environments in their ten-member ensemble of CMIP5 climate models. To test if some of the divergence in their ensemble's predictions for the future could be traced to differences between models in their simulation of severe-thunderstorm conditions in the current climate, we looked at changes in STEnvs in a subset of four CMIP5 GCMs that were best able to match a radiosonde climatology of STEnvs. Our Figure 3.5 shows that — even when focusing on high-performing models — there is disagreement on the sign of domain-mean summertime changes in future severe-thunderstorm environments under RCP8.5 forcing. For the months of June, July, and August, the outlier in the high-performing group of models is NorESM1-M, which, unlike GFDL-CM3, GFDL-ESM2M, and MRI-CGCM3, predicts a widespread aridification of the central United States and a corresponding decrease in convective instability in the 21st century. This suggests that from a storm-ingredients perspective (i.e., neglecting changes in initiation), the future severity of thunderstorms is closely tied to low-level humidification. As such, further study of low-level humidification processes seems to be a prerequisite for achieving some level of consensus among climate models about future changes in summertime severe thunderstorms.

The second nagging source of uncertainty in projections of future thunderstorm severity addressed by this chapter is the fact that previous climate model studies of United States storms have all given equal weight to CAPE and wind shear in determining how “favorable” an environment is for severe thunderstorms (Trapp et al. 2007a, 2009; Diffenbaugh et al. 2013; Gensini et al. 2013), despite the fact that observational studies have argued that shear is more important than CAPE in determining a given thunderstorm's severity (Brooks et al. 2003; Allen et al. 2011; Brooks 2013). The results of our Figure 3.8 suggest that the relative weight given to shear is not the dominant source of uncertainty in projections of future thunderstorm severity (i.e., each model's changes due to a unit increase in γ are smaller than the intermodel spread, even amongst just the high-performing models). This increases the level of confidence one may have in our results and those of previous work by Diffenbaugh et al. (2013) and others.

Overall, this chapter adds to the growing consensus that there will be more annual severe-thunderstorm-favorable combinations of CAPE and wind shear in a warm future United States, but there remain many unanswered questions about the future of severe thunderstorms. A largely unexplored subtlety in the use of CAPE-shear discriminant lines is the fact that not all storm environments above the discriminant line have equal probability of giving rise to severe thunderstorms, with environments further above the line more likely to do so than those just barely exceeding the threshold. It should be possible to glean some useful information from the mean "distance" of storm-favorable environments above any given discriminant line and refine the picture that results from only considering changes in the frequency of threshold exceedance.

The chief remaining source of uncertainty is the fact that, out of necessity, we have had to assume that the fraction of severe-thunderstorm environments developing into actual storms will be constant in time. This assumption is not well-justified, and future changes in convective inhibition, extratropical storm tracks, and other processes known to be intimately related to storm initiation would have amplifying or attenuating effects on the trends in STEnvs identified here. These subjects will be ripe for investigation as GCM resolutions continue to improve in coming years.

Appendix: Data and Methods

Calculation of CAPE and shear

In this chapter, we diagnose convective instability using convective available potential energy (CAPE), which is the vertically integrated Archimedean buoyancy of a parcel of air taken from near the surface and lifted adiabatically through a column of the atmosphere. The precise value of CAPE associated to a column of the atmosphere depends on many assumptions about the definition of a parcel, the role of entrainment, and the treatment of fusion and condensate loading. These varying conventions have quantitative, not qualitative, effects on climatological CAPE values, and no one form of CAPE has been shown to be best suited to diagnosing severe-thunderstorm environments. In this chapter we choose to use undiluted, near-surface-based, adiabatic CAPE defined as follows:

$$\text{CAPE} = \max_{p} \int_{p}^{p_s} \left(\frac{1}{\rho_p} - \frac{1}{\rho_e} \right) dp', \tag{3.2}$$

where ρ_e is the environmental air density and ρ_p the parcel density. In practice, the above integral was trapezoidally approximated by calculating the buoyancy of a near-surface parcel at a series of discrete pressure levels in the radiosonde or GCM data. Parcel densities were calculated by using a root solver to find the thermodynamic state consistent with the equivalent potential temperature of the near-surface air. For this purpose, we use an exact expression for equivalent potential temperature derived by Romps and Kuang (2010a), which includes the effects of latent heat of fusion and the different heat capacities of the water phases.

A number of measures of vertical wind shear have been used in combination with some criterion of instability to discriminate between severe and non-severe convective environments (Craven and Brooks 2004). The two previous multi-model studies of severe thunderstorm forcing in the United States have used the magnitude of the difference between the horizontal wind vector near the surface and 6 km above the surface (Trapp et al. 2007a; Diffenbaugh et al. 2013), and we do the same here, with one small difference: we take the upper-level winds from the pressure level equal to the mean of the surface pressure and 100 mbar. This ensures that the upper-level height adjusts upward with topography; with this definition, the mean height of over the CONUS is about 6 km. This has very minor effects on the sounding-by-sounding and climatological wind shear values.

Calculating these metrics of storm potential for a GCM column results in one value of CAPE and one value of shear associated to an area that is ≃100–200 km on a side, while when calculating from a radiosonde one obtains values associated to a particular weather station within a network of such stations spread hundreds of kilometers apart (Figure 3.9). To allow for comparison between the radiosonde network data and GCMs with varying resolutions, we bicubically interpolate all CAPE and shear values to a uniform 1° grid over the contiguous United States. The bicubic interpolation method was chosen for its speed, and negative values of CAPE that are generated by this interpolation are set to zero.

Radiosonde data

To produce a benchmark climatology of CAPE that is untainted by the parameterization of convection in reanalysis models, one must appeal directly to radiosonde data. For this chapter, we use the Stratosphere-troposphere Processes And their Role in Climate (SPARC) high-vertical-resolution radiosonde data (HVRRD) record, which includes daily radiosonde releases at 00 and 12 GMT from 68 stations spread across the contiguous United States (Figure 3.9) during the years 1999–2008 (World Climate Research Programme 2014). We use only the 00 GMT radiosonde releases (local mid to late afternoon), disregarding the 12 GMT radiosondes which are released during local nighttime. Common-sense filtering was

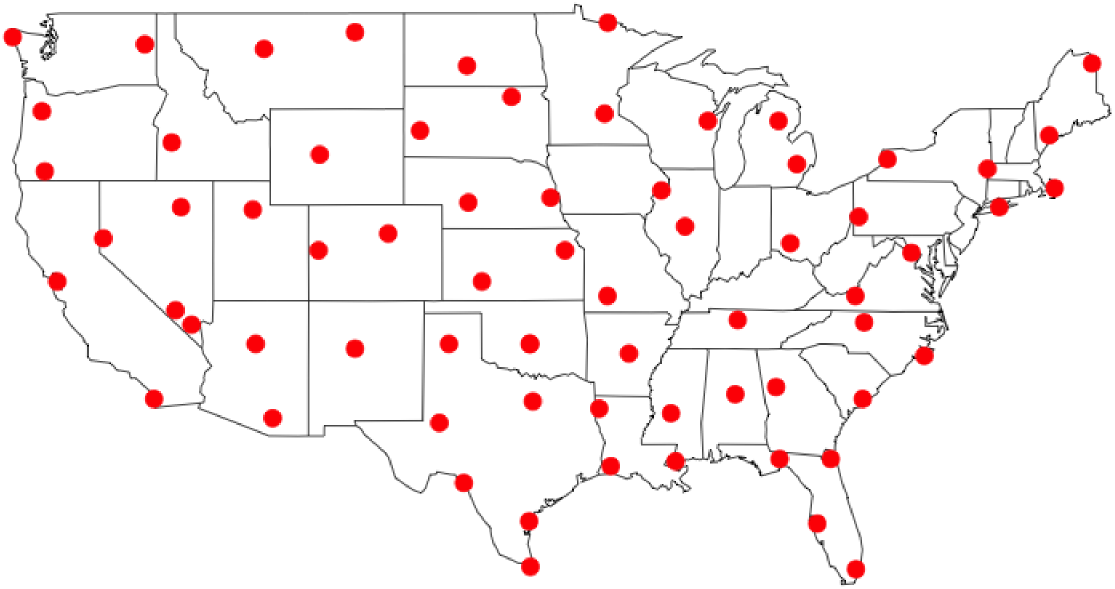

Figure 3.9: The locations of the 68 SPARC radiosonde stations in the contiguous United States.

applied to every sounding to exclude faulty data; a sounding was marked as "missing" due to any of the following indications of instrument malfunction or processing error:

- Malformed or corrupted data file
- Any pressure or elevation value missing
- Any air temperature value missing or outside the range of 100 to 400 K
- Pressure values increasing with time below 100 mbar
- Elevation values decreasing with time below 100 mbar
- Lapse rate greater than 50 $\text{K}\cdot\text{km}^{-1}$ for a 6-second interval at an elevation below 5 km
- Change in relative humidity between the first and second reports greater than 20%
- Wind speed greater than 100 $\text{m}\cdot\text{s}^{-1}$

After filtering, each legitimate sounding was interpolated to a uniform 100-meter vertical resolution.

Climate model data

In this chapter, we use output from global climate models archived in the Coupled Model Intercomparison Project, Phase 5 [CMIP5, Taylor et al. (2012)]. CMIP5 collects data from modeling groups from around the world who run a common set of experiments with the same initial conditions and forcings. At the time of writing, sub-daily 3D fields of the variables required for calculating CAPE and shear at 00 GMT are available for eleven global climate models in the CMIP5 archive. We summarize the institutional affiliations and spatial resolution of the GCMs used in this chapter in Table 3.1.

To evaluate the ability of the GCMs in our ensemble to simulate severe-thunderstorm activity in the current climate, we use data from the "historical" experiments. We take our control period to be the decade 1996–2005. This choice of decade of GCM data is dictated by the desire to match the decade covered by the radiosonde data (1999–2008) as closely as possible; since the historical experiments cover the period 1850–2005 before serving as the launch point for the future climate experiments (which run from 2006 through the end of the 21st century), the decade 1996–2005 is the closest match that does not begin to include the divergent forcing scenarios that are used for the future climate experiments. For future projections, we use the decade 2079–2088 from the RCP4.5 and RCP8.5 scenarios, which correspond to increases in global radiative forcing of $\simeq$4.5 and $\simeq$8.5 $\text{W}\cdot\text{m}^{-2}$ over preindustrial levels by the late 21st century, respectively (van Vuuren et al. 2011). This choice of decade is dictated by data availability, as some of the models in our ensemble have not submitted data to CMIP5 that extends to the year 2100.

Chapter 4

Why does tropical convective available potential energy (CAPE) increase with warming?

A recent theory argues that Clausius-Clapeyron (CC) scaling of the atmosphere's saturation deficit drives increases in tropical convective available potential energy (CAPE) with warming. Here, we test this so-called "zero-buoyancy" theory for CAPE by modulating the saturation deficit of cloud-resolving simulations of radiative-convective equilibrium in two ways: changing the sea surface temperature (SST), and changing the environmental relative humidity (RH). We find that, for earthlike and warmer SSTs, undiluted parcel buoyancy in the lower troposphere is insensitive to increasing SST because of a countervailing CC-scaling that balances the increase in the saturation deficit; however, buoyancy increases dramatically with SST in the upper troposphere. Conversely, when the RH is varied, undiluted buoyancy throughout the troposphere increases monotonically with decreasing RH. We show that the zero-buoyancy theory successfully predicts these contrasting behaviors, building confidence that it describes the fundamental physics of CAPE and its response to warming.

4.1 Introduction

Convective available potential energy (CAPE), loosely defined as the vertically-integrated buoyancy of adiabatically-lifted subcloud air, is one of the most elementary concepts in atmospheric science. Weather centers around the world calculate CAPE hundreds of times per hour to forecast atmospheric instability and issue severe storm warnings, drawing on evidence that CAPE is a predictor of thunderstorm severity (Brooks et al. 1994), lightning flash rates (Williams et al. 1992), precipitation extremes (Lepore et al. 2014), and more.

---

[1] This chapter is a slightly edited version of Seeley and Romps (2015).

CAPE is fundamental to our understanding of the atmosphere on longer timescales, too: a large majority of deep-convective parameterizations in contemporary global climate models (GCMs) rely on CAPE to compute cloud-base mass flux, which controls the convective heating and cloud cover in simulations of the coming century's climate (e.g., Table 2 of Lin et al. 2015). The skill of CAPE in predicting today's storms has also led to a number of studies that translate increases in CAPE in GCMs into projected convective hazards in a warmer climate (e.g., Diffenbaugh et al. 2013; Romps et al. 2014; Seeley and Romps 2014). Clearly, our simulations of future climate, and many of the warnings about future severe weather drawn from such simulations, depend on the physics of CAPE. What is that physics?

Unfortunately, the current generation of GCMs are run at resolutions too coarse to resolve moist convection, so they are not ideal tools for gaining a process-level understanding of what sets CAPE and why it should increase with global warming. GCMs do, however, show significantly more agreement on future increases in tropical oceanic CAPE than in midlatitude CAPE, which suggests that tropical dynamics are an attractive conceptual starting point (e.g., Sobel and Camargo 2011b; Fasullo 2011; Seeley and Romps 2015). Fortunately, there is a compelling line of evidence about CAPE from idealized simulations of tropical radiative-convective equilibrium (RCE) using higher-resolution cloud-resolving models (CRMs) that explicitly represent convective dynamics (Muller et al. 2011; Romps 2011; Singh and O'Gorman 2013, 2014). The CAPE increase seen in these CRM studies is roughly 8–12% per degree Celsius increase of sea surface temperature (SST), which agrees quantitatively with the results from GCMs. Most importantly, a theory for what processes set CAPE in RCE, and for how CAPE should change due to external forcings, was recently put forth by Singh and O'Gorman (2013) (hereafer, SO13).

The jumping-off point for the theory of SO13 is the observation that the actual buoyancies of tropical oceanic convective clouds are quite small—typically, less than 0.5 K when reported as condensate-loaded virtual temperature anomalies. This is true both in observations (e.g., Lawson and Cooper 1990; Wei et al. 1998) and numerical simulations of RCE (e.g., Sherwood et al. 2013; Romps and Charn 2015; Romps and Öktem 2015), and observed updraft velocities are correspondingly slow compared to what one would predict based on CAPE alone (Zipser and LeMone 1980). The smallness of cloud buoyancies indicates that the mean lapse rate of the tropical atmosphere is closely approximated by the lapse rate inside diluted convective clouds, a fact that motivated SO13 to consider the limit in which the buoyancy of an entraining bulk plume is exactly zero. This results in a simple picture for CAPE: an undiluted parcel has finite CAPE because the clouds that set the temperature profile of the RCE state do not develop adiabatically, but instead strongly mix with air that is subsaturated. Gravity waves quickly flatten free-tropospheric temperatures in the tropics (Bretherton and Smolarkiewicz 1989), giving the atmosphere an *entraining* lapse rate that is steeper than a moist adiabat. Since CAPE in this "zero-buoyancy" model results from the saturation deficit of air that entrains into clouds, SO13 argue that CAPE increases with warming because the saturation deficit is proportional to the saturation specific humidity, q_v^*, which scales with temperature according to the Clausius-Clapeyron (CC) relationship.

This prediction of the zero-buoyancy theory was verified by the quasi-exponential increase in CAPE with SST seen in SO13's cloud-resolving simulations of RCE.

The goal of this chapter is to rigorously determine whether undiluted parcel buoyancy and CAPE scale with the saturation deficit of the troposphere. To do so, we implement two distinct methods of modifying the saturation deficit in a CRM: by varying the SST, as in SO13, and by varying the steady-state environmental relative humidity (RH). In section 4.2, we use the zero-buoyancy model of SO13 to predict the atmosphere's contrasting responses to these two forcings. In section 4.3, we find that when the SST is increased in the CRM, undiluted buoyancy in the lower and middle troposphere does not increase because the CC-scaling of the saturation deficit is balanced by a countervailing CC-scaling of the factor that converts saturated moist static energy differences into temperature differences; we will refer to this conversion factor as β. In this warming experiment, undiluted buoyancy can only increase with SST in the upper troposphere where β asymptotes to c_p, the heat capacity of dry air. However, in section 4.4, we find that increasing the saturation deficit by reducing the RH causes undiluted buoyancy to increase throughout the troposphere because β does not change significantly as a function of RH. As shown in section 4.2, these two kinds of behavior are mathematically predicted by the equation for undiluted buoyancy given by SO13.

4.2 CAPE in the limit of zero bulk-plume cloud buoyancy

The purpose of this section is to use a simple conceptual model to predict how the buoyancy of an adiabatic parcel should depend on the SST and environmental RH of an RCE state. This simple model necessarily neglects known features of cloud dynamics such as in-cloud heterogeneity (Jonas 1990), stochastic mixing events (Romps 2010), and buoyancy sorting (Taylor and Baker 1991); nevertheless, it will become clear that it retains significant predictive power.

We begin by giving an abbreviated derivation of the zero-buoyancy model of SO13. The basic idea of the zero-buoyancy model is to use the bulk-plume moist static energy (MSE) budget to reason about $\Delta T_u = T_u - T$, where T_u is the temperature of an undiluted parcel lifted from the surface and T is the environment temperature. In the limit of zero plume buoyancy, T is given by the temperature of an entraining bulk plume. Since clouds are saturated at the environmental temperature in this limit, the MSE budget of the zero-buoyancy bulk plume is equivalent to a budget for the saturated MSE of the environment, h^*, and takes the particularly simple form

$$\partial_z h^* = -\epsilon \left(h^* - h\right) = -\epsilon L \left(1 - \mathrm{RH}\right) q_v^*. \tag{4.1}$$

In equation 4.1, ϵ is the bulk-plume fractional entrainment rate (units of m^{-1}), L is the latent heat of evaporation, h is the MSE of the environment, and the environmental subsaturation is determined by $\mathrm{RH} \simeq q_v/q_v^*$, where q_v is the environmental specific humidity and q_v^* is the saturation specific humidity at the environmental temperature and pressure. For this simple model, the MSE is defined as $h = c_pT + gz + Lq_v$, with c_p being the heat capacity of dry air and g the gravitational acceleration; this definition of MSE contains the physics we need to build intuition for CAPE even though it ignores the ice phase and the effects of water on the heat capacity of moist air.

Equation 4.1 tells us that the entrainment of air with a saturation deficit of $(1-\mathrm{RH})q_v^*$ is what pushes the environment's saturated MSE away from its value at the surface. Since an undiluted parcel (approximately) conserves its MSE, equation 4.1 can be integrated vertically to find the saturated MSE surplus, Δh_u^*, of the undiluted parcel at a given height z above the cloud base (which we take to be at z_0):

$$\Delta h_u^* = h_u^* - h^* = \int_{z_0}^{z} \epsilon L \left(1 - \mathrm{RH}\right) q_v^* \, \mathrm{d}z'. \tag{4.2}$$

To connect this to undiluted buoyancy, we just need to convert Δh_u^* into ΔT_u by defining the function β, which satisfies $h^*(T + \Delta T) - h^*(T) = \beta \Delta T$. Linearizing q_v^* about T gives $\beta = c_p + L\frac{\partial q_v^*}{\partial T}$. This yields equation 4 from SO13:

$$\Delta T_u = \frac{1}{\beta} \int_{z_0}^{z} \epsilon L (1 - \mathrm{RH}) q_v^* \, \mathrm{d}z'. \tag{4.3}$$

Let us now consider how the zero-buoyancy model predicts ΔT_u should change as the SST is increased or as the RH is reduced. In Figure 4.1, we show results from a simple version of the zero-buoyancy plume model based on thermodynamics that are consistent with the equations given so far in section 4.2; for more details on the simple zero-buoyancy model, see section S1. Figure 4.1a shows the undiluted parcel buoyancy profiles predicted by the simple zero-buoyancy bulk plume model for a control case with SST=300 K and RH=80%, for an RH perturbation where free-tropospheric RH is reduced from 80% to 60%, and for an SST perturbation of +10 K. Both perturbations to the zero-buoyancy model increase the integrated saturation deficit by a similar amount in the lower troposphere, but they have starkly different effects on the buoyancy profile. Increasing the SST has essentially no effect on the profile of buoyancy below 11 km, while reducing the RH results in an approximate doubling of the buoyancy profile throughout the depth of the convecting layer. Why does the zero-buoyancy model act this way?

Figure 4.1c shows that it is the divergent effects of these two types of forcing on β that cause their effects on undiluted buoyancy to differ so strongly. As an example, consider that both the SST perturbation and the RH perturbation increase the vertically-integrated saturation deficit at 5 km by roughly 80%, but the SST perturbation also increases β at this level by ~80%, while the effect of the RH perturbation on β is an order of magnitude smaller.

Physically, the increase of β with temperature reflects the fact that a given Δh^* corresponds to a smaller ΔT in a warmer atmosphere because Δh^* is increasingly dominated by latent enthalpy (i.e., $L\Delta q_v$) rather than sensible heat (i.e., $c_p \Delta T$) as temperature increases. Generally, in layers of the atmosphere where β is dominated by the moist term given by $L\frac{\partial q_v^*}{\partial T}$, equation 4.3 suggests that ΔT_u should be insensitive to increasing temperature because both the integrated saturation deficit and β exhibit CC-scaling. This should be the case for typical

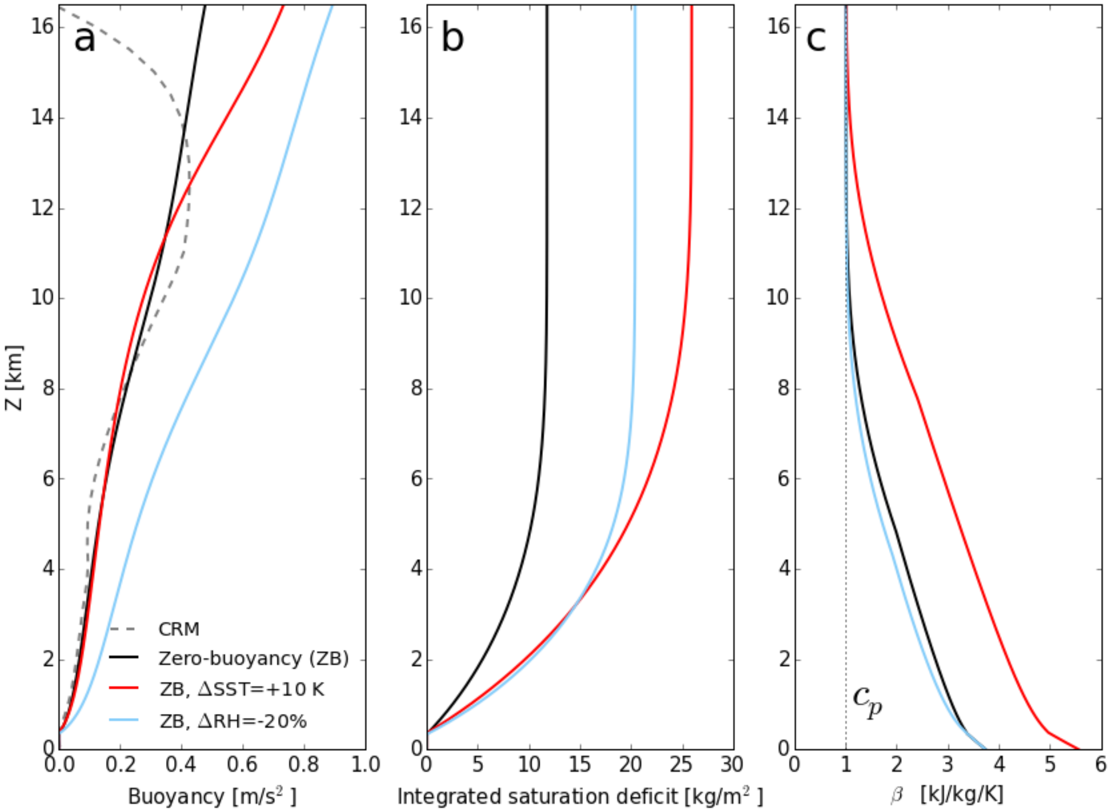

Figure 4.1: Profiles of (a) undiluted near-surface parcel buoyancy, (b) vertically-integrated saturation deficit $\int \rho(q_v^* - q_v)$ dz, and (c) $\beta = c_p + L\frac{\partial q_v^*}{\partial T}$, as predicted by the simple version of the zero-buoyancy bulk-plume model. Black lines correspond to a control case with an SST of 300 K and a free-tropospheric RH of 80%, while the red and blue lines are for a +10 K SST perturbation and a -20% RH perturbation, respectively. The zero-buoyancy model is run with a profile of bulk entrainment of the form $\epsilon(z) = 0.5/z$. Also plotted as a gray dashed line in (a) is the profile of undiluted buoyancy of an adiabatic parcel in a cloud-resolving simulation of RCE with an SST of 300 K.

lower-troposphere tropical conditions in the current climate (e.g., at a temperature of 300 K and a pressure of 1000 mb, roughly 75% of β comes from the moist term).

However, assuming that convection always extends at least to an altitude with a typical anvil temperature of ~220 K (Hartmann and Larson 2002), there is a layer of the upper atmosphere where q_v^* is small enough that β asymptotes to c_p. Even though q_v^* is small in the upper troposphere, the vertically-integrated saturation deficit is not small because it includes the saturation deficit in lower, warmer layers of the atmosphere; therefore, where $\beta \simeq c_p$, the increase of the saturation deficit that accompanies a warming atmosphere can efficiently cause increases in undiluted buoyancy. This is reflected in Figure 4.1, where the SST perturbation does increase undiluted buoyancy at altitudes above 11 km.

In this section, we have shown that the zero-buoyancy model of SO13 predicts undiluted parcel buoyancy in the lower and middle troposphere to be relatively insensitive to an SST warming perturbation, but to increase with SST in the upper troposphere. In contrast, we have also shown that the zero-buoyancy model predicts undiluted buoyancy throughout the troposphere to be quite sensitive to an RH-reduction perturbation (Figure 4.1). These differences suggest that while modulating the saturation deficit does change CAPE in the zero-buoyancy framework, exactly how the saturation deficit determines how the vertical profile of undiluted buoyancy responds. In the remaining sections of this chapter, we present the results from a CRM that is subjected to an SST-warming experiment and an RH-varying experiment to test the conclusions drawn from the simple framework presented thus far.

4.3 SST-warming experiment

All cloud-resolving simulations in this chapter were performed with Das Atmosphärische Modell (DAM; Romps 2008). For this experiment, simulations were run on a square, doubly periodic domain with a model top at 61 km and a vertical grid spacing that varies smoothly from 50 m in the boundary layer to 500 m at a height of 5 km and to 1 km at 50 km. The lower boundary was specified to be an ocean surface with a fixed SST of 290, 300, 310, or 320 K. Surface fluxes were calculated using a bulk formula, and shortwave and longwave radiation were calculated interactively; there is no ozone in these simulations, and the same vertically-constant 280-ppmv CO_2 profile was used for all simulations. Each of the four SST cases was first run to RCE over the course of approximately 400 days on a small domain (32 km width) with 2 km horizontal resolution, after which the simulations were restarted on a larger 72 km domain with 500 m horizontal resolution. The higher-resolution, larger-domain simulations were run for an additional 60 days, with statistics collected over the last 30 days of equilibrated convection. Horizontal- and time-mean vertical profiles of quantities of interest were recorded, as well as mean profiles within "cloud updrafts"; cloud updrafts were identified as grid cells with nonprecipitating condensed water mass fraction greater than 10^{-5} and vertical velocity greater than 1 m/s.

Figure 4.2a shows the buoyancy profiles of adiabatically-lifted air parcels (assuming no condensate fallout) in the four simulations of RCE over SSTs of 290, 300, 310, and 320

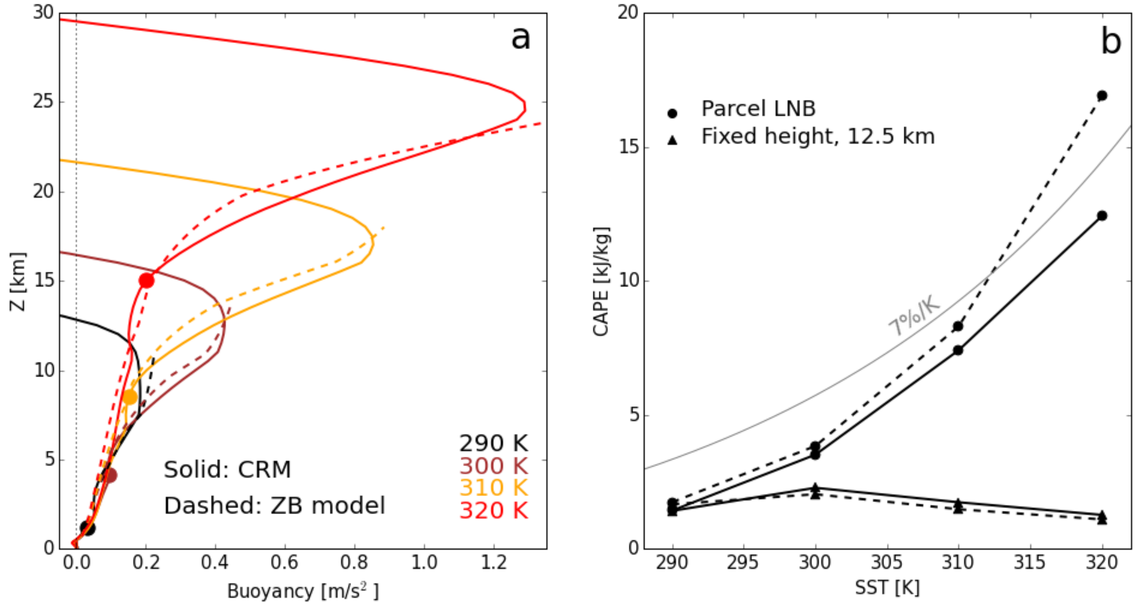

Figure 4.2: (a) Profiles of buoyancy for adiabatically-lifted near-surface air parcels for SSTs of 290 K (black), 300 K (brown), 310 K (orange), and 320 K (red). Solid lines correspond to CRM simulations of RCE, while the predictions of the complex zero-buoyancy model are plotted in dashed lines up to a temperature of 200 K. Colored circles indicate the point on the buoyancy profile above which β is dominated by c_p rather than $L\frac{\partial q_v^*}{\partial T}$. The zero-buoyancy model is run with a profile of bulk entrainment of the form $\epsilon(z) = 0.8/z$. (b) CAPE as a function of SST when integrated up to the undiluted parcel LNB (circles) or to a fixed altitude of 12.5 km (triangles). As in panel (a), solid lines are results from the CRM and dashed lines are from the zero-buoyancy model.

K. Parcels were initialized with the mean temperature, pressure, and moisture content of the near-surface CRM level, and their buoyancies were calculated by lifting through the horizontal- and time-mean environmental density profile assuming conservation of MSE - CAPE (Romps 2015) with a full treatment of the thermodynamics of water, including the ice phase.

The undiluted buoyancy profiles in Figure 4.2a from the four CRM simulations collapse onto a common curve below ~8 km, but as the SST is raised, the profiles develop an increasingly prominent peak in the upper troposphere. On these profiles, circles indicate the point where β transitions from being mostly moist ($L\frac{\partial q_v^*}{\partial T} > c_p$) to mostly dry ($L\frac{\partial q_v^*}{\partial T} < c_p$). This point serves as an approximate division between the two regimes discussed in section 4.2: where β is dominated by the moist term, the zero-buoyancy model predicts that undiluted buoyancy should be fairly insensitive to increasing SST because ΔT_u is given by the ratio of two quantities that both exhibit Clausius-Clapeyron scaling; conversely, where β is dominated by the dry term, we expect the increase in the integrated saturation deficit with atmospheric warming to be fully expressed as larger undiluted parcel buoyancy. Figure 4.2a shows that this moist-to-dry transition of β, which occurs at a higher altitude in warmer atmospheres, identifies the point in each profile where undiluted parcel buoyancy rapidly increases.

These high buoyancies in the upper troposphere define a reservoir of CAPE between the β transition point and the undiluted parcel LNB that accounts for between 85% and 99% of the total CAPE in our CRM simulations. Since the undiluted buoyancies in this layer of the atmosphere are (by definition) in a regime where increases in the saturation deficit are efficiently expressed as larger undiluted parcel temperature excesses, and since these buoyancies dominate CAPE, the SST-scaling of CAPE should bear the imprint of the Clausius-Clapeyron scaling of the saturation deficit. Figure 4.2b plots CAPE as a function of SST when integrated up the the undiluted parcel's LNB. This CAPE increases quasi-exponentially with a best-fit rate of ~7%/K over the simulated 30-K range. We also show CAPE integrated up to a fixed height of 12.5 km, which is the highest level at which all simulations have positively buoyant undiluted parcels; for this fixed upper bound, the CAPE change with SST is flat and non-monotonic because the layers of the atmosphere where undiluted buoyancy can respond to the increase in the saturation deficit are excluded. Assuming a pseudoadiabatic lifting process with complete condensate fallout slightly softens the contrast between buoyancy behavior in the lower and upper troposphere, but does not modify these conclusions. (For a pseudoadiabatic parcel, the increase of the virtual effect in the lower troposphere with SST is not balanced by an increase in condensate loading, and total buoyancy in the lower troposphere increases slightly even though the absolute temperature anomaly of the parcels remains insensitive to SST; see Fig. 2a of SO13 for pseudoadiabatic virtual temperature anomalies over a colder range of SSTs.)

Figure 4.2a also shows the undiluted parcel buoyancy profiles predicted by the zero-buoyancy model for the four SSTs we simulated with the CRM. For completeness, here we use a complex version of the zero-buoyancy plume model that is formulated with thermodynamics that includes the full effects of water on the density and heat capacity of moist air; for more details on the complex zero-buoyancy model, see the Appendix. The match between the zero-buoyancy model and the CRM results is striking. The zero-buoyancy model captures both the insensitivity of undiluted buoyancy to SST below ~8 km as well as (in the warmer simulations with larger saturation deficits) the rapid increase in buoyancy with altitude in the regime where β is predominantly dry. Figure 4.2b shows that CAPE predicted by the zero-buoyancy model also increases rapidly as a function of SST when integrated up to the CRM-diagnosed undiluted parcel LNB (in fact, it overestimates the CAPE increase in this case, because it misses the decrease of parcel buoyancy towards zero as the LNB is approached). On the other hand, when integrated up to a fixed height of 12.5 km, the zero-buoyancy CAPE as a function of SST is flat.

4.4 RH-varying experiment

For this experiment, we change the mean relative humidity of air that mixes with developing clouds in the RCE state of our CRM by manipulating the water budget outside of clouds. In convecting regions of the real tropical troposphere, relative humidities hover around 80%, with a characteristic “C” shape that has a minimum around 7 km. In fact, by generalizing the zero-buoyancy model of SO13 to incorporate detrainment of saturated air from clouds, Romps (2014) showed that this shape of tropical relative humidity results from how the strengths of two competing effects of convection—moistening by detrainment and drying by forced subsidence—typically vary with altitude. In a CRM, however, we can force the atmosphere away from its natural profile of relative humidity, isolating and manipulating the effect of environmental humidity on the lapse rate and undiluted buoyancy.

There is a deep literature regarding the sensitivity of convection to the humidity of the environment in which it develops, but our experiment is novel mainly because it considers steady-state convection. It is a commonplace observation that dry air at midlevels reduces cloud buoyancies by entrainment, effectively suppressing deep convection and reducing precipitation (e.g., Mapes and Zuidema 1996; Brown and Zhang 1997; Derbyshire et al. 2004; Takemi et al. 2004; Parsons et al. 2006). The importance of deep convective “preconditioning”—that is, the gradual erosion of a dry inhibition layer by progressively deeper cumulus development—has also been demonstrated in numerical simulations of tropical convection (Kuang and Bretherton 2006), the diurnal cycle over land (Chaboureau et al. 2004), and many other scenarios (e.g., Ridout 2002; Khairoutdinov and Randall 2006; Waite and Khouider 2010). However, these prior simulations are transient in the sense that initial profiles of environmental humidity are allowed to evolve under the influence of convection. We are interested in the steady-state behavior—what if we don’t allow shallow convection to pave the way for the clouds that make it all the way to the tropopause?

Our cloud-resolving simulations for this experiment were conducted on a 30^3 km^3 domain with doubly periodic horizontal boundaries. All simulations used the same vertical grid with 50 m spacing below 600 meters altitude, increasing continuously to a constant 100 m spacing between 1 and 15 kilometers altitude and then increasing again to 1 km spacing in the stratosphere. (This relatively high vertical resolution throughout the troposphere is required to maintain numerical stability at high relative humidities.)

The atmosphere in this experiment was destabilized by a fixed (non-interactive) radiative cooling profile of 1.5 K/day from the surface up to an altitude of 10 km, decreasing to 0 K/day linearly in altitude between 10 and 15 km. The use of non-interactive radiative cooling essentially fixes the depth of the convective layer. We first ran a control simulation to RCE over an SST of 300 K with 2 km horizontal resolution. We saved the mean vertical temperature profile from the equilibrated phase of this control run, and our forced-RH simulations were then branched from a 3D snapshot of the model state at the end of the control and run to RCE. The model state at the end of these 2 km-resolution runs for each target RH value was then interpolated to a grid with 500 m horizontal grid spacing and continued. After the simulations adjusted to the new resolution, statistics were collected over 10 days of equilibrated convection. As in the SST-warming experiment presented in section 4.3, we recorded domain-mean vertical profiles of quantities of interest as well as mean profiles within “cloud updrafts” identified by thresholds for condensed water content and vertical velocity.

A schematic of the forcings employed in our forced-RH experiments is shown in Figure 4.3a. The setup should be thought of in terms of three layers: a subcloud-layer thermodynamic “sponge” whose purpose is to maintain constant moist entropy, a free troposphere that is destabilized by radiation and nudged toward a particular value of relative humidity in the clear sky regions, and a stratospheric sponge that absorbs overshooting convection. In the stratosphere ($z > 15$ km), the only thermodynamical forcing is a nudging of layer-mean temperatures to their values from the control simulation on a timescale of 6 hours. In the subcloud layer ($z < 400$ m), temperatures were nudged locally (i.e., gridpoint by gridpoint) to the mean value at that elevation from the control simulation on a timescale of 1 minute. We use local temperature nudging, rather than nudging of the mean, because nudging layer-mean temperatures is problematic when there is an excessively large variance in low-level thermodynamical properties, as there is in simulations with very strong cold pools (the drier simulations).

Figure 4.3b shows the relative humidity forcings, which were specified by a series of smoothly-varying target RH profiles, $\mathrm{RH}^\dagger(z)$, corresponding to free-tropospheric target values in the set $\{0\%, 50\%, 75\%, 85\%, 95\%\}$. Each profile has the same shape below 400 m, with values of roughly 85% as are observed below cloud base in standard RCE, before transitioning to the varying free-tropospheric values between 500 m and 1 km. We implement the RH-forcing by nudging unsaturated grid points toward the target RH value via a mole-for-mole swap of dry air and water vapor that is enforced by source terms in the governing equations for water vapor and dry air. The forcing operates on an altitude-dependent timescale that is chosen to be short in the subcloud-layer, long in the neighborhood of cloud base (so that clouds have a chance to become saturated), and short again in the free troposphere; for more details of the relative humidity forcing framework, see the Appendix. Figure 4.3b shows the resulting steady-state environmental relative humidity profiles in our simulations.

The buoyancy profiles of adiabatically-lifted air parcels for the five simulations of RCE

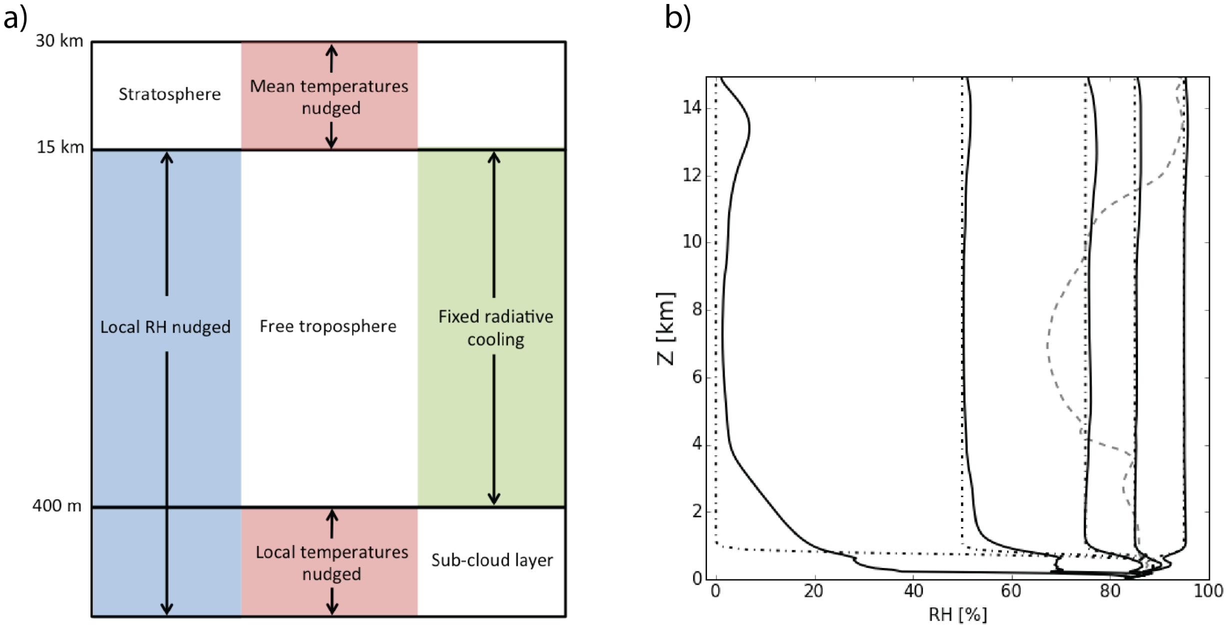

Figure 4.3: (a) A schematic of the forcings employed in the RH-varying experiment of section 4.4. In the stratosphere ($z > 15$ km), layer-mean temperatures are nudged to their values from a control simulation. In the free troposphere (400 m $\leq z \leq$ 15 km), a fixed radiative cooling profile is applied and the relative humidity outside of clouds is nudged towards a target value. In the sub-cloud layer ($z <$ 400 m), relative humidity is also nudged, and temperature is nudged gridpoint-by-gridpoint towards the mean value at that altitude from a control simulation. (b) Steady-state RH profiles from our simulations (solid lines), corresponding to forcing profiles with free-tropospheric values of 0%, 50%, 75%, 85%, and 95%. The forcing profiles are indicated by the dot-dashed lines. For reference, the relative humidity profile of an unforced RCE simulation is also shown by a gray dashed line.

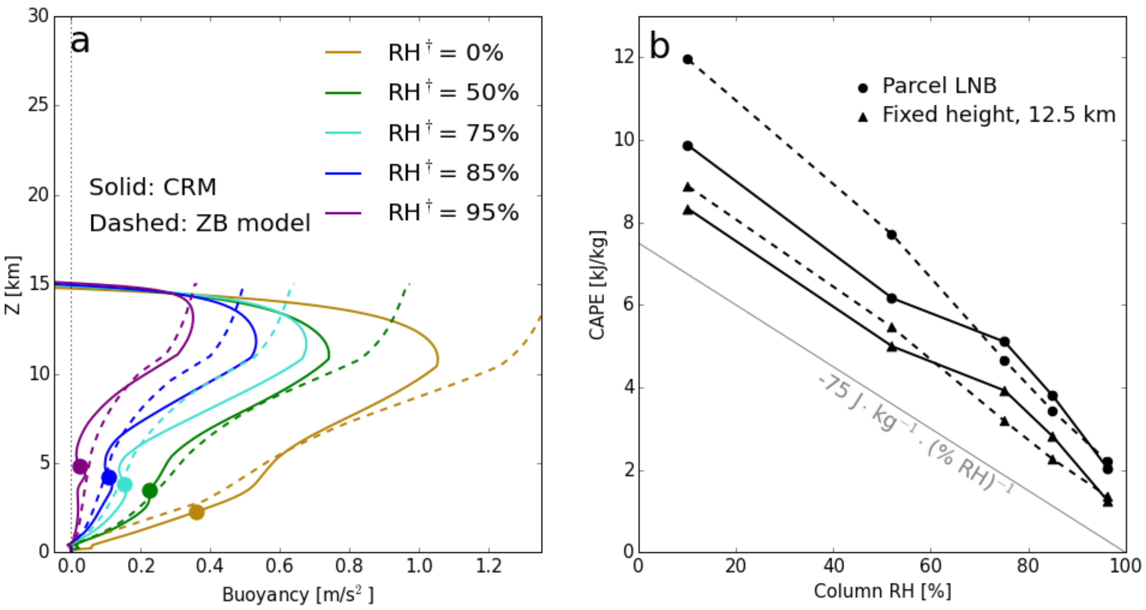

Figure 4.4: As in Figure 4.2, but for the RH-varying experiment. In both (a) and (b), solid lines are results from the CRM and dashed lines are from the zero-buoyancy model. The zero-buoyancy model is supplied with the same entrainment rate profile as in Figure 4.2 and with the corresponding relative humidity profile from Figure 4.3b. In (a), colors correspond to the range of target free-tropospheric relative humidities and colored circles mark where β transitions from being mostly moist to mostly dry. In (b), CAPE is integrated up to either the undiluted parcel LNB (circles) or to a fixed altitude of 12.5 km (triangles).

corresponding to target free-tropospheric RH values of 0%, 50%, 75%, 85%, and 95% are shown in Figure 4.4a. The buoyancy profiles in this experiment tell a very different story than those from the SST-warming experiment shown in Figure 4.2a. The undiluted parcel LNB remains fixed at ~15 km, while the buoyancy at all heights between cloud base and the LNB increases monotonically with decreasing environmental RH. This confirms, over a much wider range of RH values, the prediction of the simple zero-buoyancy model in section 4.2 that undiluted parcel buoyancy throughout the troposphere is very sensitive to the RH of air that entrains into clouds. Unlike in the SST-warming experiment, where the increase of β with SST caused the altitude of the β moist-to-dry transition point to increase from roughly 1 km to 15 km, β decreases weakly with decreasing RH, and the β transition point only shifts from 5 km down to 2.5 km. This relative insensitivity of β allows increases in the saturation deficit to be straightforwardly expressed as increases in undiluted buoyancy throughout the troposphere in the RH-varying experiment.

Also plotted in Figure 4.4a are the undiluted buoyancy profiles predicted by the complex-thermodynamics version of the zero-buoyancy model. The zero-buoyancy model is run with the same fixed entrainment rate profile as in the SST-warming experiment, but supplied with the varying RH profiles from the CRM (i.e., the steady-state profiles shown in Figure 4.3b). The zero-buoyancy model's match with the CRM results is excellent, capturing both the shape and magnitude of the increase in undiluted buoyancy with decreasing RH seen in the CRM results. When integrated up to the undiluted parcel LNB or to a fixed height of 12.5 km, CAPE in the CRM and zero-buoyancy model both decrease strongly with increasing column RH (Figure 4.4b), with a sensitivity of approximately -75 J/kg/(% RH).

4.5 Conclusions

The fact that the zero-buoyancy model of SO13 can explain the CAPE variations in a convecting atmosphere subjected to two drastically different types of forcing—increases in SST and decreases in environmental RH—implies that it captures the fundamental physics of CAPE. Building on the work of SO13, we have shown that CAPE exhibits Clausius-Clapeyron scaling because undiluted buoyancies in the upper troposphere dominate CAPE and scale with the vertically-integrated saturation deficit. This adds specificity to the widely-repeated claim that warming temperatures increase the "amount of fuel" available for deep convection—this chapter shows that while increases in q_v^* do increase the difference in saturated MSE (Δh_u^*) between an undiluted parcel and its environment, the larger Δh_u^* is only expressed as larger buoyancy in layers of the troposphere where the scarcity of water vapor forces Δh_u^* to be dominated by sensible heat rather than latent enthalpy.

As a final note, we point out that there is no *a priori* connection between changes in the buoyancy of fictional adiabatic parcels and changes in actual updraft speeds, because the clouds in CRM simulations and in the real tropical atmosphere are highly diluted (Romps and Kuang 2010a; Fierro et al. 2009). However, Figure 4.5 shows that the mean vertical velocity of the cloud updrafts in our two experiments changes in the same sense as the undiluted buoyancies: for the SST-warming experiment, the velocities collapse onto a common curve that increases with altitude and grows taller with SST, while for the RH-varying experiment, the updraft speeds increase dramatically at all altitudes in the convective layer as RH is lowered. The connection between warming SSTs, entrainment, and the vertical velocity of the most intense (i.e., most weakly entraining) updrafts was explored through the generalized two-plume zero-buoyancy model of Singh and O'Gorman (2014), but it remains unclear why the mean vertical velocity of highly diluted clouds should change in the same manner as undiluted buoyancy. Whether this is a coincidence or physically constrained is a fascinating and difficult question that we leave to future work.

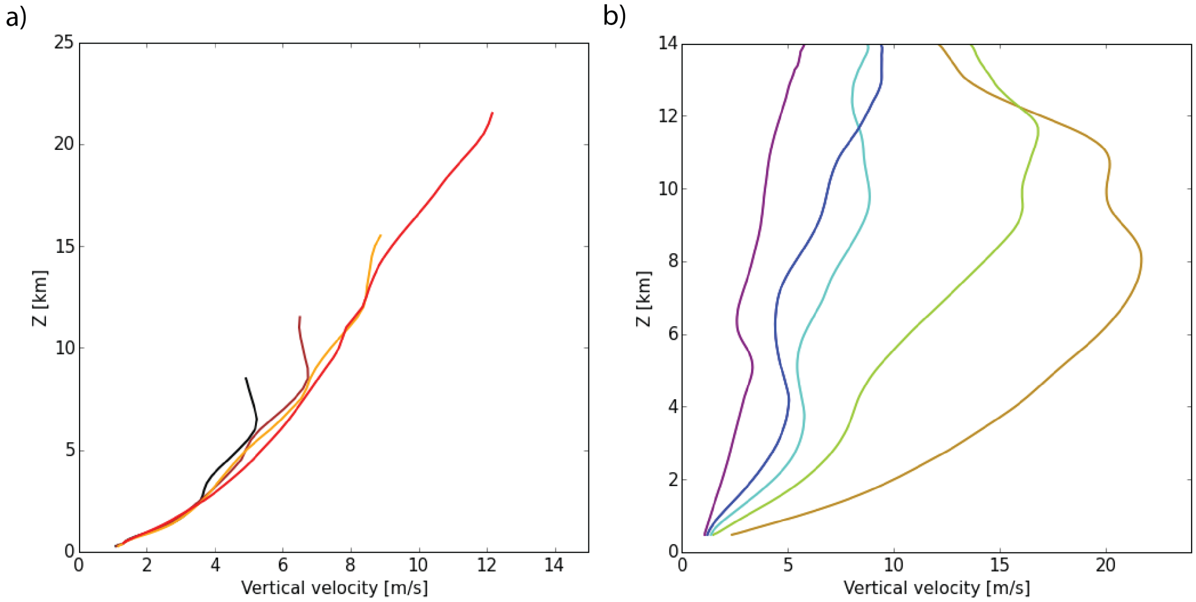

Figure 4.5: Profiles of mean vertical velocity in cloud updrafts in the CRM simulations from (a) the SST-warming experiment, and (b) the RH-varying experiment. Colors correspond to the set of SSTs and target free-tropospheric RH values as in Figures 4.2a and 4.4a. Note that (a) and (b) have different horizontal and vertical scales.

Appendix: Methods

Simple zero-buoyancy model

The simple zero-buoyancy model is based on a simplified thermodynamics in which there is no ice phase. In addition, the effect of water on the density and heat capacity of air is neglected. Accordingly, MSE is defined here as $h = c_p T + L q_v + g z$. The plume equations describing the vertical profiles of MSE, total water ($q_t = q_v + q_c$, where q_c is the non-precipitating condensed water), and pressure are:

$$\partial_z h^* = -\epsilon \left(h^* - h \right) \ , \tag{4.4}$$

$$\partial_z q_t = -\epsilon \left(q_t - q_v \right) \ , \tag{4.5}$$

$$\partial_z \log p = -g/(R_a T) \ . \tag{4.6}$$

The MSE of the environment is given by h, q_v is the specific humidity of the environment, and R_a is the dry-air gas constant. The plume equations are integrated vertically by first specifying the temperature, total water, and pressure at plume base. If the plume is initially unsaturated, as it typically is when initialized with values taken from the near-surface level of a CRM simulation, equations 4.4–4.6 are advanced with the entrainment rate ϵ set to 0 to generate a dry adiabat until saturation occurs. At and above the level of plume saturation, the specific humidity and the MSE of the environment are calculated using the supplied RH profile and the known temperature of the plume/environment. The supplied entrainment profile is then used to calculate the plume's q_t and h^* at the next vertical step with a simple forward-difference method. A root-solver is used to calculate the temperature that is consistent with the known value of h^* at the next vertical step. Any water in excess of q_v^* is dumped into the q_c category. As it is written, equation 4.5 assumes no fallout of condensed water, but our plume model includes a parameter, γ, that determines what fraction of liquid water precipitates out at each step. If $1 \geq \gamma > 0$, any new q_c that forms when stepping vertically is reduced by the factor $(1 - \gamma)$. This "precipitation" is removed at constant pressure and temperature. Since we neglect the effect of water on the density and pressure of air in this simple model, q_c only functions as a reserve of liquid water that can re-evaporate to maintain saturation after entrainment reduces the specific humidity of the plume. Iterating this procedure generates a plume/environment temperature profile. The buoyancy of an undiluted parcel is then computed by lifting a parcel that conserves its (simple) MSE, computing its temperature as a function of height, and comparing to the plume/environment temperature profile. Note that the zero-buoyancy plume is always colder than the undiluted parcel—the zero-buoyancy model does not predict an LNB. To get a value of CAPE from the buoyancy profile predicted by the zero-buoyancy model, one must supply an upper bound for the CAPE integration.

Complex zero-buoyancy model

Like the simple version, the complex zero-buoyancy model operates on the principle of neutrality between an entraining plume and its environment, but takes full account of the ice phase and the effects of water on the density and heat capacity of air. The total water mass fraction in this case is $q_t = q_v + q_l + q_s$, where q_l and q_s are the mass fractions of liquid and solid water, respectively. The MSE is given by

$$h = c_{pm}(T - T_0) + q_v(E_{0v} + R_v T_0) - q_s E_{0s} + gz, \tag{4.7}$$

where c_{pm} is the constant-pressure specific heat capacity of moist air, $T_0 = 273.16$ K is the triple-point temperature, E_{0v} is the difference in specific internal energy between water vapor and liquid at the triple-point temperature, R_v is the gas constant for water vapor, and E_{0s} is the difference in specific internal energy between water liquid and solid at the triple-point temperature. The moist-air heat capacity, c_{pm}, is given as a mass-fraction-weighted linear combination of the constant-pressure heat capacities of dry air (subscript a) and the three water phases (subscripts v, l, and s): $c_{pm} = q_a c_{pa} + q_v c_{pv} + q_l c_{pl} + q_s c_{ps}$.

The complex version of the zero-buoyancy model integrates the same plume equations as the simple version, but the pressure equation is replaced with

$$\partial_z \log p = \frac{-g}{R_m T_e} \ , \tag{4.8}$$

where $R_m = q_v R_v + (1 - q_v) R_d$ is the gas constant for moist environmental air. The vertical integration of the plume equations is carried out as for the simple model, but since we include the effects of water phases on the density of air in this case, the neutrality of the entraining plume is enforced as a constraint on density rather than temperature. A rootsolving algorithm uses the known plume density and the supplied environmental relative humidity to calculate the environmental temperature that is consistent with a neutrally buoyant plume. The complex version of the zero-buoyancy model also includes the full effects of the ice phase; q_v^* is defined with respect to liquid at temperatures warmer than the triple-point temperature (273.16 K), with respect to ice at temperatures below 240 K, and as a linear combination of the two at temperatures in between. This corresponds to a non-isothermal mixed phase regime between the triple-point temperature and the temperature of homogeneous freezing; the partitioning of condensates in the plume transitions linearly in temperature from all-liquid to all-ice between these two temperatures. (For a more complete description of the moist thermodynamics used in this model, including explicit equations for q_v^*, see the appendix of Romps (2015)). To calculate undiluted parcel buoyancy, a near-surface parcel is lifted assuming conservation of MSE - CAPE, and this parcel's density is then compared to the plume/environment density profile produced by the zero-buoyancy model.

Method for nudging RH

There are many ways one could "nudge" relative humidity in a numerical model, so here we will be explicit about how this forcing was implemented in our simulations. Our relative humidity nudging was performed by nudging the local q_v according to

$$F_{q_v} = \rho \frac{\mathrm{RH}^\dagger(z) q_v^* - q_v}{\tau}, \tag{4.9}$$

where $\mathrm{RH}^\dagger(z)$ is the target RH profile and the nudging timescale is τ. Note that F_{q_v} has units of density per time, and represents an artificial convergence of pure water vapor into the Eulerian finite volumes in the numerical model (we use "convergence" as shorthand for convergence or divergence). However, since we are interested in the effect of environmental relative humidity on the temperature profile of a convecting atmosphere, we need to adjust RH in such a way that the forcing itself has negligible effects on temperature. The convergence of water vapor does work on the gas in a finite volume, and therefore has an effect on temperature. To counteract this, we also specify a countervailing convergence of an equal and opposite number of moles of dry air per volume per time:

$$F_{q_a}(z) = -\frac{R_v}{R_a} F_{q_v}. \tag{4.10}$$

The end result of this combination of forcings is effectively a mole-for-mole swap of dry air and water vapor. The corresponding effect on the model's finite-volume energy budget was accounted for by keeping track of the enthalpies of the exchanged gases. We apply this relative humidity nudging in every model level below 15 km, but not in the stratosphere.

To minimize the possibility of convective preconditioning (i.e., the probability that a developing cloud will grow through the moist detritus of a prior convective event), we should use a short τ in the free troposphere. However, if we nudge RH locally on too short a timescale near cloud base, we will never give clouds a chance to be born. Therefore, we specify an altitude-dependent τ given by

$$\tau(z) = \begin{cases} 1 \text{ minute}, & z < 200 \text{ m} \\ 1 \text{ day}, & 200 \text{ m} \leq z \leq 600 \text{ m} \\ \frac{10^7}{z^{1.35}} \text{ seconds}, & 600 \text{ m} < z \end{cases}. \tag{4.11}$$

This profile of τ has the desirable properties of maintaining constant humidity in the subcloud-layer, giving clouds a chance to become saturated in the neighborhood of cloud base (~500 m), and quickly adjusting the RH of air outside of clouds to the target value in the free troposphere.

Chapter 5

Tropical cloud buoyancy is the same in a world with or without ice

When convective clouds grow above the melting line, where temperatures fall below zero degrees Celsius, condensed water begins to freeze and water vapor is deposited. These processes release the latent heat of fusion, which warms cloud air. Many previous studies have suggested that this heating from fusion increases cloud buoyancy in the upper troposphere. However, here we use numerical simulations of radiative-convective equilibrium with and without ice processes to argue that tropical cloud buoyancy is not systematically higher in a world with fusion than in a world without it. This insensitivity results from the fact that the environmental temperature profile encountered by developing tropical clouds is itself determined by convection. We also offer a simple explanation for the large reservoir of convective available potential energy (CAPE) in the tropical upper troposphere that does not invoke ice.

5.1 Introduction

One of the many sources of complexity in atmospheric convection is the fact that cloud water exists not just in gas and liquid form, but also in the solid phase. There is ample evidence that ice modifies the radiative properties of clouds (Irvine and Pollack 1968; Sun and Shine 1995), and such differences between ice and liquid clouds may be relevant to storm morphology (Liu et al. 1997), mesoscale cloud organization (Grabowski 2003), and high-latitude climate feedbacks (Cronin and Tziperman 2015; Mccoy et al. 2015). Ice is also crucial to the most widely-accepted mechanism for charge separation in thunderstorms (Takahashi 1978), so it seems likely that a world without ice would be a world without lightning (Williams 1989).

---

[1] This chapter is a slightly edited version of Seeley and Romps (2016).

The role of ice in determining the dynamical properties of clouds, such as their buoyancy and vertical velocity, is less well settled. However, it is commonly argued that ice is a source of buoyancy for convective clouds that grow above the melting line. In response to a debate about convective instability in the tropics raised by Xu and Emanuel (1989), Williams and Renno (1993) pointed out that accounting for ice significantly increases the convective available potential energy (CAPE) of an undiluted parcel. Reflecting on decades of aircraft observations, Zipser (2003) argued for a conceptual picture of tropical convection in which updrafts in the equatorial trough are heavily diluted by entrainment in the lower troposphere, but reinvigorated above the melting line by the release of latent heat of fusion and thereby powered into the upper troposphere. Similarly, Fierro et al. (2009) performed updraft trajectory analyses on a simulated oceanic squall line and also concluded that latent heat released by freezing condensates compensates for low-level entrainment. In a more idealized radiative-convective equilibrium (RCE) framework, Romps and Kuang (2010a) used a Lagrangian parcel model with and without ice physics to argue that the latent heat of fusion provides kinetic energy that is necessary for diluted parcels to reach the tropopause.

It is natural to conclude from these results that clouds would be less buoyant and have slower updrafts in a world without ice. The purpose of this chapter is to show that this is not the case. Here, we use cloud-resolving model (CRM) simulations of tropical RCE with and without ice processes to demonstrate that cloud dynamics—whether measured by the typical buoyancy of diluted cloud air, or the vertical velocities of cloud updrafts, or the CAPE of an undiluted parcel—are essentially unaffected by freezing condensates. The reason for the insensitivity to ice is not some coincidental balance between a buoyancy source from the latent heat of fusion and a buoyancy sink from a different ice process such as condensate loading. Instead, the insensitivity results from the fact that the environmental temperature profile encountered by developing clouds is itself determined by convection. This is true in Earth's tropics, where fast gravity waves enforce nearly moist-convective lapse rates even where there is little local convective heating, and it is also true in our simulations of RCE. Taking account of this coupled relationship between clouds and their environment reconciles our results with the common claim that ice invigorates convective clouds.

In section 5.2, we describe how ice is "turned off" in the CRM. We present the results of our RCE simulations with and without ice in section 5.3, and in section 5.4 we argue that preexisting theories for cloud buoyancy do not predict larger cloud buoyancies in a world with ice. Finally, section 5.5 gives an explanation for the top-heaviness of tropical undiluted parcel buoyancy profiles that does not invoke ice.

5.2 Ice in the cloud-resolving model

Our simulations of RCE were performed with Das Atmosphärische Modell (DAM; Romps 2008). Microphysics in DAM is treated with the six-class Lin-Lord-Krueger scheme (Lin et al. 1983; Lord et al. 1984; Krueger et al. 1995). Of the six classes of water in the microphysics scheme, three are ice: non-precipitating cloud ice, and precipitating snow and graupel.

The effects of these types of ice on the model atmosphere in DAM can be conceptually divided into several categories: 1. the latent heating of phase changes involving solid water (i.e., freezing/melting and deposition/sublimation); 2. the difference in the saturation vapor pressure with respect to ice and with respect to liquid; 3. the different heat capacities of liquid and solid; 4. the different treatment of solid and liquid cloud water by the interactive radiation scheme; 5. the different fall speeds of snow, graupel, and rain; and 6. the effect of ice microphysics on the conversion of non-precipitating condensates to precipitation. Since the focus of this chapter is on the connection between buoyancy and the thermodynamics of ice, we design our experiments to prevent effects 4, 5, and 6 from influencing our results. Effect 4 is eliminated by altering the radiation scheme to treat liquid and ice in the same way. Effect 5 is eliminated by using a homogeneous terminal velocity of 10 m/s for all hydrometeors in all simulations. Instead of eliminating effect 6, we ensure that it is present even in the simulations with "no ice", as described below. These choices allow us to focus on the thermodynamic effects of ice (effects 1, 2, and 3). We have also checked that our main results are unmodified by these simplified treatments of fall speeds and cloud radiative properties.

In fact, the first three effects of ice listed above are related through the expression for the saturation specific humidity, q_v^*; the value of q_v^* differs with respect to ice and liquid solely due to the nonzero latent heat of fusion and the difference between the heat capacity of liquid and solid water (see the appendix of Romps (2015) for explicit expressions for q_v^*). In particular, the latent heat of fusion in DAM is $L_f = E_{0s} + (c_{vl} - c_{vs})(T - T_{\mathrm{trip}})$, where the constant $E_{0s} = 3.337 \times 10^5$ J/kg is the specific internal energy difference between liquid and solid water at the triple-point temperature $T_{\mathrm{trip}} = 273.16$ K, and the specific heat capacity at constant volume of liquid water is $c_{vl} = 4216$ J/kg/K, which is roughly twice the corresponding quantity for solid water ($c_{vs} = 2106$ J/kg/K). L_f is approximately 13% of the latent heat of condensation, L_c, at the triple point.

In this chapter, we will refer to simulations and parcel calculations "with ice" and "without ice": when ice is turned on, E_{0s} and c_{vs} take their physically realistic values as listed above; when ice is turned off, $E_{0s} = 0$ and $c_{vs} = c_{vl}$ so that $L_f = 0$. Although DAM simulations without ice still keep track of the partitioning of condensed water between the liquid and solid categories, the homogenized heat capacities, fall speeds, radiative properties, and the neglect of the latent heat of fusion ensure that the two phases are treated completely identically, so the model's distinction between them has no physical consequence. In simulations with a meaningful ice phase, DAM allows for non-isothermal mixed-phase clouds by assuming that the fraction of liquid cloud condensates is a unique function of temperature, decreasing linearly from 1 at T_{trip} to 0 at 240 K. For consistency with the CRM, we assume the same mixed-phase process for our parcel calculations; the method for calculating parcel properties in the present chapter is identical to that described in detail in section 3c of Romps (2015).

5.3 RCE simulations with and without ice

The state of radiative-convective equilibrium is a first approximation to Earth's tropical atmosphere, and many aspects of RCE simulations compare very favorably to tropical observations. Distributions of cloud buoyancy in high-resolution CRMs have been shown to match the results of field campaigns quite well (e.g., Figure 2 of Romps and Öktem 2015), and simulated RCE states reproduce the "C"-shaped relative humidity profiles (Romps 2014) and trimodal cloud fraction profiles (Dessler et al. 2006) that characterize Earth's tropics. This makes RCE an excellent tool for testing theories about tropical convection.

We ran two simulations of tropical convection over a fixed sea surface temperature (SST) of 300 K, with interactive radiation and surface fluxes computed via a standard bulk formula; the two simulations differ only by the presence or absence of ice processes, determined by setting the appropriate values for E_{0s} and c_{vs} as described in section 2. Each simulation was initialized from a standard RCE sounding, with random temperature noise of amplitude 0.5 K added to the lowest model level to break the translational symmetry, and run to RCE over the course of approximately 50 days on a doubly periodic, 36-km domain with a model top at 40 km and 500-m horizontal resolution. The simulations were then restarted on the same domain but with 200-m grid spacing and run for an additional 25 days; the simulations adjusted to the higher resolution within 10 days, and statistics were collected over the last 15 days of equilibrated convection (during the equilibrated averaging period, the magnitude of the total energy tendency in the model was smaller than 0.3 W/m^2). Horizontal- and time-mean vertical profiles of quantities of interest were recorded, as well as mean profiles within "cloud updrafts". Cloud updrafts were identified as any grid cell with nonprecipitating condensed water mass fraction greater than 10^{-5} kg/kg and vertical velocity greater than 1 m/s. Our results would be largely unchanged if we had used the data from the simulations with 500-m horizontal resolution.

Figure 5.1 shows that turning on ice in our simulations increases the mean temperature of cloud updrafts above the melting line by up to nearly 2.5 K (red line). This is a very large change compared to the typical buoyancies of observed and simulated tropical oceanic convective clouds, which are less than 0.5 K when reported as condensate-loaded virtual temperature anomalies (e.g., Lawson and Cooper 1990; Wei et al. 1998; Sherwood et al. 2013; Romps and Charn 2015). However, Figure 5.1 also shows that the warming of the environmental temperature due to ice (black line) is essentially identical to the cloud warming between the altitudes of 500 m and 11 km, where clouds are positively buoyant in the mean. The fact that the latent heat of fusion released by deposition and freezing increases the temperature of both clouds and their environment—without changing the difference between these temperatures—is one of the key points of this chapter.

In Figure 5.2a, we plot the mean buoyancy of cloud updrafts in the simulations with and without ice. In both simulations cloud buoyancy is between 0.01 and 0.02 m/s^2 (i.e., an effective temperature excess of ~0.25–0.5 K) between 1 and 10 km. There is no increase in cloud buoyancy above the melting line (at roughly 4.3 km) in the simulation with ice. In fact, there is a kink in the buoyancy profile towards lower values at this altitude in the simulation

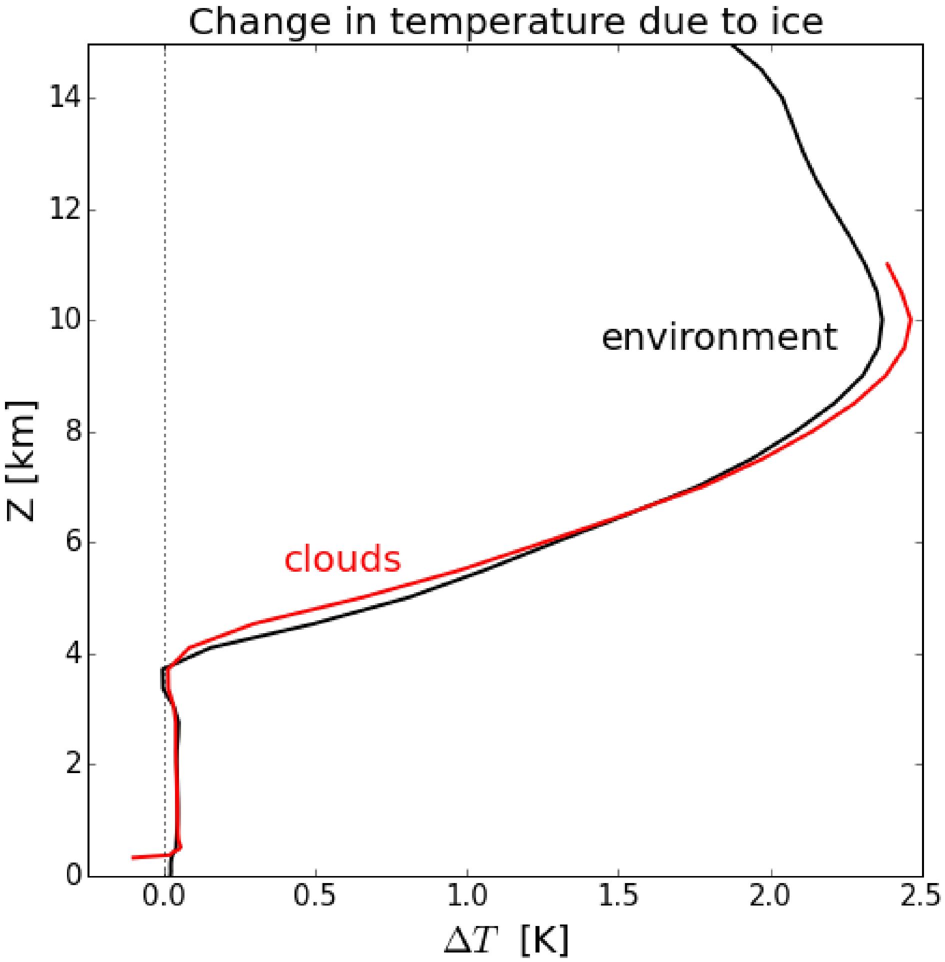

Figure 5.1: Absolute temperature differences between the simulation with ice and without ice. The environmental (i.e., time- and domain-mean) temperature difference is shown in black, and the cloud updraft temperature difference is shown in red. The cloud temperature is determined by conditionally sampling all grid points with vertical velocity larger than 1 m/s and nonprecipitating condensed water mass fraction larger than 10^{-5} kg/kg, and is plotted only where clouds are positively buoyant in the mean.

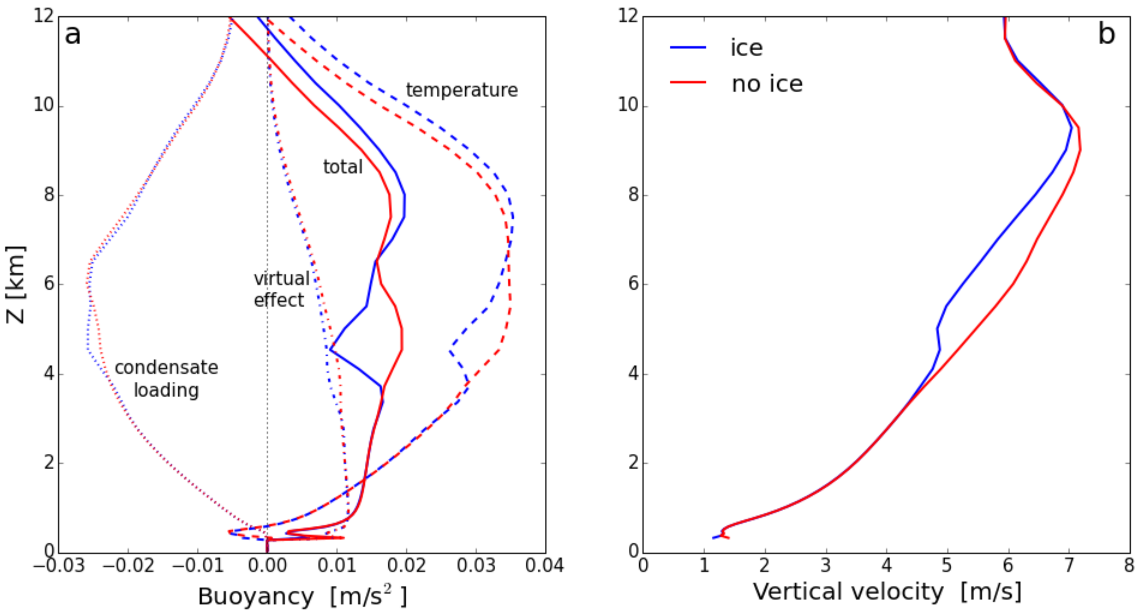

Figure 5.2: (a) Mean buoyancy of cloud updrafts in the simulation with ice (blue) and without ice (red). Total buoyancy is plotted with solid lines, buoyancy due to temperature differences is plotted with dashed lines, buoyancy due to condensate loading is plotted with dotted lines, and buoyancy due to the virtual effect is plotted with dot-dashed lines (see equation 5.1 for expressions for these contributions). (b) Mean vertical velocity of cloud updrafts in the two simulations. For both plots, cloud updraft properties are determined by conditionally sampling grid points with thresholds for vertical velocity and condensed water mass fraction (see text).

with ice. The explanation for this kink is the same as for the kink in buoyancy at the cloud base: in the presence of a vertically continuous radiative cooling rate and a vertically discontinuous static stability (discontinuities at the transition from dry adiabat to liquid moist adiabat at the cloud base, and from liquid moist adiabat to ice moist adiabat at the melting line), a steady-state profile of environmental temperature requires a discontinuity in mass flux, which is generated by a bump in the environment's potential temperature profile (i.e., a slight capping "inversion") that weeds out some of the less buoyant updrafts. In the profiles of cloud buoyancy, these bumps in potential temperature manifest as negative excursions of cloud buoyancy.

The relative insensitivity of total buoyancy to ice is not due to a compensation between the effects of ice on different sources of buoyancy. This can be seen by decomposing the buoyancy of moist air into its sources as follows:

$$b \simeq g \left[\frac{\Delta T}{T} + \left(\frac{R_v}{R_d} - 1 \right) \Delta q_v - \Delta q_{\text{con}} \right], \tag{5.1}$$

where g is the gravitational acceleration, R_v and R_d are the gas constants for water vapor and dry air, and ΔT, Δq_v, and Δq_{con} are the temperature, water vapor, and condensed water anomalies of the cloud relative to the environment, respectively. We decompose the total buoyancy into the temperature, virtual effect, and condensate-loading contributions in Figure 5.2a to show that each of the individual terms contributing to buoyancy is more or less constant between the two simulations. We also show the mean vertical velocity of cloud updrafts in Figure 5.2b. Above the melting line, the simulation with ice actually has slightly smaller updraft velocities than the simulation without ice (corresponding to the kink in buoyancy seen in Figure 5.2a), but these differences are only ~0.5 m/s.

Finally, in Figure 5.3 we show the profiles of undiluted buoyancy for near-surface air parcels lifted through the mean environmental density profiles of the two simulations. Parcels are initialized with the mean thermodynamic properties of the near-surface CRM level of the corresponding simulation, and the parcel buoyancy as a function of height is calculated by assuming conservation of MSE-CAPE, with a definition of MSE that includes the latent heat of the ice phase and the effects of liquid and solid water on the heat capacity of air (Romps 2015). To strike a balance between the idealized adiabatic and pseudoadiabatic processes, we assume that half of all condensed water falls out of the parcels immediately upon formation; our results are not overly sensitive to this choice.

There are four buoyancy profiles in Figure 5.3 because for each of the two mean environmental density profiles generated by our RCE simulations we can lift a near-surface parcel with and without ice processes enabled. (As in the simulations, ice is turned off for the parcel calculations by setting $E_{0s} = 0$ and $c_{vs} = c_{vl}$). The solid lines in Figure 5.3 show the results when the parcel's ice thermodynamics match the ice thermodynamics that produced the environmental density profile. In this case, CAPE varies by only 2.5%, increasing by 108 J/kg in the simulation with ice. If, instead, we calculate CAPE with mismatched thermodynamic assumptions—that is, if we lift a parcel with ice processes enabled through the environment from the simulation in which ice was disabled, or vice versa—the CAPE change is almost an order of magnitude larger (dot-dashed lines in Figure 5.3). Disabling ice for the parcel that is lifted through the ice-environment reduces its CAPE by 850 J/kg, while enabling ice for the parcel that is lifted through the no-ice environment increases its CAPE by a similar amount.

5.4 Theoretical discussion

It is important to distinguish between two questions that are often conflated: 1. given an environmental temperature profile, does fusion increase the buoyancy of a convecting cloud, and 2. does an atmosphere with fusion have larger cloud buoyancies than an atmosphere

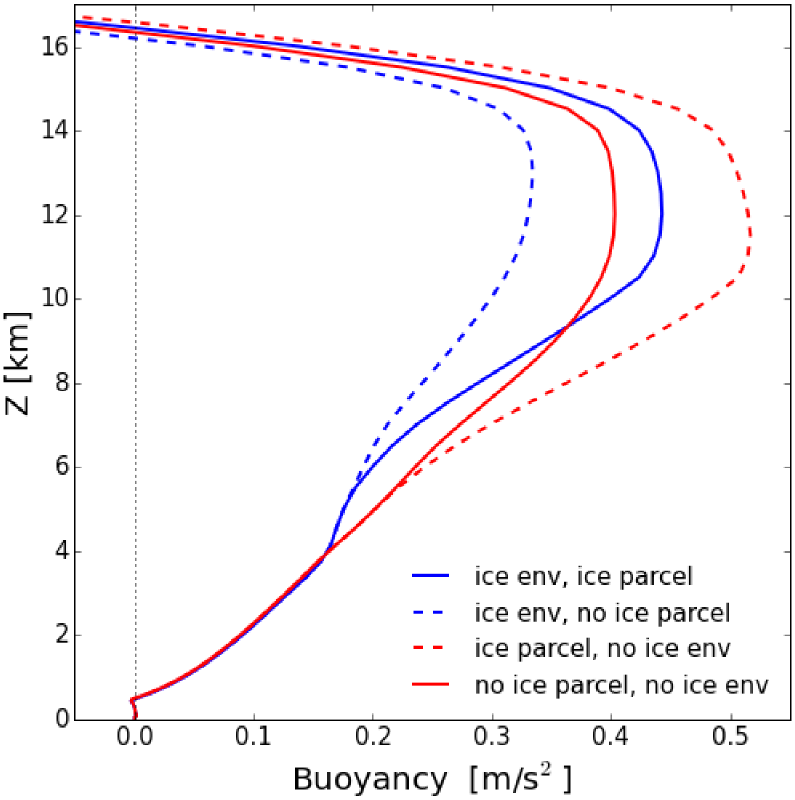

Figure 5.3: Profiles of buoyancy for undiluted parcels from the RCE simulations. The parcel properties are calculated by lifting air with the mean properties of the near-surface CRM level through the time- and domain-mean density profile, assuming conservation of MSE-CAPE. Half of all condensates are assumed to fall out of the parcel immediately upon formation. Solid lines show results when the parcel and environment ice thermodynamics match and dashed lines show when they are mismatched (see text).

with no fusion? Question 1 is the one addressed by Williams and Renno (1993), Fierro et al. (2009), and Romps and Kuang (2010a). The answer, which is "yes", can be seen in Figure 5.3 by comparing the solid blue and dashed blue curves or by comparing the solid red and dashed red curves: given an environmental temperature profile, a cloud that ascends with fusion has a higher buoyancy than a cloud that ascends without fusion. Question 2 asks whether a world with fusion has higher cloud buoyancies than a world without fusion. The answer, which is "no", can be seen by comparing the solid blue and solid red curves in Figures 5.2a and 5.3: a world with fusion does not have systematically higher cloud buoyancies than a world without fusion.

At present, there is no complete theory for what determines cloud buoyancy in a moist atmosphere. Nevertheless, there are two plausible ideas about cloud buoyancy, and neither of them would predict a significantly larger cloud buoyancy in a world with ice compared to a world without ice. One of those ideas is that actual cloud buoyancy can be described as some fraction of the undiluted cloud buoyancy. The other idea is that the actual cloud buoyancy is dictated by the mismatch in height between the profiles of latent heating and radiative cooling. We will discuss each of these in turn.

The first idea is that cloud buoyancy is some fraction of undiluted cloud buoyancy, and this idea stems from the recent theory for tropical CAPE (Singh and O'Gorman 2013). In this theory, the atmosphere is approximately neutrally stable to the commonplace moist entraining cloud. Therefore, CAPE is simply the vertical integral of the buoyancy that is given by the temperature difference between an undiluted parcel and a parcel that entrains with the typical entrainment rate. This theory has been validated with a variety of tests in large-eddy simulations (Singh and O'Gorman 2013; Seeley and Romps 2015).

Now, if all clouds had exactly the same entrainment rate and if the atmosphere were exactly neutrally stratified with respect to those clouds, then no cloud would have any buoyancy. In reality, different clouds begin with different entropies (set by the distribution of entropy in the boundary layer) and different clouds experience different amounts of dilution (set by a distribution of entrainment rates in the free troposphere). The mean cloud buoyancy will be set by both of these distributions, leading to a mean cloud buoyancy that is some fraction of the undiluted cloud buoyancy. Assuming the distributions of boundary-layer entropy and free-tropospheric entrainment are unaffected in any significant way by the presence or absence of fusion (as is the case in our simulations), the ratio of mean cloud buoyancy to undiluted cloud buoyancy should likewise be independent of the presence or absence of fusion.

Therefore, according to this idea, mean cloud buoyancy should change in proportion to undiluted cloud buoyancy. Or, averaged over the troposphere, cloud buoyancy should change in proportion to CAPE. Recall that CAPE is proportional to the integrated temperature difference between entraining and non-entraining parcel profiles. At a given height, that temperature difference is proportional to the amount of latent heat released up to that height. Therefore, neglecting the effects of lofted condensates (i.e., assuming that both entraining clouds and the undiluted parcel quickly drop their condensed water), the existence of fusion (compared to a world with no fusion) causes a fractional increase in upper-tropospheric cloud buoyancy of roughly $(L_f/L_c) \times [q_v^*(\text{melting line})/(q_v^*(\text{cloud base})]$ (i.e., the fractional increase in latent heat from fusion times the portion of the parcel's water vapor that condenses above the melting line). This predicts an increase in upper-tropospheric buoyancy of ∼4% due to fusion; the corresponding prediction for the increase in CAPE would be something closer to ∼2% since fusion affects buoyancy only in the upper troposphere while CAPE is an integral over the entire troposphere. Therefore, this line of argument predicts that mean cloud buoyancy, averaged over the troposphere, would be only ∼2% larger in a world with ice compared to a world without ice.

The second idea is that cloud buoyancies are controlled by the vertical profile of net latent heating minus radiative cooling since cloud buoyancies generate sensible heat fluxes. As pointed out by Mapes (2001), there is appreciable radiative cooling in cold layers of the atmosphere where latent heating is constrained to be quite small due to the vanishing of q_v^*; this cooling must, therefore, be balanced primarily by sensible heat fluxes (i.e., $Mc_p\Delta T$, where M is the cloud mass flux and ΔT is the temperature anomaly of the clouds). From this perspective, cloud buoyancy (roughly proportional to ΔT) in the upper troposphere exists because radiative cooling cannot be balanced by local latent heating there. It then follows that a world with ice should have about 10% more upper-tropospheric latent heating than a world without ice (since deposition releases about 10% more latent enthalpy than condensation). By this line of argument, a world with ice should have a slightly *smaller* sensible heat flux and, therefore, slightly *smaller* cloud buoyancies.

The magnitude of this effect can be estimated by comparing the need for sensible heat fluxes in our two simulations. Let $\text{LH}(z)$ (W/m^2) be the net latent heating from condensation and freezing/deposition, vertically-integrated from altitude z to the top of the atmosphere. We can use our simulation output to calculate that turning on fusion increases LH by $\leq$10% between 6 km and the anvil height of 12 km, confirming our simple estimate that there should be about 10% more upper-tropospheric latent heating in a world with ice. Therefore, assuming radiative cooling does not change, this increase in latent heating in the simulation with fusion would require a decrease in sensible heat flux, $\Delta\text{SH}(z)$, of (0.1)LH. Estimating LH as $ML_cq_v^*(1-\text{RH})$, the fractional decrease in sensible heat flux is

$$\frac{\Delta(\text{SH})}{\text{SH}} = \frac{(0.1)ML_cq_v^*(1-\text{RH})}{(Mc_p\Delta T)}. \tag{5.2}$$

Taking $L_c = 2.5 \times 10^6$ J/kg, $q_v^* \leq 3$ g/kg, $\text{RH} \geq 60\%$, $c_p = 1000$ J/kg/K, and $\Delta T \sim 1$ K, we estimate a fractional decrease in sensible heat flux of $\leq$30% in the upper troposphere of the simulation with fusion. Assuming cloud mass flux does not change, this implies a $\leq$30% decrease in the mean temperature anomaly of upper-tropospheric clouds, and a corresponding ∼10% decrease in the troposphere-mean cloud buoyancy, in the simulation with fusion.

In summary, we have two different plausible ideas about cloud buoyancy, and neither predict a significantly larger cloud buoyancy in a world with ice as compared to a world without ice. The idea based on CAPE predicts a change in cloud buoyancy of roughly +2%, while the idea based on the vertical distribution of latent and radiative heating predicts a change in cloud buoyancy of roughly −10%. In the CRM, the existence of fusion changes cloud buoyancy with variable sign and a typical magnitude of $\leq$0.01 K over the troposphere. This leads to a troposphere-averaged ice-induced change in cloud buoyancy of −4%, which sits in between the two predictions.

Generally, the claim that cloud buoyancy should be larger above the melting line due to the latent heat of fusion – made by Zipser (2003) and many others – ignores the link between cloud temperatures and environmental temperatures. But, this link is a fundamental property of a convecting atmosphere with fast gravity waves. The release of the latent heat of fusion above the melting line does not increase cloud buoyancy because that latent heat release is not a "surprise" to the environment, but is already imprinted on the environmental temperature by gravity-wave adjustment. Therefore, meteorologists on an alternate Earth with no ice phase would find cloud buoyancies and updraft speeds in the upper troposphere that are not significantly different from our own.

5.5 Why is undiluted buoyancy largest in the upper troposphere?

We have shown that the release of latent heat of fusion above the melting line is not the reason that tropical undiluted parcel buoyancies, such as in our Figure 5.3 or the observations shown in Figure 5 of Mapes (2001), are largest in the upper troposphere. What, then, is responsible for the "shape of CAPE"?

In fact, the top-heaviness of tropical undiluted buoyancy profiles can be explained with concepts borrowed from the theory for CAPE introduced by Singh and O'Gorman (2013), which has also been at the heart of recent progress in our understanding of tropical vertical velocities and relative humidity profiles (Singh and O'Gorman 2014; Romps 2014). As mentioned in section 5.4, this theory assumes that the temperature profile of the environment in an RCE state is equal to and set by the temperature of an entraining cloud plume; CAPE for an undiluted parcel is then a consequence of the fact that commonplace clouds entrain subsaturated environmental air, thereby setting an environmental temperature that is colder than that of an undiluted parcel.

Seeley and Romps (2015) pointed out that this framework predicts parcel-environment temperature differences to be maximized in the upper troposphere, where the smallness of q_v^* forces the difference in moist static energy between the undiluted parcel and the entraining cloud plume to be expressed as sensible heat ($c_p \Delta T$, where c_p is the heat capacity of dry air) rather than latent enthalpy ($L \Delta q_v$, where L is the latent heat of vaporization). More precisely, if the effect of entrainment is to reduce the moist static energy of the clouds setting the environmental temperature profile by an amount Δh^*, where $h^* = c_p T + L q_v^* + gz$, then the temperature difference between an undiluted parcel and the environment at a given height is approximately given by $\Delta h^* / \beta$, where $\beta = (c_p + L \frac{\partial q_v^*}{\partial T})$. In layers of the atmosphere where $L \frac{\partial q_v^*}{\partial T} > c_p$, Δh^* is not predominantly expressed as a parcel-environment temperature difference; this is the case in the lower troposphere for typical conditions in Earth's tropics.

It is in the upper troposphere that parcel-environment temperature differences are largest, because there $c_p \gg L\frac{\partial q_v^*}{\partial T}$. (For example profiles of β and Δh^*, see Figure 1 of Seeley and Romps (2015).)

We illustrate this point in Figure 5.4, where we show the profile of buoyancy for an adiabatically-lifted parcel from an RCE simulation that is identical to the no-ice simulation with 500 m grid spacing discussed in section 2, except that the SST was set to 310 K instead of 300 K (we use a higher SST simply because it enlarges the features of the buoyancy profile that are our focus). There is clearly a large upper-tropospheric peak in undiluted buoyancy in this simulation, despite the lack of ice physics. The black dot on the buoyancy profile marks the altitude where $c_p = L\frac{\partial q_v^*}{\partial T}$, approximately marking the altitude at which the undiluted parcel buoyancy rapidly increases due to the moist-to-dry transition of β discussed above and in Seeley and Romps (2015). These results suggest that finite and ubiquitous tropical CAPE from top-heavy buoyancy profiles is not an accident of the existence of ice, but results from simpler two-phase water thermodynamics.

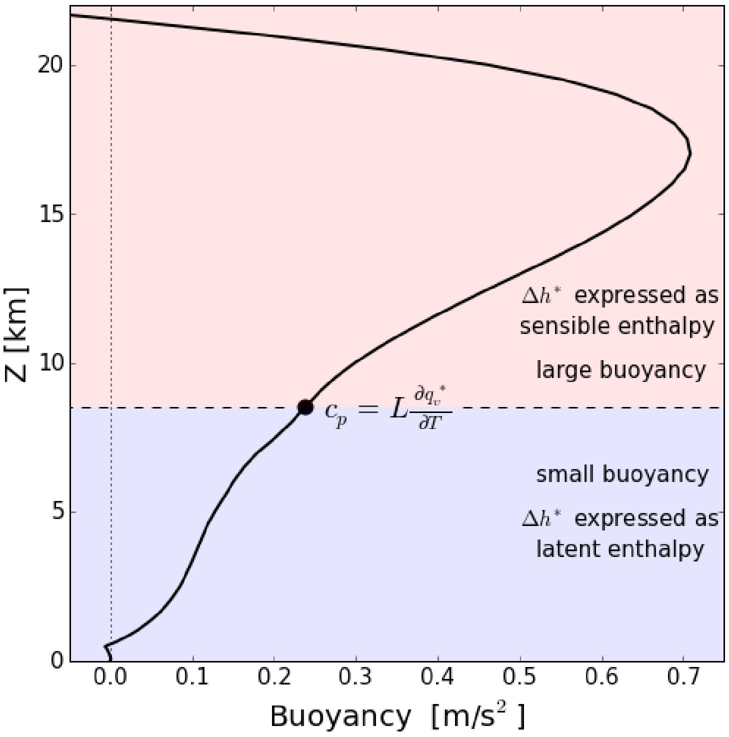

Figure 5.4: Buoyancy of an adiabatically-lifted near-surface parcel from an RCE simulation over an SST of 310 K. The dashed line and black dot mark the level where $c_p = L\frac{\partial q_v^*}{\partial T}$, which serves as an approximate division between the layer of the troposphere where the saturated MSE excess of an undiluted parcel (Δh^*) is primarily expressed as latent enthalpy ($L\Delta q_v^*$), and the layer where Δh^* is primarily expressed as sensible enthalpy ($c_p\Delta T$). Relatively large adiabatic parcel buoyancies are only expected in the sensible-enthalpy-dominated regime.

Chapter 6

FAT or FiTT? Are anvil clouds or the tropopause temperature-invariant?

The Fixed Anvil Temperature (FAT) hypothesis proposes that upper-tropospheric cloud fraction peaks at a special isotherm that is independent of surface temperature. It has been argued that a FAT should result from simple ingredients: Clausius-Clapeyron, longwave emission from water vapor, and tropospheric energy and mass balance. Here, the first cloud-resolving simulations of radiative-convective equilibrium (RCE) designed to contain only these basic ingredients are presented. This setup does not produce a FAT: the anvil temperature varies by about 40% of the surface temperature range. However, the tropopause temperature varies by only 4% of the surface temperature range, which supports the existence of a Fixed Tropopause Temperature (FiTT). In full-complexity RCE simulations, the spread in anvil temperature is smaller by about a factor of two, but the tropopause temperature remains more invariant than the anvil temperature by an order of magnitude. In other words, our simulations have a FiTT, not a FAT.

6.1 Introduction

The Fixed Anvil Temperature (FAT) hypothesis has become fairly well-accepted (Boucher et al. 2013). The basic claim of the FAT hypothesis is simple: anvil clouds preferentially form at a special isotherm that is independent of the surface temperature (Hartmann and Larson 2002). Since a fixed emission temperature for anvil clouds would tend to decouple the outgoing longwave radiation of convecting regions from the underlying surface temperature, a FAT would provide a positive feedback during global warming. Empirically, the longwave cloud feedback in global climate models (GCMs) is observed to be robustly positive, a finding for which a FAT is the most common explanation (Zelinka and Hartmann 2010), and results

---

[1] This chapter is a slightly edited version of Seeley et al. (2018b).

from multiple cloud-resolving models (CRMs) have also appeared to support the existence of a FAT (Kuang and Hartmann 2007; Harrop and Hartmann 2012; Khairoutdinov and Emanuel 2013; Singh and O'Gorman 2014). Originally proposed as a constraint on tropical cloud-climate feedback, the FAT hypothesis has recently been extended from the tropics to the global atmosphere (Thompson et al. 2017).

The plausibility of the FAT hypothesis also derives, in part, from arguments that it should result from a few basic physical ingredients. These basic ingredients include Clausius-Clapeyron control of water-vapor concentrations, longwave radiative emission from water vapor, the radiative-convective energy balance of the tropical troposphere, and mass continuity between cloudy and clear skies. Since these basic ingredients should be present both in nature and in numerical models of the atmosphere, the FAT hypothesis has appeared to rest on a solid theoretical foundation, which has boosted confidence in its implications for contemporary climate change (Zelinka and Hartmann 2011; Boucher et al. 2013).

The purpose of this chapter is to take a step back and re-evaluate the FAT hypothesis, as both an empirical result and a theoretical construct. The empirical half of this investigation is aided by the first cloud-resolving simulations of radiative-convective equilibrium (RCE) designed to contain only the basic ingredients emphasized by the literature (the "minimal-recipe" setup, described in more detail in Appendix A). The use of a model that contains no inessential complexity with respect to the phenomenon of interest is the ideal framework for hypothesis testing, and is a crucial step toward understanding the behavior of full-complexity models (Held 2005; Jeevanjee et al. 2017).

For the reader interested in whether a FAT is produced by temperature-dependent longwave radiative emission from water vapor, Figure 6.1 is the key result. There, we plot the cloud fraction profiles from the minimal-recipe RCE simulations as a function of temperature. With the anvil temperature defined as the temperature at which cloud fraction is maximum, we find that the anvil temperature varies by 50 K, or 100% of the 50-K range in simulated surface temperature. This very large anvil-temperature spread is influenced by the coldest simulation, for which cloud fraction maximizes at a much colder temperature than for the other simulations. If we restrict our attention to the simulations with surface temperatures $T_\mathrm{s} \geq 270$ K, the anvil-temperature sensitivity is reduced to 37% of ΔT_s.

Whether Figure 6.1 should be taken as evidence of a fixed anvil temperature depends, of course, on the definition of "fixed". For $T_\mathrm{s} \geq 270$ K, the changes in anvil temperature are smaller than, but of the same order of magnitude as, the changes in surface temperature: a 1 K increase in surface temperature causes about a 0.4 K increase in anvil temperature. We argue that it is not a useful approximation to consider some feature of the atmosphere as occurring at a "fixed" temperature if its temperature variations are of the same order of magnitude as the surface temperature variations; that is, the simple (albeit arbitrary) criterion we adopt is to say that feature x occuring at temperature T_x is fixed with respect to surface temperature if $\Delta T_x < 0.1 \times \Delta T_\mathrm{s}$. By this criterion, the anvil temperature is not fixed in our minimal-recipe simulations. In the next section, we seek to explain these varying anvil temperatures by probing for weak links in the arguments for the FAT hypothesis.

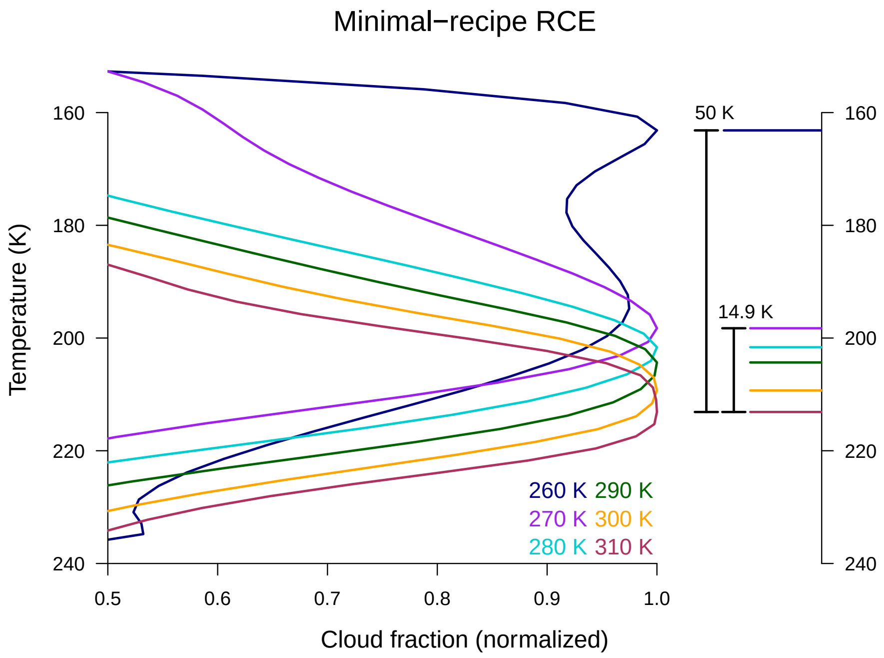

Figure 6.1: Cloud fraction profiles as a function of temperature for the minimal-recipe RCE simulations, which are forced only by longwave radiative cooling from water vapor and use a simplified microphysics scheme with no explicit temperature dependence. The profiles are normalized (i.e., divided by their maximum value) before plotting. Surface temperatures T_s between 260 K and 310 K are indicated by color. Horizontal lines mark the anvil temperatures.

6.2 How the FAT hypothesis is supposed to work

Figure 6.2 enumerates the statements that are used to justify the FAT hypothesis. A chain of reasoning similar to the one depicted here can be found in most studies concerned with the FAT hypothesis (Hartmann and Larson 2002; Larson and Hartmann 2003; Kuang and Hartmann 2007; Kubar et al. 2007; Xu et al. 2007; Eitzen et al. 2009; Zelinka and Hartmann 2010, 2011; Li et al. 2012; Harrop and Hartmann 2012; Thompson et al. 2017). The purpose of this section is to carefully step through this chain of reasoning — statement by statement — and determine if there are any weak links.

Statement 1

Statement 1 says that the radiative cooling in clear skies is mainly controlled by longwave emission from water vapor. Indeed, observations and radiative transfer codes show that tropospheric longwave cooling rates from greenhouse gases such as carbon dioxide and ozone, as well as the shortwave heating rates from water vapor and these other gases, are

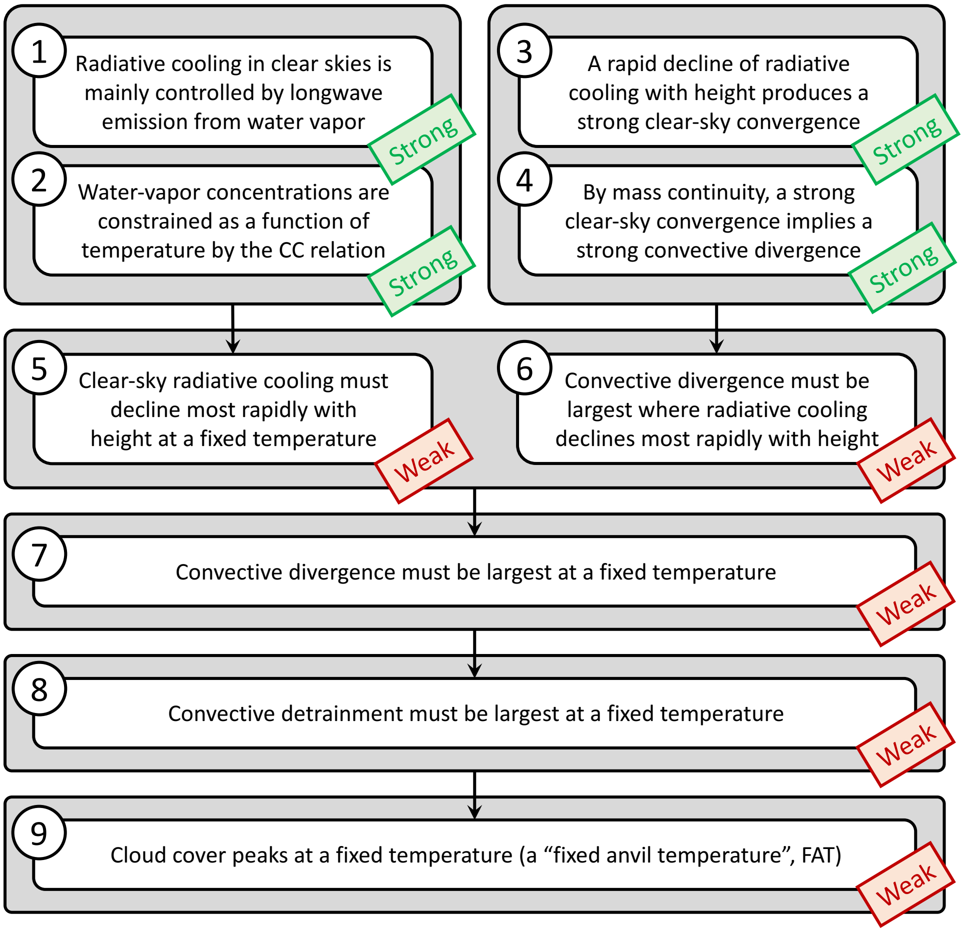

Figure 6.2: The chain of reasoning used to justify the FAT hypothesis. Statements for which we find strong support (theoretical and/or empirical) are marked "Strong", while those for which we find weak support or no support are marked "Weak".

smaller in magnitude than the longwave cooling from water vapor (Wallace and Hobbs 2006). Therefore, statement 1 is a strong link.

Statement 2

Statement 2 says that water-vapor concentrations are constrained as a function of temperature by the Clausius-Clapeyron relation. According to the Clausius-Clapeyron relation, the saturation vapor pressure p_v^* of water vapor declines quasi-exponentially as temperature drops. It is worth noting that the measure of water-vapor concentration that is directly tied to longwave emissivity is not the vapor pressure, but the absorber density $\rho_v = \mathrm{RH}p_v^*/(R_v T)$. Although ρ_v depends on the relative humidity RH as well as the temperature T, it has recently been demonstrated (and justified by theory) that relative humidity is itself a nearly fixed function of temperature in RCE (Romps 2014). To an excellent approximation, the mean water-vapor density in an atmosphere in RCE is a fixed function of the local temperature. Therefore, statement 2 is a strong link.

Statement 3

Statement 3 says that a rapid decline of radiative cooling with height produces a strong clear-sky convergence. This statement is based on an approximate steady-state energy budget for clear skies, which is typically written in a form equivalent to

$$M_e = -\frac{Q_e}{c_p\left(\Gamma_d - \Gamma\right)}\,, \tag{6.1}$$

where M_e (kg/m^2/s) is the upward clear-sky mass flux (subscript e for “environment”, value is negative), Q_e (W/m^3) is the clear-sky diabatic cooling rate (positive value for cooling), c_p (J/kg/K) is the heat capacity of air at constant pressure, Γ_d (K/m) is the dry-adiabatic lapse rate, and Γ is the actual lapse rate (Minschwaner and Dessler 2004; Kuang and Hartmann 2007). By mass continuity, the clear-sky horizontal convergence is equal to $\partial M_e/\partial z$. By equation (6.1), this is

$$\frac{\partial M_e}{\partial z} = -\frac{1}{c_p\left(\Gamma_d - \Gamma\right)}\frac{\partial Q_e}{\partial z} - \frac{Q_e}{c_p\left(\Gamma_d - \Gamma\right)^2}\frac{\partial \Gamma}{\partial z}\,. \tag{6.2}$$

If Γ did not vary with height and if Q_e were entirely due to radiation, then the clear-sky convergence would be proportional to $-\partial Q_e/\partial z$, i.e., minus the decrease of radiative cooling with height. In reality, Γ does vary with height, and the proximity of Γ to Γ_d in the upper troposphere can make the last term in (6.2) quite important. And, Q_e is not entirely due to radiation; there is also a component due to evaporation of precipitation and detrained condensates. Nevertheless, if the decline of radiative cooling is sufficiently rapid (i.e., making $\partial Q_e/\partial z$ sufficiently negative), then that will generate a strong colocated convergence. Therefore, despite the caveats, statement 3 is a strong link.

Statement 4

Statement 4 says that a strong clear-sky convergence implies a strong convective divergence. This follows from mass conservation. If M_c (kg/m^2/s) is the upward convective mass flux (subscript c for "convection"), then, in the absence of any large-scale ascent or descent, $M_e = -M_c$. Then, the convective divergence ($-\partial M_c/\partial z$) is exactly equal to the clear-sky horizontal convergence ($\partial M_e/\partial z$). In the presence of large-scale ascent or descent, this equality is violated. But even in the presence of large-scale motions, a sufficiently strong clear-sky convergence still implies a strong convective divergence. Therefore, statement 4 is a strong link.

Statement 5

Statement 5 says that the clear-sky radiative cooling must decline most rapidly with height at a fixed temperature. The literature on the FAT hypothesis has argued that this follows logically from statements 1 and 2, but this is not obvious. One can imagine a scenario in which statement 5 would follow from statements 1 and 2: if water vapor were a gray gas whose density were a fixed function of temperature, and if pressure-dependent collisional broadening did not exist, then the longwave emissivity of the atmosphere would be a fixed function of temperature. In that scenario, radiative cooling to space would be narrowly peaked around the altitude where the longwave optical depth (τ) equals one (Pierrehumbert 2010). Since the absorber density is imagined to be fixed in temperature in this scenario, this peak in radiative cooling would also occur at a fixed temperature (as long as the temperature structure above the $\tau = 1$ level were also essentially fixed). Therefore, in this scenario, radiative cooling would decline with height most rapidly at a fixed temperature, which would occur on the cold side of the $\tau = 1$ level. This behavior of a gray atmosphere is confirmed in Figure 6.6.

Of course, it is well-known that water vapor is not a gray gas: water vapor has a complex spectroscopy, with an absorption coefficient that varies by many orders of magnitude in the wavelengths of terrestrial emission (Pierrehumbert 2010). Although the non-gray spectroscopy of water vapor has been well-known for decades, it seems that the implications of this physics for the FAT hypothesis have not been sufficiently appreciated. As a result of the complex spectroscopy of water vapor, there is no single $\tau = 1$ level that applies at all wavelengths; instead, the temperature at the $\tau = 1$ level depends strongly on the wavelength of light under consideration, with relatively cold emission temperatures corresponding to relatively optically-thick wavelengths (Clough et al. 1992). Therefore, the principles of radiative transfer and Clausius-Clapeyron alone do not predict a rapid decline of radiative cooling at any particular temperature for a non-gray atmosphere. Statement 5, then, is not an obvious logical consequence of statements 1 and 2.

Even if statement 5 does not follow logically from statements 1 and 2, could it still be empirically true? Let us denote the clear-sky radiative cooling rate as R_e (W/m^3, positive value for cooling) to distinguish it from the total diabatic cooling Q_e. In Figure 6.3a, we

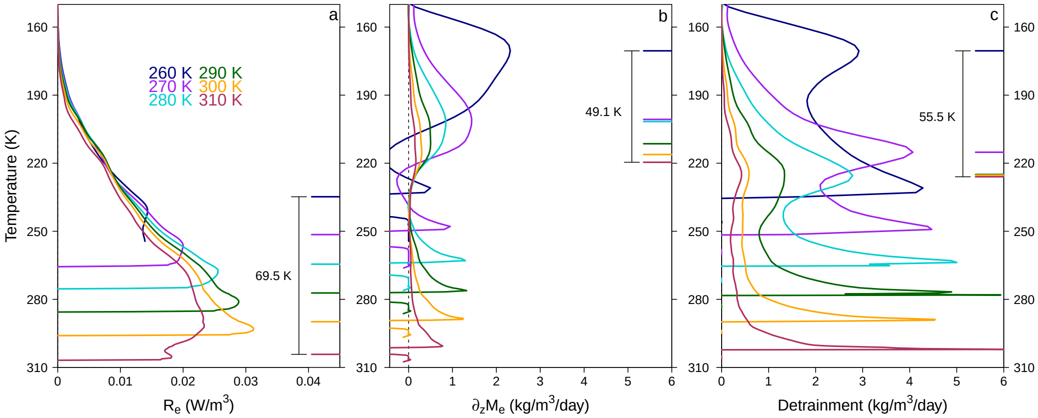

Figure 6.3: Profiles of (a) the clear-sky longwave radiative cooling rate, R_e; (b) convective divergence, $\partial_z M_e$; (c) convective detrainment, D. All profiles are from the "minimal-recipe" cloud-resolving simulations of RCE for sea surface temperature T_s in the range 260–310 K. In (a), the location of each simulation's most rapid decline of R_e with height is marked with a horizontal colored line. In (b) and (c), the horizontal colored lines mark the temperature of the upper-tropospheric ($T \leq 230$ K) maximum from each simulation. The detrainment rates plotted in (c) are obtained from equation 2 in Appendix B.

show R_e from the minimal-recipe simulations of RCE over surface temperatures ranging from 260–310 K. Plotted as a function of temperature, R_e shows a tendency to collapse to an approximately universal curve (Jeevanjee and Romps 2018). However, we find no evidence for a particularly rapid decline of R_e with height at any particular temperature. This conclusion does not depend on the units one uses to plot the radiative cooling rate (i.e., W/m^3 versus K/day); see Appendix C and Figure 6.7 for a discussion of this point. The horizontal lines in Figure 6.3a mark the temperatures where $\partial_z R_e$ is maximum, which occur in the lower troposphere of each simulation and vary by 69.5 K across the suite of simulations. In stark contrast to the narrowly-peaked radiative cooling profiles generated by a gray radiation scheme, the radiative cooling from water vapor as computed by RRTM is spread out smoothly over the depth of the troposphere. Therefore, on both theoretical and empirical merit, statement 5 is a weak link.

Statement 6

Statement 6 says that convective divergence must be largest where radiative cooling declines most rapidly with height. Although the literature has argued that statement 6 follows from statements 3 and 4, this logic is not supported by equation 6.2. Note that statement 6 *would* follow from statements 3 and 4 if the lapse rate Γ were constant with height and if Q_e were entirely due to radiation. But, it is well-known that neither of these conditions hold true for the tropical atmosphere.

Even though statement 6 is not a logical consequence of statements 3 and 4, it could still be an empirical fact. To test whether this is the case, we plot in Figure 6.3 the convective divergence from the minimal-recipe RCE simulations as a function of temperature. Comparing Figures 6.3a and 6.3b shows that the upper-tropospheric ($T \leq 230$ K) peaks in convective divergence do not occur where R_e is declining especially rapidly with height. Therefore, statement 6 is a weak link.

Statement 7

Statement 7 says that convective divergence must be largest at a fixed temperature. This would be logically implied by statements 5 and 6 if those statements held true. However, since statements 5 and 6 were found to be weak links in the chain of reasoning, the logical support for statement 7 has been undermined.

Even if the logical antecedents of statement 7 do not hold true, could statement 7 still be an empirical fact? Figure 6.3b shows that the temperature of the upper-tropospheric convective divergence peak varies by 49.1 K in the RCE simulations, which is 98% of the 50-K range in surface temperature. Therefore, statement 7 is a weak link.

Statement 8

Statement 8 says that convective detrainment must be largest at a fixed temperature. The literature argues that this follows from statement 7, which says that convective divergence must be largest at a fixed temperature. We have shown that statement 7 does not hold in our simulations, but even if it did, statement 8 would be a logical consequence only if convective detrainment D were proportional to convective divergence $\partial_z M_e$. However, it is well-known that this is not the case: the standard bulk-plume equation relating these quantities is

$$\partial_z M_e = D - E \,, \tag{6.3}$$

where E is the entrainment rate and both E and D are nonnegative (Yanai et al. 1973). Therefore, $\partial M_e/\partial z$ simply places a lower bound on D, i.e., $D \geq \partial M_e/\partial z$. Although we can expect significant detrainment where there is significant convective divergence, it is not necessarily true that this is where the largest detrainment is.

Empirically, is statement 8 true? Detrainment is notoriously hard to measure. Here, we use a bulk-plume budget for a tracer that is conserved in cloudy air to estimate the detrainment rate in our simulations (Appendix B). The profiles of detrainment estimated from this method are plotted as a function of temperature in Figure 6.3c. The upper-tropospheric detrainment peaks occur at temperatures that vary by 55.5 K, or 111% of the 50-K range in surface temperature. Therefore, statement 8 is a weak link, both empirically and theoretically.

Statement 9

Statement 9 says that the peak in cloud fraction occurs at a fixed temperature, i.e., there is a "fixed anvil temperature". The literature argues that this follows from statement 8, which is the claim that convective detrainment must be largest at a fixed temperature. We have already shown that statement 8 does not hold in our simulations, but even if it were true, statement 9 would not be a logical consequence. That inference conflates the *source* of cloudy air (i.e., detrainment) with the *stock* of cloudy air (i.e., cloud fraction), when in reality cloud fraction is controlled by both its source and its sink. In fact, it has recently been demonstrated that the anvil cloud fraction peak in RCE is not caused by an anomalously large amount of detrainment, but by the anomalously slow rate of evaporation of cloudy air in the upper troposphere (Seeley et al. 2018a). In general, since the rate of cloud decay can vary significantly with height, a peak in detrainment will not necessarily be collocated with a peak in cloud fraction. Therefore, statement 9 does not follow logically from statement 8.

6.3 Empirical evidence for a FAT

We have already shown that the anvil temperature is not fixed in minimal-recipe simulations containing only the basic ingredients emphasized by the literature (Figure 6.1); so, if there is a FAT, it is not for the reasons that have been previously proposed. Could it be that the FAT hypothesis fares better in a more standard RCE configuration, due to other processes that have not been emphasized in the literature?

We tested this idea by adding back the inessential complexity that was stripped away for the minimal-recipe tests (Appendix A). The cloud fraction profiles from these full-complexity simulations are shown in Figure 6.4. Compared to Figure 6.1, cloud fraction exhibits a much more obvious collapse in temperature coordinates, especially at warmer surface temperatures. Switching from the minimal-recipe to the full-complexity setup cuts the spread in anvil temperature by a bit less than half, from 37% to 23% of ΔT_s. Therefore, we can conclude that changes in anvil temperature are quite damped compared to changes in surface temperature in the full-complexity simulations. Further work is needed to determine whether it is temperature-dependent ice microphysics, interactive cloud radiation, shortwave absorption, or something else that pushes anvil cloud fraction toward a collapse in temperature coordinates in full-complexity simulations. However, our results have shown that a FAT is not produced by Clausius-Clapeyron control of longwave radiative cooling alone.

Although our results seem to contradict the general acceptance of the FAT hypothesis, they do not conflict with published numerical results. In the first paper on this topic, the FAT hypothesis was tested in simulations of RCE with parameterized convection (Hartmann and Larson 2002). That study raised the surface temperature by 6 K, and found that the temperature at the top of the tallest ice clouds varied by approximately 3 K, or 50% of ΔT_s. Subsequent results from CRMs found a 0.5 K change in T_a for a 2 K change in surface temperature (Kuang and Hartmann 2007), a 1 K change in T_a for a 4 K change in surface temperature (Harrop and Hartmann 2012), an 8 K change in T_a for a 15 K change in surface

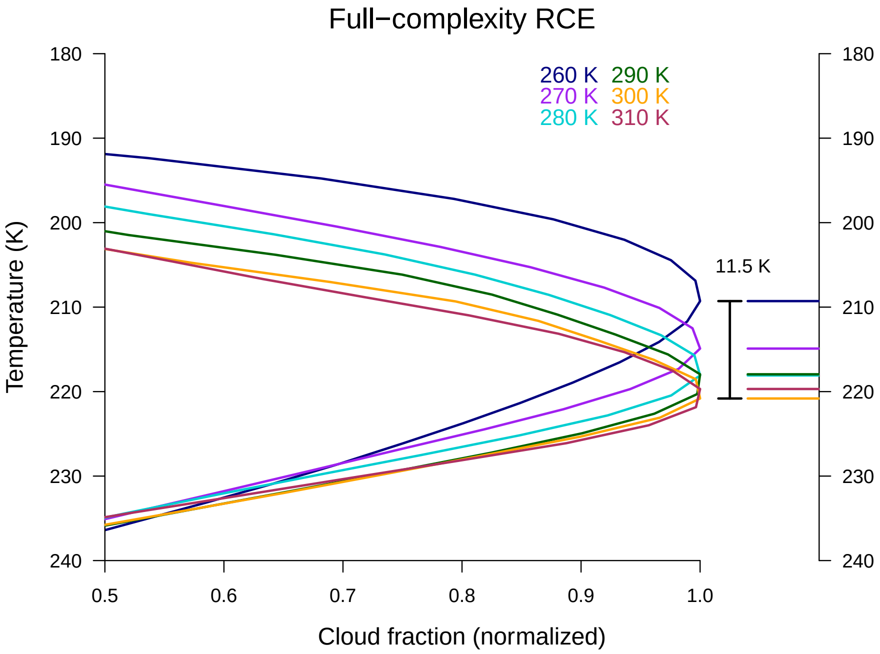

Figure 6.4: As in Figure 6.1, but for full-complexity RCE simulations. These simulations include shortwave radiative transfer, carbon dioxide, interactive cloud radiation, and temperature-dependent microphysics.

temperature (Khairoutdinov and Emanuel 2013), and a 2 K change in T_a for a 4 K change in surface temperature (Thompson et al. 2017). The most compelling evidence for a FAT appeared in a paper that was not about FAT (Singh and O'Gorman 2014); that study showed a 6 K change in T_a when the surface temperature was increased from 281 to 311 K, which is a slightly larger spread in T_a than we find in our full-complexity simulations over the same temperature range. These results in the literature have been used to support the existence of a FAT, although the reported anvil temperature sensitivities are in the range of 20–50% of ΔT_s and therefore fail our simple order-of-magnitude criterion. Our anvil temperature sensitivity of 23–37% of ΔT_s is in agreement with previous numerical results: the anvil temperature changes by less than the surface temperature, but it is not entirely fixed, either. Note that the most important temperature for the radiative impact of high clouds is not that of the cloud-fraction peak, but the average temperature at which the cloud optical depth equals 1 (looking down from space). Future analysis should quantify the difference between these two characteristic cloud temperatures.

6.4 FiTT, not FAT

Although the anvil temperature is not fixed in our RCE simulations, we find that a different property of the atmosphere is remarkably invariant with respect to surface temperature. The temperature at the radiative tropopause—where clear-sky radiative cooling rates first go to zero—varies by only 1.7 K in our minimal-recipe setup (Figure 6.5). In the full-complexity simulations, the mean tropopause temperature is warmer by 35 K, but also varies by only 1.6 K with respect to surface temperature. These tropopause temperature sensitivities are <4% of ΔT_s. In other words, we find strong evidence for a Fixed Tropopause Temperature (FiTT). This surface-temperature invariance is most obvious when the tropopause is defined *radiatively*; if we use the common lapse-rate definition of the tropopause (e.g., Fueglistaler et al. 2009), we find that the tropopause temperature varies by 11 K in the minimal-recipe simulations and by 5 K in the full-complexity simulations.

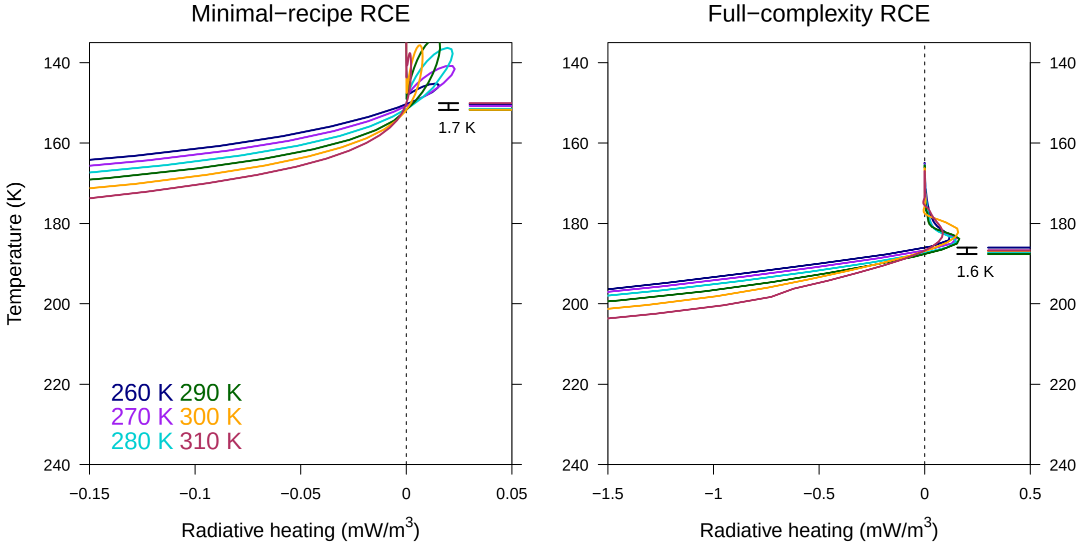

Figure 6.5: Clear-sky radiative heating rates as a function of temperature in (a) the minimal-recipe and (b) the full-complexity RCE simulations. The radiative tropopause temperatures—where radiative cooling rates first go to zero—are marked with colored horizontal lines.

Taken all together, our results motivate a disentangling of two features of the atmosphere that are often lumped together: 1) the extensive cloud fraction produced by anvil clouds, and 2) the top of the troposphere. The basic idea that the top of the troposphere occurs at a fixed temperature is strongly supported by our results — as long as the top of the troposphere is identified by the radiative tropopause, rather than the anvil temperature. Since anvil clouds do not primarily result from enhanced detrainment below the tropopause (Seeley et al. 2018a), the fact that the tropopause temperature is fixed does not imply that the anvil temperature is fixed. Indeed, the physical distance separating these two features is

5–10 km in our minimal-recipe simulations. Although the very tallest clouds (i.e., the zero-crossing of the cloud-fraction profile) must keep pace with the rising tropopause in order to maintain radiative-convective equilibrium, the *peak* in upper-tropospheric cloud fraction need not track with the rising tropopause.

If we understood why RCE in Earthlike atmospheres has a FiTT, it would simplify the way we think about our atmosphere and those of other planets where water vapor is the dominant radiatively-active gas. Unfortunately, since we do not yet have this understanding, FiTT is currently only a modeling result. The reproducibility of FiTT in other radiative-convective models should be assessed, which may become possible with results from the upcoming RCEMIP (Wing et al. 2018). But, even if a model consensus is achieved, a satisfactory explanation for FiTT will require the development of a theory for the tropopause temperature in radiative-convective equilibrium.

Appendix A: Simulations

All simulations were conducted with DAM (Romps 2008), a three-dimensional, fully compressible, nonhydrostatic CRM that computes radiative transfer with RRTM (Clough et al. 2005; Iacono et al. 2008). The simulations used a square domain with a side length of 48 km and doubly periodic horizontal boundaries. The horizontal resolution was 500 m, and the vertical grid spacing increased from 50 m in the boundary layer to a constant 250 m spacing for altitudes between 3 km and 30 km, and increased again to a spacing of 1 km between 40 km and the model top at 50 km. Surface fluxes were computed via a standard bulk aerodynamic formula. Horizontal-mean winds were damped to zero on a time scale of six hours, and wave damping was applied to the 3-dimensional stratospheric wind field.

In the "minimal-recipe" simulations, longwave emission from water vapor is the only contributor to radiative heating rates. This is accomplished by turning off shortwave radiation and zeroing out carbon dioxide, ozone, and condensed water in the radiative transfer calculations. In addition, the minimal-recipe simulations use a simplified autoconversion-based microphysics scheme that has been described in previous work (Seeley et al. 2018a). Other than the condensation and evaporation that occur during saturation adjustment, the only microphysical process included in this scheme is autoconversion of cloud condensate to rain, which is given a fixed e-folding timescale of 30 minutes. Rain is given a fixed freefall speed of 10 m/s and is allowed to evaporate in subsaturated air. In comparison, the "full-complexity" simulations include shortwave radiation, a vertically-uniform 280 ppmv of carbon dioxide, interactive cloud radiation, and use DAM's default Lin-Lord-Krueger microphysics scheme (Lin et al. 1983; Lord et al. 1984; Krueger et al. 1995). The rain-evaporation parameterization used in the minimal-recipe simulations is that of the Lin-Lord-Krueger scheme.

For each of the two model configurations, six simulations were run over fixed sea surface temperatures T_s ranging from 260 to 310 K, for a total of twelve simulations. Each simulation was initialized with thermodynamic profiles generated by analytical solutions to RCE (Romps 2016), and run to equilibrium over 1000 days with a coarser horizontal resolution (2 km).

The simulations were then restarted with 500 m horizontal resolution and run to equilibrium, with the last 50 days of the simulations being averaged for statistics. Cloudy grid points were identified as those with cloud condensate mass fraction larger than 10^{-5} kg/kg.

Appendix B: Calculating detrainment

We calculate detrainment using the bulk-plume budget for a tracer that is conserved in cloudy air. This tracer is the "purity" tracer, ϕ (kg/kg), which is set to 1 below cloud base and to 0 in clear air that is some distance away from cloudy air in the free troposphere at every time step (Romps and Kuang 2010a,b). The steady-state budget for the value of this tracer in the convective plume, ϕ_c, is

$$\partial_z \phi_c = -\varepsilon \phi_c, \tag{6.4}$$

where $\varepsilon = E/M_c$ (m^{-1}) is the fractional entrainment rate. In (6.4), we have made the approximation that the mixing ratio of the purity tracer in environmental air, ϕ_e, is 0; this is guaranteed to be very nearly true by the zeroing-out of purity in non-cloudy air at every time step. We record ϕ_c as part of the statistics collected over the last 50 days of the RCE simulations, which allows us to quantify the steady-state entrainment rate: $E = \varepsilon M_c = -M_c \partial_z \phi_c / \phi_c$. Using the equation for mass continuity of the plume ($\partial_z M_c = E - D$), we can then solve for the detrainment rate:

$$D = -M_c \partial_z \phi_c / \phi_c - \partial_z M_c. \tag{6.5}$$

The profiles of detrainment obtained by this method are plotted in Figure 2c of the main text.

Appendix C: Longwave radiative cooling from water vapor

This section focuses on the longwave radiative cooling from water vapor. One piece of the theoretical support for the FAT hypothesis is the idea that the longwave radiative cooling from water vapor should decline rapidly at a particular temperature — a temperature that is reached in the upper troposphere of Earth's current tropics (Hartmann and Larson 2002; Larson and Hartmann 2003; Kuang and Hartmann 2007; Kubar et al. 2007; Xu et al. 2007; Eitzen et al. 2009; Zelinka and Hartmann 2010, 2011; Li et al. 2012; Harrop and Hartmann 2012; Thompson et al. 2017). This claim is based on the idea that longwave emissivity controls the amplitude of radiative cooling, and that radiative cooling must therefore decline rapidly with the exponentially-falling upper-tropospheric water-vapor concentrations.

This claim appears to be true if water vapor is assumed to be a gray gas (i.e., assumed to have an absorption coefficient that is independent of wavenumber). In Figure 6.6, we compare the longwave radiative cooling rates from our minimal-recipe RCE simulations as computed by a gray radiation scheme and by RRTM (Clough et al. 2005; Iacono et al. 2008).

We arbitrarily set the absorption coefficient κ of the gray scheme to 15 kg/m^2. (Changing this value changes the temperature at which radiative cooling peaks, but not the qualitative behavior.) In the gray scenario (Fig. 6.6a,b), radiative cooling is narrowly peaked around the altitude where the longwave optical depth (τ) equals 1 (Pierrehumbert 2010). This level occurs at an approximately fixed temperature because water vapor density in RCE is a nearly invariant function of temperature. As a result, radiative cooling in this scenario declines with height most rapidly at an approximately fixed temperature (roughly 225 K) that occurs on the cold side of the $\tau = 1$ level. Therefore, Statement 5 from the main text ("Clear-sky radiative cooling must decline most rapidly with height at a fixed temperature") would appear to be true if water vapor were a gray gas.

Of course, it is well-known that water vapor is not a gray gas. What are the implications of this non-gray physics for the shape of the radiative cooling profile? When radiative transfer is computed by RRTM (Fig. 6.6c,d), the longwave cooling from water vapor is spread out smoothly over the depth of the troposphere rather than being sharply peaked at one particular level. The longwave cooling computed by RRTM still collapses onto an approximately universal curve in temperature coordinates, as has been previously demonstrated and explained theoretically (Jeevanjee and Romps 2018). But, this invariant curve declines smoothly as a function of temperature in the bulk of the troposphere, with no especially rapid decline at any particular temperature.

The simplicity of this collapse of radiative cooling profiles is lost for other ways of plotting the cooling rate. For example, when the cooling rate is expressed as a temperature tendency (i.e., in units of K/day), one gets the impression that radiative cooling changes in a complex way as a function of surface temperature (Fig. 6.7). This is true whether the cooling rate is plotted with temperature, pressure, or altitude as the vertical coordinate (Fig. 6.7a,b,c, respectively).

Under what conditions, or in what sense, is there a rapid decline in radiative cooling at the top of the troposphere? The apparent sharpness of the top of the water-vapor cooling profile can be found in the literature going back decades (e.g., Manabe and Strickler 1964; Clough et al. 1992; Hartmann et al. 2001a). These results show radiative temperature tendencies (in K/day) as a function of pressure taking on an approximately fixed value throughout most of the troposphere and then dropping to zero over the course of 100 mb or so. However, our results indicate that such a shape depends on a particular choice of coordinates and only exists over a certain range of surface temperatures. In Figure 3a of the main text, we show that radiative heating rates expressed as W/m^3 (i.e., as flux divergences) decline smoothly over the depth of the troposphere, with no particularly rapid decline or kink at any particular temperature. If we convert to the unit of K/day and use pressure as a vertical coordinate (Figure 6.7b), we do reproduce the kinked shape for surface temperatures of 300 K or warmer, but for colder surface temperatures, the kink disappears.

To check that the disappearance of the kink is not an artifact of approximations in the RRTM radiative transfer scheme, we recalculated cooling rates with the line-by-line code RFM (Dudhia 2017). The line-by-line calculations use a spectral resolution of 0.25 cm^{-1} and the results are integrated over the wavenumber range 0.25–3000 cm^{-1} to yield total

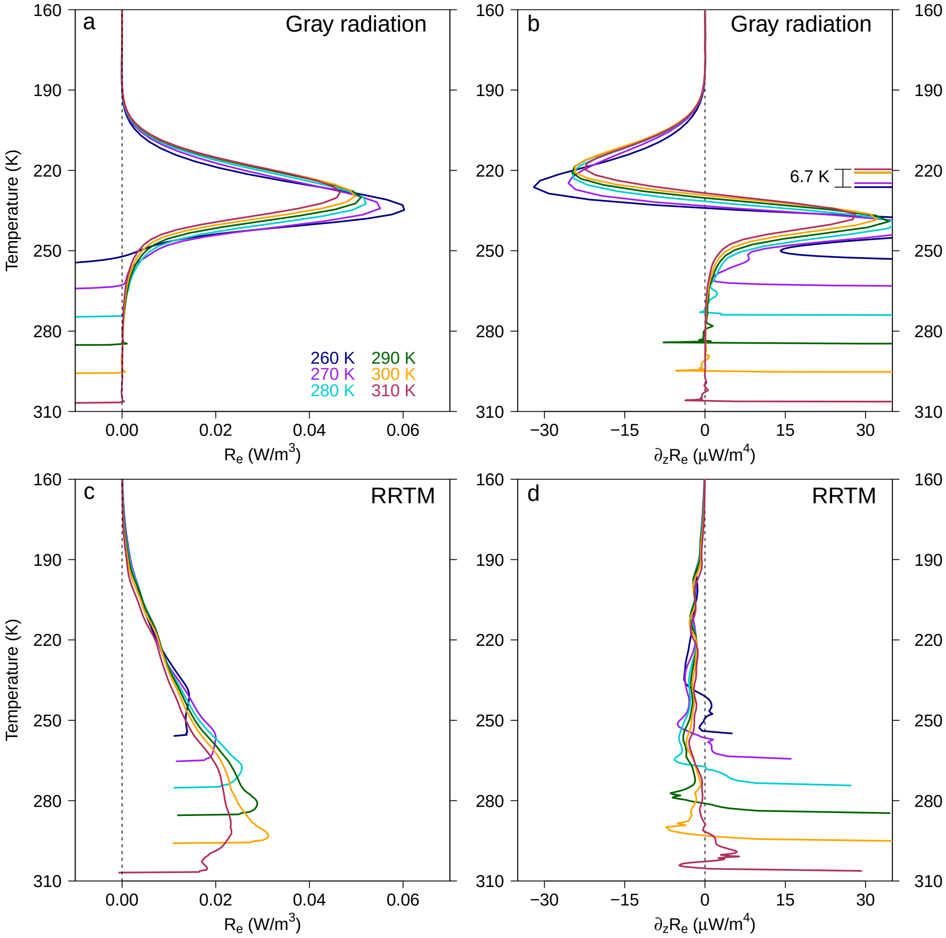

Figure 6.6: (a) Clear-sky longwave radiative cooling rates R_e (W/m^3, positive values for cooling) from the minimal-recipe RCE simulations as computed by a gray radiation scheme. (b) The rate of decline with height of the clear-sky longwave radiative cooling rate, $\partial_z R_e$, also from the gray scheme. (c,d) As in (a,b), but with radiative transfer computed by RRTM instead of the gray scheme. The surface temperature of each simulation is indicated by line color. In (b), the colored horizontal lines mark the temperatures at which radiative cooling declines most rapidly with height.

fluxes and cooling rates, and the two-stream approximation is used with a diffusivity factor of 1.66 to account for hemispheric integration. The results of the RFM calculations match the RRTM cooling profiles quite well, and reproduce the disappearance of the kink in radiative cooling at cooler surface temperatures.

Therefore, we can conclude that the ubiquity of the kinked shape of water-vapor cooling profiles in the literature derives from (a) the conventional choice of plotting coordinates, and (b) the exploration of a relatively small range of surface temperatures. However, since

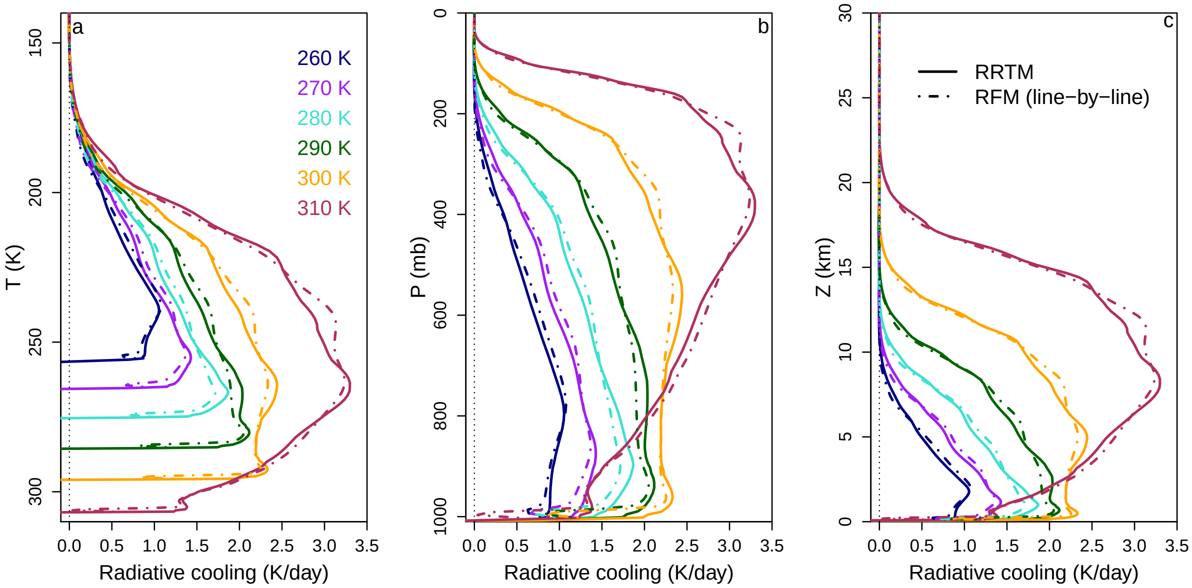

Figure 6.7: Clear-sky longwave radiative cooling from the minimal-recipe RCE simulations, expressed as a temperature tendency (K/day) and plotted as a function of (a) temperature, (b) pressure, and (c) altitude. The surface temperature of each simulation is indicated by line color. RRTM results are shown in solid lines, while RFM results are shown in dot-dashed lines.

extensive anvil clouds persist in all of our simulations, it seems erroneous to attribute them to a particular kinked shape of radiative cooling that only exists at surface temperatures similar to Earth's current tropics.

Chapter 7

Formation of tropical anvil clouds by slow evaporation

Tropical anvil clouds play a large role in Earth's radiation balance, but their effect on anthropogenic global warming is uncertain. The conventional paradigm for these clouds attributes their existence to the rapidly-declining convective mass flux below the tropopause, which implies a large source of detraining cloudy air there. Here, we test this paradigm by manipulating the sources and sinks of cloudy air in cloud-resolving simulations. We find that the anvil clouds in our simulations form because of the long lifetime of cloud condensates in the upper troposphere, not because of an enhanced source of cloudy air below the tropopause. We further show that cloud lifetimes are long in the cold upper troposphere because the saturation specific humidity is much smaller there than the typical condensed water loading of cloud updrafts, which causes evaporative cloud decay to act very slowly. Our results highlight the need for novel cloud-fraction schemes that align with this new decay-centric framework for anvil clouds.

7.1 Introduction

The cloudiest part of the tropical atmosphere is the upper troposphere (Figure 7.1). The production of this abundant high cloud can be observed during the life cycle of a single cumulonimbus: the cloudiness reaches the greatest radius in the upper troposphere, causing the cumulonimbus to resemble a blacksmith's anvil. For this reason, the extensive high clouds are referred to as anvil clouds.

Tropical anvil clouds play a large role in Earth's radiation balance by reflecting sunlight and throttling the flow of terrestrial radiation to space (Hartmann et al. 2001b; Boucher et al. 2013). However, the effect of anvil clouds on anthropogenic global warming is uncertain. One

---

[1] This chapter is a slightly edited version of Seeley et al. (2018a).

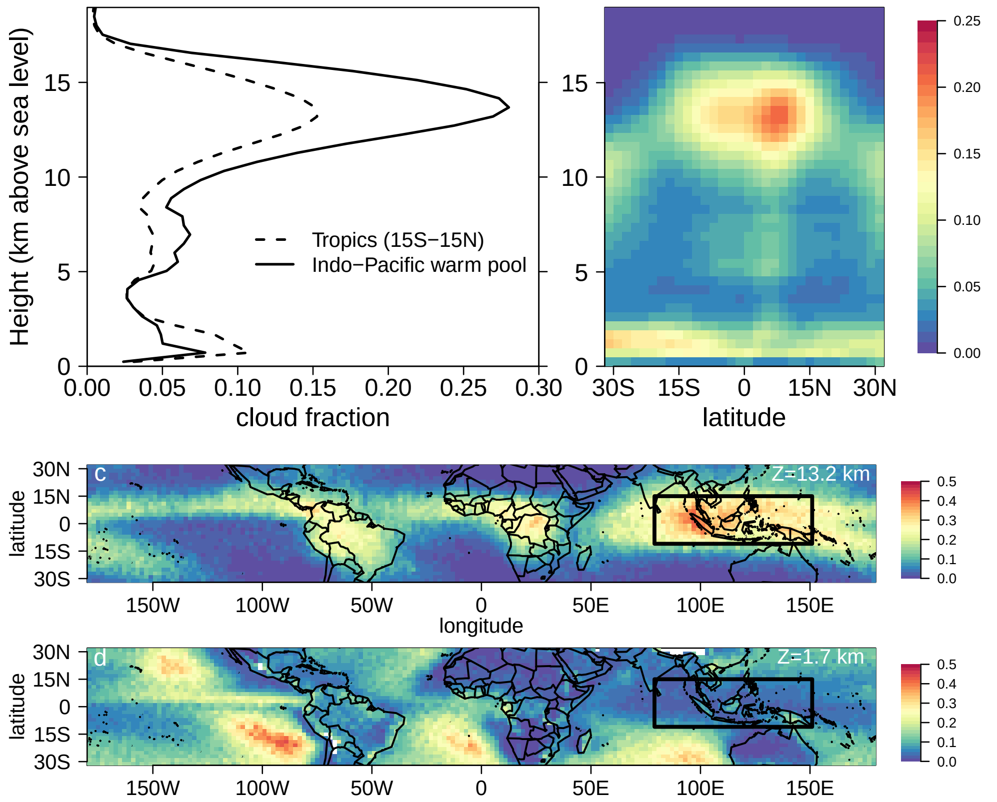

Figure 7.1: Cloud fraction from the GCM-Oriented Cloud-Aerosol Lidar and Infrared Pathfinder Satellite Observation (CALIPSO) Cloud Product (GOCCP) (Chepfer et al. 2010), averaged from 2008–2012 and plotted (a) as a function of altitude; (b) as a function of latitude and altitude (zonal average); as a function of latitude and longitude at (c) an altitude of 13.2 km and (d) an altitude of 1.7 km. In (a), the cloud fraction for the Indo-Pacific warm pool is obtained by averaging within the black boxes in panels (c) and (d). In (d), grid cells with surface topography higher than 1.7 km are left blank.

suggestion — known as the iris hypothesis — posits that anvil clouds shrink as the surface warms, thereby acting as a negative feedback on warming by allowing the surface to more easily emit radiation to space (Lindzen et al. 2001; Hartmann and Michelsen 2002; Lin et al. 2002; Mauritsen and Stevens 2015). Another idea is the Fixed Anvil Temperature (FAT) hypothesis, which proposes that anvil clouds will rise with warming so as to remain at a fixed temperature, thereby acting as a positive feedback (Hartmann and Larson 2002; Kuang and Hartmann 2007). Before we can assess these and any other potential anvil-radiative feedbacks, we must first understand the basic physical processes that produce anvil clouds.

The central question addressed in this chapter is: Why do cumulonimbus clouds resemble anvils? Or, phrased another way, why does tropical cloud fraction peak in the upper troposphere? One potential explanation is that tropospheric radiative cooling decreases to zero at the tropopause. Since convective heating is required to balance this radiative cooling, clouds must rise through most of the troposphere and then cease rising in the upper troposphere. As the argument goes, the pileup of mass as the clouds come to a halt causes the cloudy air to spread out laterally, forming the peak in cloud fraction below the tropopause. This explanation for anvil clouds has become the conventional view (Boucher et al. 2013). This paradigm is typically described in terms of clear-sky convergence (Hartmann and Larson 2002; Kuang and Hartmann 2007; Kubar et al. 2007; Zelinka and Hartmann 2010, 2011; Harrop and Hartmann 2012; Li et al. 2012; Bony et al. 2016; Hartmann 2016; Thompson et al. 2017), and is formalized mathematically by:

$$\mathcal{C} = \max\left(0, -\frac{1}{\rho}\frac{\partial M}{\partial z}\right)\tau_0. \tag{7.1}$$

Here, $\mathcal{C}$ is the cloud fraction, M is the convective mass flux (units of kg/m^2/s), and τ_0 is a constant timescale (units of s) that quantifies the lifetime of cloudy air. Since τ_0 is independent of height, cloud sinks play no role in shaping the cloud-fraction profile predicted by this clear-sky convergence (CSC) paradigm. According to the CSC paradigm, $\mathcal{C}$ maximizes in the upper troposphere because that is where clear-sky convergence, equal to $-(1/\rho)\partial M/\partial z$, is greatest.

7.2 Testing the clear-sky convergence paradigm

To assess the CSC paradigm, we use cloud-resolving simulations of tropical convection in radiative-convective equilibrium (RCE), which are well-suited to studying anvil clouds (Kuang and Hartmann 2007; Harrop and Hartmann 2012, 2016). We begin by examining the DEFAULT simulation, which is run at relatively high resolution, includes cloud-radiative interactions, and uses a realistic microphysics scheme that accounts for ice processes (Table 1). Further simulation details are provided in Appendix A.

Figure 7.2a shows the CSC paradigm's predictions for the DEFAULT simulation. This paradigm predicts an anvil peak in approximately the right location, but also predicts the largest overall cloud fraction in the lower troposphere, which disagrees with the simulation, and predicts an additional prominent mid-tropospheric peak in cloud fraction that does not exist in the CRM.

These faulty predictions can be traced back to two potential sources of error in the CSC paradigm. First, since cloudy updrafts entrain clear air as they rise through the troposphere, clear-sky convergence only puts a lower bound on the correct source term for cloudy air (e.g., Yanai et al. 1973). The correct source is the volumetric detrainment of cloud, $D/\rho = \delta M/\rho$, where δ is the bulk-plume fractional detrainment rate.

experiment	Δx	Δz	Δt	**microphysics**	**radiation**
DEFAULT	200 m	100 m	5 s	LLK	all-sky RRTM
DEFAULT_CLR	200 m	100 m	5 s	LLK	clear-sky RRTM
CTRL	2 km	250 m	20 s	simple	clear-sky RRTM
NOEVAP	2 km	250 m	20 s	simple, no evap.	prescribed
NOPEAK	2 km	250 m	20 s	simple	prescribed
LOPEAK	2 km	250 m	20 s	simple	prescribed

Table 7.1: CRM experiment configurations. Δz refers to the free-tropospheric vertical grid spacing. “LLK" microphysics refers to DAM’s default Lin-Lord-Krueger scheme (Lin et al. 1983; Lord et al. 1984; Krueger et al. 1995). The “simple” microphysics is a Kessler-type scheme based on an autoconversion timescale (Kessler 1969) described in more detail in the main text.

The second potential source of error is that cloud lifetimes may not be independent of height, as the CSC paradigm assumes. To assess the validity of the constant-lifetime assumption, we first used the water budget to diagnose the volumetric detrainment in the DEFAULT simulation. Cloudy grid cells were identified as those in which $q_c \geq 10^{-5}$ kg/kg, where q_c is the mass fraction of non-precipitating cloud condensate (this threshold was adopted from previous work, e.g. Kuang and Hartmann (2007)). We further divided cloudy air into “updraft” and “inactive” categories with a vertical velocity threshold (Appendix A). Denoting the mean condensate loading of cloudy updrafts as q_{c0}, the evaporation/sublimation rate as e and the conversion rate of cloud condensate to precipitating water as p (both with units of kg/m^3/s, averaged in time and over all non-updraft cloudy grid cells), the steady-state cloud-water budget for inactive air is

$$\delta M q_{c0} = e + p. \tag{7.2}$$

We recorded profiles of M, q_{c0}, e, and p as part of the statistics from our simulations, so that all terms in equation 7.2 except for δ are directly measured from the simulation. This allows us to diagnose the volumetric detrainment, $\delta M/\rho$. The actual cloud-lifetime profile, τ_{actual}, can then be inferred by dividing the cloud fraction by this source term.

The results of this procedure are shown in Figure 7.2b. The volumetric detrainment profile in the DEFAULT simulation has a broad resemblance to the clear-sky convergence profile, but is significantly larger in magnitude and does not go to zero except at the bottom and top of the convecting troposphere. We note that the volumetric detrainment bears little resemblance to a blacksmith’s anvil: the actual source term for cloudy air maximizes in the lower troposphere, and only varies by a factor of about 3 over the bulk of the troposphere. Therefore, the shape of the source term does not explain the top-heaviness of the cloud-fraction profile in this simulation.

The inferred cloud-lifetime profile, on the other hand, is very top-heavy. Whereas τ_{actual} hovers between 5–15 minutes at altitudes below 7 km, in the upper troposphere it grows to almost 4 hours, which is an increase of more than an order of magnitude. Therefore, the

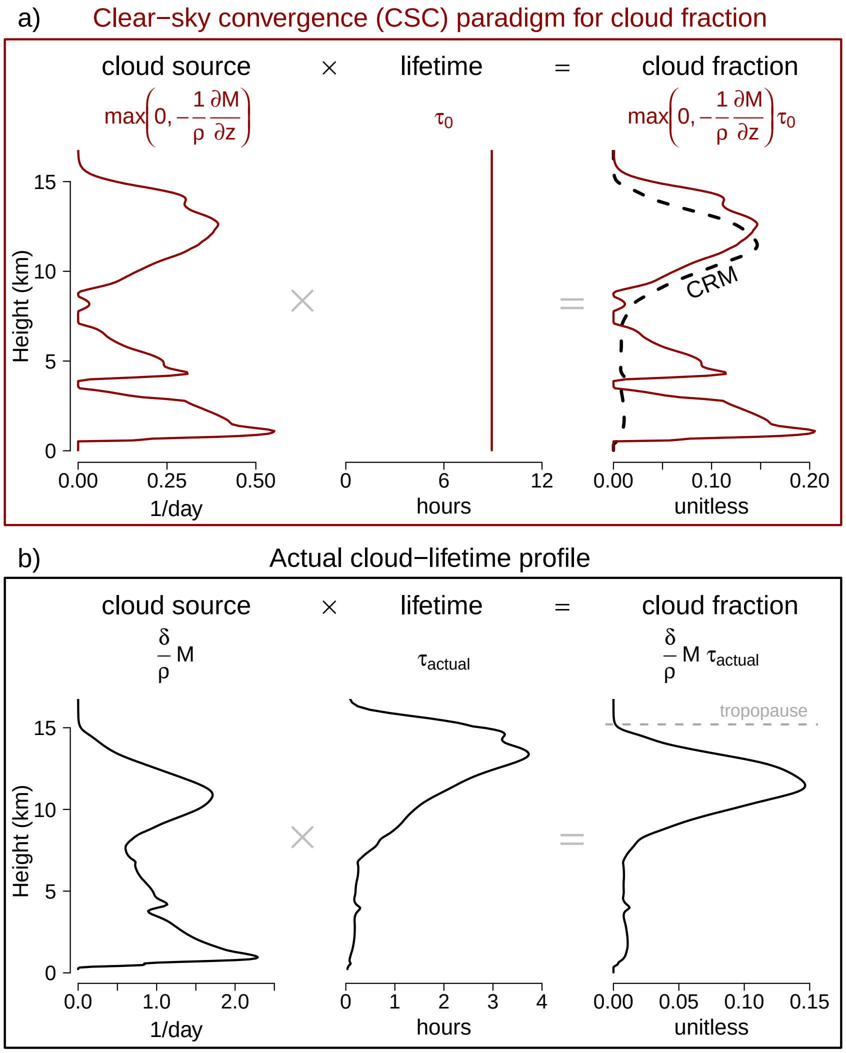

Figure 7.2: (a) The three columns inside the dark red box show how the CSC paradigm predicts cloud fraction: by taking the product of a source term (clear-sky convergence) and a vertically-uniform timescale, τ_0 (set here to 8.9 hours to obtain the best fit with the magnitude of upper-tropospheric cloud fraction). The dotted black line in the third column shows the actual time-mean cloud fraction from the CRM experiment (with the contribution from updrafts removed). (b) The three columns inside the black box show how the correct source term (the volumetric detrainment) multiplied by the actual cloud-lifetime profile (τ_{actual}) yields the cloud fraction. The tropopause is marked with a dashed gray line in the bottom-right panel.

increase in cloud lifetimes in the upper troposphere is fundamental to understanding why the cloud-fraction profile in our simulation resembles a blacksmith's anvil.

7.3 Cloud sinks shape the cloud-fraction profile

Why are cloud lifetimes so top-heavy? To answer this question, we conducted additional RCE simulations with a simplified configuration of the CRM (Table 7.2; Appendix A). The most salient aspect of the simplified CRM configuration is that microphysics was treated with a Kessler-type scheme (Kessler 1969) in order to facilitate a quantitative analysis of cloud sinks. There is no explicit ice phase in this scheme, so the only classes of water are vapor, non-precipitating cloud condensate, and precipitation (with mass fractions q_v, q_c, and q_p, respectively). Other than the condensation and evaporation that occur during saturation adjustment, the only microphysical process included in this scheme is autoconversion of cloud condensate to precipitation, which is parameterized as

$$a = -q_c/\tau_a, \tag{7.3}$$

where a (s^{-1}) is the sink of cloud condensate from autoconversion and τ_a (s) is an autoconversion timescale that we set to 75 minutes in inactive cloudy air. Despite its simplicity, the standard version of this simplified configuration (CTRL) reproduces the key features of the DEFAULT simulation: the anvil-shaped cloud fraction profile, the bottom-heavy source term, and the top-heavy cloud-lifetime profile (Figure 7.14). The similarity between the DEFAULT and CTRL simulations suggests that the basic physics of anvil clouds do not involve the details of ice microphysics, despite the fact that in nature these clouds are composed of ice crystals.

To illuminate the role of cloud sinks in shaping the cloud-fraction profile, we re-ran the CTRL simulation with evaporation of cloud condensate artificially prevented (the NOEVAP experiment, in which precipitation is the only microphysical sink of cloud water; Appendix A). Figure 7.3 shows the result: preventing evaporation of cloud condensate strongly increases cloud fraction in the lower troposphere, but has only a modest effect on cloud fraction in the upper troposphere. This stark contrast is a result of Clausius-Clapeyron: very little condensed water can evaporate into subsaturated air at cold temperatures, so precipitation *already* serves as the dominant pathway for cloud decay in the upper troposphere even when evaporation is turned on. (Here and throughout, we use the term "evaporation" to refer to both evaporation and sublimation, and we use "precipitation" to refer to both precipitation and sedimentation.) On the other hand, the warmer temperatures of the lower troposphere ordinarily lead to fast evaporation of detrained cloud condensate, which allows for a large increase in cloud fraction when evaporation is prevented. The NOEVAP experiment shows that if clouds at all altitudes were forced to decay in the manner of upper-tropospheric clouds — that is, by precipitating out, rather than evaporating — cloud fraction would be bottom-heavy rather than top-heavy in our simulations.

7.4 Analytical model of cloud decay

Since the vertically-varying sinks of cloudy air play a leading role in shaping the cloud-fraction profile in our simulations, a viable theory for anvil clouds must account for how cloud

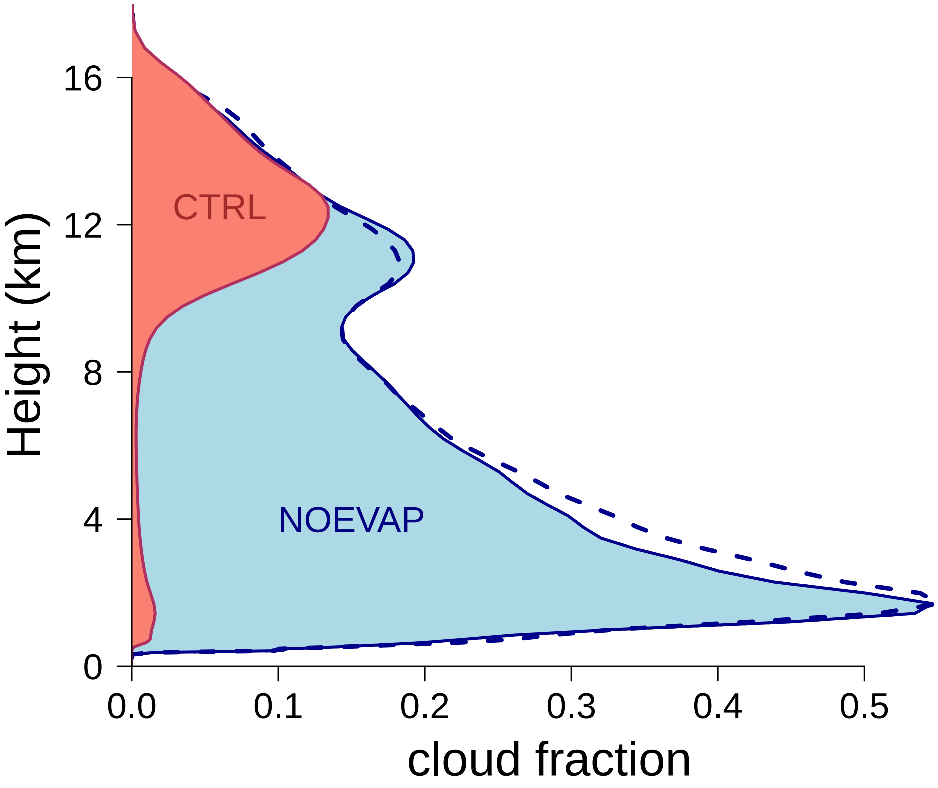

Figure 7.3: Cloud fraction from the CTRL and NOEVAP experiments (solid lines with colored shading). In NOEVAP, evaporation of cloud condensate is prevented while holding environmental relative humidity and detrainment fixed from CTRL as described in Appendix A. The dashed blue line shows the cloud fraction predicted for the NOEVAP experiment by the new framework for anvil clouds. Because of the large cloud fraction in the lower troposphere of NOEVAP, the version of the new framework that accounts for cloud overlap (equation 7.25) is used here.

lifetimes change over the depth of the troposphere. Here we derive an analytical model for cloud lifetimes that incorporates the physics of evaporation, dilution, and precipitation as sinks of cloud condensate.

Consider a cylindrical cloud with initial radius r_0 and constant height h. We assume the cloud is initially filled with turbulence with a uniform eddy velocity of v_0, and that the cloud's boundary r expands radially outward at a rate proportional to the cloud's internal eddy velocity v with constant of proportionality c. For a quiescent environment and in the limit of no dissipation, the cloud conserves its kinetic energy as it grows, which implies that the product rv is constant in time and that the cloud's area A grows linearly in time:

$$A(t) = A_0\left(1 + t/\kappa\right), \tag{7.4}$$

where $A_0 = \pi r_0^2$ is the cloud's initial area and $\kappa \equiv r_0/(2cv_0)$ is a constant with dimensions of time. κ can be interpreted as the amount of time it takes the cloud to grow in area by an amount equal to its initial area A_0. We treat κ as a tuning parameter (Appendix B), which is set to 19 minutes for all figures in the main text.

To determine the lifetime of the cloud, we use its bulk water budget (i.e., the cloud's properties are assumed to be homogeneous). We will first model a cloud whose only sink of condensed water is from mixing with environmental air, and then add the effects of precipitation. Initially, the cloud has total water mass fraction $q_t = q_{c0} + q_v^*$, while the cloud's environment has total water $\mathrm{RH}q_v^*$, where RH is the environmental relative humidity and q_v^* is the saturation specific humidity. Therefore, under the influence of mixing, the cloud's q_t evolves in time according to

$$\frac{dq_t}{dt} = -\left(\frac{1}{\kappa + t}\right)\left[q_c(t) + q_v^*(1 - \mathrm{RH})\right]. \tag{7.5}$$

As long as the cloud is saturated, its vapor mass fraction is pegged at the saturation value q_v^*, and equation 7.5 is really the governing equation for the cloud's condensed water q_c. The solution is analytic, and since we define cloudy air as having $q_c \geq 10^{-5}$ kg/kg, we can set $q_c(t) = 10^{-5}$ to solve for the "mixing-only" lifetime of the cloud, $\tilde{\tau}_{\mathrm{mix}}$:

$$\tilde{\tau}_{\mathrm{mix}} = \kappa \chi_c, \tag{7.6}$$

where

$$\chi_c \equiv \frac{q_{c0} - 10^{-5}}{q_v^*(1 - \mathrm{RH}) + 10^{-5}}. \tag{7.7}$$

χ_c is a very important parameter in cloud decay physics, because it measures the efficiency with which mixing causes cloudy air to decay: if one part of cloudy air with an initial condensate loading of q_{c0} mixes with χ_c parts of environmental air with a saturation deficit of $q_v^*(1-\mathrm{RH})$, the cloudy parcel will become clear. We will see that χ_c is key to understanding the top-heaviness of cloud-fraction profiles in our simulations.

So far, we have neglected an important sink of cloud condensate in decaying clouds: precipitation. If precipitation (parameterized by equation 7.3, in accordance with our simulations) were the only process causing the cloud to decay, its lifetime would be given by:

$$\tilde{\tau}_{\mathrm{precip}} = \tau_a \log\left(q_{c0}/10^{-5}\right). \tag{7.8}$$

Combining the effects of precipitation and mixing, then, equation 7.5 is modified to

$$\frac{dq_t}{dt} = -\left(\frac{1}{\kappa + t}\right)\left[q_c(t) + q_v^*(1 - \mathrm{RH})\right] - q_c(t)/\tau_a, \tag{7.9}$$

which again yields an analytic solution for $q_c(t)$. The new expression for the cloud's lifetime

$\tilde{\tau}_{\text{new}}$ is:

$$\tilde{\tau}_{\text{new}} = \tau_a \left[W\left(ae^b\right) - b \right]; \tag{7.10a}$$

$$a = \frac{\kappa}{\tau_a}\left(\frac{q_{c0}}{10^{-5}}\right) + \frac{q_v^*(1-\text{RH})}{10^{-5}}; \tag{7.10b}$$

$$b = \frac{\kappa}{\tau_a} + \frac{q_v^*(1-\text{RH})}{10^{-5}}, \tag{7.10c}$$

where W is the Lambert W function.

For cloud fraction, what matters is not just the lifetime of the decaying cloud but its time-integrated area. Therefore, it is convenient to define an "effective lifetime", τ, such that a cloud that has constant area of A_0 during a lifetime of length τ would produce the same time-integrated cloud fraction as a cloud that grows as it decays for a lifetime of $\tilde{\tau}$:

$$\tau = \int_0^{\tilde{\tau}} \frac{A(t)}{A_0}\, dt. \tag{7.11}$$

For mixing-induced decay, the effective lifetime is therefore

$$\tau_{\text{mix}} = \kappa\left(\chi_c + \frac{\chi_c^2}{2}\right). \tag{7.12}$$

The effective lifetime for precipitation-only decay is already given by equation 7.8 since such a cloud decays in place, while the effective lifetime for mixing and precipitation combined is

$$\tau_{\text{new}} = \tilde{\tau}_{\text{new}} + \frac{\tilde{\tau}_{\text{new}}^2}{2\kappa}. \tag{7.13}$$

Equation 7.13, with $\tilde{\tau}_{\text{new}}$ given by equations 7.10, is an analytical expression for the effective lifetime of a cloud as a function of its initial condensed water q_{c0}, environmental saturation deficit $q_v^*(1-\text{RH})$, mixing timescale κ, and precipitation timescale τ_{a}.

7.5 Cloud lifetimes are top-heavy due to slow evaporation

The analytical model of cloud decay presented in the previous section allows us to understand why cloud lifetimes are top-heavy. In Figure 7.4a, we plot χ_c from the CTRL experiment. In the lower troposphere, $\chi_c < 1$, and mixing easily evaporates cloudy air. In the upper troposphere, however, the updraft-mean condensate loading q_{c0} becomes much larger than the environmental saturation deficit $q_v^*(1-\text{RH})$, and $\chi_c \gg 1$. This "mismatch" between the amount of condensed water delivered by clouds and the ability of the environment to absorb it can occur because updraft condensate loading is not constrained by the local environmental temperature — unlike the saturation deficit, which must decline exponentially with decreasing temperature due to Clausius-Clapeyron. As a consequence, when upper-tropospheric clouds mix with environmental air, they can easily bring that environmental air to saturation with plenty of cloud condensate to spare. This greatly enhances the time-integrated area of decaying clouds in the upper troposphere.

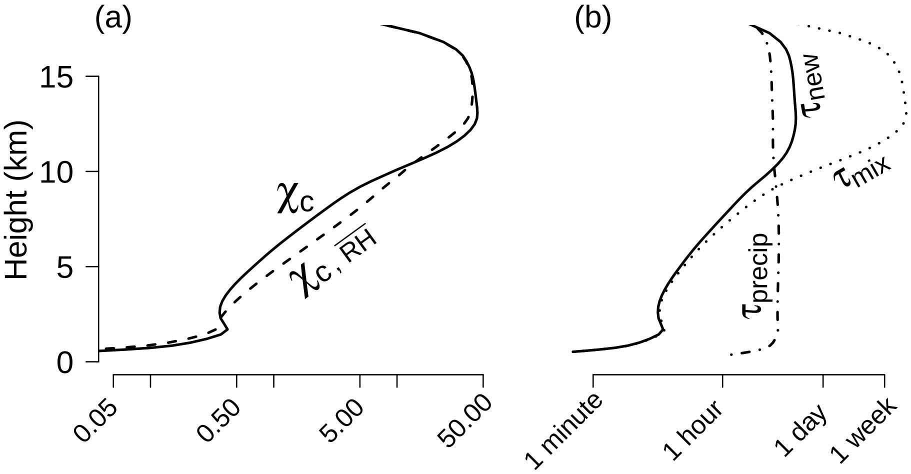

Figure 7.4: (a) The profile of χ_c from the CTRL experiment (eqn. 7.7). χ_c gives the number of parts of environmental air with which one part of cloudy air must mix in order to become clear. The dashed line shows χ_c calculated with relative humidity (RH) set to its tropospheric-mean, $\overline{\text{RH}}$. (b) From the CTRL experiment, effective cloud lifetimes from mixing and precipitation considered individually (τ_{mix} and τ_{precip}, eqns. 7.12 and 7.8) and in combination (τ_{new}, equation 7.13).

Although the saturation deficit is given by $q_v^*(1 - \text{RH})$, it is important to note that the profile of χ_c is driven by q_v^*, not vertical variations in RH. The dashed curve in Figure 7.4a shows χ_c calculated with RH set to its tropospheric mean. Clearly, the growth in χ_c with height is caused by the rapid exponential decay of q_v^*, not the relatively high RH of the upper troposphere.

The efficiency of mixing-induced decay is a key determinant of a cloud's lifetime. In Figure 7.4b, we plot the effective cloud lifetime from mixing alone, τ_{mix}. Because of the dependence of τ_{mix} on χ_c (equation 7.12), effective cloud lifetimes due to mixing are extremely top-heavy, ranging from only a few minutes in the lower troposphere to over 1 week in the upper troposphere. Also plotted in Figure 7.4b is the effective cloud lifetime due to precipitation alone, τ_{precip} (equation 7.8). Unlike the top-heavy τ_{mix}, τ_{precip} is roughly constant throughout the bulk of the troposphere.

The analytical expression for τ_{new} (equation 7.13) combines the physics of mixing and precipitation. Therefore, τ_{new} is driven to large values in the upper troposphere by the ballooning of τ_{mix} (Figure 7.4b). Note, however, that the largest upper-tropospheric values of τ_{mix} significantly exceed τ_{new} there, because actual cloud lifetimes are limited by precipitation even in the limit of no evaporation. Indeed, Figure 7.4 shows that the decay pathway for clouds transitions from a fast, mixing-dominated regime in the lower troposphere ($\tau_{\text{new}} \simeq \tau_{\text{mix}}$) to a slower, precipitation-dominated regime in the upper troposphere ($\tau_{\text{new}} \simeq \tau_{\text{precip}}$). This is further confirmed by comparing the microphysical sinks of cloud condensate averaged over decaying clouds: in both DEFAULT and CTRL, evaporation far outweighs precipitation as a sink in the lower troposphere, whereas precipitation dominates at the anvil level (Figure 7.15). Although the analytical model is highly idealized, results from a more complex model of cloud decay that numerically solves the diffusion equation are nearly identical to the analytical theory (Appendix C, Figure 7.11).

7.6 A new framework for anvil clouds

Putting the effective lifetime predicted by the analytical model of cloud decay together with the correct source term for cloudy air yields the “new framework" for anvil clouds:

$$\mathcal{C} = \frac{\delta M}{\rho}\tau_{\text{new}}. \tag{7.14}$$

Equation 7.14 is the first-order Taylor-expansion of a more general equation for cloud fraction that acounts for overlap between clouds (Appendix D); to prevent the unphysical result of cloud fraction that exceeds 1, the more general equation should be used when cloud fraction is not small compared to 1 (as in the lower troposphere of the NOEVAP experiment shown in Figure 7.3).

In the top row of Figure 7.5, we compare the performance of the CSC paradigm and the new framework in the CTRL experiment. As in the DEFAULT experiment, the CSC paradigm predicts the largest cloud fraction in the lower troposphere. On the other hand, the new framework correctly places the anvil peak in the upper troposphere. The new framework predicts the top-heavy shape of the cloud-fraction profile even though the source term (the volumetric detrainment, diagnosed from the water budget) maximizes in the lower troposphere. It is the ballooning of cloud lifetimes in the upper troposphere — which is predicted by the analytical expression for τ_{new} — that causes the large peak in cloud fraction there in the CTRL experiment.

When cloud evaporation is prevented, as in the NOEVAP experiment, this key difference between the lower and upper troposphere is erased. With no retuning of parameters, the new framework accurately predicts the bottom-heavy cloud-fraction profile of the NOEVAP experiment (dashed blue line, Figure 7.3; in the new framework, evaporation is prevented by setting the environmental RH to 1 in the analytical expression for cloud lifetimes.) Without fast evaporation of condensates in the lower troposphere, cloud lifetimes only vary by a factor of about 2 over the bulk of the troposphere (Figure 7.11) — causing cloud fraction to peak in the lower troposphere, where there is the most detrainment.

Figure 7.5 also shows results from two experiments in which the radiative-cooling profiles were modified to produce different clear-sky convergence profiles (the NOPEAK and LOPEAK experiments; Appendix A). In the NOPEAK experiment, the clear-sky conver-

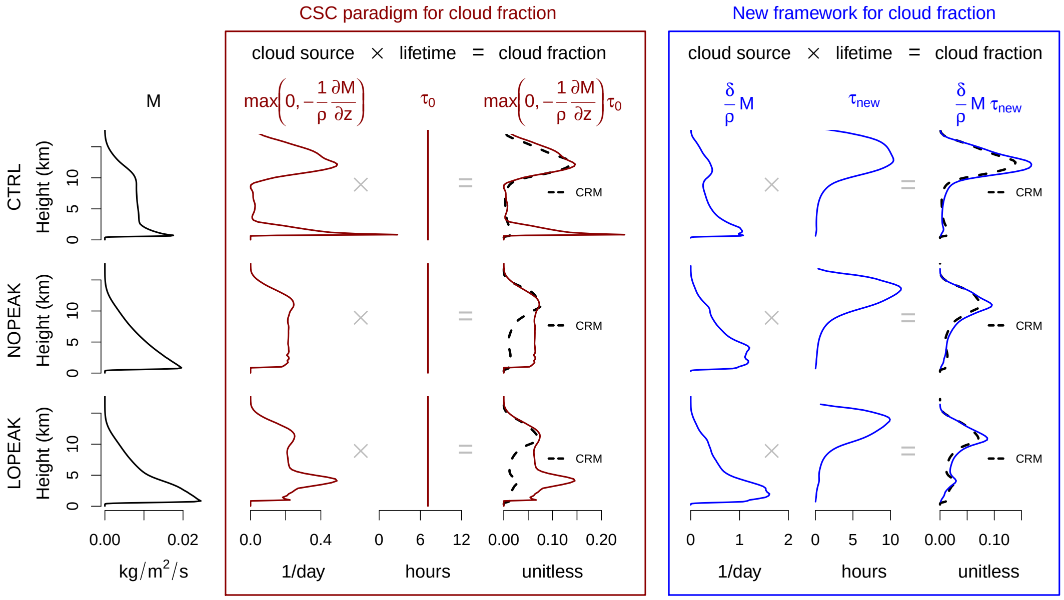

Figure 7.5: Comparison of the CSC paradigm and the new framework for anvil clouds (red and blue boxes, respectively). The three rows correspond to the three experiments (CTRL, NOPEAK, and LOPEAK, respectively). In each row, the first column shows the convective updraft mass flux M. The next three columns, color-coded in dark red, show how the CSC paradigm for anvil clouds predicts cloud fraction (fourth column) as the product of a source term (clear-sky convergence, second column) times a vertically-uniform timescale, τ_0 (third column). The final three columns, color-coded in blue, likewise show how the new framework for anvil clouds predicts cloud fraction (seventh column) as the product of a source term (the volumetric detrainment, fifth column) times an analytic expression for cloud lifetime τ_{new} that varies with height (sixth column). The dotted black lines in the fourth and seventh columns show the actual cloud fraction from the CRM experiment (with the contribution from active updrafts removed).

gence profile has no peaks. The CSC paradigm, therefore, predicts no peak in cloud fraction for this experiment, but the CRM results show that the anvil peak remains (middle row of Figure 7.5). In the LOPEAK experiment, the clear-sky convergence peaks in the lower troposphere, which causes the CSC paradigm to predict the largest cloud fraction in the lower troposphere, coincident with the most rapid vertical variation in M. But, this is incorrect: the anvil peak remains in the upper troposphere (bottom row of Figure 7.5). The new framework explains the results of both experiments: the anvil clouds are not due to a peak in cloud source, but to the peak in effective cloud lifetimes in the upper troposphere. The new framework can also accurately predict cloud fraction in the DEFAULT experiment (Appendix E, Figures 7.12–7.13).

7.7 Discussion

Are there other potential explanations for anvil clouds besides that offered by the new framework? One could argue that the anomalously high relative humidity of the upper troposphere (e.g., Romps 2014) slows the evaporation of clouds, leading to a peak in cloud fraction there. However, Figure 7.6a shows that the vertical variation in RH makes only a minor contribution to the top-heaviness of mixing-induced cloud lifetimes. One might also argue that adiabatic compressional heating due to compensating subsidence evaporates clouds in the middle and lower troposphere, but is too weak in the upper troposphere to evaporate the clouds. The cloud lifetime due to subsidence heating is given by

$$\tau_{\text{subside}} = \frac{1}{w_{\text{subside}}} \left(\frac{q_{c0} - 10^{-5}}{\partial_z q_v^*} \right), \tag{7.15}$$

where w_{subside} is the environmental subsidence velocity, approximately given by $-M/\rho$ since the area fraction of cloudy updrafts is very nearly 0. However, Figure 7.6b shows that τ_{subside} is more than an order of magnitude larger than τ_{new}, and so is irrelevant. Another potential explanation for anvil clouds is that active cloud updrafts may slow down and bunch up as they approach the tropopause, leading to a large cloud fraction. To the contrary, however, Figure 7.6c shows that the area occupied by updrafts themselves is negligible above the boundary layer.

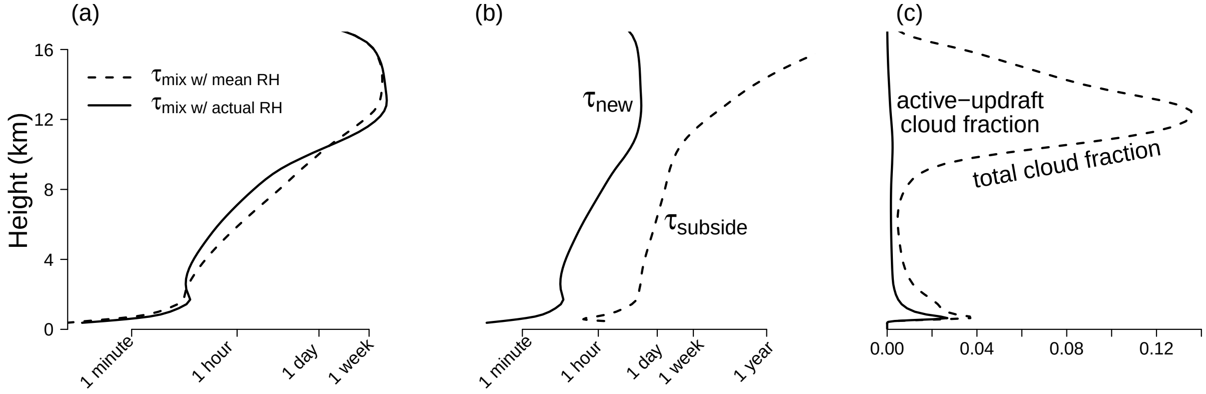

Figure 7.6: (a) From the CTRL experiment, the effective cloud lifetime from mixing-induced decay alone, τ_{mix} (i.e., neglecting precipitation as a sink of cloud condensate; eqn. 7.12), both with the actual environmental RH from the simulation and with RH set to its tropospheric mean. (b) Effective cloud lifetime τ_{new} compared to τ_{subside}. (c) Total cloud fraction from the CTRL experiment compared to the area occupied by active updrafts alone.

Finally, one might attribute the long lifetime of cloud condensates in the upper troposphere not to slow evaporation, but to the radiative heating gradients within upper-tropospheric clouds, which are known to drive intra-cloud circulations (Harrop and Hartmann 2016; Schmidt and Garrett 2013). However, using a simulation in which clouds are rendered invisible to radiation (DEFAULT_CLR; Appendix A and Figure 7.16), we show that these cloud-radiative interactions have a minor impact in our simulations.

Taken all together, our results show that the formation of tropical anvil clouds in our simulations — that is, the top-heavy profile of cloud fraction that resembles a blacksmith's anvil — is fundamentally due to the slow evaporation of cloud condensates in the upper troposphere. This highlights the importance of correctly parameterizing the sinks of cloud condensate in global climate models (GCMs). Most GCMs do not account for vertically-varying cloud sinks in their computation of cloud fraction; for example, the most common type of cloud-fraction parameterization used in current-generation GCMs is based on relative humidity alone (Tompkins 2005; Geoffroy et al. 2017), which we have shown has little to do with the anvil peak. This common modeling practice, when applied to our simulations, would produce an anvil peak in the upper troposphere — but not for the right reason. Since anvil clouds provide potentially large climate feedbacks, the community should focus on developing parameterizations of cloud fraction that capture the physics of cloud decay as identified in this chapter. Such schemes might be trusted to predict changes in cloud fraction with global warming and to determine whether anvil clouds produce a positive or negative radiative feedback.

Appendix A: Cloud-resolving model experiments

The cloud-resolving model (CRM) used in this chapter is DAM, a three-dimensional, fully-compressible, nonhydrostatic CRM (Romps 2008). All simulations were conducted on a square domain with a side length of 64 km and doubly periodic horizontal boundaries. Horizontal-mean winds were damped to zero on a time scale of six hours. The SST was fixed at 300 K for all simulations and surface fluxes were computed via a standard bulk aerodynamic formula.

In all simulations, cloudy grid cells were identified as those in which $q_c \geq 10^{-5}$ kg/kg, where q_c is the mass fraction of non-precipitating cloud condensate. We further divide cloudy air into "updraft" and "inactive" categories with a vertical velocity threshold: cloudy updrafts have $w \geq w_0(z)$, while inactive cloudy air has $w < w_0(z)$. The threshold w_0 ramps up linearly in altitude from 10^{-5} m/s at an altitude of 500 m to a constant of 2 m/s at altitudes above 3 km.

For the DEFAULT and DEFAULT_CLR simulations, the horizontal resolution was 200 m, and the vertical grid spacing increased from 50 m in the boundary layer to a constant 100 m spacing for altitudes between 2 km and 16 km, and increased again to 1 km between 24 km and the model top at 30 km. The time step was 5 s, which was sub-stepped to satisfy a CFL condition. These simulations were restarted from equilibrated lower-resolution simulations and run to statistical equilibrium, after which statistics were collected over 10 days of model time. All figures in this manuscript based on these experiments are made from data that were averaged over this equilibrated 10-day period.

The microphysics scheme for these simulations was DAM's default six-class Lin-Lord-Krueger scheme (Lin et al. 1983; Lord et al. 1984; Krueger et al. 1995). The Lin-Lord-Krueger scheme includes parameterizations for 28 different ice- and liquid-water microphysical processes.

These simulations were forced by radiative transfer as computed by RRTM (Clough et al. 2005; Iacono et al. 2008), using a trace gas profile with no ozone and a constant volume mixing ratio of 280 ppmv CO_2. For DEFAULT, the effect of cloud liquid and ice condensate on radiative transfer was included, while for DEFAULT_CLR, these effects were removed.

For the CTRL, NOEVAP, NOPEAK, and LOPEAK experiments, the horizontal resolution was 2 km, and the vertical grid spacing increased from 50 m in the boundary layer to a constant 250 m spacing for altitudes between 2 km and 16 km, and increased again to 1 km between 22 km and the model top at 30 km. The time step was 20 s, which was substepped to satisfy a CFL condition. The CTRL experiment was forced by clear-sky radiative transfer computed by RRTM, while the NOEVAP, NOPEAK, and LOPEAK experiments were forced by prescribed radiative cooling profiles described in more detail below. These simulations were run to statistical equilibrium, after which statistics were collected over 25 days of model time. All figures in this manuscript based on these experiments are made from data that were averaged over this equilibrated 25-day period.

For the CTRL, NOEVAP, NOPEAK, and LOPEAK experiments, microphysics was treated with a simple Kessler-type scheme (Kessler 1969) in order to facilitate a quantitative analysis of cloud sinks. There is no explicit ice phase in this scheme, so the only classes of water are vapor (with mass fraction q_v), non-precipitating cloud condensate (q_c), and precipitation (q_p). Other than the condensation and evaporation that occur during saturation adjustment, the only microphysical process included in this scheme is autoconversion of cloud condensate to precipitation, which is parameterized according to equation 7.3 with an autoconversion timescale that we discuss in more detail below. Precipitation is given a fixed freefall speed of 10 m/s and is allowed to evaporate in subsaturated air.

In inactive air, we set $\tau_a = 75$ minutes. In cloudy updrafts, τ_a was varied with height in order to approximately emulate the updraft-mean condensate loading from the DEFAULT simulation, which uses DAM's default six-class Lin-Lord-Krueger scheme (Lin et al. 1983; Lord et al. 1984; Krueger et al. 1995). By trial and error, we found that a reasonable match is achieved with a τ_a that ramps down from 30 minutes at and below an altitude of 500 m to a constant of 3.5 minutes at altitudes above 3 km. Figure 7.7 shows that the cloud fraction, updraft-mean cloud condensate loading, and precipitation flux from CTRL are similar to those from DEFAULT.

The subsections below detail further aspects of the CRM configuration in the NOEVAP, NOPEAK, and LOPEAK experiments.

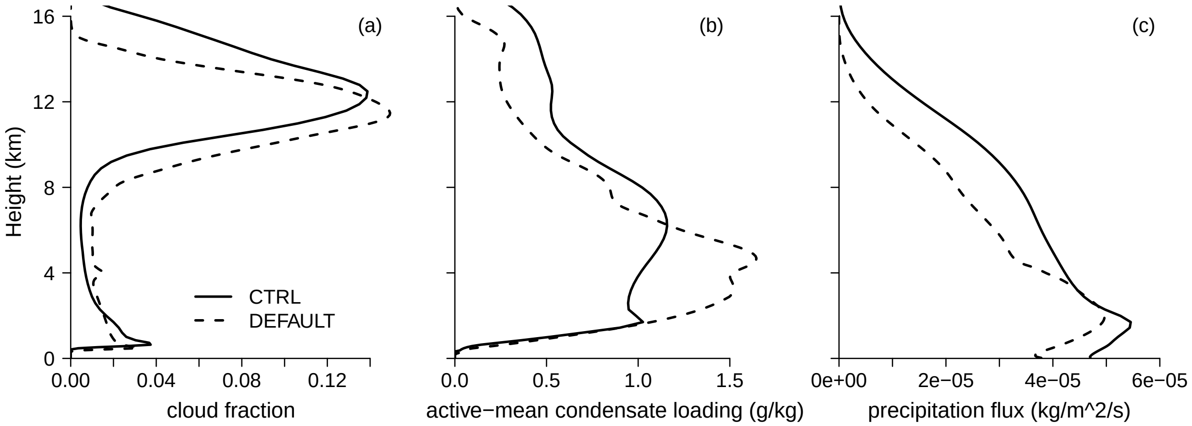

Figure 7.7: (a) Cloud fraction, (b) updraft-mean non-precipitating cloud condensate q_c, and (c) precipitation flux in the CTRL and DEFAULT simulations. For DEFAULT, q_c includes non-precipitating cloud liquid and cloud ice and the precipitation flux includes rain, snow, and graupel. For CTRL, neither q_c nor the precipitation flux are differentiated into liquid and ice subspecies because of the simple microphysics scheme used in that simulation.

NOEVAP experiment

The NOEVAP experiment was designed to be as similar to the CTRL experiment as possible except for the fact that cloud condensate is not allowed to evaporate in NOEVAP. Evaporation of cloud condensate was prevented in this experiment by intervening in the saturation-adjustment step of the CRM integration. Ordinarily, the job of the saturation adjustment routine is to move water between the vapor phase and condensed phases to ensure that grid cells are neither supersaturated, nor subsaturated in the presence of condensed water. Supersaturations are eliminated by moving vapor to the condensed phases. Subsaturations in the presence of condensed water are corrected by evaporating/sublimating the condensed phase until the grid cell is either saturated or devoid of condensed water. The outputs of this saturation adjustment routine are tendencies of water vapor q_v and non-precipitating cloud condensate q_c, which (in a standard simulation) are then used as source terms in the governing equations for the water species in the model.

In NOEVAP, the saturation adjustment routine is initially called at each time step as usual. But, if the output of the saturation adjustment routine calls for evaporation of non-precipitating cloud condensate, those tendencies are not passed to the governing equations for water. If the saturation adjustment routine calls for condensation, everything proceeds as normal. In this way, cloud condensate is allowed to form but is prevented from evaporating in the NOEVAP experiment. Note that precipitation is still allowed to evaporate in this experiment.

Preventing the evaporation of cloud condensate has two obvious effects on the atmosphere: 1) it reduces the mean relative humidity, because evaporation of detrained cloud condensates is an important source of water vapor in the free troposphere; and 2) it reduces the evaporative cooling in clear air, thereby reducing the amount of gross convective heating that is required to balance the sum of radiative and evaporative cooling in steady-state RCE. Since our intention with the NOEVAP experiment is to turn off cloud evaporation but keep everything else the same, it is desirable to correct for these two knock-on effects.

Therefore, the environmental relative humidity (RH) in NOEVAP was nudged toward the RH profile from CTRL on a timescale of $\tau_{\mathrm{RH}} = 15$ minutes. The results of this experiment are not sensitive to the value of τ_{RH} for $\tau_{\mathrm{RH}} \leq 1$ hour. This nudging was only applied to non-cloudy grid cells in order to avoid interfering with the cloud decay process, and was enacted by a forcing term in the governing equation for water vapor F_{q_v} of the form

$$F_{q_v} = \rho \frac{\mathrm{RH}^{\dagger} q_v^* - q_v}{\tau_{\mathrm{RH}}}, \tag{7.16}$$

where $\mathrm{RH}^{\dagger}$ is the target RH from the CTRL experiment and q_v^* is the saturation specific humidity.

The main concern with the reduced evaporative cooling in NOEVAP is that there would be less convective mass flux and, consequently, less cloudy-air detrainment than in the CTRL experiment. Since our goal with this experiment is to change the sink of cloud condensate without changing the source, we modified the radiative cooling profile in the NOEVAP experiment until the volumetric detrainment rate in the free troposphere matched that from CTRL. Figure 7.8 shows that these forcings produced a close match between the RH and volumetric-detrainment profiles in the CTRL and NOEVAP experiments.

NOPEAK and LOWPEAK experiments

Here we describe our technique for producing a cloud-resolving RCE simulation with a desired profile of clear-sky convergence (as in the NOPEAK and LOPEAK experiments). The basic idea of our forcing scheme is to modify the radiative cooling rate until a desired convective mass flux profile is obtained. Let $M^{\dagger}$ be the desired mass flux profile, and let M_i be the measured mass flux from our simulation, averaged over a period with index i of duration Δt. Likewise, Q_i is the measured radiative cooling rate averaged over period i. The fractional error in the mass flux profile over period i is $f_i = (M^{\dagger} - M_i)/M^{\dagger}$. This error is then used as a correction to the radiative cooling rate $Q_{i+1} = Q_i(1 + f_i)$. This corrected cooling rate will produce a new profile of convective mass flux during period $(i+1)$, which will again be compared to the desired profile and used to produce a further correction to the cooling rate to be used during period $(i + 2)$, and so on, until the cooling profile converges and a quasi-steady state is reached. We use an averaging window of $\Delta t = 6$ days, which sensitivity tests showed was sufficiently long for convective mass flux to equilibrate appropriately to the updated radiative cooling profiles.

At altitudes below 900 m (i.e., in the vicinity of the dry-convective boundary layer), we simply apply a vertically-uniform cooling rate of -0.011 (-0.015) W/m^3 in the NOPEAK

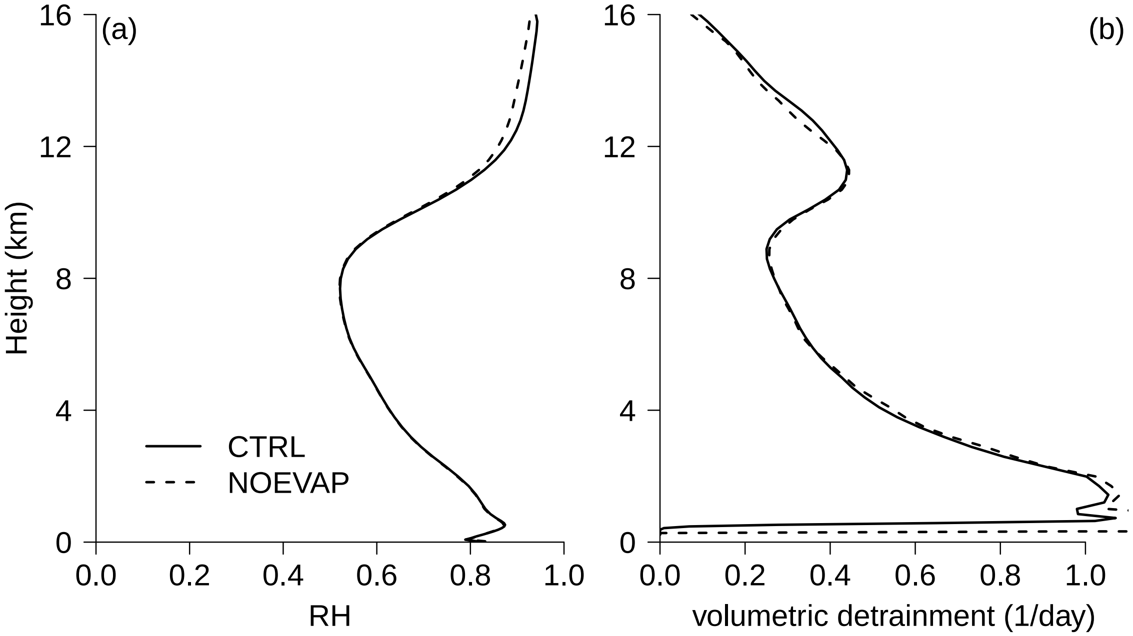

Figure 7.8: (a) Relative humidity, and (b) volumetric detrainment from the CTRL and NOEVAP experiments.

(LOPEAK) experiments. Since there is no net radiative cooling (or convective mass flux) in the stratosphere, at altitudes above 18.5 km we simply relax the temperatures to their domain-mean values from the CTRL simulation on a timescale of 6 hours. Finally, since the NOPEAK and LOPEAK simulations have, respectively, roughly 1.5 and 1.75 times as much tropospherically-integrated radiative cooling as the CTRL simulation, the bulk surface fluxes are uniformly scaled up by these factors in these two experiments. This serves to keep all three experiments on moist lapse rates rooted to a common near-surface air temperature of 298.5 ± 0.25 K. Our results do not depend on this modification of the surface fluxes. Figure 7.9 shows the steady-state radiative cooling and cloudy updraft mass flux profiles from the CTRL, NOPEAK, and LOPEAK experiments.

Appendix B: Optimizing κ

In the analytical model of cloud decay presented in section 7.4, κ appears as a free parameter (with units of seconds) that characterizes the rate of turbulent cloud spreading; according to equation 7.4, κ is the amount of time it takes for a cloud to grow by an amount equal to its initial area A_0. Here we optimize the value of κ used for the analytical expression

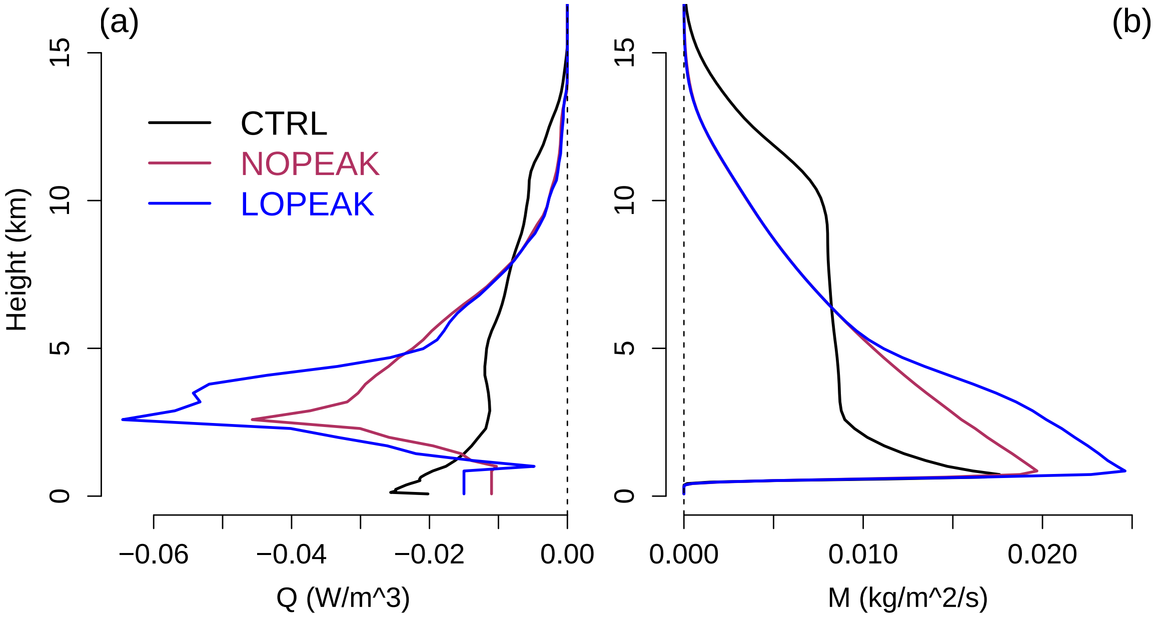

Figure 7.9: (a) Radiative cooling, and (b) cloudy updraft mass flux from the CTRL (black), NOPEAK (maroon), and LOPEAK (blue) experiments.

for cloud lifetimes for the CTRL, NOEVAP, NOPEAK, and LOWPEAK experiments.

Let $\mathcal{C}_i(z)$ be the actual cloud-fraction profile (with active updrafts removed) measured in the CRM from an experiment indexed by i, and let $\mathcal{C}_i^\dagger(z)$ be the cloud-fraction profile predicted for that experiment by the new framework with a particular value of κ (i.e., predicted by equation 7.14 from the main text, with the volumetric detrainment diagnosed as described in the main text and τ_{new} given by equation 7.13). We define the following cost function

$$\text{cost function} = \sum_{i=1}^{3} \frac{1}{z_{\text{top}}} \int_0^{z_{\text{top}}} \left[\mathcal{C}_i(z) - \mathcal{C}_i^\dagger(z)\right]^2 \mathrm{d}z, \tag{7.17}$$

where $i = 1$ corresponds to the CTRL experiment, $i = 2$ to the NOPEAK experiment, and $i = 3$ to the LOPEAK experiment. We optimize the value of κ by minimizing this cost function.

Figure 7.10 shows the value of the cost function for κ in the range of 1–80 minutes. The cost function has a minimum at $\simeq$19 minutes, which we take to be the “best” value κ_{best} used throughout this manuscript. The minimum in the cost function is fairly broad — κ can be varied by a factor of 2 in either direction without much degradation of the fit, as can be seen in the bottom row of Figure 7.10. For larger values of κ (corresponding to increasingly slow turbulent mixing), predicted cloud lifetimes in the lower troposphere become unrealistically long, cloud fraction becomes too large, and the fit becomes worse.

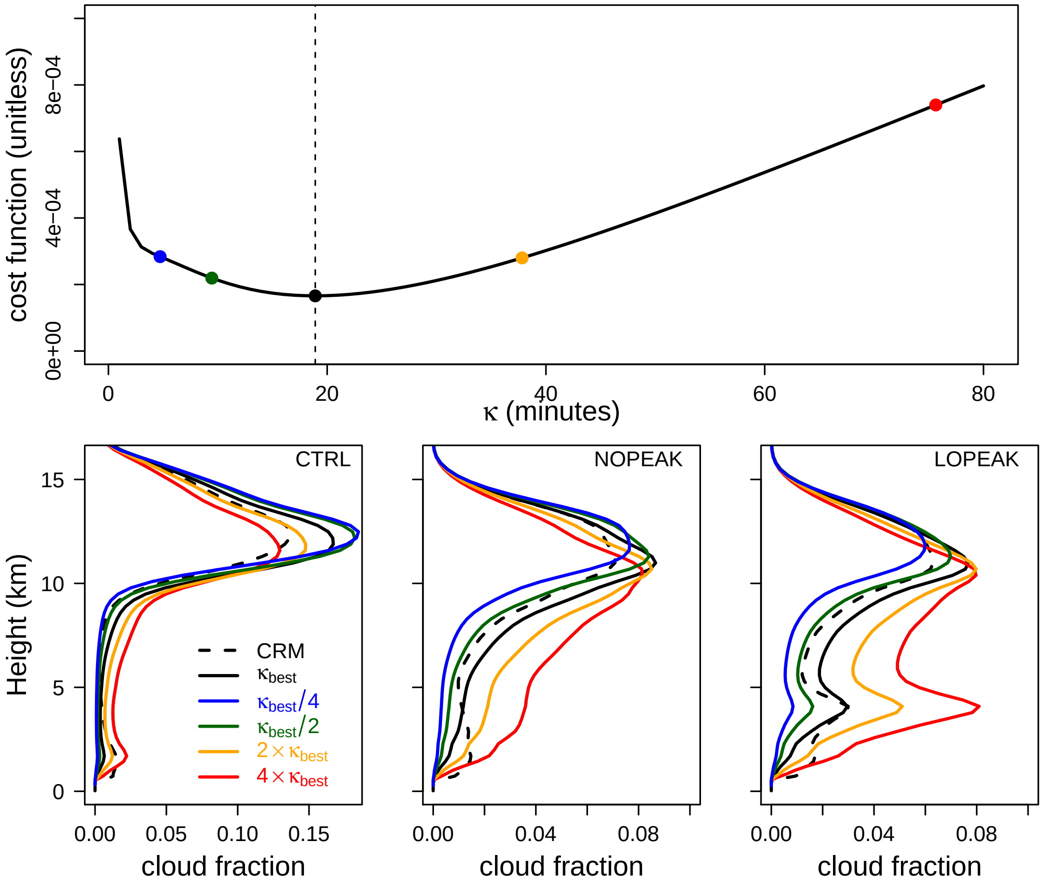

Figure 7.10: (Top panel) The value of the cost function given by equation 7.17 for κ in the range of 1–80 minutes. The black circle marks the minimum at $\kappa_{\text{best}} = 19$ minutes, while the blue, green, orange, and red circles mark values of κ_{best} scaled by factors of 0.25, 0.5, 2, and 4, respectively. (Bottom row) The cloud-fraction profiles predicted by the new framework for the CTRL, NOPEAK, and LOPEAK experiments, for the values of κ shown in the top panel.

Appendix C: Numerical cloud decay model

The analytical model of cloud decay presented in section 7.4 uses a bulk water budget, which means that mixing occurring at the edge of the cloud is instantaneously distributed throughout the entire cloud volume. Here we present a second model of decaying clouds that does not make this bulk assumption. Instead, we numerically solve the diffusion equation.

We assume that our decaying cloud consists of a radially-symmetric distribution of water vapor $q_v(r,t)$ and cloud condensate $q_c(r,t)$. The cloud begins life when it is detrained as a saturated top-hat with initial radius r_0 and condensate mass fraction q_{c_0}:

$$q_c(r,0) = \begin{cases} q_{c_0}, & r \le r_0 \\ 0, & r > r_0 \end{cases} \tag{7.18}$$

$$q_v(r,0) = \begin{cases} q_v^*, & r \le r_0 \\ \mathrm{RH}q_v^*, & r > r_0 \end{cases} \tag{7.19}$$

where RH is the environmental relative humidity at the detrainment level.

The governing equations for q_v and q_c take the form of the radial diffusion equation with sources and sinks that account for the processes of saturation adjustment and precipitation:

$$\partial_t q_v = k\left[\partial_r^2 q_v' + \frac{1}{r}\partial_r q_v'\right] + e(r,t) \quad ; \tag{7.20}$$

$$\partial_t q_c = k\left[\partial_r^2 q_c + \frac{1}{r}\partial_r q_c\right] - e(r,t) - p(r,t) \quad , \tag{7.21}$$

where k (m^2/s) is the turbulent diffusivity, $e(r,t)$ (1/s) is the evaporation rate, and $p(r,t)$ (1/s) is rate at which cloud condensate is converted into precipitation.

Equations 7.20 and 7.21 are integrated numerically with an implicit Euler method. We discretize the radial coordinate r with 1000 points of size $\Delta r = 100$ m, and discretize the time coordinate with steps of length $\Delta t = 20$ s. The integration method is as follows. First, the distributions of q_v and q_c are diffused according to the radial diffusion operator acting alone. Second, a "saturation adjustment" step occurs, in which the evaporation is diagnosed as follows: at each grid point, condensed water is converted into vapor until $q_v = q_v^*$ or all q_c has evaporated. Third, cloud condensate is removed by precipitation, which is parameterized according to equation 7.3 in order to match the microphysics scheme in the CRM experiments. At each time step, the radius of the cloud is the largest value of r at which $q_c(r,t) \ge 10^{-5}$. This procedure is repeated until the cloud's radius has shrunk to 0, at which point the cloud has reached its lifetime $\tilde{\tau}$ and is considered dead. As in the analytical cloud decay model presented in section 7.4, the effective lifetime of the cloud is diagnosed according to equation 7.11. This model of cloud decay has two free parameters: the initial radius r_0 and the diffusivity k.

Although the analytical and numerical cloud decay models differ in their details, they produce very similar results. In Figure 7.11, we show the effective cloud lifetimes predicted by the two models of cloud decay for the CTRL, NOEVAP, NOPEAK, and LOPEAK experiments. For the analytical model, the value of the free parameter κ is set to 19 minutes (Appendix B). For the numerical model, the diffusivity k is set to 500 m^2/s and the initial radius r_0 is set to 2 km. For the NOEVAP experiment, evaporation is prevented in the cloud decay models by setting RH = 1.

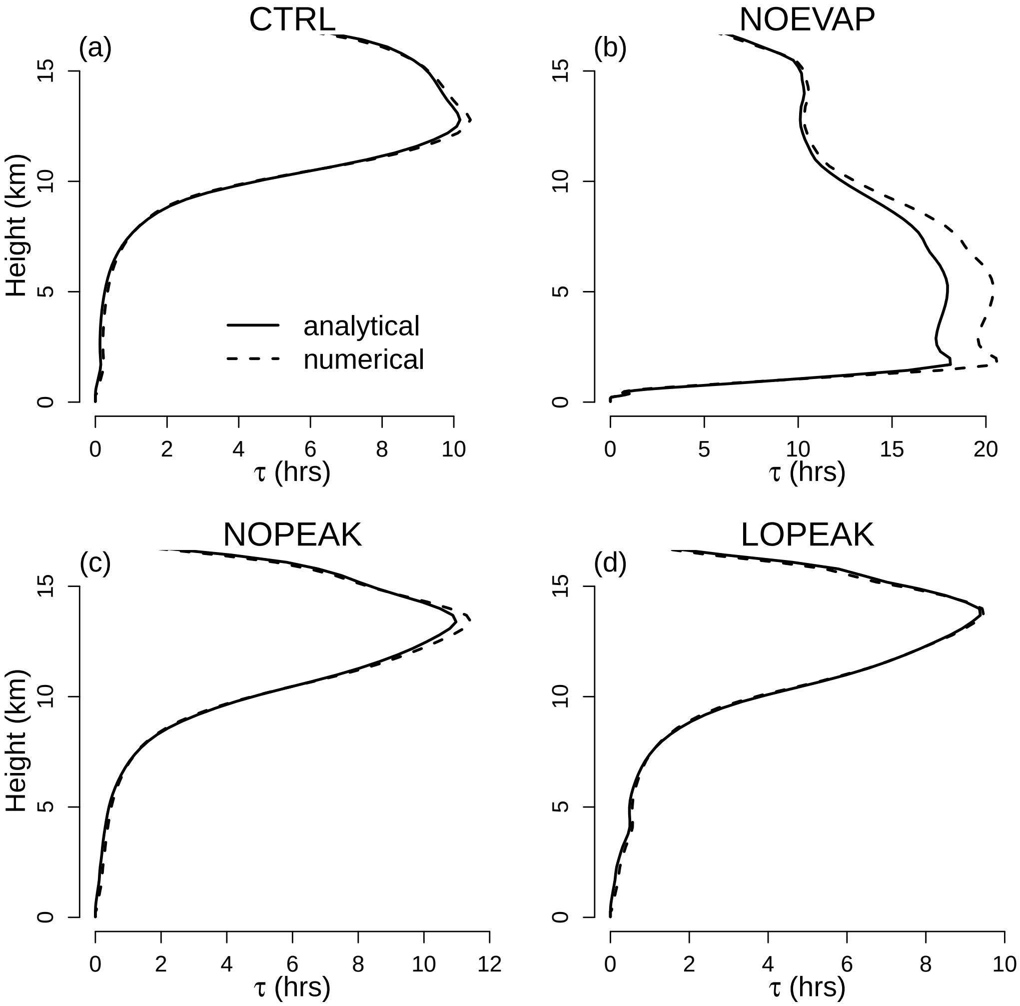

Figure 7.11: Effective cloud lifetimes τ_{new} predicted by the analytical and numerical models of cloud decay. Results are shown for four experiments discussed in the main text: (a) CTRL, (b) NOEVAP, (c) NOPEAK, and (d) LOPEAK. For the analytical model, the free parameter κ is set to 19 minutes. For the numerical model, the turbulent diffusivity κ is set to 500 m^2/s, and the initial radius r_0 is set to 2 km.

Appendix D: Cloud fraction in RCE

Here we derive an expression for steady-state cloud fraction in radiative-convective equilibrium. Consider a layer of an atmosphere in a square domain with side length L, observed during a time interval of length Δt, during which n cylindrical clouds are born, grow, and die within that layer. Considered individually, each cloud contributes a time-mean fractional area, C, given by

$$C = \frac{\int_0^{\tilde{\tau}} A(t)dt}{L^2 \Delta t}. \tag{7.22}$$

If the clouds have random overlap in space and time, the time-mean cloud fraction $\mathcal{C}(L^2\Delta t)$ during this interval is

$$\mathcal{C}(L^2\Delta t) = 1 - (1 - C)^n. \tag{7.23}$$

The number of clouds that form during this interval, n, is given by

$$n = \left(\frac{\delta M}{\rho}\right)\left(\frac{1}{A_0}\right) L^2 \Delta t. \tag{7.24}$$

The first term on the RHS of equation 7.24 is the volumetric detrainment rate, with M (kg/m^2/s) the convective mass flux and δ (1/m) the bulk-plume fractional detrainment rate.

To find the steady-state cloud fraction $\mathcal{C}$, we take the limit of equation 7.23 as $L^2\Delta t \to \infty$. This yields

$$\mathcal{C} = 1 - \exp\left[-\left(\frac{\delta M}{\rho A_0}\right)\int_0^{\tilde{\tau}} A(t)dt\right]. \tag{7.25}$$

Taylor-expanding the exponential to first order yields

$$\mathcal{C} = \left(\frac{\delta M}{\rho}\right)\int_0^{\tilde{\tau}}\left(\frac{A}{A_0}\right)dt. \tag{7.26}$$

This is the result we would have obtained had we assumed no overlap between the clouds rather than random overlap. Note that equation 7.26 will make an unphysical prediction of $\mathcal{C} > 1$ in the limit of very large detrainment or very long cloud lifetimes; in such cases one should use equation 7.25 instead.

Recognizing $\int_0^{\tilde{\tau}} (A/A_0)\, dt$ as the effective lifetime from equation 7.11, we obtain our equation for steady-state cloud fraction in RCE, valid in the limit of small cloud fraction:

$$\mathcal{C} = \frac{\delta M}{\rho}\tau. \tag{7.27}$$

Note that equation 7.27 only accounts for the area occupied by decaying clouds, which overwhelmingly dominate cloud fraction above the boundary layer. For completeness, though, we can also include the area occupied by active convective mass flux $M/(\rho w)$, where w is the mean updraft velocity:

$$\mathcal{C} = \frac{M}{\rho}\left[\delta\tau + \frac{1}{w}\right]. \tag{7.28}$$

Appendix E: Applying the new framework to the DEFAULT simulation

The new framework for anvil clouds can, in principle, be applied to any CRM simulation, including DEFAULT. The challenge is that for DEFAULT, the precipitation timescale τ_a

that enters into the expression for τ_{new} is an emergent property of the Lin-Lord-Krueger microphysics scheme — rather than a known parameter of the CRM, as it is for the simulations that use the simple microphysics scheme. This means that for DEFAULT there are now two unknown parameters entering into the new framework for anvil clouds: κ and τ_{a}, which control the rates of turbulent cloud spreading and precipitation, respectively. Therefore, we must perform a two-parameter optimization to find the best values for these timescales. As in Appendix B, we define the cost function

$$\text{cost function} = \frac{1}{z_{\text{top}}} \int_0^{z_{\text{top}}} \left[\mathcal{C}(z) - \mathcal{C}^{\dagger}(z)\right]^2 \mathrm{d}z, \tag{7.29}$$

where $\mathcal{C}(z)$ is the actual cloud-fraction profile from the DEFAULT experiment (with active updrafts removed) and $\mathcal{C}^{\dagger}(z)$ is the cloud-fraction profile predicted by the new framework for a particular set of κ and τ_{a} values. Figure 7.12 shows the result of minimizing the cost function given by equation 7.29. The optimal values are $\kappa = 7.5$ minutes and $\tau_{\text{a}} = 43$ minutes. Note that this value of κ is about a factor of 2 smaller than the best-fit κ found in Appendix B for the lower-resolution simulations, which suggests that turbulent mixing is more efficient at finer horizontal resolution.

The right panel of Figure 7.12 shows that the new framework makes a very good prediction for the cloud-fraction profile of the DEFAULT simulation with these parameter values. This successful prediction requires using both the correct source term (the volumetric detrainment) and the correct cloud-lifetime profile (τ_{new}). If the CSC paradigm's source term (the clear-sky convergence) is used in conjunction with τ_{new}, the predicted cloud fraction has the correct top-heavy shape but is significantly too small in magnitude; on the other hand, if the correct source term (the volumetric detrainment) is used in conjunction with the CSC paradigm's constant-lifetime assumption, the predicted cloud-fraction profile is bottom-heavy, in stark contrast to the CRM results (Figure 7.13). Only when cloud fraction is predicted by the new framework is a good fit obtained.

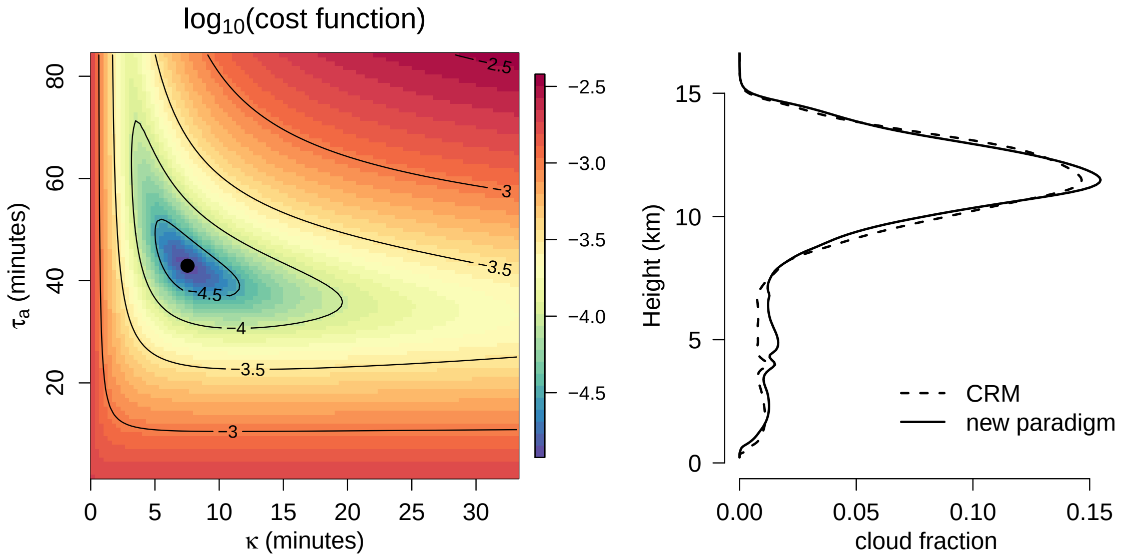

Figure 7.12: (left) The base-10 logarithm of the cost function given in equation 7.29, for a range of κ and τ_{a} values. The best-fit values ($\kappa = 7.5$ minutes and $\tau_{\mathrm{a}} = 43$ minutes) are indicated with the filled black circle. (right) The cloud-fraction profile (with active updrafts removed) from the DEFAULT simulation (dashed line), as compared to the cloud-fraction profile predicted by the new framework (equation **??**) with the best-fit values of κ and τ_{a} (solid line).

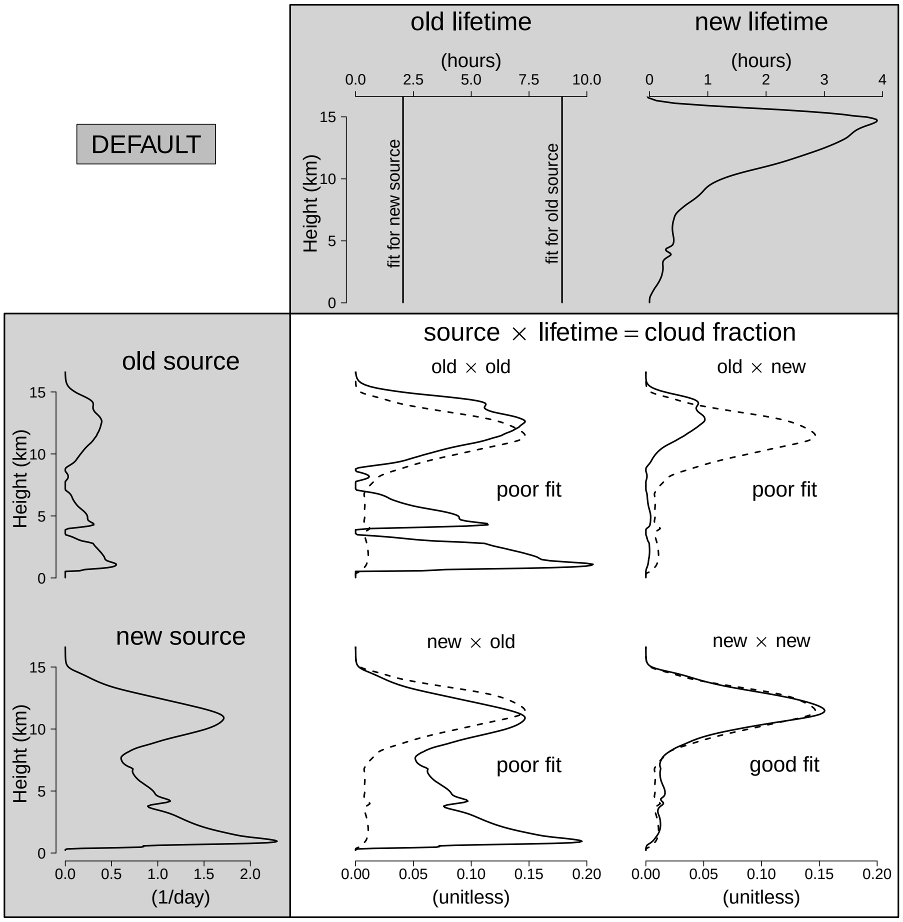

Figure 7.13: For the DEFAULT experiment: (top row) the cloud-lifetime profiles used by the CSC paradigm and the new framework (for the vertically-uniform cloud-lifetime profiles used by the CSC paradigm, separate values are fit for each of the two possible source terms); (first column) the cloud-source profiles used by the CSC paradigm and new framework; (four plots inside the black box) all possible products of these two sources and two lifetimes, which give four different predictions for the cloud-fraction profile. The actual cloud-fraction profile from the CRM is shown by the dashed line in the four plots inside the black box. Only when the new source (the volumetric detrainment, $\delta M/\rho$) is multiplied by the new cloud-lifetime profile (τ_{new}) is a good fit to the CRM obtained.

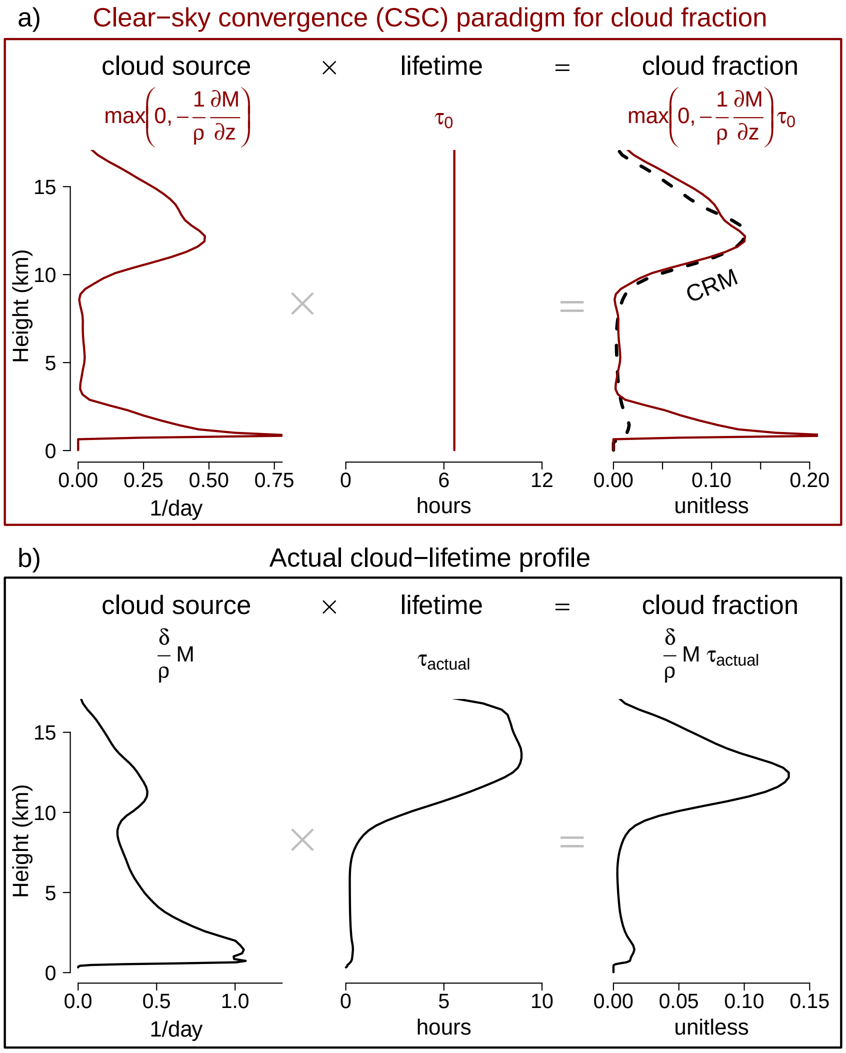

Figure 7.14: As in Figure 7.2, but for the CTRL experiment rather than DEFAULT.

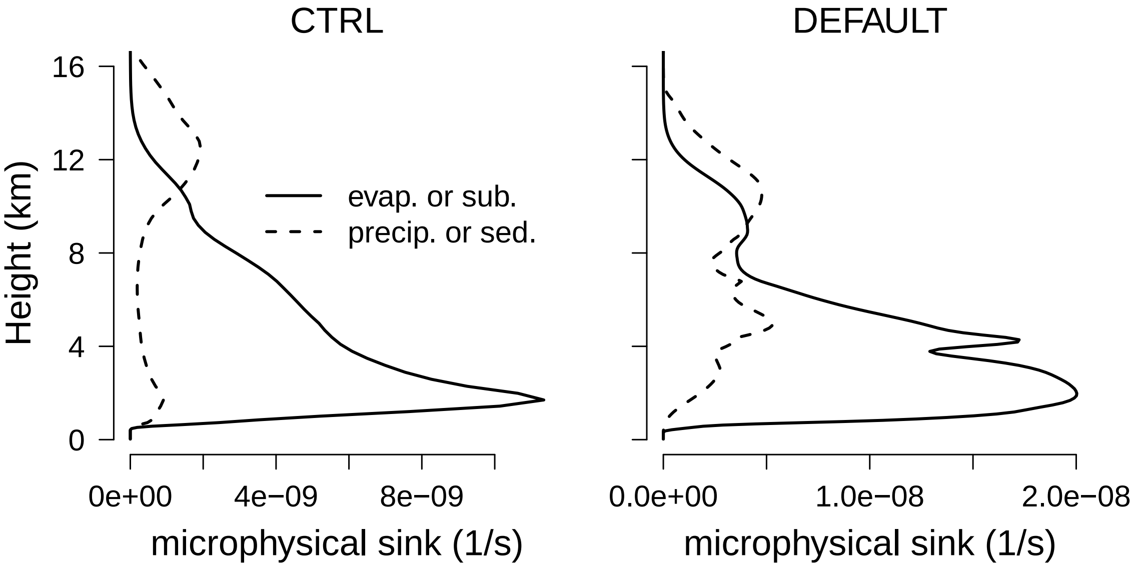

Figure 7.15: Microphysical sinks of non-precipitating cloud condensate, averaged in time and over inactive grid cells, for the (left) CTRL and (right) DEFAULT experiments. Solid lines show the sum of evaporation and sublimation, while dashed lines show the sum of precipitation and sedimentation (in the CTRL experiment, sublimation and sedimentation are both identically zero because of the simplified microphysics scheme in that simulation.

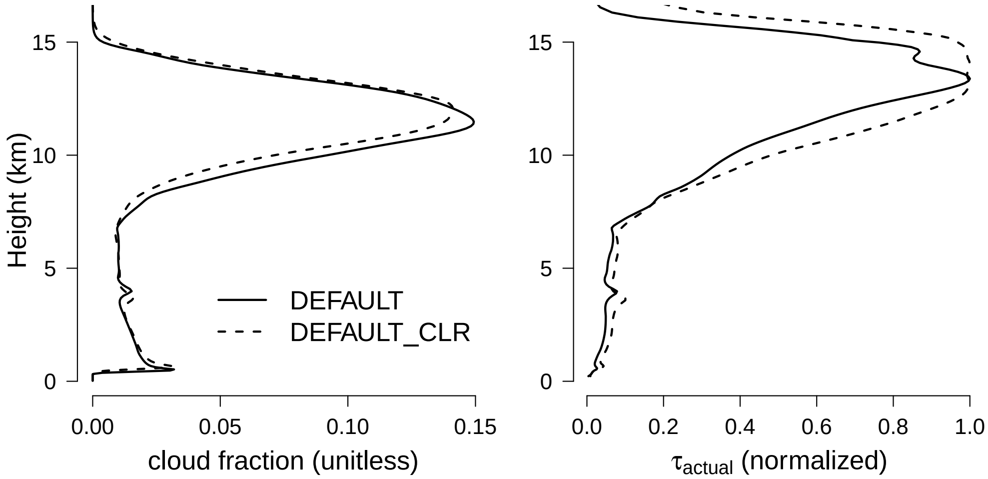

Figure 7.16: (left) Cloud fraction from the DEFAULT and DEFAULT_CLR simulations. In DEFAULT_CLR, cloud condensate is zeroed out in the radiative transfer calculations, rendering clouds invisible to radiation; the results show that the cloud-fraction profile is fairly insensitive to this change. (right) Diagnosed cloud-lifetime profiles (τ_{actual}) from the two simulations, normalized by their maximum values. As in Figure 7.2, τ_{actual} is diagnosed by dividing the measured cloud fraction (with actuve updrafts removed) by the measured volumetric detrainment. The similarly-shaped τ_{actual} profiles of the two experiments — in particular, the order-of-magnitude increase in cloud lifetimes in the upper troposphere shared by both profiles — shows that cloud-radiative interactions are not responsible for the ballooning of cloud lifetimes in the upper troposphere.

Bibliography

Allen, J. T., D. J. Karoly, and G. A. Mills, 2011: A severe thunderstorm climatology for Australia and associated thunderstorm environments. *Australian Meteorological and Oceanographic Journal*, **61**, 143–158.

Allen, J. T., D. J. Karoly, and K. Walsh, 2014a: Future Australian severe thunderstorm environments, Part A: A novel evaluation and climatology of convective parameters from two climate models for the late 20th century. *Journal of Climate*, **27**, 3827–3847.

— 2014b: Future Australian severe thunderstorm environments, Part B: The influence of a strongly warming climate on convective environments. *Journal of Climate*, **27**, 3848–3868.

Bony, S., B. Stevens, D. Coppin, T. Becker, K. A. Reed, A. Voigt, and B. Medeiros, 2016: Thermodynamic control of anvil cloud amount. *Proceedings of the National Academy of Sciences*, 201601472.

Boucher, O., D. Randall, P. Artaxo, C. Bretherton, G. Feingold, P. Forster, V.-M. V.-M. Kerminen, Y. Kondo, H. Liao, U. Lohmann, P. Rasch, S. K. Satheesh, S. Sherwood, B. Stevens, X. Y. Zhang, and X. Y. Zhan, 2013: Clouds and Aerosols. *Climate Change 2013: The Physical Science Basis. Contribution of Working Group I to the Fifth Assessment Report of the Intergovernmental Panel on Climate Change*, 571–657.

Bretherton, C. S. and P. K. Smolarkiewicz, 1989: Gravity waves, compensating subsidence, and detrainment around cumulus clouds. *Journal of the Atmospheric Sciences*, **46**.

Brooks, H. E., 2013: Severe thunderstorms and climate change. *Atmospheric Research*, **123**, 129–138.

Brooks, H. E. and C. A. Doswell, 2001: Some aspects of the international climatology of tornadoes by damage classification. *Atmospheric Research*, **56**, 191–201.

Brooks, H. E., C. A. Doswell, and J. Cooper, 1994: On the environments of tornadic and nontornadic mesocyclones. *Weather and Forecasting*, **9**, 606–618.

Brooks, H. E. and N. Dotzek, 2008: *Climate Extremes and Society*, Cambridge University Press, chapter The spatial distribution of severe convective storms and an analysis of their secular changes. 35–54.

Brooks, H. E., J. W. Lee, and J. P. Craven, 2003: The spatial distribution of severe thunderstorm and tornado environments from global reanalysis data. *Atmospheric Research*, **67**, 73–94.

Brown, R. G. and C. Zhang, 1997: Variability of Midtropospheric Moisture and Its Effect on Cloud-Top Height Distribution during TOGA COARE*. *Journal of the Atmospheric*

Sciences, **54**, 2760–2774.

Carlson, T. N. and F. H. Ludlam, 1966: Conditions for the occurrence of severe local storms. *Tellus*, **20**.

Chaboureau, J., F. Guichard, J. Redelsperger, and J. Lafore, 2004: The role of stability and moisture in the diurnal cycle of convection over land. *Quarterly Journal of the Royal Meteorological Society*, **130**, 3105–3117.

Chepfer, H., S. Bony, D. Winker, G. Cesana, J.-L. Dufresne, P. Minnis, C. J. Stubenrauch, and S. Zeng, 2010: The GCM-Oriented CALIPSO Cloud Product (CALIPSO-GOCCP). *Journal of Geophysical Research*, **115**, 1–13.

Clough, S. A., M. J. Iacono, and J.-L. Moncet, 1992: Line-by-line calculations of atmospheric fluxes and cooling rates: application to water vapor. *Journal of Geophysical Research*, **97**.

Clough, S. A., M. W. Shephard, E. J. Mlawer, J. S. Delamere, M. J. Iacono, K. Cady-Pereira, S. Boukabara, and P. D. Brown, 2005: Atmospheric radiative transfer modeling: A summary of the AER codes. *Journal of Quantitative Spectroscopy and Radiative Transfer*, **91**, 233–244.

Craven, J. P. and H. E. Brooks, 2004: Baseline climatology of sounding-derived parameters associated with deep moist convection. *National Weather Digest*, **28**, 13–24.

Cronin, T. W. and E. Tziperman, 2015: Low clouds suppress Arctic air formation and amplify high-latitude continental winter warming. *Proceedings of the National Academy of Sciences*.

Dai, A., 2006: Recent climatology, variability, and trends in global surface humidity. *Journal of Climate*, **19**, 3589–3606.

Derbyshire, S. H., I. Beau, P. Bechtold, J.-Y. Grandpeix, J.-M. Piriou, J.-L. Redelsperger, and P. M. M. Soares, 2004: Sensitivity of moist convection to environmental humidity. *Quarterly Journal of the Royal Meteorological Society*, **130**.

Dessler, A. E., S. P. Palm, and J. D. Spinhirne, 2006: Tropical cloud-top height distributions revealed by the Ice , Cloud , and Land Elevation Satellite (ICESat)/ Geoscience Laser Altimeter System (GLAS). *Journal of Geophysical Research*, **111**, 1–11.

Diffenbaugh, N. S., M. Scherer, and R. J. Trapp, 2013: Robust increases in severe thunderstorm environments in response to greenhouse forcing. *Proceedings of the National Academy of Sciences of the United States of America*, **110**, 16361–16366.

Diffenbaugh, N. S., R. J. Trapp, and H. E. Brooks, 2008: Does global warming influence tornado activity? *Eos, Transactions, American Geophysical Union (EOS)*, **89**, 553–554.

Doswell, C. A., H. E. Brooks, and M. P. Kay, 2005: Climatological estimates of daily local nontornadic severe thunderstorm probability for the United States. *Weather and Forecasting*, **20**, 577–595.

Dudhia, A., 2017: Journal of Quantitative Spectroscopy & Radiative Transfer The Reference Forward Model (RFM). *Journal of Quantitative Spectroscopy and Radiative Transfer*, **186**.

Eitzen, Z. A., K. M. Xu, and T. Wong, 2009: Cloud and radiative characteristics of tropical deep convective systems in extended cloud objects from CERES observations. *Journal of Climate*, **22**, 5983–6000.

Etminan, M., G. Myhre, E. J. Highwood, and K. P. Shine, 2016: Radiative forcing of carbon dioxide, methane, and nitrous oxide: A significant revision of the methane radiative forcing. *Geophysical Research Letters*, **43**, 12,614–12,623.

Fasullo, J., 2011: A mechanism for landâĂŞocean contrasts in global monsoon trends in a warming climate. *Climate Dynamics*, **39**.

Fierro, A. O., J. Simpson, M. A. LeMone, J. M. Straka, and B. F. Smull, 2009: On How Hot Towers Fuel the Hadley Cell: An Observational and Modeling Study of Line-Organized Convection in the Equatorial Trough from TOGA COARE. *Journal of the Atmospheric Sciences*, **66**, 2730–2746.

Fritsch, J. M., R. J. Kane, and C. R. Chelius, 1986: The contribution of mesoscale convective weather systems to the warm-season precipitation in the United States. *Journal of Climate and Applied Meteorology*, **25**, 1333–1345.

Fueglistaler, S., A. E. Dessler, T. J. Dunkerton, I. Folkins, Q. Fu, and P. W. Mote, 2009: Tropical Tropopause Layer. *Reviews of Geophysics*, 1–31.

Gensini, V. A. and W. S. Ashley, 2011: Climatology of popotential severe convective environments from North American regional reanalysis. *Electronic Journal of Severe Storms Meteorology*, **6**, 1–40.

Gensini, V. A., C. Ramseyer, and T. L. Mote, 2013: Future convective environments using NARCCAP. *International Journal of Climatology*, **34**, 1699–1705.

Geoffroy, O., S. Sherwood, and D. Fuchs, 2017: On the role of the stratiform cloud scheme in the inter-model spread of cloud feedback. *Journal of Advances in Modeling Earth Systems*, 423–437.

Gordon, I. E., L. S. Rothman, C. Hill, R. V. Kochanov, Y. Tan, P. F. Bernath, M. Birk, V. Boudon, A. Campargue, K. V. Chance, B. J. Drouin, J. Flaud, R. R. Gamache, J. T. Hodges, D. Jacquemart, V. I. Perevalov, A. Perrin, K. P. Shine, M. H. Smith, J. Tennyson, G. C. Toon, H. Tran, V. G. Tyuterev, A. Barbe, A. G. Császár, V. M. Devi, T. Furtenbacher, J. J. Harrison, J. Hartmann, A. Jolly, T. J. Johnson, T. Karman, I. Kleiner, A. A. Kyuberis, J. Loos, O. M. Lyulin, S. T. Massie, S. N. Mikhailenko, N. Moazzen-ahmadi, H. S. P. Müller, O. V. Naumenko, A. V. Nikitin, O. L. Polyansky, J. V. Auwera, G. Wagner, J. Wilzewski, P. Wcis, S. Yu, and E. J. Zak, 2017: The HITRAN2016 molecular spectroscopic database. *Journal of Quantitative Spectroscopy & Radiative Transfer*, **203**, 3–69.

Grabowski, W. W., 2003: Impact of ice microphysics on multiscale organization of tropical convection in two-dimensional cloud-resolving simulations. *Quarterly Journal of the Royal Meteorological Society*, **129**, 67–81.

Hansen, J., M. Sato, R. Ruedy, L. Nazarenko, A. Lacis, G. A. Schmidt, G. Russell, I. Aleinov, M. Bauer, S. Bauer, N. Bell, B. Cairns, V. Canuto, M. Chandler, Y. Cheng, A. D. Genio, G. Faluvegi, E. Fleming, A. Friend, T. Hall, C. Jackman, M. Kelley, N. Kiang, D. Koch, J. Lean, J. Lerner, K. Lo, S. Menon, R. Miller, P. Minnis, T. Novakov, V. Oinas, and J. Perlwitz, 2005: Efficacy of climate forcings. *Journal of Geophysical Research*, **110**.

Harrop, B. E. and D. L. Hartmann, 2012: Testing the Role of Radiation in Determining Tropical Cloud-Top Temperature. *Journal of Climate*, **25**, 5731–5747.

— 2016: The role of cloud heating within the atmosphere on the high cloud amount and top-of-atmosphere cloud radiative effect. *Journal of Advances in Modeling Earth Systems*.

Hartmann, D. and K. Larson, 2002: An important constraint on tropical cloudâĂŘclimate feedback. *Geophysical Research Letters*, **29**, 10–13.

Hartmann, D. L., 2016: Tropical anvil clouds and climate sensitivity. *Proceedings of the National Academy of Sciences*, **113**, 8897–8899.

Hartmann, D. L., J. R. Holton, and Q. Fu, 2001a: The heat balance of the tropical tropopause, cirrus, and stratospheric dehydration. *Geophysical Research Letters*, **28**, 1969–1972.

Hartmann, D. L. and M. L. Michelsen, 2002: No evidence for iris. *Bulletin of the American Meteorological Society*, **83**, 1345–1349.

Hartmann, D. L., L. A. Moy, and Q. Fu, 2001b: Tropical convection and the energy balance at the top of the atmosphere. *Journal of Climate*, **14**, 4495–4511.

Held, I. M., 2005: The Gap between Simulation and Understanding in Climate Modeling. *Bulletin of the American Meteorological Society*, 1609–1614.

Huang, Y. and M. B. Shahabadi, 2014: Why logarithmic? A note on the dependence of radiative forcing on gas concentration. *Journal of Geophysical Research Atmospheres*, 683–689.

Huang, Y., X. Tan, and Y. Xia, 2016: Inhomogeneous radiative forcing of homogeneous greenhouse gases. *Journal of Geophysical Research Atmospheres*, 2780–2789.

Iacono, M. J., J. S. Delamere, E. J. Mlawer, M. W. Shephard, S. A. Clough, and W. D. Collins, 2008: Radiative forcing by long-lived greenhouse gases: Calculations with the AER radiative transfer models. *Journal of Geophysical Research Atmospheres*, **113**, 2–9.

IPCC, 2012: *Managing the Risks of Extreme Events and Disasters to Advance Climate Change Adaptation*. Cambridge University Press, Cambridge, UK and New York, NY, USA.

Irvine, W. M. and J. B. Pollack, 1968: Infrared optical properties of water and ice spheres. *Icarus*, **360**, 324–360.

Jeevanjee, N., P. Hassanzadeh, S. Hill, and A. Sheshadri, 2017: A Perspective on Climate Model Hierarchies. *Journal of Advances in Modeling Earth Systems*.

Jeevanjee, N. and D. M. Romps, 2018: Mean Precipitation Change from a Deepening Troposphere. *Proceedings of the National Academy of Sciences*, **in press**.

Johns, R. H. and C. A. Doswell, 1992: Severe local storms forecasting. *Weather and Forecasting*, **7**, 588–612.

Jonas, P. R., 1990: Observations of cumulus cloud entrainment. *Atmospheric research*, **25**, 105–127.

Kelly, D. L., J. T. Schaefer, and C. A. Doswell, 1985: Climatology of non-tornadic severe thunderstorm events in the United States. *Monthly Weather Review*, **113**, 1997–2014.

Kessler, E., 1969: On the continuity and distribution of water substance in atmospheric circulations. *Atmospheric Research*, **38**, 109–145.

Khairoutdinov, M. and K. Emanuel, 2013: Rotating radiative-convective equilibrium simulated by a cloud-resolving model. *Journal of Advances in Modeling Earth Systems*, **5**, 816–825.

Khairoutdinov, M. and D. Randall, 2006: High-Resolution Simulation of Shallow-to-Deep Convection Transition over Land. *Journal of the Atmospheric Sciences*, **63**, 3421–3436.

Krueger, S. K., Q. Fu, K. N. Liou, and H.-N. S. Chin, 1995: Improvements of an ice-phase mcrophysics parameterization for use in numerical simulations of tropical convection. *Journal of Applied Meteorology*, **34**.

Kuang, Z. and C. S. Bretherton, 2006: A Mass-Flux Scheme View of a High-Resolution Simulation of a Transition from Shallow to Deep Cumulus Convection. *Journal of the Atmospheric Sciences*, **63**, 1895–1909.

Kuang, Z. and D. L. Hartmann, 2007: Testing the Fixed Anvil Temperature Hypothesis in a Cloud-Resolving Model. *Journal of Climate*, **20**, 2051–2057.

Kubar, T., D. L. Hartmann, and R. Wood, 2007: Radiative and Convective Driving of Tropical High Clouds. *Journal of Climate*, **20**, 5510–5527.

Kunkel, K., T. Karl, H. E. Brooks, J. Kossin, J. Lawrimore, D. Arndt, L. Bosart, D. Changnon, S. Cutter, N. Doesken, K. Emanuel, P. Groisman, R. Katz, T. Knutson, J. O'Brien, C. Paciorek, T. Peterson, K. Redmond, D. Robinson, J. Trapp, R. Vose, S. Weaver, M. Wehner, K. Wolter, and D. Wuebbles, 2013: Monitoring and understanding trends in extreme storms: state of knowledge. *Bulletin of the American Meteorological Society*, **94**, 499–514.

Larson, K. and D. L. Hartmann, 2003: Interactions among Cloud, Water Vapor, Radiation, and Large-Scale Circulation in the Tropical Climate. Part I : Sensitivity to Uniform Sea Surface Temperature Changes. *Journal of Climate*.

Lawson, R. P. and W. A. Cooper, 1990: Performance of Some Airborne Thermometers in Clouds. *Journal of Atmospheric and Oceanic Technology*, **7**, 480–494.

Lepore, C., D. Veneziano, and A. Molini, 2014: Temperature and CAPE Dependence of Rainfall Extremes in the Eastern United States. *Geophysical Research Letters*.

Li, Y., P. Yang, G. R. North, and A. Dessler, 2012: Test of the Fixed Anvil Temperature Hypothesis. *Journal of the Atmospheric Sciences*, **69**.

Lin, B., B. a. Wielicki, L. H. Chambers, Y. Hu, and K. M. Xu, 2002: The Iris hypothesis: A negative or positive cloud feedback? *Journal of Climate*, **15**, 3–7.

Lin, J.-L., T. Qian, T. Shinoda, and S. Li, 2015: Is the Tropical Atmosphere in Convective Quasi-Equilibrium? *Journal of Climate*.

Lin, Y.-L., R. D. Farley, and H. D. Orville, 1983: Bulk parameterization of the snow field in a clou model. *Journal of Climate and Applied Meteorology*, **22**.

Lindzen, R., M. Chou, and A. Hou, 2001: Does the earth have an adaptive infrared iris? *Bulletin of the American Meteorological Society*, 417–432.

Liu, C., M. W. Moncrieff, and E. J. Zipser, 1997: Dynamical Influence of Microphysics in Tropical Squall Lines: A Numerical Study. *Monthly Weather Review*, **125**, 2193–2210.

Lord, S. J., H. E. Willoughby, and J. M. Piotrowicz, 1984: Role of a Parameterized Ice-Phase Microphysics in an Axisymmetric, Nonhydrostatic Tropical Cyclone Model. *Journal of the Atmospheric Sciences*, **41**, 2836–2848.

Manabe, S. and R. F. Strickler, 1964: Thermal equilibrium of the atmosphere with a convective adjustment. *Journal of the Atmospheric Sciences*, **21**.

Mapes, B. E., 2001: Water's Two Scale Heights: The Moist Adiabat and the Radiative Troposphere. *Quarterly Journal of the Royal Meteorological Society*, 2353–2366.

Mapes, B. E. and P. Zuidema, 1996: Radiative-Dynamical Consequences of Dry Tongues in the Tropical Troposphere. *Journal of the Atmospheric Sciences*, **53**, 620–638.

Marsh, P. T., H. E. Brooks, and D. J. Karoly, 2007: Assessment of the severe weather environment in North America simulated by a global climate model. *Atmospheric Science Letters*, **8**, 100–106.

Mauritsen, T. and B. Stevens, 2015: Missing iris effect as a possible cause of muted hydrological change and high climate sensitivity in models. *Nature Geoscience*, 8–13.

Mccoy, D. T., D. L. Hartmann, M. D. Zelinka, P. Ceppi, and D. P. Grosvenor, 2015: Mixed-phase cloud physics and Southern Ocean cloud feedback in climate models. *Journal of Geophysical Research Atmospheres*, 9539–9554.

Merlis, T. M. and M. Henry, 2018: Simple Estimates of Polar Amplification in Moist Diffusive Energy Balance Models. *Journal of Climate*, 5811–5824.

Minschwaner, K. and A. E. Dessler, 2004: Water Vapor Feedback in the Tropical Upper Troposphere: Model Results and Observations. *Journal of Climate*, 1272–1282.

Mlawer, E. J., V. H. Payne, J. S. D. Moncet, M. J. Alvarado, and D. C. Tobin, 2012: Development and recent evaluation of the MT_CKD model of continuum absorption. *Philosophical Transactions of the Royal Society A*, **370**, 2520–2556.

Mlynczak, M. G., D. P. Kratz, , D. R. Feldman, , and W. D. Collins, 2016: The spectroscopic foundation of radiative forcing of climate by carbon dioxide. *Geophysical Research Letters*, **43**.

Muller, C. J., P. A. OâĂŹGorman, and L. E. Back, 2011: Intensification of Precipitation Extremes with Warming in a Cloud-Resolving Model. *Journal of Climate*, **24**.

National Weather Service, 2014: Severe weather definitions. `http://www.spc.noaa.gov/faq/`.

NOAA Storm Prediction Center, 2012a: Annual US killer tornado statistics. `http://www.spc.noaa.gov/climo/torn/fataltorn.html`.

— 2012b: Warning coordination meteorology. `http://www.spc.noaa.gov/wcm/`.

Parsons, D. B., K. Yoneyama, and J.-L. Redelsperger, 2006: The evolution of the atmosphere-ocean systems over the tropical western Pacific following the arrival of a dry intrusion. *Quarterly Journal of the Royal Meteorological Society*, **126**.

Pierrehumbert, R. T., 2010: *Principles of Planetary Climate*. Cambridge University Press.

Rasmussen, E. N., 2003: Refined supercell and tornado forecast parameters. *Weather and Forecasting*, **18**, 530–535.

Rasmussen, E. N. and D. O. Blanchard, 1998: A baseline climatology of sounding-derived supercell and tornado forecast parameters. *Weather and Forecasting*, **13**, 1148–1164.

Ridout, J. A., 2002: Sensitivity of Tropical Pacific Convection to Dry Layers at Mid- to Upper Levels: Simulation and Parameterization Tests. *Journal of the Atmospheric Sciences*, **59**, 3362–3381.

Robinson, E. D., R. J. Trapp, and M. E. Baldwin, 2013: The geospatial and temporal distributions of severe thunderstorms from high-resolution dynamical downscaling. *Journal of Applied Meteorology and Climatology*, **52**, 2147–2161.

Romps, D. M., 2008: The Dry-Entropy Budget of a Moist Atmosphere. *Journal of the Atmospheric Sciences*, **65**, 3779–3799.

— 2010: A Direct Measure of Entrainment. *Journal of the Atmospheric Sciences*, **67**.

— 2011: Response of Tropical Precipitation to Global Warming. *Journal of the Atmospheric Sciences*, **68**, 123–138.

— 2014: An Analytical Model for Tropical Relative Humidity. *Journal of Climate*, **27**.

— 2015: MSE minus CAPE is the true conserved variable for an adiabatically lifted parcel. *Journal of the Atmospheric Sciences*, 0–13.

— 2016: Clausius-Clapeyron scaling of CAPE from analytical solutions to RCE. *Journal of the Atmospheric Sciences*, **73**.

Romps, D. M. and A. B. Charn, 2015: Sticky thermals: Evidence for a dominant balance between buoyancy and drag in cloud updrafts. *Journal of the Atmospheric Sciences*, 0–29.

Romps, D. M. and Z. Kuang, 2010a: Do Undiluted Convective Plumes Exist in the Upper Tropical Troposphere? *Journal of the Atmospheric Sciences*, **67**, 468–484.

— 2010b: Nature versus Nurture in Shallow Convection. *Journal of the Atmospheric Sciences*, **67**.

Romps, D. M. and R. Öktem, 2015: Stereo photogrammetry reveals substantial drag on cloud thermals. *Geophysical Research Letters*.

Romps, D. M., J. T. Seeley, D. Vollaro, and J. Molinari, 2014: Projected increase in lightning strikes in the United States due to global warming. *Science*, **346**, 851–854.

Schmidt, C. T. and T. J. Garrett, 2013: A Simple Framework for the Dynamic Response of Cirrus Clouds to Local Diabatic Radiative Heating. *Journal of the Atmospheric Sciences*, **70**, 1409–1422.

Seeley, J. T., N. Jeevanjee, W. Langhans, and D. M. Romps, 2018a: Formation of tropical anvil clouds by slow evaporation. *Geophysical Research Letters*, **in review**, 1–15.

Seeley, J. T., N. Jeevanjee, and D. M. Romps, 2018b: FAT or FiTT : Are anvil clouds or the tropopause temperature-invariant? *Geophysical Research Letters*, **in review**, 1–17.

Seeley, J. T. and D. M. Romps, 2014: The effect of global warming on severe thunderstorms in the United States. *Journal of Climate*, **28**.

— 2015: Why does tropical convective available potential energy (CAPE) increase with warming? *Geophysical Research Letters*, **42**.

— 2016: Tropical cloud buoyancy is the same in a world with or without ice. *Geophysical Research Letters*, **43**, 1–8.

Sherwood, S. C., S. Bony, O. Boucher, C. Bretherton, P. M. Forster, J. M. Gregory, and B. Stevens, 2015: Adjustments in the forcing-feedback framework for understanding climate. *Bulletin of the American Meteorological Society*, 217–228.

Sherwood, S. C., D. Hernández-Deckers, M. Colin, and F. Robinson, 2013: Slippery Thermals and the Cumulus Entrainment Paradox. *Journal of the Atmospheric Sciences*, **70**.

Singh, M. S. and P. A. O'Gorman, 2013: Influence of entrainment on the thermal stratification in simulations of radiative-convective equilibrium. *Geophysical Research Letters*,

40.

— 2014: Increase in moist-convective updraft velocities with warming in radiative-convective equilibrium. *Quarterly Journal of the Royal Meteorological Society*, **17**.

Sobel, A. H. and S. J. Camargo, 2011a: Projected future seasonal changes in tropical summer climate. *Journal of Climate*, **24**, 473–487.

— 2011b: Projected Future Seasonal Changes in Tropical Summer Climate. *Journal of Climate*, **24**, 473–487.

Sun, Z. and K. P. Shine, 1995: Parameterization of ice cloud radiative properties and its application to the potential climatic importance of mixed-phase clouds. *Journal of Climate*, **8**, 1874–1888.

Takahashi, T., 1978: Riming Electrification as a Charge Generation Mechanism in Thunderstorms. *Journal of the Atmospheric Sciences*.

Takemi, T., O. Hirayama, and C. Liu, 2004: Factors responsible for the vertical development of tropical oceanic cumulus convection. *Geophysical Research Letters*, **31**, 4–7.

Taylor, G. R. and M. B. Baker, 1991: Entrainment and detrainment in cumulus clouds. *Journal of the Atmospheric Sciences*, **48**.

Taylor, K. E., R. J. Stouffer, and G. A. Meehl, 2012: An overview of CMIP5 and the experiment design. *Bulletin of the American Meteorological Society*, **93**, 485–498.

Tebaldi, C. and R. Knutti, 2007: The use of the multi-model ensemble in probabilistic climate projections. *Philosophical Transactions of the Royal Society A*, **365**, 2053–2075.

Thompson, D. W. J., S. Bony, and Y. Li, 2017: Thermodynamic constraint on the depth of the global tropospheric circulation. *Proceedings of the National Academy of Sciences*.

Tompkins, A. M., 2005: The parametrization of cloud cover. *Moist Processes Lecture Note Series*.

Trapp, R. J., N. S. Diffenbaugh, H. E. Brooks, M. E. Baldwin, E. D. Robinson, and J. S. Pal, 2007a: Changes in severe thunderstorm environment frequency during the 21st century caused by anthropogenically enhanced global radiative forcing. *Proceedings of the National Academy of Sciences of the United States of America*, **104**, 19719–19723.

Trapp, R. J., N. S. Diffenbaugh, and A. Gluhovsky, 2009: Transient response of severe thunderstorm forcing to elevated greenhouse gas concentrations. *Geophysical Research Letters*, **36**.

Trapp, R. J., B. A. Halvorson, and N. S. Diffenbaugh, 2007b: Telescoping, multi-model approaches to evaluate extreme convective weather under future climates. *Journal of Geophysical Research*, **112**.

Trapp, R. J., E. Robinson, M. Baldwin, N. S. Diffenbaugh, and B. Schwedler, 2011: Regional climate of hazardous convective weather through high-resolution dynamical downscaling. *Climate Dynamics*, **37**, 667–688.

van Klooster, S. and P. Roebber, 2009: Surface-based convective potential in the contiguous united states in a business-as-usual future climate. *Journal of Climate*, **22**, 3317–3330.

van Vuuren, D. P., J. Edmonds, M. Kainuma, K. Riahi, A. Thomson, K. Hibbard, G. Hurtt, T. Kram, V. Krey, J.-F. Lamarque, T. Masui, M. Meinshausen, N. Nakicenovic, S. Smith, and S. Rose, 2011: The representative concentration pathways: an overview. *Climatic*

Change, **109**, 5–31.

Verbout, S. M., H. E. Brooks, L. M. Leslie, and D. M. Schultz, 2006: Evolution of the U.S. tornado database: 1954-2003. *Weather and Forecasting*, **21**, 86–93.

Waite, M. L. and B. Khouider, 2010: The Deepening of Tropical Convection by Congestus Preconditioning. *Journal of the Atmospheric Sciences*, **67**, 2601–2615.

Wallace, J. M. and P. V. Hobbs, 2006: *Atmospheric Science: An introductory survey*. Elsevier Inc., 2nd edition.

Wei, D., A. M. Blyth, and D. J. Raymond, 1998: Buoyancy of Convective Clouds in TOGA COARE. *Journal of the Atmospheric Sciences*, **55**, 3381–3391.

Williams, E. R., 1989: The tripole structure of thunderstorms. *Journal of Geophysical Research*, **94**, 13151.

Williams, E. R. and N. Renno, 1993: An Analysis of the Conditional Instability of the Tropical Atmosphere. *Monthly Weather Review*, **121**, 21–36.

Williams, E. R., S. A. Rutledge, S. G. Geotis, N. Renno, E. Rasmussen, and T. Rickenbach, 1992: A radar and electrical study of tropical "hot towers". *Journal of the Atmospheric Sciences*, **49**.

Wilson, D. J. and J. Gea-Banacloche, 2012: Simple model to estimate the contribution of atmospheric CO2 to the Earth's greenhouse effect. *American Journal of Physics*, **306**.

Wing, A. A., K. A. Reed, M. Satoh, B. Stevens, S. Bony, and T. Ohno, 2018: Radiative âĂŞ convective equilibrium model intercomparison project. *Geoscience Model Development*, **11**, 793–813.

World Climate Research Programme, 2014: SPARC US high vertical resolution radiosonde data. http://www.sparc-climate.org/data-center/data-access/us-radiosonde/.

Xu, K.-M. and K. A. Emanuel, 1989: Is the tropical atmosphere conditionally unstable? *Monthly Weather Review*, **117**.

Xu, K.-M., T. Wong, B. Wielicki, L. Parker, B. Lin, Z. Eitzen, and M. Branson, 2007: Statistical Analyses of Satellite Cloud Object Data from CERES . Part II : Tropical Convective Cloud Objects during 1998 El Niño and Evidence for Supporting. *Journal of Climate*, 819–842.

Yanai, M., S. Esbensen, and J.-H. Chu, 1973: Determination of bulk properties of tropical cloud clusters from large-scale heat and moisture budgets. *Journal of the Atmospheric Sciences*, **30**.

Zelinka, M. D. and D. L. Hartmann, 2010: Why is longwave cloud feedback positive? *Journal of Geophysical Research*, **115**, 1–16.

— 2011: The observed sensitivity of high clouds to mean surface temperature anomalies in the tropics. *Journal of Geophysical Research: Atmospheres*, **116**, 1–16.

Zipser, E. J., 2003: Some views on "Hot Towers" after 50 years of tropical field programs and two years of TRMM data. *Meteorological Monographs*.

Zipser, E. J. and M. A. LeMone, 1980: Cumulonimbus vertical velocity events in GATE. Part II: synthesis and model core structure. *Journal of the Atmospheric Sciences*, **37**, 2458–2469.